Ultra-Robust Graphene Based Bio-Nanocomposites and Their Electronic Applications

A Dissertation
Presented to
The Academic Faculty

by

Kesong Hu

In Partial Fulfillment
of the Requirements for the Degree
Doctor of Philosophy in the
School of Materials Science and Engineering

Georgia Institute of Technology
May 2016

Ultra-Robust Graphene Based Bio-Nanocomposites and Their Electronic Applications

Approved by:

Dr. Vladimir V. Tsukruk, Advisor
School of Materials Science and Engineering
Georgia Institute of Technology

Dr. Zhiqun Lin
School of Materials Science and Engineering
Georgia Institute of Technology

Dr. Kyriaki Kalaitzidou
Woodruff School of Mechanical Engineering
Georgia Institute of Technology

Dr. Eric Vogel
School of Materials Science and Engineering
Georgia Institute of Technology

Dr. Satish Kumar
School of Materials Science and Engineering
Georgia Institute of Technology

Date Approved: December 16th, 2015

Dedicated to my family

ACKNOWLEDGEMENTS

I appreciate the financial support from the Air Force Office of Scientific Research for the study on the bioinspired nanocomposites. I would like to take this opportunity to express my appreciation to my academic advisor, Dr. Vladimir V. Tsukruk, who has been guiding and inspiring me for the last four and half years, and made significant impact not only in my research career but also in my entire life. I also want to thank Dr. Kyriaki Kalaitzidou, Dr. Satish Kumar, Dr. Zhiqun Lin, and Dr. Eric Vogel, who devoted their precious time to serve on my PhD proposal and defense committees. Special thanks to Dr. Satish Kumar, Dr. Eric Vogel, Dr. David Kaplan, and Dr. Luzinov, who provided tremendous support to my ongoing research activity by sharing their expertise, insights, and instruments.

Dr. Maneesh K. Gupta and Dr. Dhaval D. Kulkarni were senior members in our group and mentored me to initiate the lab work in this study. All SEMA members have contributed to the excellent working environment and the perfect collaboration chemistry in the entire lab. I would thank everybody for sharing their passion, intelligence, talent, and patience to help me arrive at this stage. Specifically, Dr. Yi Yin, Dr. Chunhong Ye, Dr. Ikjun Choi, Rui Xiong, Lorenzo Tolentino, Anise Grant, Ruilong Ma, Paul Zackowski, and Michael Russel have provided significant collaboration or assistance at different stages of my research for multiple meaningful projects, which stand no chance to be as impactful as they are without their help. Special thanks also go to Dr. Wenzhuo Wu from Prof. Zhong Lin Wang's group for offering great opportunities to expand the application of graphene oxide-silk fibroin system to triboelectric nanogenerators.

Lastly, I appreciate the unconditional support from my parents and my wife, Shuai Xiang. They founded the basis of my pursuit of my gem of the academic crown – Doctor of Philosophy. The love and everything they have granted me can never be paid back equally, but I will try for my entire life.

TABLE OF CONTENTS

LIST OF TABLES

LIST OF FIGURES

SUMMARY

This study is focused on the fundamental principles of fabricating graphene based bio-nanocomposite materials and optimizing their structural and functional properties for prospective bioelectronics applications. The status of the research on graphene based functional nanocomposites has been critically reviewed and the motivation and challenges to develop ultra-robust, functional nanocomposite films are presented. Biopolymers and biomaterials, such as silk fibroin and cellulose nanocrystals, in addition to graphene oxide are chosen as the matrix, binding and reinforcing components, respectively, to investigate the optimized interfacial interactions between biomaterials and the heterogeneous graphene derivatives with various degrees of chemical functionalization.

Two different aspects of the graphene based bio-nanocomposites were the foci of this study: 1) the mechanical enhancement by the synergistic interactions between the nanofiller components and biopolymer matrix, and 2) the effective improvement of electrical properties of the graphene oxide components in the bio-nanocomposite for prospective electrical and sensing applications. Specifically, the major achievements can be summarized by the following:

- The interfacial interactions between silk fibroin and graphene oxide has been carefully tuned through layer-by-layer assembly to elucidate the optimized surface interactions for heterogeneous components in bio-nanocomposites. Record-high mechanical properties have been reported for the ultra-thin graphene oxide-silk fibroin nanocomposites fabricated here, including Young's modulus of 145 GPa, ultimate stress of 330 MPa, and toughness of 2.2 MJ m^{-3} for 50-nm-thick membranes. Theoretical analysis suggested that an interphase reinforcing region between the graphene oxide and the silk fibroin components due to the high-density of randomized weak interactions at the matrix-filler interface.

- Spin assisted layer-by-layer assembly approach has been refined and dynamic spinning routine has been suggested to unfold the protein molecules during the adsorption, spreading, and assembly process. The distinctive morphology and secondary structures of the silk molecules have been carefully imaged by high-resolution atomic force microscopy and quantified by Fourier transform infrared spectroscopy. As a result, the enhanced interfacial interactions further improved the mechanical properties of the resulting silk fibroin-graphene oxide nanocomposite to show extremely high Young's modulus of 170 GPa and toughness of 3.4 MJ m^{-3}. The interfacial strength and the interphase thickness are 100% and 50% higher, respectively, than those of the samples made by the static spin coating method.

- Thin films were fabricated by vacuum filtration of graphene oxide – silk fibroin mixtures to fabricate graphene "bio-paper" with significant improvement in mechanical properties and water resistance in contrast to pristine graphene oxide papers. The ultimate stress, Young's modulus, and toughness are 300 MPa, 26 GPa, and 2.8 MJ m^{-3}, respectively, which are 330%, 330%, and 370% higher than the pristine graphene oxide papers. An innovative technique has been applied to reduce patterned surface of the graphene bio-paper to restore its electrical conductivity by using active metal as the reducing agent. In neutral pH and ambient conditions, the electrical conductivity of the reduced graphene oxide bio-paper was around 1300 S m^{-1} being comparable to those of the doped silicon and conducting polymers.

- The metal-assisted graphene oxide reduction technique has been extensively investigated and optimized for efficient and effective fabrication of electrically conductive patterns that are used for flexible electronics. The electrical conductivity of the samples largely depends on the thickness of the reduced layer and the extent of the oxygen removal (C/O ratio). By varying the reducing pH, time, and number of cycles, the highest electrical conductivity reaches 15200 S m^{-1}, and the work function of the reduced graphene oxide surface could be tuned over a range of 0.7 eV, from 4.9 eV for pristine graphene oxide to 4.2 eV for reduced samples.

- A combination of 1D and 2D nanomaterials using cellulose nanocrystals and graphene oxide has been suggested for high performance nanocomposite thin films for excellent mechanical, optical, and electrical properties. By avoiding extensive content of soft biopolymer matrix, the unique combination between these two conventional nanofillers with excellent mechanical properties resulted in synergistic strengthening and toughening effect, showing unprecedented high ultimate strength (650 MPa), toughness (3.8 MJ m^{-3}), and elastic modulus (169 GPa). In addition, the optical and electrical properties are also characterized with 50% optical transmittance at 550 nm and 5000 S m^{-1} electrical conductivity.

- A new type of human-tactile sensing materials using the metal-graphene oxide electrodes has been demonstrated based on the electrochemical reaction between active metal and graphene oxide surface. The tactile sensing performance of this novel hybrid material is extensively tested in various experimental and practical settings. The self-powered bio-touch sensor can output over 800 mV open circuit voltage upon actuation with tunable output level by varying the electrode gap size and metal species. The response speed is higher than 20 Hz with a unique ability to fabricate 2-D touch pads with fewer electrodes.

Flexible electronics, especially those that are potentially useful for biomedical applications, is a big opportunity as well as challenge for the advancement of the functional bio-nanocomposite research. Graphene based bio-nanocomposites are promising to bridge the excellent mechanical properties and the effective electrical conductivities in the prospective bioelectronics. We suggest that the understanding of the integration of biopolymers and graphenes using versatile assembly techniques and the successive chemical modification of the electrical properties of the nanocomposite discussed in this study is critically important and inspiring for tackling the challenges faced by the employment of flexible and robust structural and bio-microelectronic materials.

Chapter 1 Introduction to polymer nanocomposites

1.1 Background

Synthetic polymer (nano)composite materials were introduced centuries ago and used as structural components due to their much improved mechanical properties, chemical inertness and stability, versatile processing techniques, and reduced cost. [1, 2] For many traditional composite materials, polymers conventionally serve as elastomeric and flexible matrices by contributing high elasticity, strength, flexibility, controlled surface and bulk properties, and other unique physical properties. In this chapter, the background of nanocomposites will be introduced by reviewing the polymeric matrices and inorganic fillers, respectively. Challenges and motivations of the proposed study will also be presented in the end of this chapter.

1.1.1 Choice of polymeric matrices

Benefiting from almost infinite choices of monomers and chemistries available, polymer matrices can be precisely tuned and controlled to exhibit the whole spectrum of physiochemical properties for very different applications, including hydrophobicity, ionozibility, crystallinity, transparency, toughness, strength, densities, and degradability. [3, 4, 5, 6, 7, 8]

Among the structural polymeric matrices for the advanced nanocomposites, elastomers, thermoplastics, epoxy, block copolymers, and hydro/aerogels are used widely due to their unique physical and chemical properties, which can be tailored to various applications. [2, 9, 10, 11, 12, 13] For example, elastomers are highly stretchable polymers consisting of lightly crosslinked (chemically or physically) long chains. [14, 15] In contrast, epoxy resins contain rigid segments and are very heavily crosslinked so that their stiffness, as well as their brittleness, are extremely high. [16, 17] Thermoplastic polymers are reinforced by physically

ordered domains which are not chemically crosslinked so they can be shaped, melted, and recycled.

Block copolymers are essentially composed of two or more chemically divergent polymer chains that are covalently linked end to end in order to create complex nanoscale morphologies. [2, 9, 11] One of the biggest benefits of the block copolymers is that the physiochemical properties of the resulting materials can be tuned by adjusting the content of species that make up the chain and the lengths of each component. [18, 19] Block copolymers have the inherent advantage of possessing heterogeneous properties, *e.g.*, amphiphilicity, which are controlled by microphase states with sharp interfaces and tailored 3D morphologies. [20] Hydrogels or aerogels with their porous morphology and permeable properties can be swollen in water or contain gas, which can be used for scaffolds, catalyst support, controlled release/adsorption, shock absorbance, and low-density thermal or electromagnetic shielding. [21, 22, 23, 24, 25]

Natural biomaterials have drawn huge attention from the researchers as well as the general public because of their intricate and inspiring structures and superior performance, one outstanding example of which is silkworm silk. Silkworms have been cultivated for thousands of years to produce textile silk fibers. Thanks to its hierarchical molecular structure, pristine silk fiber is one of the strongest natural biomaterials, with 600-800 MPa ultimate stress and 18% ultimate strain.[1, 2] Consequently, silk sutures have been used in surgical operations for centuries due to the outstanding mechanical properties, in addition to their inherent biocompatibility and relatively good biodegradability.[1, 2]

However, until a few decades ago was silk fibroin (SF) - the prevailing protein constituent of silk fiber – studied systematically. Silk fibroin consists of two protein chains connected by disulfide bond[3, 4], where the molecular weight is between 130 and 390 kDa due to the various degrees of hydrolyzation and degradation.[4, 5] The longer protein chain is composed of alternating predominant hydrophobic and relatively short end-capping hydrophilic amino acid sequences, which grant the amphiphilicity of the material.[3, 6] The non-neutral amphiphilicity brings the aqueous processibility of the silk fibroin, but the prevailing hydrophobic segments make the aqueous solution unstable due to hydrophobic

interactions and sequential crosslinking. In spite of that, silk fibroin is also sensitive to pH value, salt ions and high temperature, in presence of which the solution may undergo gelation. As a result, silk fibroin solutions are usually prepared with ultra-pure water for the minimum amount of time and stored at low temperature and mildly basic environment. Ionic liquids are also reported to be a good solvent of silk fibroin, essentially depending on the concentration and species of the anions.[7]

The secondary structure of silk fibroin, i.e. molecular conformation, defines its physical and chemical properties. Antiparallel β-sheet crystals can be induced by abrupt drying, shear straining, water annealing, and alcohol treatment.[8, 9] The β-sheet crystals are a few nanometers in size[10, 11] and work as nano-filler and crosslinker in the amorphous matrix, dramatically giving rise to the mechanical properties. β-sheet crystals induced by different methods exhibit various shapes, sizes and packing orders, affecting the mechanical properties and hydration.[9] The methanol treated ultrathin silk fibroin layer-by-layer (LbL) membranes have been reported to be ~8 GPa Young's in modulus and 0.5-3% of elongation-to-break.[8] Due to the technical difficulties in directly extracting silk fibroin from the silkworm glands, reconstituted SFs are commonly used in research and production.[3, 8, 12, 13-19] Reconstituted SFs are made from the dissolved and dialyzed pristine silk fibers (see the Experimental section for detail). To date, reconstituted SFs have been made into threads[2], films[8], hydrogels[16], scaffolds[17], capsules[1] and biocompatible coatings[18] by drop casting, chemical modification/crosslinking, lyophilization and LbL deposition. Molecular level engineering of the material is also undertaking its way due to the progressive understanding of its secondary structures and the relationship between the structures, properties and processing conditions.

Despite significant efforts, the mechanical properties of polymer matrices can be considered to be modest in many cases. Indeed, the elastic modulus of linear amorphous polymers is usually around several gigapascals in their bulky glassy states except some famous examples of rigid polymers and polymer fibers with highly oriented polymer chains. [2] Moreover, the mechanical strength of polymer materials will further decrease by several orders of magnitude when heated above the glass transition temperature. Therefore, a variety of high performance inorganic fillers are frequently introduced as important

reinforcing components in order to significantly improve the structural strength of polymer composites and induce some additional functional properties (*e.g.*, thermal or electrical conductivity).

1.1.2 Reinforcing components

Conventional polymer composites are usually fabricated from a relatively compliant matrix and stiff inorganic fillers in the form of fibers, laminates, or particles. The philosophy of the fabrication of high performance composite materials is to synergistically combine the strengths of multiple constituents and optimize the primary mechanical properties. Glass fibers, carbon fibers, wood sheets, metal particles, and inorganic mineral particles are all common fillers in conventional composites composed of continuous matrices of thermoplastic polymers, rubbers, hydrogels, or thermosets. However, conventional polymer composites suffer from some common issues caused by very dissimilar properties of matrices and components, which include modest improvement of mechanical strength, reduced compliance, catastrophic failure caused by interfacial defects and weak interfacial bonding, accelerated degradation caused by mismatching of coefficient of thermal expansion, and significant manufacturing cost in some cases. [26]

On the other hand, nanocomposite materials with nanoscale fillers have emerged in the past couple decades as a promising novel class of materials which take advantage of greatly increased interfacial area, higher loads, controlled interfacial interactions, and higher overall compliance. The mismatch of the physical properties is much less critical and the interfacial area between the filler and the matrix is maximized so that the interfacial strength can be much improved. [27] Currently, multifunctional nanocomposites with improved mechanical performances are primarily fabricated by addition of pre-treated carbon nanotubes and nanofibers [28, 29], inorganic nanoparticles [28, 30], and metal nanostructures. [30, 31, 32]

Among various reinforcing nanoscale components, clay, carbon nanotubes, and metal/ceramic nanoparticles are the most common nanofillers employed in the past two decades to fabricate a variety of high performance nanocomposite materials. [25, 33, 34, 35, 36, 37, 38, 39, 40, 41, 42] Clay nanoparticles (*e.g.*, montmorillonite, MMT) possess excellent

mechanical strengths and optical transparency, they are relatively cheap, and can be easy pre-treated and dispersed in a common solvents and even in an aqueous environment. [25, 33] The 2D geometry of the MMT nanoparticles is also beneficial for their self-assembly in organized layered morphologies, which are important to anisotropic stress transfer applicatoins. The mechanical performance of these nanomaterials can show much improvement compared to traditional composites. For instance, the ultimate strength MMT/poly(vinyl alcohol) (PVA) nanocomposites can reach around 220 MPa with the elastic modulus as high as 19 GPa. [43] However, because MMT is a stiff inorganic platelet filler the limited flexibility and biodegradability of these nanocomposite can be compromised.

In addition, cellulose nanocrystals (CNCs) is a unique whisker shaped bio-originated nanofiller that have emerged as an important biodegradable, biorenewable reinforcing components in nanocomposites. [44, 45, 46, 47, 48] CNC is purified from wood pulp by acid hydrolysis process. The length of CNCs is around 250 nm and the diameter varies from 3-10 nm. The rod-shaped nanoparticle of CNC is usually negatively charged due to the presence of the $–SO_3H$ groups from the acid hydrolysis.[44, 45] Due to the high crystallinity of the material, the elastic modulus of the single CNC is around 150 GPa. And the surface charge of the CNC greatly facilitates the strong ionic interactions between the components in the nanocomposites.[48]

Metal and carbon nanoparticles show exceptional reinforcing properties and can add electrical conductivity, catalytic activity, and plasmonic properties. [4, 40, 41, 42] However, metal nanoparticles are not readily dispersable in polymeric matrices due to the hydrophobicity of the nanoparticles and limitations of the ligands utilized. Therefore, grafting of nanoparticles with various polymeric ligands or growing metal nanoparticles *in situ* have been implemented. [49, 50, 51, 52] Alternatively, metal oxide nanoparticles show good aqueous processibility, functional properties, and high mechanical strengths compared to corresponding metal nanoparticles, but their integration in polymer matrices can be challenging. [53, 54, 55]

Carbon black is the most commonly used nanomaterial in industry for mechanical reinforcement and damping in synthetic rubbers, thermal properties of polymeric materials, and electrical modification in polymer matrices. [56, 57, 58] Carbon black are mainly amorphous materials with their moderate physiochemical properties in all major aspects. However, these fillers are abundant, can be readily functionalized, and are very inexpensive. The surface-to-volume ratio of carbon black is lower than that of activated carbon and its mechanical and electrical properties are not comparable to its crystalline carbon cousins, thus novel carbon-based fillers have been intensively elaborated in the past two decades.

Recently, carbon nanotubes and buckyballs have become much more sophisticated and popular nanostructures. They are seen as one of the most promising nanofilling materials because of their low density, extremely high aspect ratio (nanotubes), minute dimensions, outstanding mechanical and thermal properties, good chemical inertness, and tunable electrical properties. [34, 35, 36, 37, 59] However, the progress in nanocomposites made by using carbon nanotubes is still continuing and great challenges still remain to be resolved. Among most critical unresolved issues are poor aqueous dispersability, stubborn contaminations, excessive aggregation, high cost, poor control of surface chemistries, and low interfacial interactions with the polymeric matrix. Significant efforts in the development of these nanocomposites are summarized in a number of books and reviews and will not be considered here. [60, 61, 62, 63, 64] Recently, various modern graphene materials have emerged as a new class of prospective components for advanced nanocomposites with intriguing new opportunities for the integration into polymer matrices.

1.1.3 Graphene-based nanocomposites

Indeed, the number of publications on graphene-based nanocomposites has grown exponentially in recent years from almost non-existing records before 2006 to almost two thousand in the past two years (**Figure 1.1**). Even prior to 2010, less than two hundred publications can be counted in total with no significant records found before 2006 (which probably caused in particular by a terminology gap).

However, since the year of 2010 the number of peer-reviewed publications on graphene-based nanocomposites has surged greatly and keeps growing exponentially. Apparently the

Nobel Prize in Physics for graphene has drawn vast attention from the materials community and brought a dramatic number of new research groups to this field. Indeed, the number of the graphene nanocomposite publications appeared only in past two years exceeds several times those ***ever published*** in this field (Figure 1.1). Therefore, even if some comprehensive reviews have been recently published on this topic mostly in 2010-2014 (see summary of some recent reviews below) the overall landscape changed dramatically in the past two years alone and, therefore, it is necessary to summarize again very recent results and discuss the newest trends in this fast evolving field.

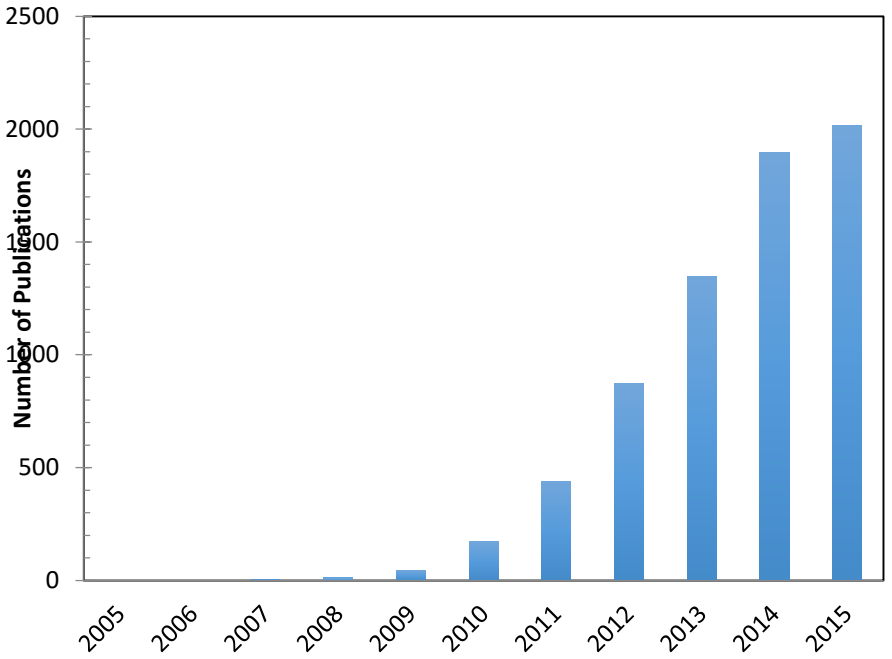

Figure 1.1 Number of the peer-reviewed publications (articles and reviews) containing the keywords "graphene" and "(nano)composite(s)" since 2005. The data for the year of 2015 is off trend due to database lag. Data source: Web of Knowledge, Thomson Reuters.

Overall, polymer-graphene (here under a general term of "graphene" we usually imply not just traditional monolayer graphenes but also various chemical derivatives if not specified otherwise) nanocomposites show not only record mechanical properties but also impressive functional properties, such as electrical (semi-) conductivity, unique photonic/optical transportation, anisotropic transport, low permeability, and fluorescence quenching. It has already been demonstrated that the introduction of even a small fraction of a graphene component can dramatically improve the mechanical performance of the variety of the polymeric matrices and some extraordinary reinforcing and functional

properties have been reported very recently. Graphene materials and their various derivatives show tremendous potential in revolutionary enhancement of mechanical, electrical, thermal, and chemical properties of polymeric materials relevant for a wide range of emerging demanding applications (**Figure 1.2)**. [34, 65, 66, 67, 68, 69, 70, 71]

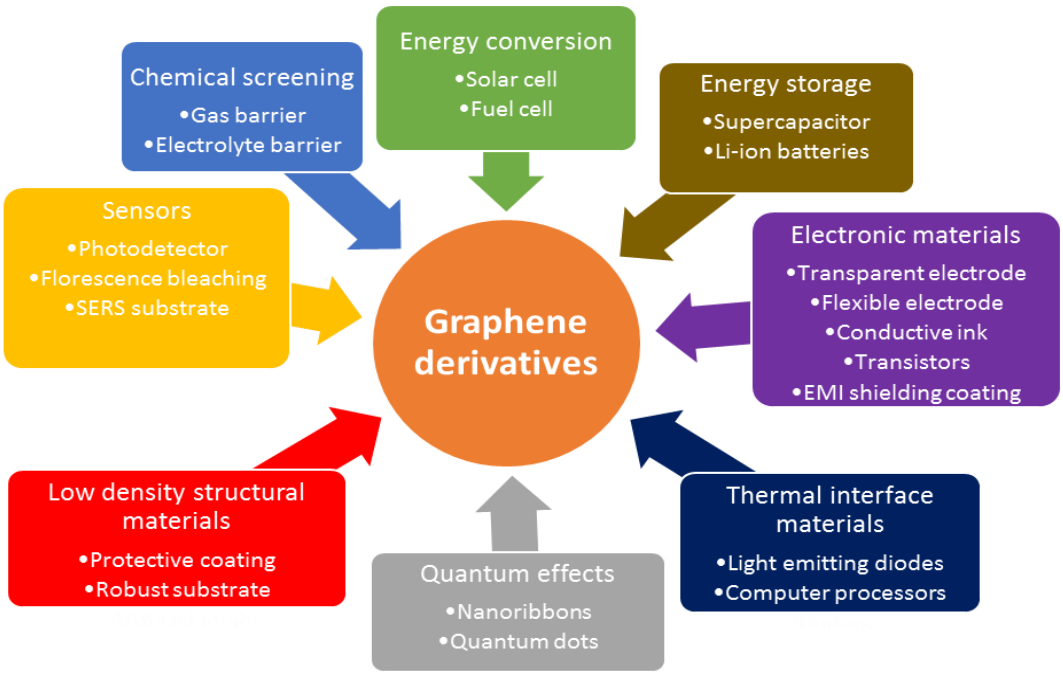

Figure 1.2 Graphene derivatives show promising results for various fields, including energy conversion [65], energy storage [66], electronic materials [67], quantum effects [68], low density structural materials [69], sensors [70], chemical screening applications [34], and thermal interface materials [71].

It is worth to note that although the current research activities are greatly focused on the understanding of fundamental phenomena and utilization of the excellent properties of the graphene materials as efficient nanofillers, the next exploding area on the graphene material research relevant to nanocomposite materials might be the development of atomic multi-stacking of heterogeneous 2D structures (also known as "van der Waals crystals") with promising extraordinary functional properties. [72]

The initial results on graphene-polymer nanocomposites are summarized in a number of excellent recent reviews as briefly introduced here. In an important "early" publication, Kim *et al.* provided a general review on graphene-polymer nanocomposites. [73] Kuilla *et al.* introduced examples from different combinations of polymers with graphene materials

in addition to presented general background on graphene and its derivatives. [74] Compton *et al.* focused on graphene and graphene oxide, and discussed the properties of these nanofillers in detail. [75]

In their review, Huang *et al.* paid major attention to devices made of polymer-graphene nanocomposites and the other constituents including metal, semiconductor, and organic small molecules. [76] Yang *et al.* critically evaluated the fabrication of graphene multilayers, including graphene-polymer nanocomposite thin films fabricated by layer-by-layer assembly. [77] Young *et al.* reviewed graphene-polymer nanocomposites and discussed the modeling, fabrication, and characterization of these materials. [78] Among the most recent reviews, Wu *et al.* discussed the structures and general functional applications of the nanocomposites made from chemically modified graphenes. [79] Finally, very recently Sun *et al.* provided insight on the integration of both graphene and carbon nanotube materials in polymer nanocomposites. [34]

In this review, we focus on very recent (mostly published in 2010-2013) and the most spectacular results of the outstanding mechanical as well as other physical properties of the polymer-graphene nanocomposite materials, and discuss some fundamental properties and the processing approaches of such nanocomposites. We highlight the fundamental properties and critical characteristics of graphene materials as prospective reinforcing nanofillers, their chemical and physical functionalities, the interfacial interactions important for the effective reinforcement, and the methods of the fabrication of these materials. Finally, we briefly summarize the theoretical works and experimental efforts on the optimization of the elastic modulus values, strength, deformation, and toughness, major mechanical characteristics and discuss the results of the ultimate mechanical performance of such nanocomposites with variable composition, chemistry, and morphology.

1.1.4 Graphene and graphene derivatives as prospective filler nanomaterials

In this section, we provide a brief reminder of the fundamental properties and microstructure of graphene materials of different types. Similar to carbon nanotubes, basic graphene is composed of only carbon atoms, but it is a 2D flat sheet rather than rolled up monolayer of carbon. Benefiting from its pure sp^2 hybridization network, graphene

materials frequently possess record characteristics of mechanical, thermal and electrical properties. The most important materials characteristics for our discussion are: the highest, 1 TPa, elastic modulus [80], very high, 5.1×10^3 W m^{-1} K^{-1} thermal conductivity [81], and the highest known intrinsic electrical conductivity of 6×10^5 S m^{-1}. [82] Among the most interesting and fundamental properties we should mention the theoretical van der Waals thickness of individual graphene sheets of 0.34 nm, which is the thinnest 2D nanofiller known to date (**Figure 1.3a**). [83] Other critical parameters of these materials are extremely high aspect ratio (ratio of lateral dimensions to the thickness) and high intrinsic flexibility.

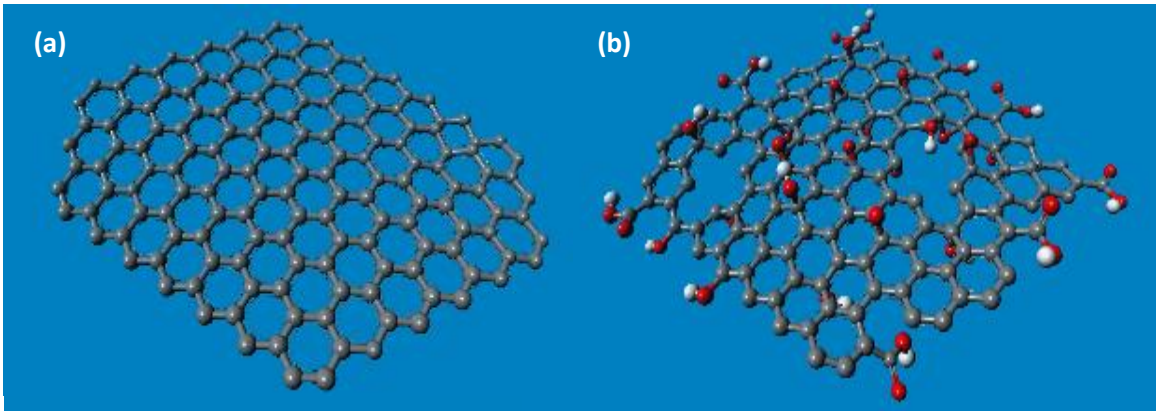

Figure 1.3 Atomistic structures of individual sheets of basic graphene (a) and graphene oxide (b). The atoms are color-coded: grey – carbon, red – oxygen, and white – hydrogen.

Pristine graphene is usually obtained or synthesized by mechanical exfoliation of graphite and chemical vapor deposition (CVD). [83] Mechanical cleavage or exfoliation of highly ordered pyrolytic graphite (HOPG) is an original top-down method that can easily produce large quantity of graphene sheets with different microscopic dimensions, individual or multilayered flakes, and modestly defective microstructure.

CVD synthesis of graphene uses carbon-rich precursors (*e.g.*, methane) and recombines the carbon atoms on the surface of metal foil (copper or nickel) in inert atmosphere at over 1000°C. [73] By controlling the reaction parameters, such as the ratio of the different precursors, temperature, and substrates, single, double or multiple layer graphene with various sizes can be produced. The synthesis of graphene does not require catalysts in gas phase that are hard to be removed, and the size of graphene can be controlled from nanoscale to millimeter scale, giving it huge potentials for nanocomposite applications. However, both mechanical exfoliation and the CVD synthesis result in defective and

heterogeneous structures. Moreover, time and energy consumption for their fabrication are high for real mass-production of consistent graphene materials in large quantities.

Therefore, different graphene derivatives that partially preserve the extraordinary properties of graphene materials and overcome some of their deficiencies have attracted more attention. One of the most popular graphene derivatives, which can be utilized for the fabrication of polymer-graphene nanocomposites is graphene oxide with excellent mechanical properties. Even though preliminary studies show that the biocompatibility of graphene oxide is good in many cases [84, 85], extensive investigation needs to be carried out to discriminate cytotoxicity and metabolic accumulation for prospective biomedical applications. [86]

Graphene oxide (GO) is an oxidized graphene derivative, which can be widely used as an alternative or precursor for graphene materials due to its high dispersibility and processibility in aqueous environment. [8, 87, 88] It is produced from mineral graphite flakes by thermal oxidation method invented by Hummers and modified by successors. [89] The resulting single atomic layers graphene-like material possess high density of epoxy and hydroxyl groups on both sides of the basal carbon plane and carboxyl groups around their edges (Figure 1.3b). [90] Recent studies of surface defect distribution using electrostatic force microscopy (EMF) [91, 92, 93] demonstrated the heterogeneous distribution of nanoscale (~100 nm across) oxidized domains which completely dissipate after chemical reduction to graphene (**Figure 1.4**). [94]

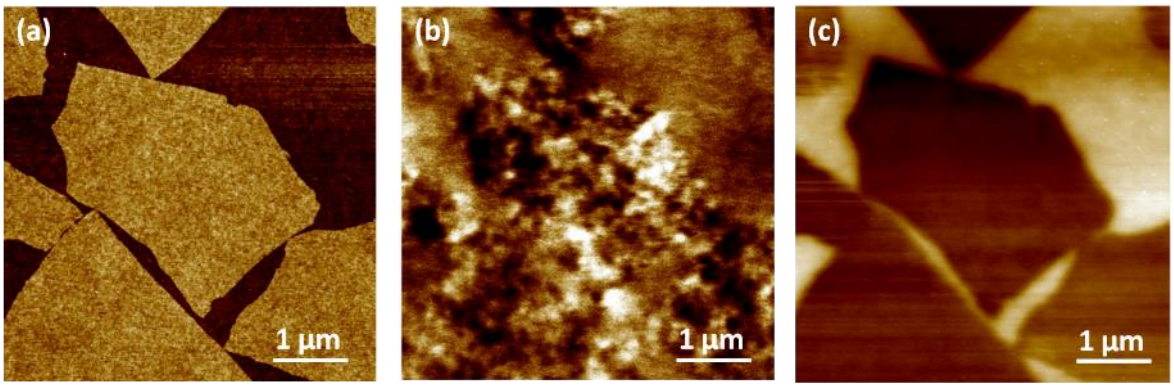

Figure 1.4 (a) Topography, (b) EFM-phase image before reduction, and (c) after chemical reduction of the same graphene oxide flakes.

Molecular simulations have shown the bonding energy and shear strength have been significantly improved by inducing the surface and edge functionalities on graphene sheets, which is critically important for their integration into polymer matrix. [95] The ratio of carbon and oxygen in graphene oxide materials is close to 2:1, the overall surface coverage with oxidized regions can reach 60-70%, and point defects are present among the honeycomb primary structure, all reflecting an intense and highly localized oxidization processes (Figure 1.3b). [3, 74, 75, 96]

The theoretical thickness of graphene oxide is around 0.72 nm, doubling that of the pristine graphene due to the presence of additional prominent bulky surface functionalities resulting from the oxidation process. [3] It is worth to note that the actual thickness of graphene oxide flakes might be slightly larger due to surface contaminants, organic adsorbates, underlying substrate roughening, or occasional presence of bulkier functionalities. [3, 69]

Although lacking electrical merits of graphene and being somewhat inferior in ultimate mechanical performance, graphene oxide and corresponding derivative materials still exhibit huge potential in nanocomposite fabrications due to its outstanding mechanical properties, high flexibility, high bonding potential, and extremely high aspect ratios. The elastic modulus of a single graphene oxide sheet is as high as 250 GPa despite the high concentration of local defects, which is much higher than that demonstrated by the most of known fillers. [97, 98] This high tensile strength is combined with high lateral flexibility, which facilitates nanocomposite flexibility but can be problematic during processing. Graphene oxide flakes are negatively charged in slightly acidic and basic conditions due to the surrounding carboxyl groups. The zeta potential of graphene oxide decreases progressively with higher pH values and can be as low as -50 mV at pH=10.5. [88] Graphene oxide does not precipitate in most polar solvents and can be incorporated into correspondingly charged polyelectrolyte matrices. [3, 87]

Even pure graphene oxide materials without any polymer matrices show outstanding performance. Graphene oxide “paper” made by vacuum-assisted self-assembly (VA-SA) and evaporation methods possess very high values of the elastic modulus of 18-36 GPa, with only water molecules serving as binders. [99, 100, 101] Localized water molecules link

the neighboring graphene oxide flakes by hydrogen bonding while free water molecules that are intercalated in the interlayer spacing of graphene oxide layers lubricate the inter-layer slippage, which in turn decreases the efficiency of stress transfer between layers. That is why the reported values of the mechanical characteristics of different graphene oxide papers strongly depend upon local humidity conditions and might disagree in some cases. To this end, it has been demonstrated that the covalently bonded graphene oxide paper with the use of organic, ionic, or polymeric crosslinkers possesses enhanced elastic modulus as compared to pure graphene oxide paper. The elastic modulus as high as 120 GPa can be reached with dense crosslinking. [99]

It is also worth noting that graphene oxide can be reduced to graphene-like structures with similar mechanical and conductive properties by chemical, electrochemical, thermal, hydrothermal, and photothermal reducing techniques. [102, 103] Hydrazine, hydriodic acid (HI), electron complexes in liquid ammonia, metal particles, sodium hydroxide, and infrared laser illumination can all remove the oxygen-containing groups from the graphene oxide surfaces and restore proper hybridization of sp^2 electronic orbitals. [104, 105, 106, 107, 108] Metal foil and laser beam can directly pattern graphene oxide films with controlled localization of the reduced regions. Aluminum foils have been employed to reduce graphene oxide paper with intercalated natural binders with controlled surface patterning and depth distribution. [109] Light-induced and plasmon-assisted graphitization of amorphous carbon may also be applied to pattern the reduction of graphene oxide. [110] These patterned reduced graphene oxide (rGO) materials can be made ready for integration of into flexible electronic devices. However, the rGO electronic materials are normally flimsy and polymer matrices are usually considered to work as mechanical support for their proper functioning.

1.1.5 Interfacial interactions and polymer matrices

Interfacial interactions between polymers and graphene-based materials play a key role in the mechanical integrity of the corresponding nanocomposite and their mechanical performance. Due to the homogeneous carbon composition of graphene without other functionalities, the interactions with polymers are limited to weak van der Waals forces, π-

stacking, and hydrophobic-hydrophobic interactions. [111, 112] Van der Waals forces are universal attractive interactions between molecules generated by the transient or permanent dipoles of the molecules. Although very weak, these forces contribute the major part of interfacial attractions between graphene and common polymers like polyethylene due to intimate contact and very large specific surface area. [113] A special case of π-π interactions is especially important for the graphene materials with the electron-rich aromatic rings interacting with a variety of chemical species with phenyl rings, which can act as strong bonding sites. [114, 115] Then, π-stacking can adapt to different space organizations and significantly enhance bonding in graphene nanocomposites. Hydrophobic-hydrophobic interactions are another common means for binding graphene in hydrophobic polymer matrices.

In contrast, graphene oxide possesses abundant oxygen-containing polar functionalities, such as epoxide, carbonyl, hydroxyl, and carboxyl groups. [102] The choices of functionalization and resulting interactions with various polymers are much more versatile for graphene oxide materials. Furthermore, covalent grafting of polymer chains on graphene oxide surfaces can achieve a better blending of graphene oxide component and the polymer matrix. [116] The mechanical strength of the covalent bonds is the highest among the intermolecular interactions and the compatibility of grafted graphene oxide is much better due to the replacement of exposed functionalities. Polymers that are terminated with hydroxyl groups are directly used to crosslink the graphene oxide sheets with their carboxyl groups through esterification. The interfacial crosslinking dramatically increases the modulus of the nanocomposite, but the compliance can be compromised due to the permanent and interlocking structure caused by the covalent crosslinking. [116] The electrostatic interactions are also strong and restorable alternatives to covalent bonding for graphene oxides with polar functionalities. Due to the strong electrostatic interactions and restorability of these interactions during variable strain loading, the nanocomposites can be much stronger and tougher than their counterparts without graphene oxide fillers. [3]

Hydrogen bonding between two highly polarized donor and acceptor groups are abundant for graphene oxides. The epoxide, hydroxyl, carbonyl, and carboxyl groups on graphene oxide are all highly polarized with oxygen atom being the negative center. [75] As a result,

graphene oxide can bond with various polar polymers, especially polyelectrolytes and proteins, through hydrogen bonding networks and polar interactions. [117] Due to the high density of the highly polar functionalities, the interfacial strength of the polymer-graphene nanocomposites with hydrogen bonding network can be as high as, if not higher, than that of the covalently crosslinked nanocomposites. The toughness of such hydrogen bonded nanocomposites is greatly improved due to the *in situ* restoration ability of the hydrogen bonds, which is another advantage over the permanent nature of the covalent crosslinking. [69]

It is worth noting that graphene oxide has recently been suggested as amphiphilic material, meaning that their heterogeneous surface contains both hydrophobic and hydrophilic domains, which can interact concurrently with very different functionalities of hydrophobic and hydrophilic nature. [118] The amphiphilicity of graphene oxide suggests two important facts: (1) graphene oxide is readily bonded with either polar or non-polar polymers to improve the mechanical properties of the nanocomposites; and (2) the strength of the interface can be further improved if a matching heterogeneous polymer interfaces are chosen. For every domain on the graphene oxide surface, either hydrophobic graphitic areas or hydrophilic oxidized areas, the amphiphilic macromolecules can spontaneously assemble to maximize the interfacial interactions. However, more studies on a wider spectrum of polymeric matrix and nanofiller compositions are needed to fully reveal the principles of the enhancing heterogeneous interactions.

For comparative purposes, we summarized the common bondings which are characteristic for graphene-based materials, spatial range of interactions, and their relative strengths in **Table 1.1**. [119, 120, 121, 122] Apparently, it is ideal to utilize all possible interactions in the nanocomposite, not just covalent bonding, to ultimately fabricate a strong as well as tough system. As we also indicated in Table 1.1, all the weaker interactions are restorable on site after being broken, which is favorable to prevent macroscopic failures and facilitate the mechanisms of self-healing of nanocomposites.

Table 1.1 Intermolecular interactions relevant to graphene components.

Interaction	Strength (kJ mol^{-1})	Bond length (nm)	Restorability	Example
Covalent	355 - 730 [119]	0.15 - 0.26 [119]	N	C-C backbone
Hydrophobic	$40r$ [120] [a]	<0.3	Y	Protein-graphene
π-stacking	8 - 12 [121]	0.5 [121]	Y	Polystyrene-graphene
Coulombic	5.8 - 232 [119] [b]	0.3 - 1.0 [119]	Y	Polyelectrolyte-graphene oxide
Hydrogen	4 - 20 [119]	0.24 - 0.35 [119]	Y	Poly(vinyl alcohol)-graphene oxide
Van der Waals	2 - 4 [119]	0.3 - 0.5 [122]	Y	Any two molecules

[a] r is the radius (nm) of solute molecules in water.
[b] Varies largely by different dielectric constants of media.

1.2 Theoretical grounds for the selection of nanofillers

Due to the extreme contrasts in composition, interactions, and properties between the dissimilar components in nanocomposites, conventional models of composite reinforcement have issues in describing the mechanical performances of the new materials with non-traditional reinforcing nanofillers. Therefore, in this section we will briefly refresh several common models that are used to evaluate the mechanical properties (mostly the elastic modulus value) of the nanocomposites based on the geometry, dispersion, and interfacial properties, and their applicability to graphene-polymer materials considered here.

Yong's modulus is the intrinsic property that represents the mechanical strength of the nanocomposite under modest deformations. Unlike ultimate strength and ultimate strain, Young's modulus values only reflect the stress-strain behavior on the initial state of the loading process, and can be predicted by models unlike other mechanical characteristics. For instance, the popular Takayanagi model for the fiber/laminate composite systems predicts simple rules of mixing under different types of stress transfers: [2]

$$E_{\parallel} = E_m \nu_m + E_f \nu_f \qquad (1.1)$$

$$\frac{1}{E_{\perp}} = \frac{\nu_m}{E_m} + \frac{\nu_f}{E_f} \qquad (1.2)$$

where $E_{\parallel}$ and $E_{\perp}$ represent the Young's modulus parallel and perpendicular to the direction of fiber axis or laminate plain, respectively; $E_m$and E_f are the Young's modulus of the matrix and the filler, respectively; ν_m and ν_f are the volume fractions of the matrix and the filler, respectively.

The Takayanaqi model assumes sharp interfaces, perfect bonding, and complete stress transfer across the interface. It is a reliable model for evaluating the upper ($E_{\parallel}$) and lower ($E_{\perp}$) limits of the aligned fiber nanocomposites and laminated composites. However, due to the discontinuous nature of the nanofillers, Takayanagi model fails to count the end effect of the nanofillers, which plays a significant role in the well dispersed nanocomposite systems.

1.2.1 Models for particulate nanocomposites

Kerner has proposed another model to describe the lower limit of the shear modulus of the particulate-reinforced polymer composites with spherical particles and perfect particle/particle and particle/matrix bonding: [2, 123]

$$\frac{G_c}{G_m} = \frac{\frac{G_f \nu_f}{a} + b}{\frac{G_m \nu_f}{a} + b}; \qquad (1.3)$$

$$a = (7 - 5\sigma_m)G_m + (8 - 10\sigma_m)G_f;\ b = \frac{\nu_m}{15(1-\sigma_m)}.$$

where G is the shear modulus; σ is the Poission's ratio; v is the volume fraction; and subscripts c, m, and f represent composite, the polymeric matrix, and the particulate fillers, respectively. The number of components in the nanocomposite system is not limited, so it is suitable to analyze the complex multicomponent systems.

For particulate reinforced elastomers with carbon black and silica, Guth and Smallwood proposed a simple model to predict the lower bound shear modulus of the nanocomposite. [2, 124] The increase in the shear modulus of the composite is only related to the volume

fraction of the particulate fillers. This model assumes perfectly spherical fillers, complete adhesive bonding, and uniform dispersion, which are challenging to realize in nanocomposites.

1.2.2 Models for nanocomposites with anisotropic fillers

Halpin-Tsai model was developed for composites with nanoparticle fillers of various geometries, including rods, disks, and spheres. [3, 125] It provides well-defined shape factor and is widely adapted for composite behavior analysis. [40, 69, 126] Also, Halpin-Tsai model considers the distribution of the 2D aligned anisotropic fillers as well as 3D randomly oriented fillers with different shapes. For composite materials with parallel aligned short platelets, the Halpin-Tsai equation is presented as: [127]

$$E_{\parallel} = \left[\frac{1+2\alpha\eta_{\parallel}v_f}{1-\eta_{\parallel}v_f}\right]E_m \qquad (1.4)$$

where $\eta_{\parallel} = \frac{E_f/E_m - 1}{E_f/E_m + 2\alpha}$; $E_{\parallel}$ and E_m are the Young's modulus of the parallel aligned nanocomposite and the matrix, respectively; α is the aspect ratio of the nanofiller. It is worth noting that when the aspect ratio is very high, the Halpin-Tsai equation regresses to the rule of mixture. When the aspect ratio is low (approaching spherical particles), the equation regresses to the common inverse rule of mixture for composite materials.

For randomly orientated nanoparticles, the Halpin-Tsai considers the contribution of the transverse mode, modifying its format to the following:

$$E_{random} = mE_{\parallel} + nE_{\perp} \qquad (1.5)$$

where $E_{\perp} = \left[\frac{1+2\eta_{\perp}v_f}{1-\eta_{\perp}v_f}\right]E_m$; $\eta_{\parallel} = \frac{E_f/E_m - 1}{E_f/E_m + 2}$; m and n are the coefficients that evaluating the contributions from the longitudinal mode and the transverse mode. [2, 128]

Another development, the average-stress theory (Mori-Tanaka model) calculates the elastic stress field around an ellipsoidal particle in order to derive the longitudinal and transverse Young's moduli [129]:

$$E_{\parallel} = \left[\frac{A}{A+\nu_f(A_1+2\sigma_m A_2)}\right] E_m \qquad (1.6)$$

$$E_{\perp} = \left\{\frac{2A}{2A+\nu_f[-2\sigma_m A_3+(1-\sigma_m)A_4+(1+\sigma_m)A_5 A]}\right\} E_m \qquad (1.7)$$

where *A*, *A1* through *A5* are model-specific coefficients that are primarily functions of the physical properties and geometries of the filler and the matrix.[2, 129] By adjusting the geometry parameters of this model, the filler could be represented as high-aspect ratio fibers or platelets and even spheres. However, it should be pointed out that the Mori-Tanaka model treats the geometries of fillers based on ellipsoidal parameters, while the Halpin-Tsai model treats the fibers as cylinders and considers rectangular platelets.

Finally, Jäger–Fratzl model predicts the elastic modulus of the layered, nacre-like biocomposites, where the flexible polymeric matrix regressed to a minute binder of the dominating stiff inorganic phases in the form: [130]

$$E_c = \left[\frac{8\nu_m(1+\sigma_m)}{E_m {\nu_f}^2 \alpha^2} + \frac{1}{\nu_f E_f}\right]^{-1} \qquad (1.8)$$

In order to compare predictions of different models, we calculated the expected increase of the elastic modulus with increasing filler content for different filler shapes as predicted by different mechanical models (**Figure 1.5**). This brief comparative analysis shows that the careful selection of an appropriate model with consideration of composite properties and morphologies is critical for the prediction of the properties of nanocomposites.

It is striking to see that differences in the predicted values among various models can easily reach 200%. On the other hand, it is worth noting that spherical particulates have much weaker reinforcing effect on the nanocomposite properties due to the high specific surface area. Randomly distributed platelets should result in the strongest isotropic nanocomposites, while aligned fibers or platelets exhibit a similar but direction-dependent reinforcement effect in the anisotropic nanocomposites.

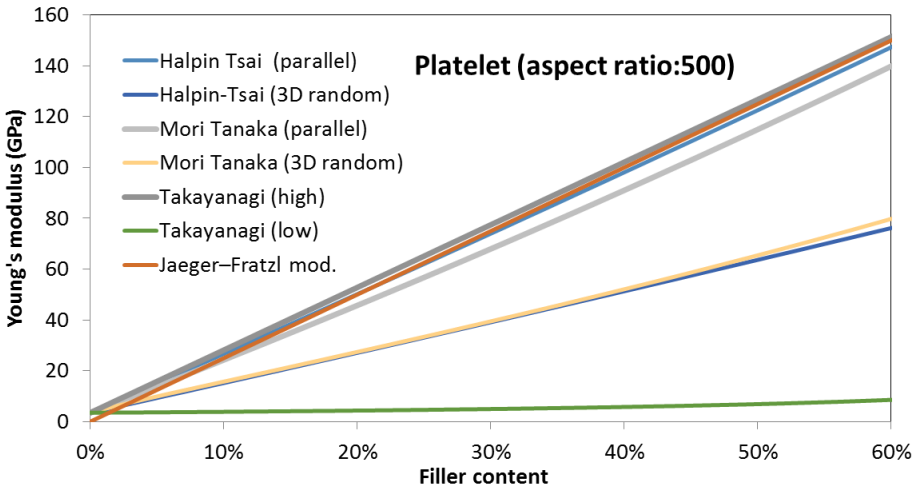

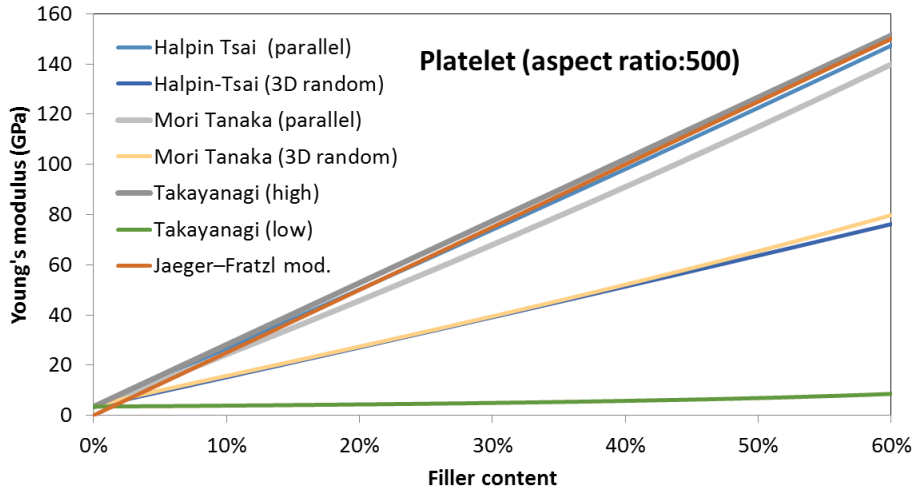

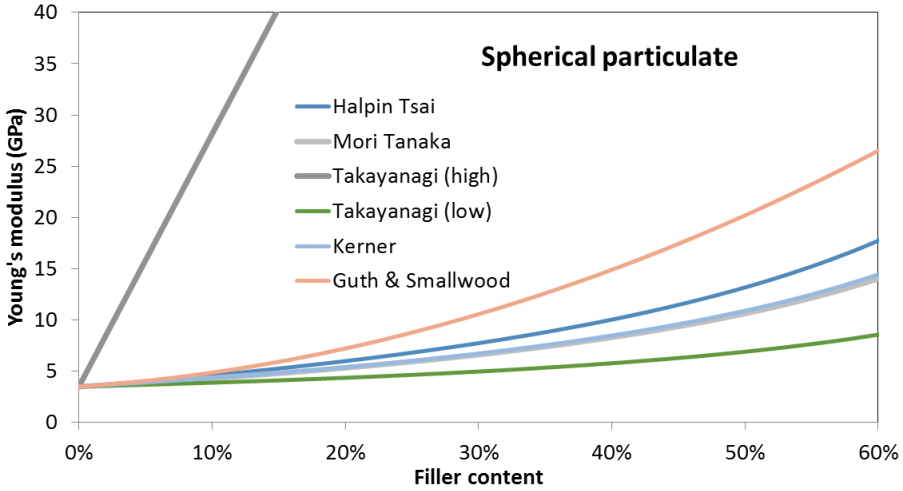

Figure 1.5 Calculations of the theoretical values of elastic modulus predicted by different models described above with the elastic modulus of 150 GPa and 3.5 GPa, and Poisson's ratio of 0.25 and 0.4 for the filler and the matrix, respectively.

Overall, the existing mechanical models, which have been developed for conventional composite materials are generally suitable for coarse evaluation of the nanocomposite behavior. However, these models ignore some critical differences and unique characteristics of nanocomposites, such as developed interfaces and complex morphologies. For example, all the models discussed above assume an ideal non-slipping bonding condition between the filler and the matrix and sharp interface between them, which is not the case for graphene-polymer nanocomposites. Therefore, more adequate mechanistic models should be developed especially those which consider the role of interphases, end-to-end interactions, and extremely high specific interfacial area.

1.2.3 Interphases in nanocomposites

In the special case of nanocomposites, the extremely large surface-to-volume ratio might result in high binding efficiency. On the other hand, the strong interfacial binding might alter the macromolecular conformation in the vicinity of the filler surface. Such a transitional zone might alter the properties of polymer matrix with gradual change across the interface. This region is called "interphase" in contrast to the conventional sharp interface with an abrupt change in property and composition. [131] The additional reinforcing effect comes from the interphase layer of the polymer matrix. The stronger but ultrathin interphases are usually ignored in regular composites due to a minute contribution to the overall mechanical properties.

In nanocomposite materials, however, the mechanical properties of the interphase region might play significant role. For instance, an interphase model has been suggested to account for the exceedingly high elastic modulus of polymer-graphene oxide nanocomposites. [126, 132] The model assumes that the adsorption of polymers on graphene oxide surfaces alters the modulus of the adsorbed polymer layer. By estimating the modulus change, adsorption ratio, and the specific surface area of graphene oxide, the model adjusted the volume fraction of the nanofiller to an effective value after the polymer adsorption. This model adequately described the experimental data collected for nanocomposites studied.

1.3 Processing of the graphene-polymer nanocomposites

The ultimate properties of graphene-based polymer nanocomposites are critically dependent upon the processing conditions in the course of nanocomposite fabrication. [133, 134, 135] The functionality of graphene components is critical to lower filler loading rate, make them highly dispersed and organized sheets within polymer matrix to enhance overall performance of nanocomposites. In particular, the mechanical properties such as Young's modulus, ultimate tensile strength and strain, and flexural strength are expected to be controlled by a composition of specific surface area, aspect ratio, organization, and loading content of graphene materials. Dispersion state, interfacial strength, affinity of components, and spatial organization are all of great importance in determining the final stiffness, strength, toughness, and elongation of polymer nanocomposites under various loading conditions. [136, 137, 138, 139, 140]

The pre-treatment procedures and the fabrication methods dictate the fine morphology and physical/chemical properties of graphene-based polymer nanocomposites. For different graphene-polymer nanocomposites known to date, the extent of dispersion and exfoliation of graphitic layers is controlled by applied shear force, temperature, and solvent polarity. Effective control of restacking, wrinkling, and aggregation of graphene sheets is required for the development of functional nanocomposites with high performance. In fact, extremely flexible and high-aspect ratio graphene components are prone to random wrinkling, buckling, or folding during processing which dramatically affect the ultimate performance. In the case of the graphene oxide post-reduction, the degree of dispersion can be influenced by the hydrophobic nature of reduced graphene oxide sheets and dewetting processes at the interfaces.

The choice of fabrication methods is determined by the functionalization of integrated graphitic sheets. Traditional fabrication routines include solution-based processing [139, 141, 142, 143, 144] and melt-based processing. [145, 146, 147] Among most popular approaches for chemical modification and assembly are *in situ* polymerization, chemical grafting, latex emulsion blending, LbL assembly, and supramolecular self-assembly. [3, 148, 149, 150, 151, 152] For the *in situ* polymerization method, intercalated monomers within expanded graphite

clusters can promote their efficient exfoliation into single sheets throughout the polymer matrix based on catalysis reactions. [153]

The solution processing maximizes filler dispersion in polymer matrix by using pre-suspended single layer graphene sheets. The different solvents (aqueous to organic) can be used for dissolve graphene materials including graphene oxide and reduced graphene oxide. This approach has been widely exploited due to its high dispersion efficiency, facile and fast fabrication step, and a high level of control on component behavior. Disadvantages of this approach is challenges in finding common solvents, toxic solvent utilization, thin-film limitation, difficulties in solvent removal, and common aggregation issues during solvent evaporation stage. [154, 155]

On the other hand, the melt-based mixing is a solvent free process in which applied mechanical shear force make the fillers distributed in the polymer matrix using screw extruder or blending mixer. [145, 156] This method allows stacked graphite or reduced graphene oxide to be exfoliated into viscous polymer melt by suppressing unfavorable interactions and inducing component dispersion. The melt mixing is recognized a practical approach that can be adapted to the graphene-based polymer nanocomposites. However, thermal heating and high local mechanical stresses can affect the stability of components, their shapes, and the reduction state of graphene oxide sheets. Several examples of various processing approaches will be discussed below.

1.3.1 Examples of solution-based processing

Solution mixing methods have been employed as a powerful strategy widely utilized in a combination with high shearing (*e.g.*, due to ultrasonication) for a range of polymer matrices including poly(vinly alcohol) (PVA) [157, 143], poly(methyl methacrylate) (PMMA) [141], polyurethane (PU) [139], and polyaniline (PANI) [158]. Water-soluble PVA, which is nontoxic and hydrophilic polymer, has been used for the fabrication of graphene oxide nanocomposite films by simple solution mixing, which enables the graphene oxide components to be dispersed on a molecular scale and aligned in the polymer matrix. [159] The authors suggested that the resulting homogeneous dispersion and preferential alignment of graphene oxide sheets in PVA matrix combined with the strong interfacial

interactions accounted for the much improved mechanical properties in the nanocomposite films.

In another case of solution-based process, the intense ultrasonication was employed to exfoliate graphite oxide materials into single-layer graphene oxide sheets that results in better graphene oxide dispersion in the polymer matrix. [160] The effect of ultrasonication of the solution with graphene oxide on the final mechanical properties of GO-PVA nanocomposites was explored in other study. [161] In this study, graphene oxide solution treated under different ultrasonication conditions and water was then mixed with the PVA solution, and stirred at room temperature. The ultrasonication time has been considered as a critical factor to determine the ultimate reinforcement in a nanocomposite system via the controlled exfoliation of graphene oxide component. The fabrication of nanocomposites with fully exfoliated graphene oxide sheets and maximum sheet size has been demonstrated for the optimal power input of the ultrasonication.

Recently, Wajid *et al.* have reported a comparative study of a freeze drying and solution mixing strategies for high-strength conductive pristine graphene/epoxy nanocomposites. [162] Aggregation-resistant polyvinlypyrrolidon (PVP)-stabilized graphene dispersions have been obtained with the choice of the matrix in consideration. The authors demonstrated that PVP modification can effectively stabilize the graphene component and enhances the interfacial interactions between graphene filler and matrix due to the polarity and affinity of the ring structure on PVP component. Additionally, polymer-stabilized graphene dispersions in water can be freeze-dried and then re-dispersed with aid of stirring and sonication prior to the final curing process. The authors reported that the ability to increase dispersion of graphene component led to enhanced mechanical properties by about 40% at 0.46 vol% of graphene loading. Moreover, the nanocomposites also showed a very low electrical percolation threshold at 0.088 vol% of graphene content.

Poly(e-caprolactone) (PCL) is a biodegradable and biocompatible aliphatic polyester with good resistance to water, solvents and oil, which is synthesized for biomedical and biomaterials applications. [163] Ning *et al.* have reported a fabrication route for obtaining graphene-polymer nanocomposites by covalent bonding of PLC and well dispersed,

chemically reduced graphene oxide for biodegradable tissue engineering. [163] The covalently-linked and chemically reduced graphene-based nanocomposite showed improved mechanical properties and electrical conductivity for nanocomposites with homogeneously dispersed graphene component. The subsequent chemical bonding of the components after rigorous solution mixing was critical for the stabilization of the finely-dispersed morphology and the strong interfacial bonding between components.

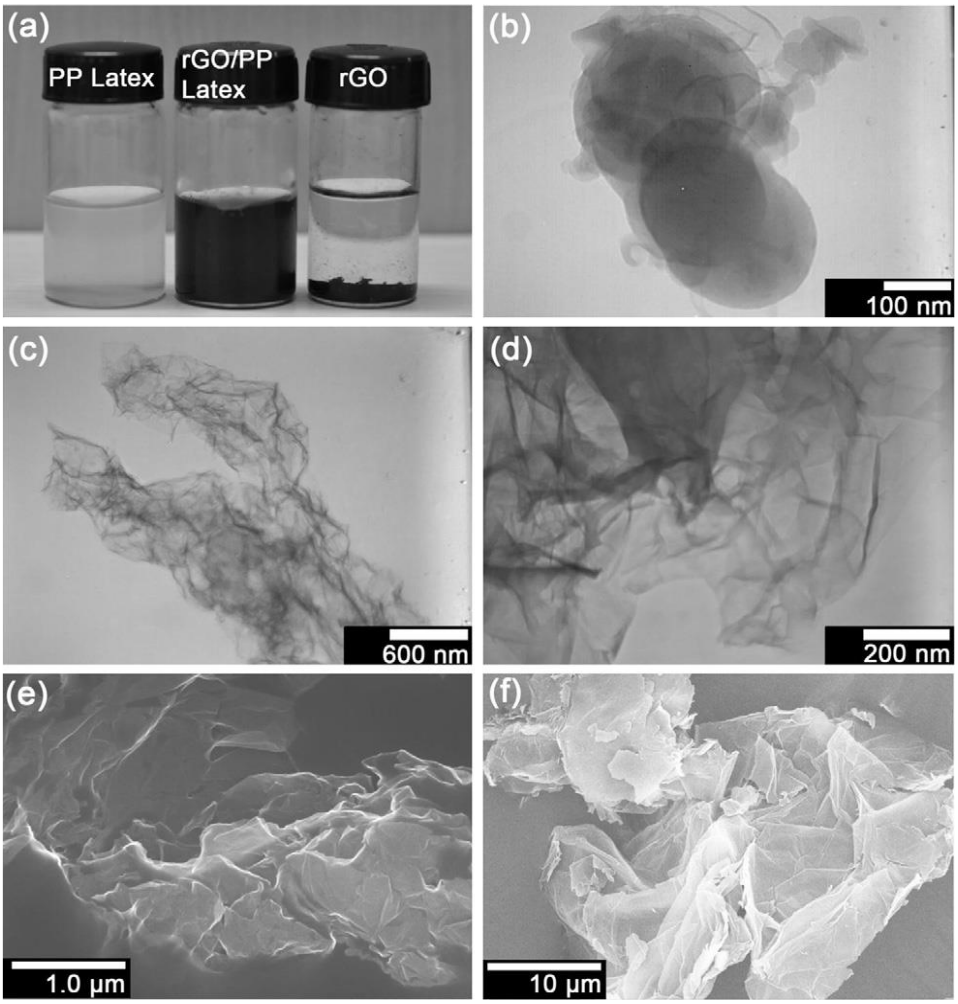

Figure 1.6 (a) Aqueous suspensions of PP latex and graphene oxide. (b) TEM image of PP latex. (c)(d) TEM images of the rGO/PP latex composite dispersed in water before filtration. (e) SEM image of fracture surface of the rGO/PP composite (after hot-press molding. (f) SEM of agglomerated rGO nanosheets. [164] Copyright 2013. With permission of Elsevier.

It is known that a popular semi-crystalline thermoplastic polymer, polypropylene (PP) is a dielectric material, which is employed in capacitors due to its outstanding dielectric properties. It has been demonstrated that the dielectric constant of PP can be substantially enhanced if conductive graphene is incorporated. In fact, Wang *et al.* demonstrated

graphene-filled nanocomposites by mixing PP latex with graphene oxide (**Figure 1.6**). [164] The reduced graphene oxide (rGO) and PP nanocomposites were prepared through a emulsion polymerization followed by an *in-situ* chemical reduction of graphene oxide and a subsequent filtration.

The introduction of latex-type morphology has been recognized a versatile and environmental friendly approach to fabricate polymer nanocomposite with a fine dispersion and spatial stability as compared to traditional melt mixing of bulk polymer components. [164] The rGO/PP nanocomposites prepared by the emulsion method revealed the homogeneous dispersion of reduced graphene oxide nanosheets in the PP matrix, which facilitates a strong interactions at the interface (Figure 1.6). Moreover, the ultralow percholation threshold of 0.033 vol% was observed with the dielectric permittivity of the nanocomposites increasing by three orders of magnitude.

In another study, Lalwani et al have reported a thermal crosslinking method for laminated polymeric nanocomposites and investigated the efficacy of graphene nanostructures as reinforcing agents for highly cross-linked nanocomposites. [165] Biodegradable and biocompatible nanocomposites have been prepared from polypropylene fumarate (PPF) with very low concentration of reinforcing graphene component of 0.01−0.2 wt%. The graphene oxide sheets have been dispersed under sonication as individual nanoparticles in the PPF polymer matrix with high cross-linking density. The resulting nanocomposites showed significantly increased mechanical properties, which were considered appropriate for bone tissue engineering.

1.3.2 Examples of melt-based processing

In a recent study, melt mixing under high shear force has been employed for the fabrication of graphene-based nanocomposites with polylactide (PLA) and polyethylene terephthalate (PET) as matrices. [166, 167, 168] As another example, elastomer/ graphene platelets nanocomposites have been developed by a melt compounding method. [169] Thick graphene platelets (partially exfoliated materials) from graphite intercalated compounds obtained using thermal shock followed by ultrasonication were exploited in this study. This material was mixed with an elastomer—ethylene–propylene–diene monomer rubber (EPDM) using

a two-roll mill and then crosslinked through vulcanization. Increased graphitic contents led to the enhanced tensile strength and reduced strain at fracture due to confinement effects. Electrically and thermally conductive elastomeric nanocomposites have been obtained with a modest percolation threshold.

It has been demonstrated that the melt extrusion process promotes the exfoliation of reduced graphene oxide in the various polymer matrixes of different polarity such as isotactic poly(propylene) (iPP), poly(styrene-co-acrylonitrile) (SAN), polyamide 6 (PA6) and polycarbonate (PC), yielding thermoplastic nanocomposites with uniformly dispersed graphene materials. [170] Similar to the conventional expanded graphite, graphene oxide can be converted into thermally reduced graphite oxide with very low bulk density by rapid thermal heating process. In this study, the reduced graphite oxide materials were obtained by oxidation of graphite followed by thermal expansion at 600°C. As a result, the functionalized graphene with large specific surface areas of 600 to 950 $m^2 g^{-1}$ exhibited exfoliation during processing.

The enhancement of the flame retardancy with addition of graphite oxide has been suggested to be related to the oxidation barrier of natural graphite and the graphite oxide. [171] To exploit this phenomenon, graphite oxide with different oxidation degrees or graphene materials were blended with PS matrix to serve as a flame retarding additive. Melt mixing the graphite oxide and graphene with the PS was conducted under different melt-mixing conditions. The incorporation of low concentration of graphene (5 wt%) showed the enhanced flame retardant properties (increased by 50 %) as compared to the pristine PS material.

Melt mixing can be employed for post treatment after solution processing as described in a recent study. [172] Song *et al.* have presented PP nanocomposites with homogeneous dispersion of CNTs and reduced graphene oxides obtained via a facile polymer-latex-coating. A combination of this routine with subsequent melt-mixing has been considered for developing an advanced hybrid nanocomposites. PP-based nanocomposites were obtained by mixing graphite oxide and CNTs with PP latex (a water-based emulation of maleic anhydride grafted isotactic polypropylene), followed by a reduction of graphite

component to the partially reduced state. The ternary system of PP/rGO/CNTs showed a continuous interconnected network of reduced graphite oxide and CNTs **(Figure 1.7)**. [172] This processing strategy enabled the uniform dispersion of two different carbon components that resulted in remarkable multiple synergy in their mechanical properties, electrical conductivity, and thermal conductivity.

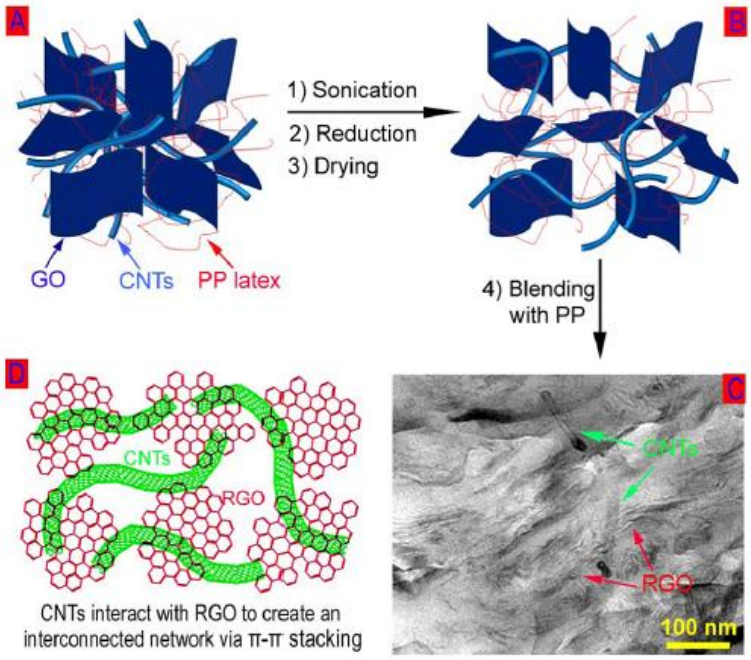

Figure 1.7 (A) and (B): the formation of interconnected network of rGO and CNTs using PP latex as a dispersing agent. (C) TEM image of PP/RGO/CNTs ternary system. (D) Schematic of strong interactions between RGO and CNTs via stacking. [172] Copyright 2013. With permission of Institute of Physics.

The formation of the strong chemical bonding between graphene sheets and polymer matrices via covalent interactions has been considered an attractive route for the modification of functionalized graphene oxide components with mostly preserved intrinsic structure and properties. In recent study, Gao *et al.* have demonstrated the efficient grafting of poly[(dimethylamino)ethyl methacrylate] (PDMAEMA) brushes onto graphene oxide sheets via "grafting–from" process. [173, 174] Two step grafting methods included a non-covalent modification of graphene oxide surfaces by pyrene terminated initiator via π- π interaction followed by *in situ* surface-initiated atom transfer radical polymerization (SI-ATRP) **(Figure 1.8)**.

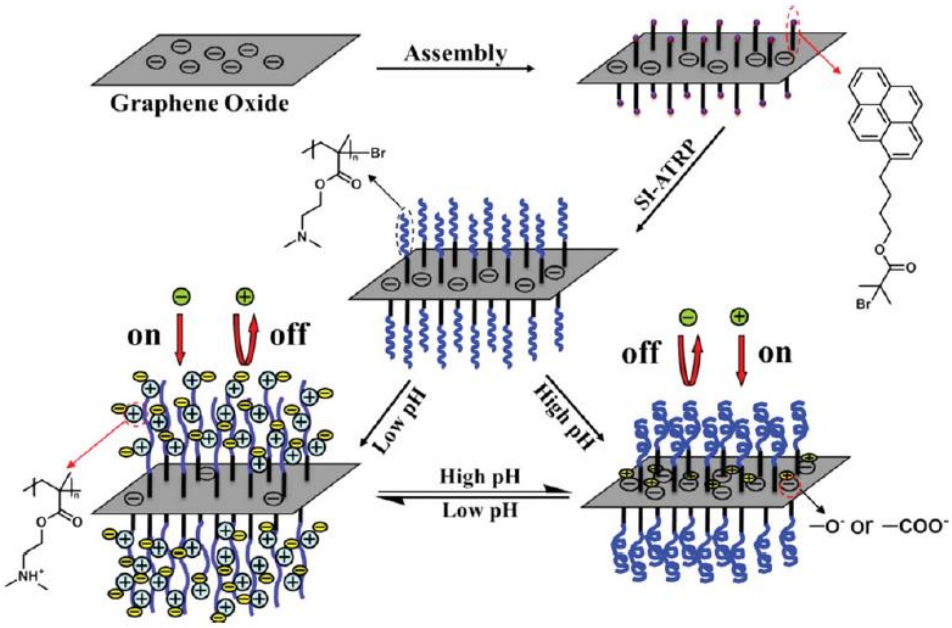

Figure 1.8 The preparation of PDMAEMA-modified graphene oxide and charging state of the GO-g-PDMAEMA composite at different pH values. [173] Copyright 2013. With permission of John Wiley & Sons.

The resulting positively charged PDMAEMA brush layer has been used for the modification of the negatively charged graphite oxide sheets to produce GO-g-PDMAEMA hybrid fillers. These nanostructures exhibit zwitterionic behavior because of the presence of different functional groups including phenol hydroxyl, carboxyl, and amine groups and further demonstrated the ability of these composite systems to serve a template for metal nanoparticle synthesis. [173]

By using similar brush-modification approach, Shen *et al.* have proposed an efficient strategy for the chemical modification of graphene oxide sheets and demonstrated the preparation of polycarbonate (PC)/(GO-epoxy) nanocomposites with strong interfacial interactions. [175] In this study, an epoxy-containing layer was coupled to graphene oxide sheets via the ‘‘grafting to’’ method and then mixed with PC matrix by solution casting. In addition, terminal epoxide groups were exploited to covalently connect two graphene oxide sheets together, which resulted in the efficient crosslinking of graphite oxide layers via a coupling reaction. The residual functionalized sites in the grafted epoxy chains also formed chemical bonds with the PC matrix that thereby led to the enhanced mechanical properties of these nanocomposites.

The high pseudocapacitance of PANI arising from the versatile redox reactions and corresponding color changes allow for use in electrochemical capacitors and for electrochromic colorimetric applications. [176, 177] Wei *et al.* have described a facile electropolymerization method for the preparation of PANI-graphite oxide nanocomposite films by electrodeposition of aniline monomers in sulfuric acid solution onto indium tin oxide (ITO) coated with graphite oxide. In other study, Zhu *et al.* reported the interfacial polymerization method for the fabrication of PANI nanofibers with graphite oxide materials with excellent interfacial strength due to the enhanced specific surface area. [178] The elongated fibrous structures were synthesized via a facile surface initiated interfacial polymerization method. A random growth of PANI fibers derived from the PANI coated graphite oxide sheets, which are instrumental in enhanced interfacial strength were directly observed with TEM.

In alternative approach, Ning *et al.* reported the one-step template-free polymerization of 3D hybrid materials composed of 2D fish scale-like PANI morphologies on graphene oxide sheets and carbon nanotubes. [179] These multicomponent nanomaterials were synthesized by a one-step process using a simplified template-free oxidative polymerization method. As a result, complex 3D microstructures assembled from hybrid PANI nanosheets combined with graphite oxide sheets were assembled. In this approach, the graphite oxide sheets were readily dispersed in an aqueous solution and further acted as nucleation sites for PANI deposition to fabricate hybrid reinforcing elements.

In situ polymerization has also been demonstrated to provide another efficient means to help intercalate the graphene fillers in diverse polymer matrices including PS, PMMA, polystyrene sulfonates (PSS), polyimides (PI), and PET. [180, 181, 182] One recent study demonstrated graphene oxide/PI nanocomposites based on 4,4-bisphenol A dianhydride, 4,4-oxydiphthalic anhydride, and diaminodiphenyl methane (MDA) as comonomers. [183] In one example, the addition of a small amount of graphite oxide component (0.03–0.12 wt%) was found to significantly improve the mechanical properties of PI nanocomposites without a substantial decrease of film transparency (sustained above 80% in 500–800 nm range).

Overall, although solution and melt mixing methods offer lots of benefits in the processing of graphene-based polymer nanocomposite in terms of scalability and processing time, but they are limited in the level of control of the microstructure due to predominantly random distributions of the flexible fillers during mixing process and their easily crumpling and folding. To obtain higher ordering, unfolded states, and control over the orientation of loaded graphene sheets a step-wise LbL assembly has been considered in several recent studies.

1.3.3 LbL assembly of graphene components

Well known LbL assembly is an efficient fabrication approach for the development of ultrastrong and robust thin and ultrathin films, membranes, and coatings with high strength, controlled adhesion, flexibility, and environmental stability. [184, 185, 186, 187, 188, 189] These organized layered assemblies can provide a route to precisely engineer the graphene-polymer interface and control the distribution and content of graphene component on a molecular level by alternating deposition of two complementary components from graphene filler suspension and polymer solution. [77] Furthermore, the morphology of the nanocomposite films can be finely tuned by the deposition mode, solvent removal procedure, or applied shear force through either direct dipping or spin and spray assisted LbL methods. On the other hand, vacuum-assisted assembly employs micro-flow at the filter/solution interface thus making the deposition process continuous. [69] However, the vacuum-assisted method cannot control precisely the arrangement of different components in the resulting nanocomposite paper.

To date, only few studies have employed LbL assembly for the fabrication of graphene-based nanocomposites. However, long ago the use of graphite oxide layered assemblies was demonstrated for the intercalated graphene oxide and poly (diallyldimethylammonium chloride) (PDDA) components. [190] The chemical and electrochemical post-reduction led to conductive nanocomposite films with high structural uniformity and chemical stability. In another study, Kovtyukhova *et al.* investigated multilayer assemblies by alternate adsorption of anionic colloidal graphene oxide sheets and cationic poly (allylamine hydrochloride) (PAH). [191] Multilayer films have been formed by dip-assisted LbL

assembly, which facilitated controlled coverage on the substrate and low surface roughness. Cassagneau *et al.* reported multilayer assembly of graphene oxide and polyelectrolyes (PDDA/GO/PEO) by a dip-assisted LbL method based on electrostatic and epitaxial adsorption of polymers for lithium ion battery electrode applications. [152]

Zhao *et al.* fabricated multilayer films of PVA and exfoliated graphene oxide by a hydrogen bonding LbL method and measured their mechanical properties. [144] The dip-assisted LbL fabrication enabled the formation of the uniform ultrathin multilayer nanofilms with high homogeneity in morphology and flake orientation and led to a significant improvement of mechanical strength and a manifold increase of nanocomposite strength with respect to the original polymer matrix.

In recent development, Zhu *et al.* compared the mechanical and electrical properties of the PVA/rGO nanocomposites with the same composition fabricated by either dip-assisted LbL assembly or vacuum-assisted method. [192] Their results revealed that the final mechanical properties are largely determined by the micro-morphology of the well-layered nanocomposites, which is concluded from the almost identical mechanical properties of both series of samples. On the other hand, the electrical conductivities are predominantly affected by the dispersed nanostructures of the nanocomposites because the transportation of electrons is predominantly dependent on the tunneling barrier among the finely distributed conductive components.

Recently, Li *et al.* have fabricated hybrid multilayered films based on negatively charged graphene oxide nanosheets and polyoxometalate clusters with cationic polyelectrolytes using traditional dip-assisted electrostatic LbL assembly. [117] Film formation was followed by UV photoreduction of graphene oxide sheets by taking an advantage of the photocatalytic activity of embedded clusters without the use of toxic chemicals. This approach enabled the formation of uniform and large-area nanocomposite films with precisely controlled thickness on various substrates by varying the number of deposited graphene oxide layers.

In a study from our group, ultrathin free-standing graphene oxide/polyelectrolyte multilayers were fabricated based synthetic polyelectrolytes (PSS/PAH) by a spin-assisted

LbL assembly in a combination with Langmuir Blodgett (LB) deposition (**Figure 1.9**). [3] This combined LbL-LB fabrication strategy facilitated the fabrication of a highly integrated nanocomposite membrane with large lateral dimensions (centimeters) and a thickness of around 50 nm by suppressing wrinkling and folding of graphene oxide sheets during deposition procedure. Micromechanical measurements on these freely suspended nanocomposite membranes revealed dramatic enhancement of the mechanical properties with the elastic modulus increased by an order of magnitude to about 20 GPa at only 8.0 vol% graphene oxide loading content (see more discussion below). [3]

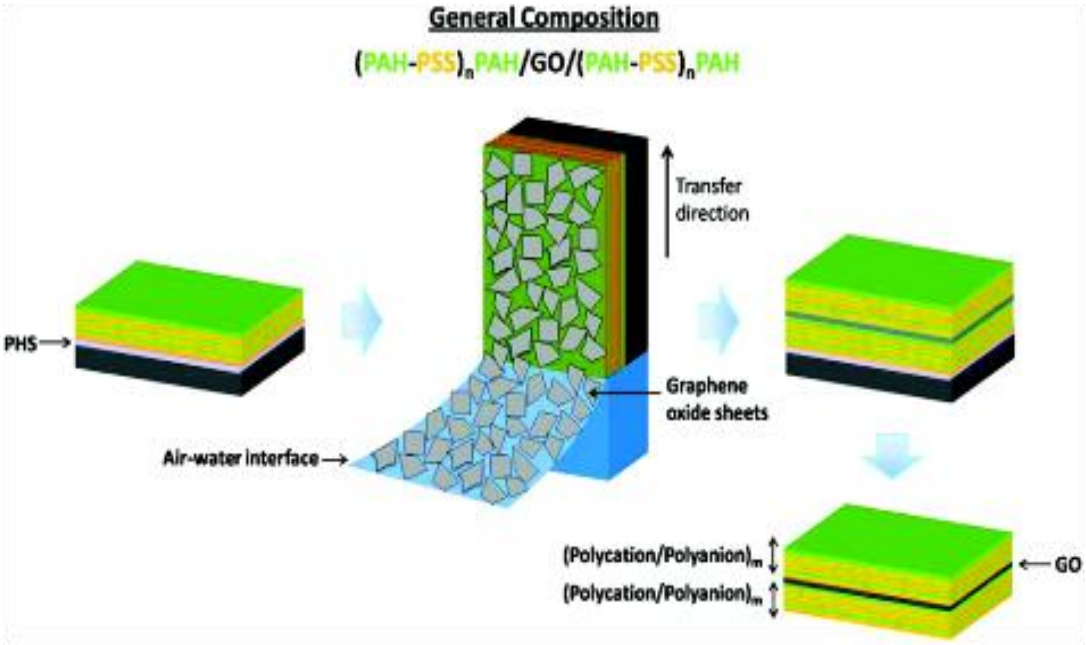

Figure 1.9 Fabrication of ordered and hierarchical multilayered graphene oxide-polyelectrolyte nanomembranes via combination of LbL and LB techniques. [3] Copyright 2010. American Chemical Society.

In another very recent example, conductive nanocomposite films from PS microspheres wrapped by graphene oxide sheets were prepared via LbL assembly followed by graphite oxide reduction. [193] The nanocomposite films with a graphene conductive network were fabricated by hot pressing graphene-wrapped PS microspheres into thin films with network-like morphology. The use of PS polymer latex facilitated the uniformity of the graphene filler distribution in the polymer matrix. The combination of latex technology and LbL assembly offers a facile, efficient, and environmentally-friendly method for the

fabrication of electrically conductive graphene/PS nanocomposites with well-developed network morphology.

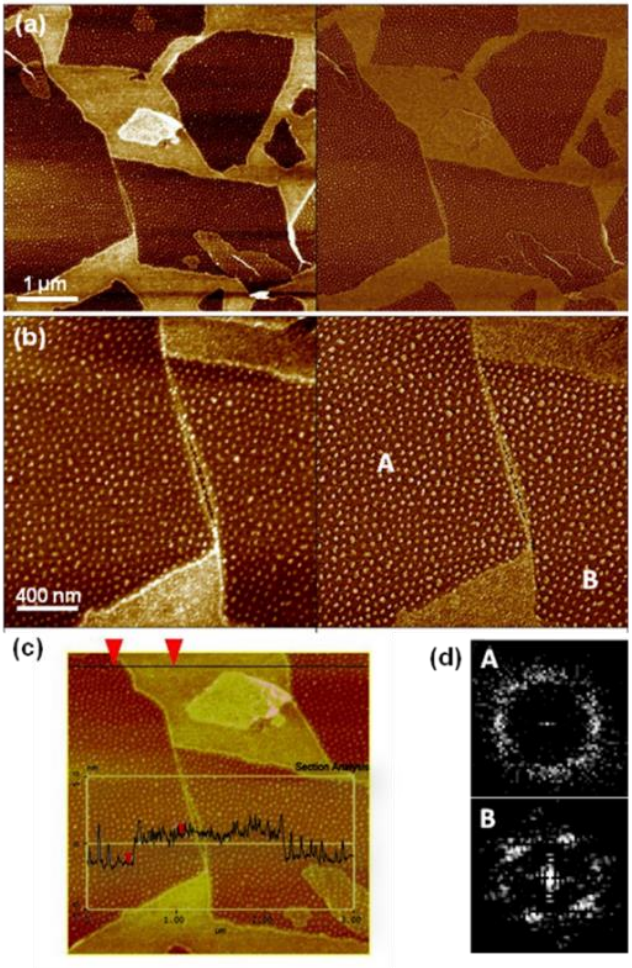

Figure 1.10 AFM topography (left) and phase (right) of (a, b) GO /PS28P2VP28 star copolymer at pH 2 for surface pressures of 15 mN/m; (c) The height profile of corresponding topography image; (d) FFT of domain morphologies for A and B regions from Figure 3b. z-scale: 5 nm (topography) and 30° (phase). [194] Copyright 2013. American Chemical Society.

Supramolecular self-assembly has also been recognized a method to enhance the interfacial adhesion based on diverse chemical functionality. [194] In a recent study, interface-mediated assembly method have been exploited for the fabrication of micelle-decorated graphene oxide sheets with ordered polymer morphology. Amphiphilic heteroarm star copolymers (PS_nP2VP_n and PS_n(P2VP-*b*-P*t*BA)$_n$ (n= 28 arms)) were adsorbed on the pre-suspended graphene oxide sheets at the air-water interface due to the peculiar surface activity of graphene oxide sheets. The resulting bilayer nanocomposites are composed of flat graphene oxide sheets uniformly covered with a highly ordered and discrete assemblies of

unimolecular micelles of amphiphilic star macromolecules in pancake conformation. This organized morphology of polymer material at graphene oxide sheets has been attributed to the strong affinity among positively charged pyridine groups of star polymers onto the negatively charged basal plane and the edges of graphene oxide **(Figure 1.10)**.

Nanocomposites of PVA matrix with functionalized (sulfonated) graphene oxide components show fibrillar, dendritic and rod like structures under different processing conditions. [195] Since reduced graphene oxide has a limited dispersion in aqueous medium, the anchoring of $–SO_3H$ group on the graphene oxide surface prior to chemical reduction with hydrazine offers a promising method for producing a highly conducting and dispersible graphene-based materials in an aqueous medium. The fibrillar morphology, highly branched dendritic morphology, and rod-like structures were all observed due to hydrogen-bonded controlled supramolecular organization with different balances of interfacial interactions.

After all, the dispersing and processing techniques all serve the purpose of fully reveal the structural and functional properties of graphenes. After discussion of various processing routines, in the next section, we will consider the mechanical properties of resulting nanocomposites in conjunction with their composition, morphology, and processing conditions.

1.4 Mechanical properties of graphene–polymer nanocomposites

It is well known that strong mechanical interfaces play a key role in the fabrication of tough nanocomposites as has been briefly been discussed above. [196, 197] Carbon nanomaterials also offer an advantage of fabricating multi-functional composites with high electrical and thermal conductivities along with strong mechanical properties. The most important factor along with the increased specific interfacial area is the control of the stress transfer across the interface, which can be achieved by means of covalent bonding, electrostatic interactions, hydrogen bonding, or van der Waals interactions.[198, 199, 200] It is expected that the strength of the filler material would dominate the properties of the composite material

but, in fact, it is the interfacial strength that usually controls the ultimate mechanical properties. Fine dispersion of a reinforcing component determines the high specific interfacial area. Poor dispersion or excessive aggregation of the carbon nanomaterials in the polymer matrix results in a decreased interfacial area along with weakening interfaces thereby leading to poor mechanical properties.

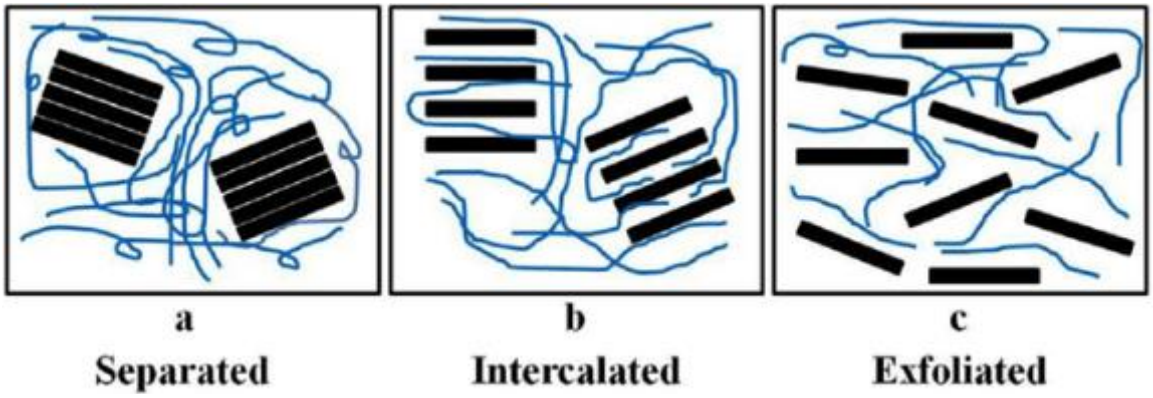

Figure 1.11 Representative dispersing scenarios of laminated nanofillers in polymer matrix. [201]

Figure 1.11 shows the different scenarios encountered during polymer nanocomposite fabrication with laminated reinforcing materials. [201] It is widely accepted that the efficient exfoliation of stacked laminates followed by intercalation can improve the interfacial strength and dramatically rise the interfacial area thus leading to stronger nanocomposite materials. Efficient intercalation can lead to stronger interfacial interactions and a localized improvement in the properties of the composite. Thus, a uniform dispersion and exfoliation of graphitic components inside the polymer matrix are both important for improved performance.

Carbon nanomaterials are usually difficult to disperse in the polymer matrix and their simple mixing results in the formation of a weak interface and significant aggregation leading to poor mechanical properties if special efforts are not applied. [202, 203] Most frequently, carbon nanomaterials are functionalized to ease the dispersion and improve the chemical interactions with the polymer matrix. Numerous studies on functionalization of the carbon materials have been reported. [135, 204 , 205] But the properties of these nanocomposites still fall short of the expected characteristics considering superior properties of many nanofillers. Theoretically, it is not possible to achieve a complete stress transfer across the interface but the fabrication of a strong interface for the efficient stress

transfer is essential to maximize the mechanical strength. [206] However, further development might be hindered due to a poor dispersion of these reinforcing nanostructures within the polymer matrix.

The mechanical properties of a composite material are judged based on the enhancement of the performance as characterized by the elastic modulus, tensile strength, elongation, and toughness.[207] It is difficult to obtain a multicomponent material exhibiting record values for all these factors due to conflicting reinforcing mechanisms. Usually, efforts to improve one of these characteristics show an adverse effect on the other factors. Thus, selective improvement of one or more of these mechanical characteristics is usually considered as a priority depending on a specific end-application.

However, many applications require high toughness thus requiring a balance between increasing mechanical strength, elastic modulus, and the preservation of materials compliance. Considering that the toughness value relates to overall energy dissipation and is formally evaluated by the area under the stress-stain curve, a material that can withstand high stress under maximum elongation will possess the highest toughness. Adding stiff nanofillers and tailoring strong polymer-filler interactions, a usual routine for reinforcement, frequently results in higher elastic modulus and mechanical strength but lower ultimate elongation. However, more compliant interfacial interactions might result in a slippage mechanism to be activated at the polymer-filler interface well before the ultimate fracture. The materials would eventually fail under higher load and thus demonstrates higher toughness. Thus, finding the optimum combination of reinforcing and deformational mechanisms should be carefully considered for the design of graphene-polymer nanocomposites with ultimate mechanical performance.

Graphene-based derivatives are mechanically strong but flexible that makes them an ideal nanofiller component for the fabrication of high-performance multi-functional polymer nanocomposites with high toughness. [74, 133] Graphene oxide components incorporated into different polymer matrices might result in a dramatic improvement in the mechanical properties such as elastic modulus, tensile strength, elongation, and toughness. A high level

of dispersion, flexible sheets, and a rich balance of interfacial interactions play the key roles as will be illustrated with selected examples from recent studies.

1.4.1 Graphene papers

Graphene oxide sheets can be assembled into highly-layered paper-like structures as fabricated by a vacuum-assisted assembly technique. [101, 116, 133, 134] These popular strong "paper" materials show very good mechanical properties including elastic modulus of 30-40 GPa, strength of 120 MPa, and toughness of 0.26 MJ m^{-3}. [133] Chen *et al.* reported similar paper-like materials using reduced graphene oxide and achieved 300 MPa ultimate strength, around 40 GPa elastic modulus, and higher toughness of 1.22 MJ m^{-3}. [208] However, despite these examples, the ultimate values reported are still well below those of the pristine graphene oxide materials or predicted by mechanical models. Furthermore, the reported mechanical properties of the graphene oxide papers are frequently divergent, inconsistent, poorly reproducible, and difficult to control. [134, 209]

In original graphene paper materials, water molecules have been considered to be intercalated between the graphene oxide flakes. [134] Submolecular water layers are suggested to act as a binder, which enables the hydrogen bonding network between water molecules and the oxygen-containing functionalities on the surface of the graphene oxide, thereby, linking the neighboring flakes together. However, hydrogen bonding represents weak forces compared to ionic or covalent interactions and even a high density of the bonding network might be compromised by a high mobility of small molecules. Moreover, an excessive amount of water (several molecular layers of water molecules) can act as a plasticizer or lubricant in the layered graphene oxide paper that can compromise its mechanical strength. As an alternative option, borate-assisted crosslinking of graphene oxide papers has been suggested to fabricate extremely strong, yet, brittle materials. [99]

Additional crosslinking of graphene oxide sheets in the multi-layered papers has been suggested to improve mechanical performance. [101, 116, 210] It is plausible to employ flexible polymers with proper side or main chain functionalities as the binder in graphene oxide materials with various oxidized surface functionalities. For example, the carboxyl

functional groups primarily located around the edge of the graphene oxide flakes are available for chemical crosslinking with amine groups to reinforce the inter-flake binding.

Cheng *et al.* have reported successful crosslinking of graphene oxide flakes with 10,12-pentacosadiyn-1-ol (PCDO) monomers via esterification (**Figure 1.12a**). [116] The monomers can be polymerized after intercalation to form a conjugated polymer with an integrated network of covalently bonded graphene oxide sheets.

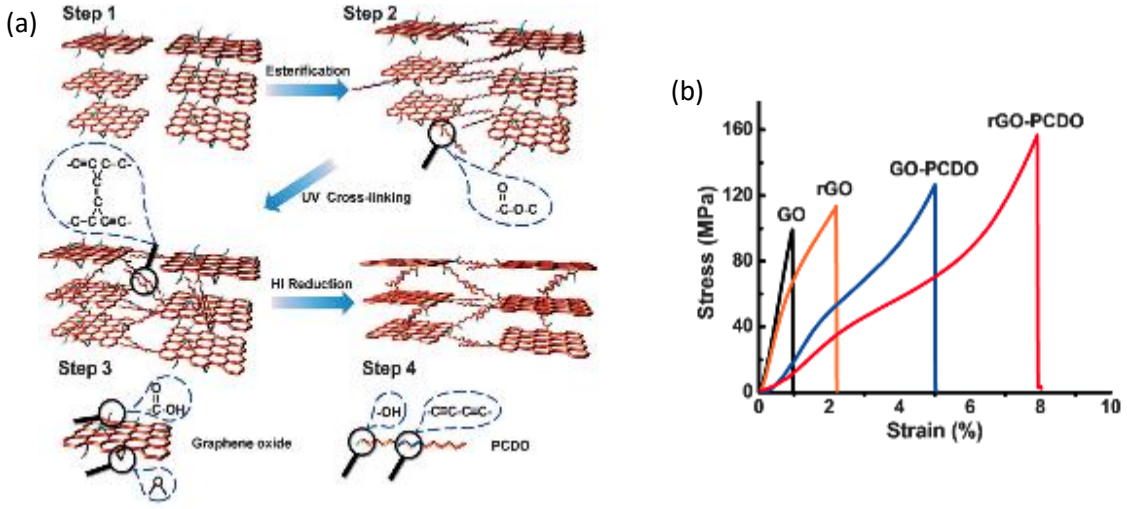

Figure 1.12 Schemes of the esterification, crosslinking, and reduction of the graphene oxide nanocomposites and corresponding changes of mechanical properties . [116] Copyright 2013. With permission of John Wiley & Sons.

The resulting material fabricated in this study is significantly tougher than the regular graphene/graphene oxide based polymeric nanocomposites without crosslinking. The toughness reached a record value of around 3.0 MJ m^{-3}, with a 120 MPa tensile strength, and significant, 5%, elongation to break. The authors claimed that the reason for such outstanding mechanical properties is the multiple strengthening mechanisms, including hydrogen bonding, entropic elasticity of the polymeric binders, covalent bonding between the graphene oxide and the polymer as well as between polymer chains themselves. The chemical reduction of graphene oxide further improved the mechanical properties of the nanocomposite, resulting in a tensile strength of about 160 MPa, 8% elongation to break, and around 4.0 MJ m^{-3} toughness (**Figure 1.12**). The crosslinking through the edge functionalities is inspiring because such reinforcement maintains the hydrogen bonds. This network acts at the initial stress thus facilitating large flexibility and compliance with

covalent bonding adding strength at small strain. The synergistic strategy employed in this research is important for developing robust graphene-based polymer nanocomposites.

Further reinforcement of the nanocomposite films can be realized by controllably reducing the graphene oxide sheets using a green and facile aluminum reduction strategy with controlled depth and pattern of microscopic regions. [109] The toughness of the chemically reduced graphene nanocomposite films was not compromised as a result of this treatment, but the strength is increased by 100% to above 300 MPa, and the elastic modulus increased to 26 GPa (Figure 1.13). The mild and environmental friendly strategy to restore the electrical properties and dramatically improve the mechanical properties introduced in this study can be widely applied to almost all graphene oxide based nanocomposite materials without the concern of excessive damage of the polymeric binders, which is always a critical issue if the traditional harsh and toxic reducing techniques are employed.

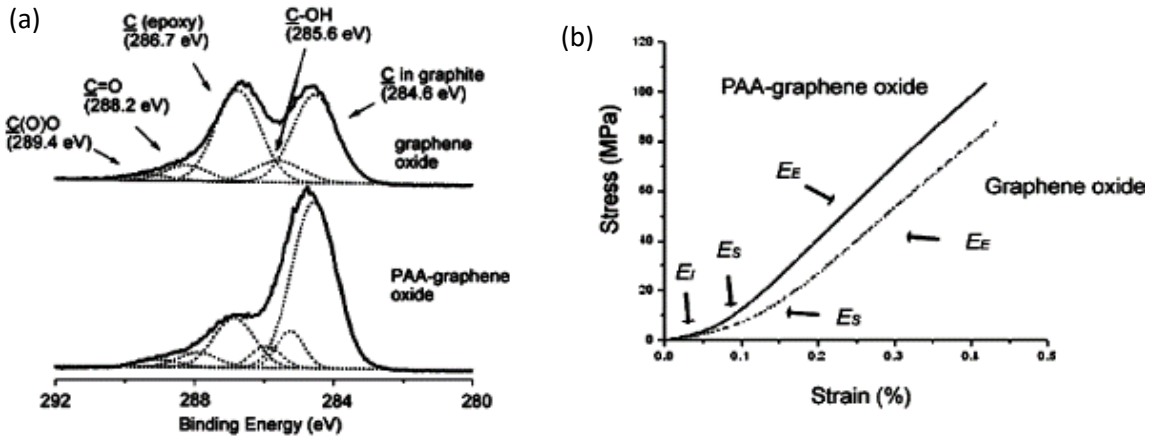

Figure 1.13 (a) XPS spectra of the graphene oxide paper and the PAA modified graphene oxide paper, showing effective chemical crosslinking; (b) stress-strain curves of the PAA modified and pristine graphene oxide papers, respectively. [101] Copyright 2009. With permission of American Chemical Society.

In another study, Park *et al.* reported robust paper-like materials from graphene oxide sheets crosslinked by polyallylamine (PAA). [101] PAA contains periodic reactive amine groups along the polymer backbones which are ready to react with the oxygen-containing functionalities on graphene oxide surfaces **(Figure 1.13a)**. By adding 21% of PAA in the graphene oxide suspension and by employing extensive sonication, the homogeneous mixture can be initially formed. After filtration of this suspension, uniform paper-like

morphologies can be achieved. The mechanical properties of the PAA-cross-linked graphene oxide paper are somewhat improved as compared to the non-modified graphene oxide paper (Figure 1.13).

The ultimate stress increased from 82 MPa to 91 MPa, whereas the ultimate strain slightly decreased from 0.4% to 0.32%. A significant improvement was observed in the elastic modulus values of the nanocomposites as well. The elastic modulus measured at three different stages of loading (*i.e.*, initial, straightening, and maximum) was significantly higher for the graphene oxide paper with PAA-modified components, reaching the highest value of 33 GPa (Figure 1.13b). The authors suggested that the modification of graphene oxide with a PAA component is critical for the efficient mechanical reinforcement by chemical crosslinking, but the overall reinforcing effect is modest when compared to the other results reported in literature.

The subdued effect on the mechanical properties of the PAA-crosslinked graphene-polymer nanocomposites may be due to macroscopic aggregation caused by the strong chemical interactions between PAA and graphene oxide materials. In order to obtain a homogeneous dispersion to assure uniform morphology, the initial mixture underwent extensive sonication. It is suggested that during the sonication the graphene oxide flakes are broken into smaller pieces, which undermines the strength characteristics of the resulting nanocomposites. Also, it is worth noting that although the dispersion is homogeneous after sonication, the presence of small aggregated nanoparticles compromises the final mechanical performance.

Similar results have been reported by Tian *et al.*, who used polyethyleneimine (PEI) to crosslink dopamine-functionalized graphene oxide materials. [210] The paper-like materials fabricated by vacuum-assisted method were additionally crosslinked with relatively high, 30%, PEI content. These crosslinked papers showed very high elastic modulus of about 100 GPa and excellent ultimate mechanical strength of 210 MPa. However, the ultimate strain of these crosslinked nanocomposites has significantly decreased to around 0.2% due to the inevitable dense and poorly deformable covalent chemical crosslinking network with low molar weight component (**Figure 1.14**).

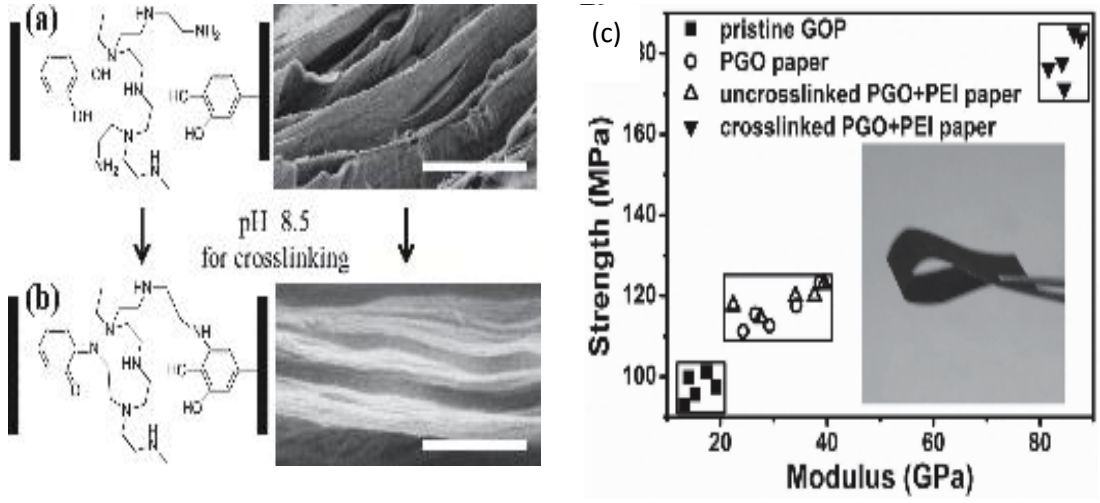

Figure 1.14 The chemical structure and SEM morphologies of the graphene oxide paper before (a) and after (b) PEI crosslinking. (c) Summary of the mechanical performance of the PEI crosslinked graphene oxide paper. [210] Copyright 2013. With permission of John Wiley & Sons.

1.4.2 Graphene-polymer nanocomposites via weak interfacial interactions

Another strategy for toughening the graphene oxide-polymer nanocomposites is employing restorable network rather than permanent covalent bonding. Hydrogen bonding, hydrophobic interactions, electrostatic attractions, and polar-polar interactions with the potential of self-restoration and large deformation are considered for this purpose (Table 1.1). The network of such multiple weak interactions can facilitate significant reinforcement and compensate the weaker individual bindings. Elastomeric synthetic and biological materials might be efficient binders due to their wide spectrum of chemical compositions and functions. In addition, their easy processability, high mobility, conformational flexibility are important advantageous features as well.

In recent study, Kulkarni *et al.* exploited electrostatic interactions to bind the negatively charged graphene oxide sheets and oppositely charged polyelectrolyte multilayers. [3, 135] Negatively charged monolayer graphene oxide flakes in high concentration (60% of surface coverage) were incorporated into the polyelectrolyte matrix without folding and wrinkling (Figure 1.9). The multiple electrostatic interactions at the graphene oxide-polyelectrolyte interface resulted in a significant toughening the ultrathin membrane by 500%, from 0.4 MJ m^{-3} to a high value of 1.9 MJ m^{-3} (**Figure 1.15**). [3] The application of

LbL assembly significantly increased the interaction area of the two components, thus optimizing the stress transfer condition during large strain. The content of graphene oxide required to achieve to achieve the optimum toughness was only 3.3 vol.%, owing to the high density of electrostatic interactions and the ability to restore the interactions under large strains.

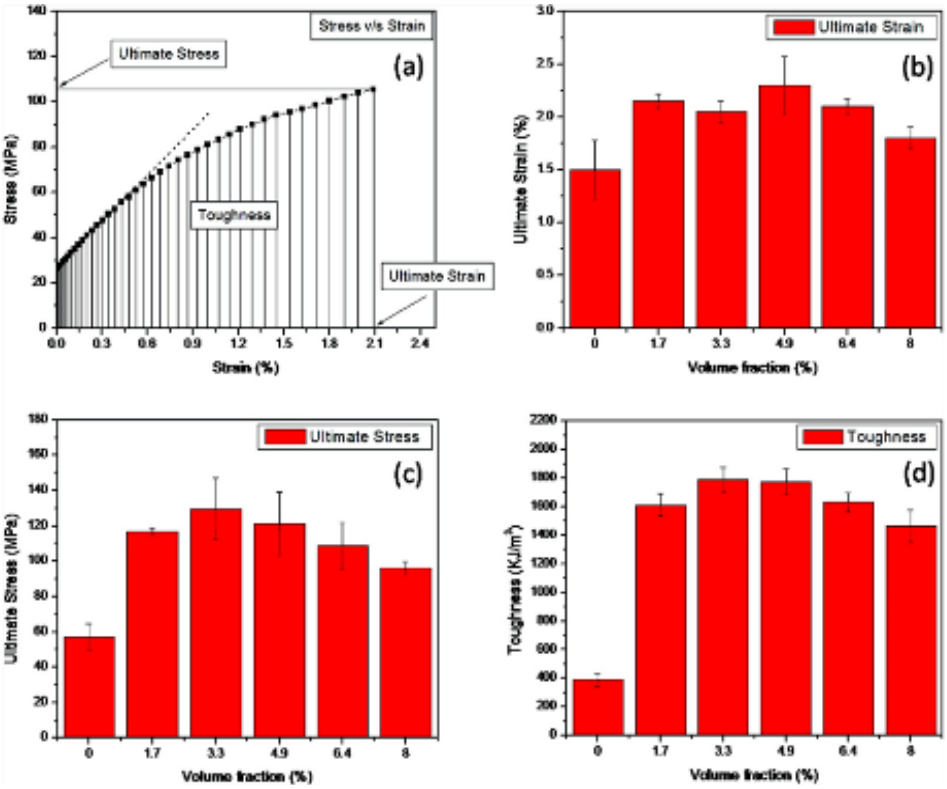

Figure 1.15 Representative stress-strain curve (a) of the graphene oxide-polyelectrolyte nanomembranes and the effect of graphene oxide content on the mechanical properties: (b) ultimate strain, (c) ultimate stress, and (d) toughness. [3] Copyright 2010. With permission of American Chemical Society.

Meanwhile, the elastic modulus value increased by 8-fold to 18 GPa; the ultimate stress increased by 120% to 130 MPa, and the ultimate strain increased by 50% to 2.3% (Figure 1.15). The increase in strain is unusual for graphene oxide reinforced polymeric materials because the ultra-strong graphene oxide tends to make the nanocomposite brittle. However in this case, the interactions are either too strong (*e.g.*, covalent bonding) or too weak (*e.g.*, van der Waals force), facilitating the stress distribution and the constituent reorganization. Utilizing moderate but high density interactions to bind graphene oxide and the polymeric component is a plausible philosophy to develop new nanocomposites with balanced mechanical properties.

The formation of hydrogen bonding networking is the most utilized reinforcement mechanism for the integration of graphene oxide component in various polymeric matrices. In another recent study, Putz *et al.* have compared the effect of the incorporation of graphene oxide nanofillers in the matrices of such different matrices as PVA (hydrophilic) and PMMA (hydrophobic). [211] Due to the contrasting hydrophobicity of these matrices, the reinforcing effects caused by the addition of graphene oxide are very different. As 64% of graphene oxide is added to the hydrophilic PVA matrix, the strong hydrogen bonding networking results in dramatically increased elastic modulus of 36 GPa and significantly improved tensile strength of 80 MPa (**Figure 1.16a**). However, the strain to failure of these nanocomposites plunged from 14.2% to 0.25% thus indicating stiffening of the reinforced material.

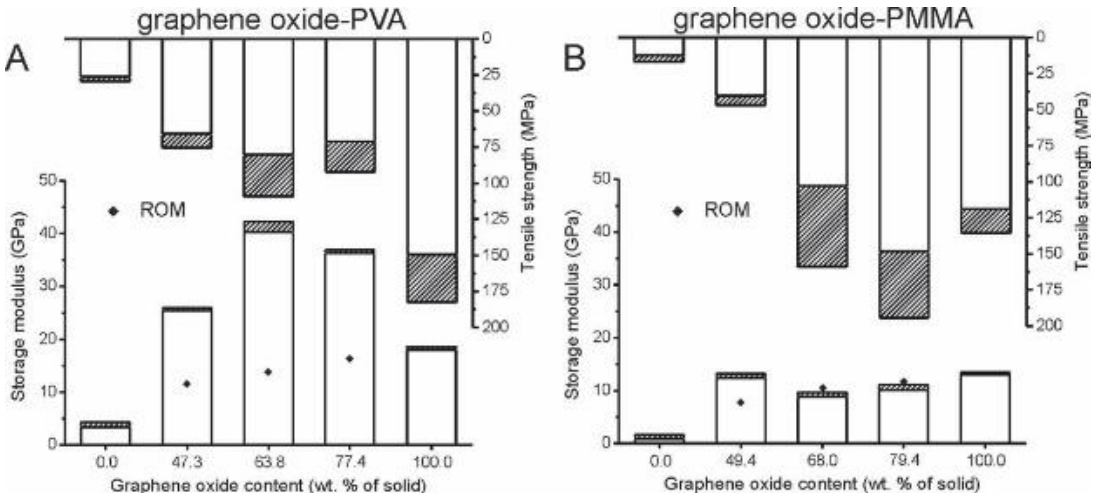

Figure 1.16 Storage moduli and tensile strengths of: A) PVA-based and B) PMMA-based nanocomposites. The average and maximum values are shown by the white and shaded bars, respectively. [211] Copyright 2010. With permission of John Wiley & Sons.

The change in mechanical properties is attributed to the strong hydrogen bonding between PVA matrix and graphene oxide. In contrast, for the hydrophobic PMMA matrix, the hydrogen bonding is much weaker because the PMMA molecules can only serve as hydrogen bond acceptors through the ester oxygen. As a result, the Young's modulus of the 68% graphene oxide filled PMMA matrix is very modest, around 6 GPa only (Figure 1.16). But on the other hand, the ultimate strain is higher, around 2.6% (Figure 1.16).

In different study, Li *et al.* have reported the effect of addition of a small content of graphene oxide in PVA matrix and the load transfer using polarized Raman spectroscopy.

[212] Addition of 3% of graphene oxide to the PVA matrix caused a modest increase in the storage modulus value by 50% to around 6 GPa. On the other hand, the ultimate strength increased by 100% to 60 MPa with minimal compromise of the ultimate strain (decreased from 180% to 155%).

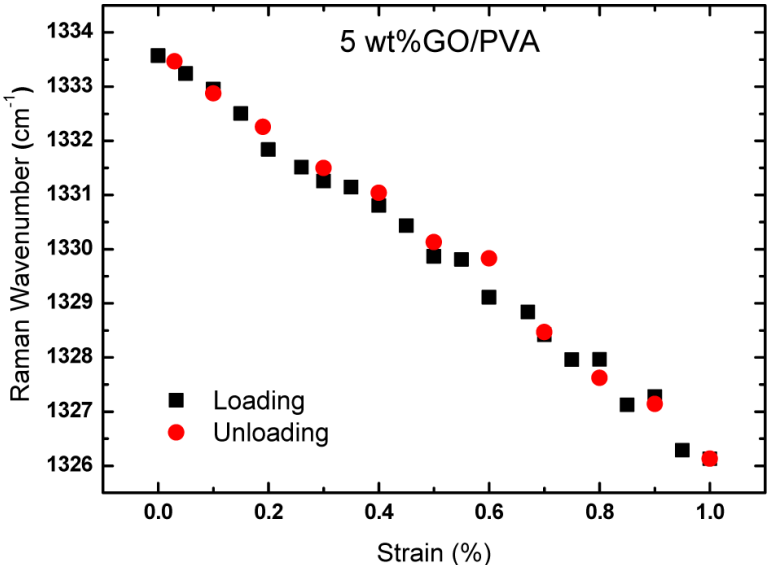

Figure 1.17 Shift of the D band position with strain to the PVA-graphene oxide nanocomposite for loading and unloading. [212] Copyright 2013. With permission of American Chemical Society.

In this study, the authors have employed Raman spectroscopy to understand the stress development in these nanocomposites and observed the shift of the D band of graphene oxide material as a function of engineering strain (**Figure 1.17**). The D band of the graphene oxide embedded in the nanocomposite shifted linearly and reversibly from 1333.5 cm^{-1} to 1326 cm^{-1} when 1.0% strain was applied, indicating good interfacial transfer between the nanofiller and the matrix (Figure 1.18). [212] Although the calculated modulus value for graphene oxide is much smaller than the widely accepted value (200-250 GPa), the use of Raman spectroscopy to monitor the strain in the nanocomposite can be considered an important approach to the understanding of the reinforcement and load transfer mechanism between graphene oxide sheets and various polymer matrices.

Xu *et al.* have also reported the mechanical strengthening of reduced graphene oxide to the PDMS matrix using Raman spectroscopy. [213] The authors demonstrated that the elastic modulus, toughness, damping capability, and strain energy density were all increased by 42%, 39%, 673%, and 43%, respectively, with the addition of only 1% graphene

component. Also, a G band shift rate in Raman measurements of 11.2 cm^{-1} per 1% strain for compression and 4.2 cm^{-1} per 1% strain for tensile stress was observed for these nanocomposites. These values are much higher than the common values reported for the graphene sheets embedded in PDMS matrix. [214] The higher shift rate of the Raman bands in Xu's results was primarily attributed to the efficient bonding of monolayers of reduced graphene oxide sheets to the hydrophobic PDMS matrix in contrast to the stacked graphitic platelets without proper functionalities as used in the other studies.

Interaction of graphene oxide with the polymer matrices can be enhanced by chemical functionalization of graphene oxide surfaces. In order to crosslink epoxy resin with graphene oxide, Bao *et al.* functionalized graphene oxide surface with hexachlorocyclotriphosphazene and glycidol treatment to graft chains with epoxide groups. [17] The functionalized graphene oxide was mixed with epoxy oligomer and polymerized in situ to fabricate dispersed and crosslinked morphologies. The resulting highly crosslinked nanocomposites with only 2% graphene oxide content showed an improvement in elastic modulus from 1.5 GPa to 3.2 GPa. The ultimate strength also improved to 217 MPa when 4% graphene oxide was added.

In another recent study, graphene oxide was solution mixed with ultra-high molecular weight polyethylene (PE) and hot pressed to prepare a composite film. [215] Addition of small quantities of graphene oxide increases the mechanical properties of the neat PE films with the composite having 0.5 wt. % graphene oxide showing the best tensile strength. Moreover, the biocompatibility of these nanocomposites was tested and no negative effect on the cell growth was observed.

1.4.3 Incorporation of graphene fillers into nanocomposites

To date, very few results have been reported on the fabrication of polymer nanocomposites with a pristine graphene component. This is primarily due to the chemical inertness of graphitic surfaces and difficulties in the exfoliation. Graphene is highly hydrophobic and non-dispersable in most conventional organic solvents, which is another challenge for materials processing. The range of interactions between graphene and various polymer matrices is very limited as well. Hydrophobic-hydrophobic interactions and π-π stacking

are usually employed to enhance interfacial interactions with proper polymer matrices like PS but they are not extremely strong. [114]

Among recent studies, Laaksonen *et al.* reported graphene-nanofibrillated cellulose (NFC) nanocomposites as mechanically robust materials. [216] The approach employed genetically engineered materials to match the properties of the two components, which opens wide opportunities for the field of bio-nanocomposites. The authors exploited a di-block protein, which can bind graphene layers through hydrophobic interactions and cellulose fibrils with biological recognition terminal group, to crosslink the different components (**Figure 1.18**).

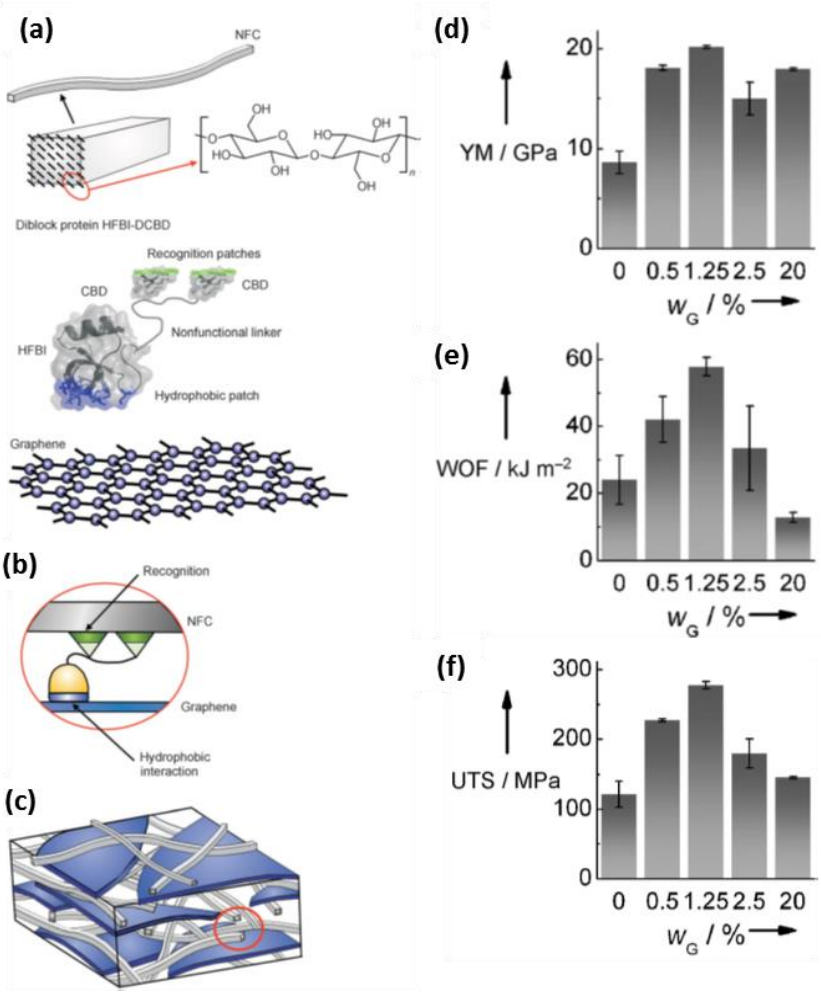

Figure 1.18 (a)-(c) The assembly of the graphene-NFC nanocomposites; (d)-(f) Mechanical properties of the graphene nanocomposites: Young's modulus (YM), work of fracture (WOF), and ultimate tensile stress (UTS) versus the weight fraction of graphene in the nanocomposite, respectively. [216] Copyright 2011. With permission of John Wiley & Sons.

The elastic modulus, ultimate strength and toughness increased to 20 GPa, 280 MPa, and about 5 MJ m^{-3}, respectively, with only 1.25 wt% graphene added (Figure 1.18d-f). Virtually all polymeric materials can be engineered to fit in this strategy and bond strongly with graphene. However, the genetic modification requires significant synthetic efforts and long term screening and purification procedures.

Another approach for the incorporation of graphene components into polymeric matrices is the *in-situ* reduction of graphene oxide. Li *et al.* have reported graphene-PVA nanocomposites through mixing of graphene oxide suspension and PVA solution. [217] The mechanical properties of the nanocomposite were already excellent even before chemical reduction of graphene oxide component with the ultimate stress and ultimate strain reaching 120 MPa and 1.2%, respectively. After HI reduction, the ultimate stress, ultimate strain and stiffness increased significantly to 190 MPa, 2.6%, 11 GPa, respectively. The reinforcement is claimed to be strong because of the restoration of the defected carbon network and the reduction of the interlayer spacing after the chemical reduction of graphene oxide. However, the real reinforcing mechanism is still unclear because the strength of the affinity between PVA matrix and the reduced graphene oxide which is hydrophobic is not clarified.

1.4.4 Hydrogels reinforced by graphene derivatives

Hydrogels are known for their wide range of applications including tissue engineering, drug delivery, and energy storage owing to their large specific surface area, high compliance, responsive behavior, and biocompatibility. [218, 219, 220, 221, 222, 223, 224] In particular, polymer hydrogels are promising for biomedical applications including controlled drug release, enzyme immobilization, sensors and actuators, and as tissue culture substrates. However, conventional hydrogels show modest mechanical properties such as low mechanical strength and low elastic modulus. Thus, significant efforts are devoted to improving mechanical properties (mostly mechanical strength and toughness) of the hydrogels by employing organic and inorganic cross-linkers, hydrophilic silica particles, and functionalized clay nanoplatelets as reinforcing agents.

Recent studies have reported the incorporation of graphene and graphene oxide into hydrogel structures as well. In particular, Shen *et al.* have reported the fabrication of graphene oxide-PAA hydrogels and investigated the mechanical, thermal, and swelling behavior of these reinforced hydrogels (**Figure 1.19**). [225] The functional groups on the graphene oxide surface were used as anchoring sites for the *in situ* polymerization of PAA matrix by N,N-methylenebisacrylamide (BIS). Moreover, the oxygenated functionalities also enabled the formation of the network of hydrogen bonds of graphene oxide with the compliant PAA matrix.

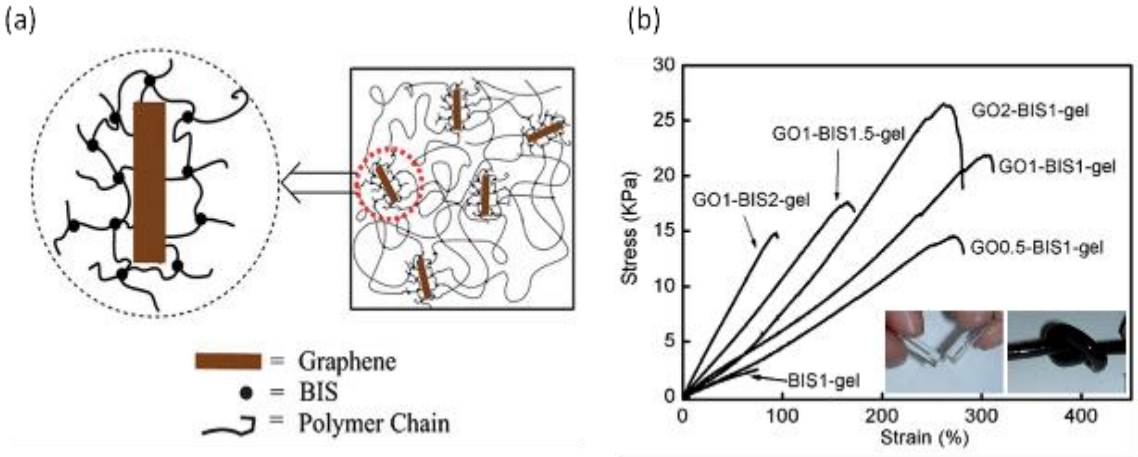

Figure 1.19 (a) Scheme of the crosslinked gel network consists of graphene, BIS, and PAA; (b) Stress-strain curves of PAA gels with different combinations of GO and BIS contents. The inset shows the photographs of BIS-gel and GO-BIS gel from left to right, respectively. [225] Copyright 2012. With permission of Royal Society of Chemistry.

The analysis of the stress-strain behavior of the hydrogels fabricated with and without the graphene oxide component showed that the incorporation of graphene oxide sheets resulted in a significant increase in the elongation to break up to 300% (Figure 1.19). Also, the nanocomposite PAA hydrogels with graphene oxide were found to be more ductile and capable of sustaining large deformation and complex shear force fields. The simultaneous increase in the mechanical strength and ductility was attributed to the strength of graphene oxide.

Poly (N-isopropylacrylamide) (PNIPAAm) is a material of choice for thermoresponsive applications owing to the ability of polymer chains to undergo a reversible coil-to-globule transition at the Lower Critical Solution Temperature (LCST). [226, 227, 228, 229] PNIPAAm is

considered for biomedical applications such as drug delivery on-demand, however, the poor mechanical properties with low compressive modulus and poor elastic recovery limit its use. Thus, graphene-based PNIPAAm nanocomposites have gained attention as a prospective material exhibiting enhanced mechanical properties along with high temperature sensitivity.

Thermoresponsive graphene-nanocomposite PNIPAAm hydrogels were fabricated by Mariani *et al.* [230] Graphene was dispersed in N-methyl pyrrolidone by subjecting graphite to ultrasound treatment. The resulting solution was mixed with NiPAAm monomer and polymerized using a frontal polymerization technique. Mechanical analysis of the resulting nanocomposites revealed that the addition of graphene into the hydrogel matrix resulted in a material with thermoplastic behavior. The storage modulus and viscosity of hydrogels increased with the increase in graphene content; however, at higher concentrations, a significant decrease in the mechanical strength of these nanocomposites was observed possibly due to the slippage of the sheets at higher loading rates.

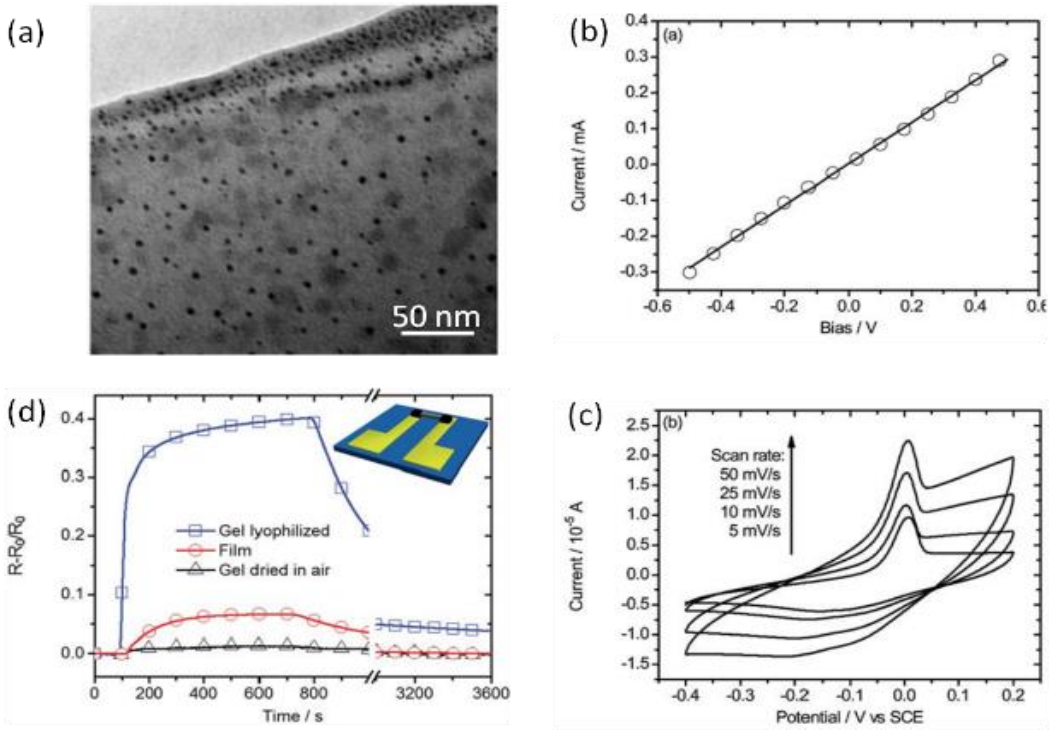

Figure 1.20 (a) TEM of a GO/PPy nanocomposite sheet with platinium nanoparticles embedded, (b) I-V curve of a lyophilized GO/PPy hydrogel, (c) cyclic voltammograms of GO/PPyl hydrogel in 0.1 M LiClO4 at different scan rates, and (d) Ammonia gas sensing performance of three devices with different sensing elements. [232] Copyright 2011. With permission of Royal Society of Chemistry.

In another study, pH-responsive and thermal-responsive graphene oxide hydrogels have been fabricated by covalently attaching graphene oxide sheets to PNIPAM-co-AA microgels in water. [231] However, the mechanical properties of these reinforced hydrogels were not mentioned. Hydrogels made from conducting polymers such as polypyrrole (PPy) can be promising for electrochemical and energy storage applications. Shi *et al.* demonstrated the fabrication of graphene oxide-PPy hydrogels using *in situ* polymerization of monomer in graphene oxide solution and tested for their electrical properties (**Figure 1.20**). [232]

Graphene oxide components, which are known for their effective gelation properties, are expected to have a strong interaction with the conducting polymer resulting in a cross-linked network. Indeed, the hydrogels showed a frequency independent storage modulus and the values were much higher than the loss modulus suggesting the fabrication of strong hydrogels (Figure 1.20). These hydrogels were much stronger than the other graphene oxide based-hydrogels reported in literature due to the strong π-π interaction between the graphene oxide and PPY matrix. The enhanced crosslinking and the high moduli of conjugated polymer with a stiff backbone both contributed to improved mechanical performance.

1.5 Other functional properties and applications

Besides the strong mechanical performance which has mostly been discussed above, graphene materials play a critical role in the fabrication of polymer nanocomposites with novel functionalities. Most important functionalities addressed in current studies are enhanced optical, electrical, thermal, or barrier properties. To date, graphene components have been included in a variety of polymer matrices such as epoxy polymers, PS, PANI, Nafion, and poly (3,4-ethyldioxythiophene) to fabricate nanocomposites with new functionalities. [233, 234, 235] The percolation threshold, conductivity, and mechanical properties of the nanocomposites were tested for prospective applications including supercapacitors, transparent conducting electrodes, gas barrier membranes, and biosensors. [150, 236, 237, 238]

However, to improve the functional performance of the nanocomposite, efficient dispersion of the graphene components inside the polymer matrix without aggregation should be implemented. This is a challenging task for potentially functional matrices similarly to those discussed above for mechanical performance. For instance, as was mentioned before inert graphene is difficult to disperse in the commonly used organic solvents and also in the functionalized polymer matrices. Thus, efforts to employ reduced graphene oxide or decorate the surface of graphene or graphene oxides with different functionalities are needed for improving the dispersibility and functionality. [74, 237, 239]

1.5.1 Graphene-polymer nanocomposites for sensing applications

In one of the earlier studies, reduced graphene oxide was mixed with Nafion, a well-known membrane-type material. [240] The resulting mixed solution was used for the fabrication of an electrochemically active polymer nanocomposite. These materials were used as a sensing platform to detect trace levels of toxic elements such as lead and cadmium. It was observed that the resulting Nafion-reduced graphene oxide films possess a high sensitivity towards metal ions and exhibit an improved detection limit of 0.02 μg L^{-1} for selected metal ions.

Graphene-PANI nanocomposites have also been fabricated for hydrogen sensing applications. [241] Hydrogen sensing of the nanocomposite material was compared with that of PANI nanofibers and graphene sheets. The nanocomposite films were found to have a much higher sensitivity for hydrogen gas detection than films fabricated solely from graphene sheets or PANI nanofibers. In another study, graphene oxide-PP nanocomposites have further been fabricated by polymerization of pyrrole in graphene oxide solution. [232] These hydrogels were used as a sensing element in a chemoresistor sensor to detect ammonia gas. The lyophilized graphene oxide-PP composites showed a good sensitivity towards ammonia with a 40% increase in sensitivity detected if pores remind open under wet conditions.

Several recent developments include the fabrication of multicomponent polymer nanocomposites from silica and other oxide particles coated with graphene oxide for detection of dopamine [242] and monitoring of mammalian nervous cells, proteins and E.coli

cells [243, 244, 245]; conducting reduced graphene oxide-polymer with high barrier and gas sensing properties [246, 247] and electrochemical sensing of isomers [248]. Methanol-sensitive nanocomposites with enhanced characteristics from PANI-graphene oxide nanocomposites [249], amplified colorimetric sensors for target DNA detection [250, 251], sensing skins for detection of volatile organic vapors [252], advanced electrochemical electrodes for peroxide and glucose detection for food control [253], and electrically conductive aerogels for catalysis and sending applications [254] have also been reported.

1.5.2 Graphene-polymer nanocomposites as gas barriers

Solid, non-porous fillers with a high surface area to volume ratio are one of the prime necessities in fabricating polymer nanocomposite thin films to prevent the permeation of gas and water molecules through the film. Food, electronics, Li-ion batteries, and fuel cells are sensitive to the presence of gases such as oxygen and moisture and require protective/active elements. [150, 255] Strong and modestly flexible metal thin films such as aluminum foils form an excellent barrier against these elements, however, presence of pin holes and defects during stretching, bending, and handling limits their broad use.

On the other hand, flexible polymer nanocomposites offer an alternative due to their high mechanical strength combined with high transparency and a tendency to reduce the permeation of gases and moisture through the films. Traditionally, clay-based polymer nanocomposites known for their low permeability to gases and moisture are exploited for these applications. [256] However, recent studies have also reported the use of graphene for gas barrier and gas sensing applications owing to its non-permeable sheets-like structures.

For instance, Yang *et al.* deposited graphene oxide sheets alternatively with PEI polymer to form a stacked polymer nanocomposite to investigate the oxygen barrier properties of these films (**Figure 1.21**). [255] A 91 nm thick film comprising of 10 bilayers of 0.1 wt% graphene oxide and 0.2 wt% PEI on top of PET supporting film showed an improved oxygen permeability of 2.5×10^{-20} cm^2 s^{-1} Pa^{-2}. This low permeability is comparable to the oxygen permeability observed in case of 100 nm thick SiOx nanocoatings. Also, these films were found to be useful for gas separation with a H_2/CO_2 selectivity (*i.e.*, the ratio of permeabilities of different gasses, H_2 and CO_2) higher than 383.

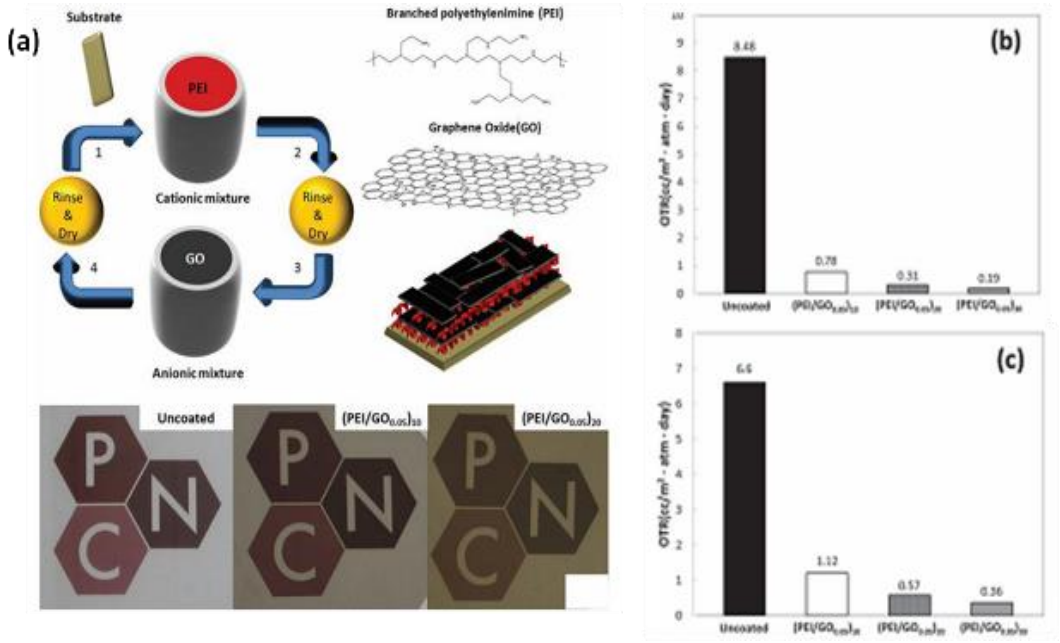

Figure 1.21 (a) LbL assembly of PEI-GO nanocomposites as gas barrier films. Oxygen transmission rate of PEI-GO composites assembled on PET, measured at 23oC under (b) 0% RH and (c) 100% RH. [255] Copyright 2013. With permission of John Wiley & Sons.

In recent studies, a significant reduction of oxygen and carbon dioxide permeation and potentials for high selectivity of hydrogen permeation have been reported for in-situ polymerized, paper-like, and LbL graphene oxide-conjugated polymer nanocomposite films. [255, 257, 258] In another study, high moisture barrier properties combined with high transparency has been reported for robust graphene-based polyimide nanocomposite materials. [259] Graphene oxide-polymer films have been reported as flammable-resistant coatings caused by their high gas barrier properties and reduced oxydation [260] as well as highly elastomeric nanocomposites, which combine low permeability with good electrical conductivity. [150]

1.5.3 Graphene-polymer nanocomposites for photovoltaic applications

Graphene components as well as traditional carbon nanotubes are well known as hole transport materials, which can be effective in fabricating organic photovoltaic materials. [261] However, these nanocomposite materials are frequently deposited from highly acidic aqueous solutions, which adversely affects the common ITO electrodes and degrades the device performance.

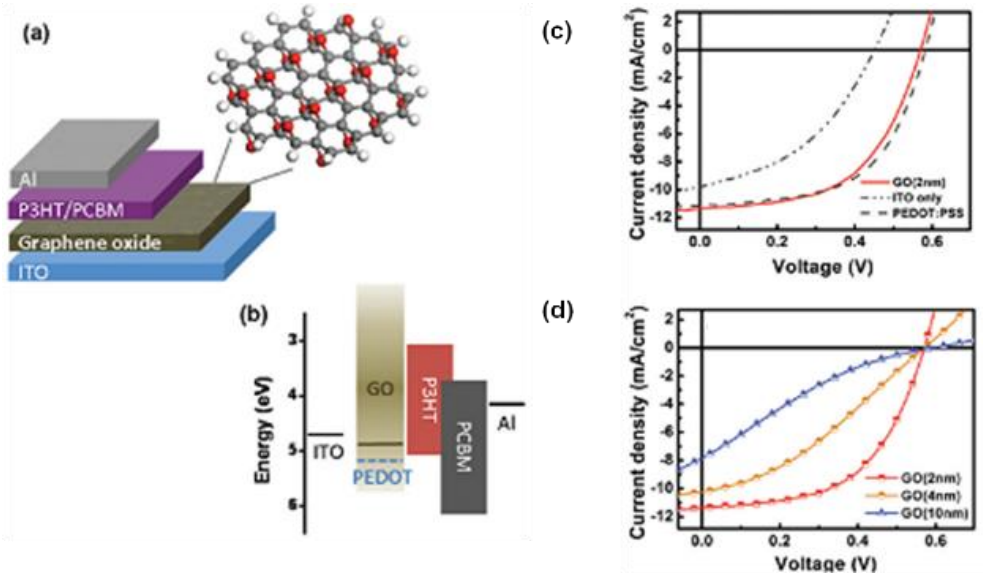

Figure 1.22 Device schematic (a) and energy level diagram (b) of the photovoltaic device structure consisting of ITO/GO/P3HT:PCBM/Al components. Current-voltage characteristics of (c) photovoltaic devices with no hole transport layer (curve labeled as ITO) and (d) ITO/GO/P3HT:PCBM/Al with different GO thicknesses. [262] Copyright 2010. With permission of American Chemical Society.

Chhowalla *et al.* demonstrated the use of graphene oxide as alternative, solution processable hole-transport material in organic photovoltaic films (**Figure 1.22**). [262] Graphene oxide thin films were obtained from neutral solutions between the photoactive poly(3-hexylthiophene) (P3HT) : phenyl-C61-butyric acid methyl ester (PCBM) layer and transparent conducting ITO electrode. This design resulted in a dramatic improvement of the photovoltaic efficiency and were comparable to the devices fabricated using traditional poly(3,4-ethylenedioxythiophene) (PEDOT):PSS pair. Also, the use of non-aqueous solvents for the deposition of graphene oxide was suggested for further improvement of the device performance and to ensure the reliability of these films.

Thin layers with graphene oxide and carbon nanotubes were also used as a replacement for PEDOT:PSS in P3HT:PCBM layers in a tandem devices. [263] The regular and inverted tandem photovoltaic cells fabricated in this study showed a significant increase in open-circuit voltage (V_{oc}) by 84% and 80% of the sub-cell V_{oc}. Power conversion efficiency (PCE) as high as 4.1% was achieved for these modified tandem cells. The tandem cells showed high transparency in the near-infrared region and were expected to work well with tandem cells with a low band gap polymer component. Also, doping of the carbon

nanotubes was expected to further improve the charge recombination at the interface. This study indicates that graphene oxide can effectively serve as the hole transport component and electron blocking layer for photovoltaic and light-emitting applications.

Recent publications in this field discussed all-polymer-graphene nanocomposites with various graphene components and conjugated polymer matrices for a variety of related applications including those for optoelectronic phenomena [264, 265] and other energy-related and broader prospective applications [266, 267, 268]. Additional recent results include a combination of graphene with solid polymer electrolytes and dye-sensitized solar cells [269, 270], fabrication of nanocomposites with photoluminescent quenching [271], non-covalent integration of variously reduced graphene oxide and stamping transfer into bulk heterojunction polymer solar cells [272, 273, 274, 275, 276].

1.5.4 Graphene-polymer nanocomposites with high thermal conductivity

Decreases in the size of electronic devices necessitate the fabrication of high density electronics leading to an increase in the heat generation. Fillers with high thermal conductivities efficiently transfer the phonons, however, the transport is slowed down at the polymer-filler interfaces in polymer nanocomposites due to the amorphous characteristics of the polymer with low thermal conductivity and imperfect interfacial binding. [277]

Graphitic nanoplatelets, which are composed of a few graphitic layers were incorporated in the epoxy matrix at different loading concentrations and the nanocomposites were tested for their thermal conductivities. [278] A linear increase in the thermal conductivity of the nanocomposite was observed for higher graphene content. The incorporation of 5 wt% graphene oxide in the epoxy matrix resulted in a 4 times higher thermal conductivity than the neat polymer and can be further increased by incorporating 20 wt% of graphene oxide. Finally, thermal conductivity increased by up to 20 times for a graphene loading of 40 wt%. Expanded graphite was acid-functionalized and used as a filler material for fabrication of polymer nanocomposities with high electrical conductivity. [279] At similar loadings, functionalized graphite was found to be more effective filler for improving the thermal conductivity of the polymer nanocomposites.

A number of recent publications addressed improving of thermal conductivity graphene-polymer nanocomposites such as in silane-crosslinked graphene oxide nanocomposites [280] and in nanocomposites with strong interfacial interactions [280,281]. Several recent studies reported nanocomposites with enhanced thermal conductivity and dimensional stability [280], fabrication of dielectric epoxy thermosets with increased thermal conductivity [282], design of stable nanocomposites which exhibit a high dielectric constant and low dielectric loss along with high thermal conductivity [283], improving thermal properties of polyimide and polyamic acid matrices [284], and controlling thermoelectrical properties of PANI films [285].

1.5.5 Graphene-polymer nanocomposites with electrical conductivity

Graphene oxide is known to become highly conductive upon chemical reduction or thermal reduction or a combination of chemical and thermal reduction techniques. [102, 103, 104, 105, 106, 107, 108] The extent of the restoration of the electrical conductivity during reducing procedure is largely dependent on the effectiveness of the removal of the oxygen-containing functionalities, especially the epoxide groups, from the surface and restoration of carbon-carbon sp^2 bonds. [102] Therefore, graphene oxide-polymer nanocomposites are potentially useful for integration into electronic devices if proper reducing treatment is applied.

Graphene oxide incorporated into a PDMS matrix was found to show unique electric properties. [286] On application of an electric field of low strength, the composite showed a lower conductivity compared to the neat power due to the blockage of ion transport by the graphene oxide network. Further increase in the electric field resulted in nonlinear conductivity that is progressively more sensitive to the applied electric field. At high electric field, the electrical conductivity is dominated by the electron transport across the graphene oxide network which can be tuned by varying the oxidation state, the volume fraction of graphene oxide, and morphology. The authors suggested that the unique electrical properties combined with high mechanical strength has potential applications as field electromagnetic field protective materials or insulation materials in high voltage power system and electronic devices.

In other study, Koratkar *et al.* compared the electrical conductivity of multi-walled carbon nanotube-PS materials and graphene-PS nanocomposites fabricated by mixing the filler materials followed filtration and drying. [287] The conductivity of the nanocomposites was found to increase significantly but still was several orders of magnitude lower than the PS films with carbon nanotubes. Further, selective localization of graphene was achieved by adding PLA into the matrix. PLA interacts poorly with graphene and the higher viscosity of PLA compared to PS results in the isolation of PLA in the matrix. As a result of this phase separation, graphene migrates into the hydrophobic PS regions, which resulted in a decrease in the percolation threshold for electrical conductivity to 0.075 vol %.

PP-graphene oxide nanocomposites with electrical conductivity were fabricated by *in situ* polymerization using Ziegler-Natta catalyst. [288] The use of a supported catalyst system helped overcome the incompatibility between polar graphene oxide and non-polar PP matrix. Although, the nanocomposites showed a poor electrical conductivity of 0.3 S m^{-1} at a 4.9 wt% loading, it enabled a means of incorporating graphene oxide into a variety of incompatible polymer matrices.

Nanocomposite films of polypyrrole, a well-known conducting polymer and graphene functionalized with sulfonic acid groups were electrochemically deposited from aqueous solutions containing pyrrole monomer, sulfonated graphene, and dodecyl benzene sulfonic acid. [289] The negatively charged sufonated graphene resulted in the doping of the polypyrrole during the polymerization process. The resulting composite films with 40 wt% sulfonated graphene sheets showed a specific capacitance of 285 F g^{-1} at a discharge rate of 0.5 A g^{-1} with improved electrochemical stability. In another study, isocyanate functionalization of graphene oxide and its subsequent reduction after solvent blending within the PS matrix resulted in a highly dispersed uniform nanocomposite film at a graphene oxide loading of 2.4 vol%. [133] These nanocomposites revealed a percolation threshold for electrical conduction of 0.1 vol% graphene oxide, which is three times lower than the values obtained for other filler materials.

Stable nanocomposite films of graphene oxide and PANI nanofibers were prepared by vacuum filtration to form a layered material with the PANI nanofibers sandwiched between

the graphene oxide layers (**Figure 1.23**). [158] These mechanically robust and flexible nanocomposite films with 44% graphene oxide showed a 10 times higher electrical conductivity than the pristine PANI nanofiber films. These films were further employed in the fabrication of supercapacitor microdevices and resulted in a 210 F g^{-1} electrochemical capacitance at a discharge rate of 0.3 A g^{-1}.

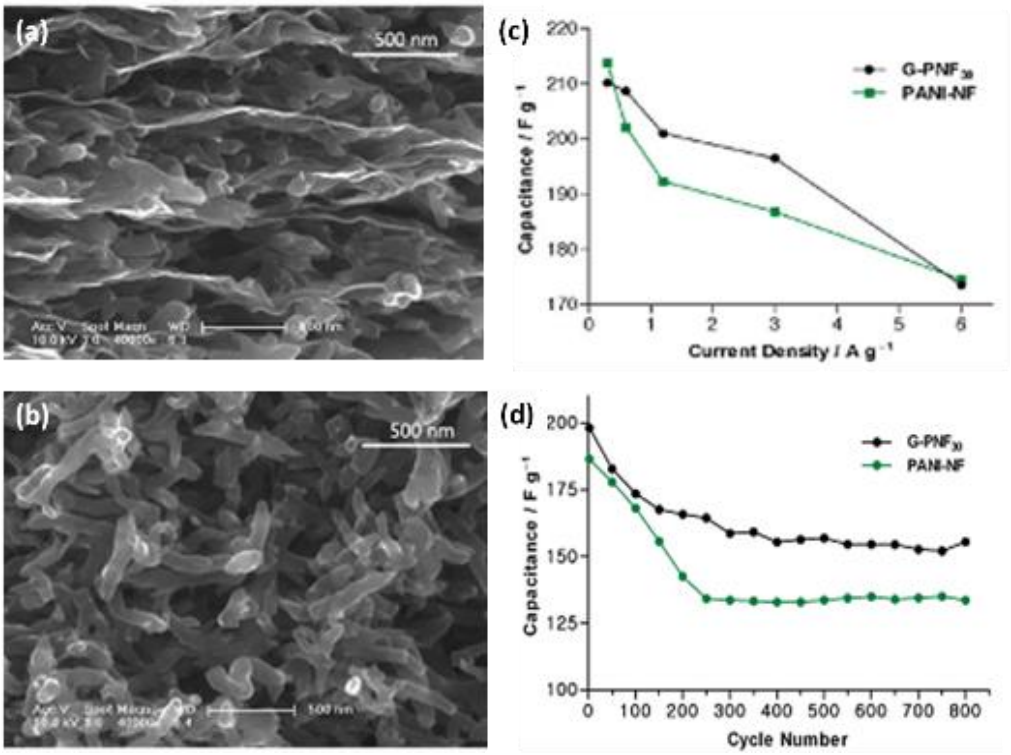

Figure 1.23 Cross-section SEM images of (a) pure chemically converted graphene and (b) graphene-PANI nanofiber composite film. (c) Plot of specific capacitance versus current density of graphene-PANI composite and PANI, and (d) cycling stability of graphene-PANI composite and PANI films. [158] Copyright 2010. With permission of American Chemical Society.

Flexible PANI electrodes doped with graphene oxide were fabricated by *in situ* polymerization of aniline in the presence of graphene oxide. [290] Incorporation of graphene oxide resulted in a remarkable enhancement in the electrical conductivity and specific capacitance of the nanocomposite materials as compared to individual PANI materials. The nanocomposite showed an electrical conductivity of 1000 S m^{-1} at a PANI:GO ratio of 100:1 and specific capacitance of 531 F g^{-1} (compared to 216 F g^{-1} for pure PANI). This process was further improved by incorporation of carbon nanotubes into the GO-PANI composite. [179] For this material, graphene oxide was mixed with carbon nanotubes to form a 3D network and further mixed with PANI by a one-step template-free process. The PANI

formed a fish scale-like structure on the graphene oxide sheets aided by electrostatic interaction, hydrogen bonding, and π-π interaction. These multicomponent nanocomposite materials exhibited a specific capacitance of 589 F g^{-1} and retained 81% of its initial capacitance even after 1000 cycles.

Different graphene-PANI nanocomposites were prepared by the use of polymerized ionic liquid. [291] Graphene sheets were dispersed in N,N-dimethylformamide (DMF) and polymerized ionic liquid poly(1-vinyl-3-butylimidazolium chloride) (PIL) in order to stabilize the dispersion. PIL was found to adsorb on the graphene surface due to non-covalent π-π interaction and helped in stabilizing the graphene dispersion in DMF. Aniline was polymerized on the surface of the PIL stabilized graphene sheets and resulted in a 5 times higher electrical conductivity at a 21 wt% loading due to excellent electronic transport of graphene and the π-π interactions with the PANI. Graphene-PANI nanocomposites were fabricated by in situ polymerization of graphene oxide and aniline followed by the reduction of graphene oxide. [234] The relative concentration of polymer and the graphene filler was tuned by varying the mass ratio of graphene in mixed suspension. The nanocomposites with 80 wt% graphene showed a remarkable specific capacitance of 480 F g^{-1} at a current density of 0.1 A g^{-1} along with good reliability.

Chemically reduced graphene oxide was stabilized with cationic PEI to fabricate supercapacitors. [292] The charged polymer component ensured good dispersibility of reduced graphene oxide and acted as binding sites for negatively charged carbon materials. These hybrid films showed an interconnected network of carbon structures with well-defined pores to enable the diffusion of ions through the interconnected morphology. Finally, these conducting nanocomposites showed a good specific capacitance of 120 F g^{-1} even at a high scan rate of 1 V s^{-1}.

3D porous structures of reduced graphene oxide and cellulose composites were fabricated by ball milling, template shaping, coagulating, and lyophilization. [293] Ball milling ensured the formation of homogeneous hydrogel composed of reduced graphene oxide embedded in cellulose matrix, improved thermal stability, and enhanced crystallinity of the cellulose matrix inside the nanocomposite. Reduced graphene oxide along with the coagulation

effect of cellulose material facilitated the preservation of 3D porous morphology during freeze-drying and the conducting material. This nanocomposite material with a GO/cellulose ratio of 70:100 showed a modest electrical conductivity of 15 S m^{-1}. Also, these composites showed an ideal capacitive behavior and showed a specific capacitance of 71 F g^{-1} at a current density of 0.5 A g^{-1}.

Among numerous recent publications on this topic we would like to note several selected studies on inkjet printing of nanocomposite films with highly conductive patterns [294], high performance and flexible electromagnetic shielding nanocomposites [294], elastic and conducting hydrogels with double network morphology [295], and conducting melt-spun nanocomposite fibers [296]. Among other interesting developments are free-standing flexible graphene-PANI papers with good cycling stability [297], polycarbonate nanocomposites with much improved electrical conductivity [298], a variety of natural electroconductive cellulose nanocomposites [299, 300], electrical memory devices from conjugated polymers and reduced graphene oxides [301], and melt processed polyamide conductive films [302].

1.6 Status and Issues

This review has briefly summarized recent efforts on the materials selection, binding approaches, processing methods, theoretical models, design rules, and resulting mechanical, thermal, electrical and other functional properties of graphene-polymer nanocomposites. Graphene derivatives have outstanding mechanical properties and versatile functionalities to bind with various polymeric materials. Generally, the ultimate performance might be potentially outstanding as has been already demonstrated on a number of occasions.

Solution and melt mixing, LbL assembly, vacuum-assisted routines, and *in situ* polymerization have unique characteristics and their own advantages for the fabrication of graphene-based nanocomposites with ultimate mechanical and functional properties. Critical issues are related to homogeneous dispersion in initial mixed states and fine

dispersion with exfoliations of individual layers and the establishment of the interconnected morphology. Choosing the appropriate dispersion technique or the combination of processing techniques and finding proper functionalized components is critical for reaching the best mechanical performance as illustrated with major characteristics such as those collected for a number of representative nanocomposite

In conclusion, the best performing graphene-polymer nanocomposites presented in **Table 1.2** in terms of the most important mechanical properties for the ultimate mechanical applications such as the elastic modulus value and toughness are visualized in **Figure 1.24**. The data points which are related directly to numbering from Table 1.2 are also color-coded to reflect their ultimate mechanical strength in terms of stress-to-brake values.

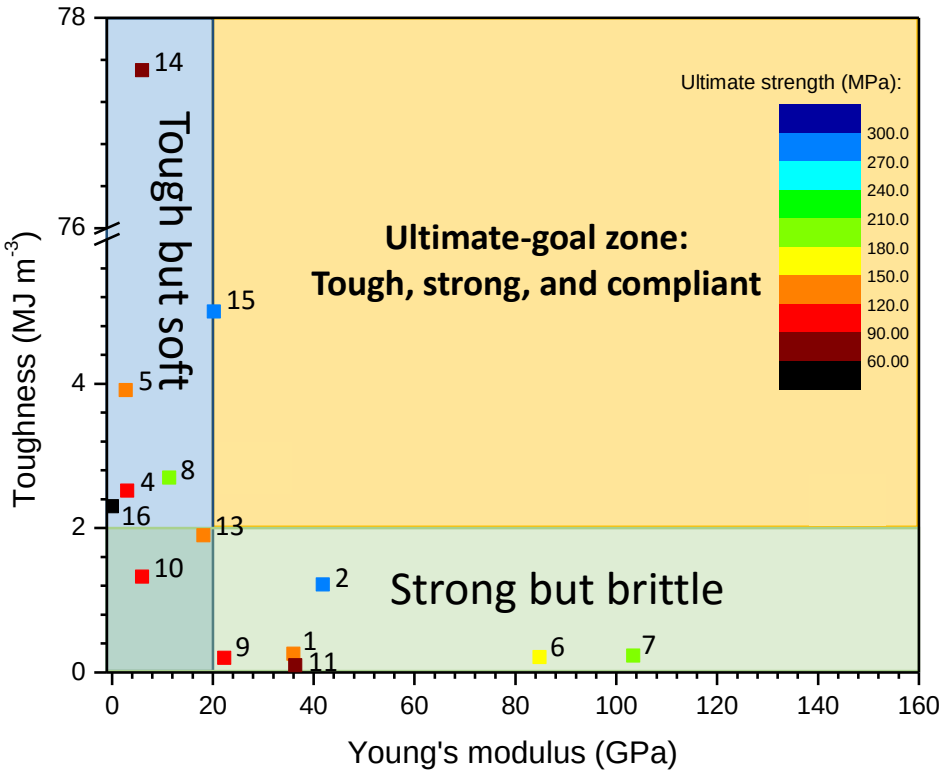

Figure 1.24 Mechanical properties of the graphene-polymer nanocomposites in the toughness-modulus space with data points color-coded with ultimate strength and numbered according to Table 1.2.

Table 1.2 The mechanical properties of the recent polymer-graphene nanocomposites.

	No.	Materials [reference]	Form	Polymer content (%)	Fabrication method	Ultimate strength (MPa)	Young's modulus (GPa)	Ultimate strain (%)	Toughness (MJ m^{-3})
Graphene derivative predominant	1	GO [133]	microfilm (paper)	0	VA-SA	120	36	0.42	0.26
	2	rGO [208]		0	VA-SA + thermal annealing	293.3	41.8	0.83	1.22
	3	GO-PCDO [116]		6.5 wt	VA-SA + crosslinking	106.6	2.5-3.6	4.5	2.52
	4			~6.5 wt	VA-SA + crosslinking + HI reduction	129.6	1.5-4	6.9	3.91
	5	GO-PEI [210]		14.7 wt	VA-SA + immerse crosslinking	179	84.8	0.23	0.21
	6				VA-SA + vacuum-assisted crosslinking	209.9	103.4	0.22	0.23
	7	rGO-PVA [217]		20 wt	drop cast + HI reduction	190	11.4	2.6	2.7
	8	GO-PAA [101]		21 wt	VA-SA	91	11.3-33.3	0.32	0.2
	9	GO-PMMA [211]		31 wt	VA-SA	102.9	6	2.58	~1.3
	10	GO-PVA [211]		34 wt		80.2	36.4	0.25	0.1
Polymer predominant	11	GO-PAH/PSS [3]	Ultrathin membrane	96.7 vol	SA-LbL + Langmuir Blodgett	130	18.2	2.3	1.9
	12	GO-PVA [212]	Film	97 wt	drop cast	62	~6	155	77.5
	13	Graphene-NFC [216]	microfilm (paper)	98.75 wt	VA-SA	278	20.2	3.2	~5
	14	Graphene-PDMS [213]	Film	99 wt	shear mixing + spin coating	3.4	~2.3×10^{-3}	135	2.3

This summary plot shows that the majority of the best results reported to date for graphene-polymer nanocomposites are traditionally skewed to different axis and can be grouped in two very dissimilar groups. First group represents tough graphene-polymer nanocomposites with record values of toughness, which, however, do not show very high mechanical performance in terms of elastic modulus (mostly below 20 GPa) and the ultimate mechanical strength. Second group of materials includes mechanically strong nanocomposites with the extremely high elastic modulus value of 100-150 GPa (higher than steel), which, however, possess lower toughness due to their brittle behavior (well below 2 MJ m^{-3}).

A wide area of the potentially best performing tough, strong, and compliant graphene-polymer nanocomposites (central region) remains largely intact currently. Only few recent cross the critical lines, which separate these data from two traditional groups (Figure 1.24). Currently, such a general pattern, which is common for many composite materials leaves exciting opportunities for the synergistic reinforcement of the universal mechanical properties of graphene-polymer nanocomposites, which, apparently will be explored in the near future. Materials reported to date in Table 1.2.

Finally, various theoretical models with different assumptions are used to predict the mechanical properties of the graphene-polymer nanocomposites with various successes. The validity of the predicted values by different models largely depends on the assumptions made by the models which are not always valid for these nanocomposite materials with developed interphases.

Besides the mechanical properties of the graphene enhanced polymer nanocomposites, the functional properties of such materials are also very important for wide applications, in which the electrical properties is fundamental. Although graphene show superior electronic properties, the high cost and the lack of efficient manufacture and distribution methods prevent its practical applications. Graphene oxide holds promising potentials as the precursor of graphene in electronic applications. However, the controllable reduction techniques still require significant improvements. Moreover, the unique electrical and

chemical activity of graphene oxide is also subject to intensive investigation to fully unveil the functional applications of this material without harsh chemical modifications.

Chapter 2 Research Goals, Objectives, and Overview

2.1 Goals

The goal of this study is to (1) *understand the fundamental principles of the interfacial interactions* in bio-nanocomposites via comprehensive investigation of the influences of the morphology, secondary structure, surface charge, concentration, and organization of graphene oxide, biomolecules (silk fibroin), and biomaterials (cellulose nanocrystals), (2) *design ultra-robust and flexible graphene based bio-nanocomposites* using the fundamental understanding obtained from the model system studied, and (3) *elucidate the mechanism of the metal-mediated chemical modification of graphene oxide and the electronic transport characteristics of the graphene based bio-nanocomposites* via facile and eco-friendly strategies. And as the comprehensive and ultimate goal, the documentation of the key principles for the integration of inorganic nanofillers with biomacromolecules exhibiting optimal structural and functional performance for mechanical and bioelectronics applications is the core value of this study that is constantly implemented throughout the research process.

Thus, in an effort to address the fundamental and engineering aspects separately, the study will be divided into two parts. In the first part, the combination of silk fibroin and graphene oxide is chosen as a model system to understand the binding mechanism of these two diversely originated materials on the molecular level. Assembly techniques will be employed to accurately build up the interfaces between silk fibroin and graphene oxide, ruling out the distribution problem of the conventional nanocomposites, and direct molecular imaging using high-resolution atomic force microscopy will provide visual proofs of the specific adsorption of the molecules. Molecular conformation of the silk fibroin is also a critical parameter that can be manipulated to investigate the influence of entropy on the properties of the bio-nanocomposites. Mechanical models are going to be proposed to offer theoretical support of the experimental results. As another example of

the high-performance bio-nanocomposite material, cellulose nanocrystal will also be employed to combine with graphene oxide with the aim of proposing new category of bio-nanocomposite materials predominantly using nanofillers of various physical dimensions to replace the weak polymeric matrix materials.

The mechanism of inducing electrical conductivity of the graphene oxide in these bio-nanocomposites are investigated in a great detail in terms of dynamics, kinetics, and spatial confinement. By employing a new reduction technique using metal as reductant, the underlying chemistry needs to be clarified in order to fully leash the powerful and versatile potential of the new technique. Multiple characterization techniques will be employed to determine the efficiency and effectiveness of the reduction processes that include defect healing, oxidation removal, and reestablishment of the electronic transport routes, including X-ray photoelectron spectroscopy for chemical states of the elements, 4-probe measurement of the electrical conductivity, Raman mapping for the reduction resolution study, etc. The non-invasive reduction technique is the key to open up the avenue of the post-treatment for electrical conductivities of the graphene oxide bio-nanocomposites, which is critical for the fast development of the flexible bio-electronics.

In the second part, the engineering aspect of this study will be focused on improving the mechanical properties of the bio-nanocomposite films by varying contents of the nanofillers in the bio-nanocomposites and improving interfacial binding between the components. Different thickness scales of the bio-nanocomposite films from dozens of nanometers to a few micrometers will be fabricated by various self-assembly techniques and superior mechanical properties are expected throughout the whole spectrum of films. Other biopolymeric components are also studied in addition to silk in order to combine multiplex unique characteristics of different nanocomponents. 1D and 2D combination of nanofillers is studied for advanced mechanical, electrical and optical properties by eliminating the passive and weak polymeric matrix. In addition, the electrical properties of the graphene oxide in the bio-nanocomposite films will be significantly improved while avoiding using harsh treatment conditions or toxic reagents. In order to corporate the mechanical robust bio-nanocomposite films into flexible electronics systems, microscopic patterning techniques will also be utilized to arbitrarily control the shape and depth of the

electrically conductive pattern of the modified graphene oxide. Finally, the functional properties of the graphene oxide films will be investigated in conjunction with the electrical conductivity of the substrate, and self-powered tactile sensors developed from the concept are demonstrated.

2.2 Objectives

In the proposed goals, the following technical objectives would be addressed (and summarized in **Figure 2.1**):

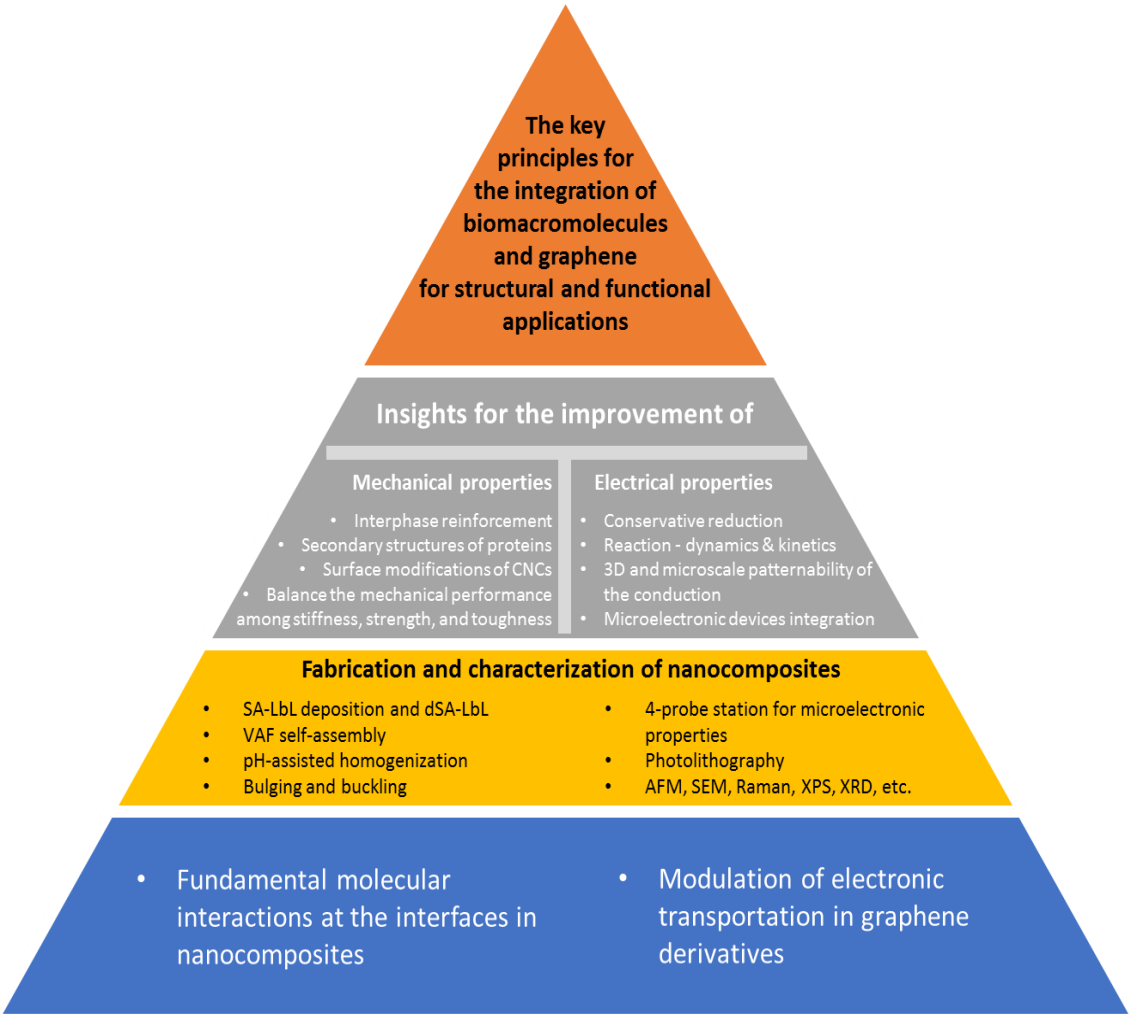

Figure 2.1 Illustration of research goals and technical objectives.

Task 1 – Ultra-robust bio-nanocomposites based on graphene and biomacromolecules

- Fabricating ultra-robust graphene oxide-silk fibroin bio-nanocomposites using the SA-LbL assembly and investigating the strong interfacial interactions by measuring the mechanical properties of the nanomembranes by bulging and buckling techniques. The correlation between the strong mechanical properties and the effective interfacial interactions is to be established by the mechanical analysis and generalized by suggesting new model for strongly binding nanocomposite systems with significant contribution from the interphase region between the nanocomponents.

- Elucidating the effect of the secondary structure of the soft phase molecules (silk fibroin) on the interfacial interactions and stress transfer of the bio-nanocomposites by refining the spin coating process and suggesting the dynamic spinning of the biomacromolecules. The effectiveness of the dynamic spinning process for modifiying the secondary structures of the biomacromolecules is to be illustrated by high-resolution imaging techniques and secondary-structure-sensitive spectroscopies. The improved interfacial interactions between the graphene oxide components and the biomacromolecular components are to be demonstrated by mechanical strenthening and theoretical model analysis.

- Formulating mechanically strong graphene oxide paper by introducing the bio-macromolecular binder (silk fibroin) to the graphene oxide aqueous suspension during the vacuum-filtration process. The homogeneous distribution of the nanocomponents in the mixture is to be realized by the adjustment of the repulsive forces between the graphene oxide flakes. The mechanical properties of the modified graphene oxide paper is to be characterized by tensile tests and compared to those of the pristine graphene oxide papers.

- Combining stiff nanofillers of various dimensions (1D cellulose nanocrystals and 2D graphene oxide) directly by eliminating the weak and insulating polymeric matrix to realize the optimized stress distribution and improved optical and electrical properties in the bio-nanocomposites. The interfacial interactions between the cellulose nanocrystals and graphene oxide flakes are improved by surafece charge modifications using polyelectrolyte prime layers for maximized columbic attractions. Optical and electrical

properties are optimized by proper post-treatments to achieve multifunctional bio-nanocomposite thin films to facilitate the practical applications in the bioelectronics.

Task 2 – Programmable induction of the electrical conductivity of the graphene biopaper

- Reduction of the graphene oxide in the biomacromolecule bonded paper and inducing the electrical conductivity of the material while protecting the bio-binder (silk fibroin) from degradation using the facile and mild metal-assisted spontaneous electrochemical reaction. The effective and localized reduction is to be demonstrated by various imaging and quantification techniques; and the electrical properties of the reduced graphene paper are to be characterized and compared with other commonly used flexible or organic electronic materials.

- Investigation of the dynamics and kinetics of the reducing reaction, and manipulation of the electrical properties based on the kinetics. The reduction conditions, including time period, pH, and the content of the insulating bio-binders are to be individually screened to figure out the optimized combination of parameters for the desired electrical and electronic properties while keeping the mechanical integrity of the graphene biopapers. The overall mechanism and reaction routes of the metal-assisted spontaneous electrochemical reactions are to be suggested based on the experimental data and classical thermodynamics theories of chemical reduction potentials.

- Demonstration of the applicable path for fabricating microelectronic devices by the programmable reduction technique using photolithography for patterned electrically conductive areas on the flexible graphene oxide paper substrate. The optimization of the patterning parameters for the highest resolution of the reduced patterns are to be conducted. Self-powered tactile sensors are to be shown as an example of utilizing the unique chemical properties of graphene oxide to develop novel functional materials that are active for sensing and actuation applications.

2.3 Organization and composition of dissertation

Chapter 1 is a critical review of the graphene-polymer nanocomposites. Graphene-based materials have prompted the development of nanocomposites for emerging applications in need of superior mechanical, thermal, electrical, optical, and chemical performance. These nanocomposites exhibit outstanding structural and functional properties by synergistically combining the characteristics of both components if proper structural organization is achieved. Here, we briefly introduce the materials and basic interfacial interactions in the graphene-polymer nanocomposites and the corresponding theoretical models that are capable of predicting the mechanical performances of such nanocomposites. Then, we discuss various assembly techniques that are available for effectively incorporating the strong and flexible graphene-based components into polymer matrices by the utilization of a set of weak and strong interfacial interactions available in functionalized graphenes. We discuss mechanical performance and briefly summarize other physical (thermal, electrical, barrier, optical) properties which are controlled by processing conditions. Finally, we present the status and current issues of the graphene-based polymer nanocomposites by discussing the major opportunities and challenges.

Chapter 2 describes the scientific goals and technical objectives of the work discussed in this dissertation, which are organically assembled based on the integration of graphenes and biomacromolecules for structural and functional applications. This chapter also provides a concise overview and brief description of the general structure and contents of the dissertation.

Chapter 3 introduces the experimental techniques that critically support the studies presented in this dissertation. It includes materials preparation, sample fabrication, and characterization techniques. Materials preparation and sample fabrication processes include oxidation of graphite, dissolution of silk, spin assisted LbL (SA-LbL) assembly, vacuum-assisted filtration, and electrochemical reduction of graphene oxide. Characterization techniques mechanical properties measurement, interphase reinforcement model and data analysis approaches, ellipsometry, atomic force microscopy, scanning electron microscopy, X-ray diffraction, X-ray photoelectron spectroscopy, and Raman

spectroscopy. In the following chapters the experimental details sections are provided as supplementary descriptions for specialized application and further experimental details including specific parameters are supplied.

Chapter 4 reports that graphene oxide (graphene oxide) – silk fibroin (silk fibroin) nanocomposite membranes were fabricated by SA-LbL technique. Ultrathin (50 nm) graphene oxide-silk fibroin nanocomposite membranes possess outstanding mechanical properties. The unique fabrication approach of SA-LbL allows precise control of filler concentration by varying the number of filler layers. By this method, we were able to vary the graphene oxide concentration from 1.7 to 23.5 vol.%. The modulus, ultimate stress, ultimate strain and toughness were all found to increase linearly within this range of graphene oxide concentration and no sign of modulus saturation is observed even at concentrations of 23.5 vol.%, for which a 149 GPa tensile modulus was recorded. The high values of mechanical properties, namely 77 GPa tensile modulus, 282 MPa ultimate stress and 2.2 MJ m^{-3} toughness of the optimized 11.5 vol.% sample, originate from the effective 2-D graphene oxide filler, the β–sheet nanocrystals of the silk fibroin matrix, and the dense H-bonding interactions between the alternating quasi-single-molecular layers. In addition, a strong silk fibroin-graphene oxide interphase is proposed to predominantly facilitate the high elastic moduli that exceed the theoretical values predicted by Halpin-Tsai model. Benefiting from the ultrastrong mechanical performances, rapid fabrication process and inherent biocompatibility, the potential applications for the graphene oxide-silk fibroin nanomembranes include nanosensing, protective coating, bio-encapsulation and energy harvesting.

Chapter 5 expands the results from Chapter 4 and proposed that ultrathin and robust nanocomposite membranes were fabricated by incorporating graphene oxide (GO) sheets into a silk fibroin (SF) matrix by a dynamic spin-assisted layer-by-layer assembly (dSA-LbL). We observed that in contrast to traditional SA-LbL reported earlier fast solution removal during dropping of solution on constantly spinning substrates resulted in largely unfolded biomacromolecules with enhanced surface interactions and suppressed nanofibril formation. The resulting laminated nanocomposites possess outstanding mechanical properties, significantly exceeding those previously reported for conventional LbL films

with similar composition. The tensile modulus reached extremely high values of 170 GPa, which have never been reported for graphene oxide based nanocomposites, the ultimate strength was close to 300 MPa, and the toughness was above 3.4 MJ m^{-3}. The failure modes observed for these membranes suggested the self-reinforcing mechanism of adjacent graphene oxide sheets with strong 2 nm thick silk interphase composed mostly from individual backbones. This interphase reinforcement leads to the effective load transfer between the graphene oxide components in reinforced laminated nanocomposite materials with excellent mechanical strength that surpasses those known today for conventional flexible laminated carbon nanocomposites from graphene oxide and biopolymer components.

In **Chapter 6**, we report on a novel way for facile writing-in of electrically conductive microscopic patterns by a localized electrochemical reduction with micron-scale resolution on robust bio-graphene paper under ambient conditions. These robust biopapers with enhanced toughness and stability in wet-environment were assembled by replacing traditional synthetic binders with heterogeneous hydrophilic-hydrophobic biopolymer "binder"-silk fibroin. This "binder" matches closely to the patched, amphiphilic nature of graphene oxide surfaces that result in outstanding mechanical performance of tough but flexible bio-graphene paper. This green approach can be valuable for future inexpensive, disposable, biodegradable paper with written electrical circuitries integrated into biolelectronic, flexible, and conformal devices such as artificial sensing skin.

In **Chapter 7**, the novel approach to chemically tuning the electronic properties of bio-bond graphene paper is suggested, which allows for the facile fabrication of large area, flexible, robust, and highly conductive films. A layer of anodic metal deposited on the surface of the initial laminated graphene oxide-silk films with micron thickness is used to initiate the fast and spontaneous electrochemical reduction of graphene oxide to the electrically conductive states at predetermined depths under ambient conditions. By controlling the reaction conditions, a wide range of conductivities from those common for semiconductors to semi-metals can be achieved at different stages of the defect-removal process. Ultimately, the electrical conductivity can be increased over six orders of magnitude from about 1 x 10^{-2} S/m for pristine bio-bond graphene oxide paper up to 1.5 x

10^4 S/m for fully transformed film. The conductivity achieved is by far the highest among the reduced graphene oxide papers using environmentally friendly techniques, and moreover, the mechanical performance and flexibility remains extremely high. We propose the mechanism responsible for this process involves the balance of the internal potential drop due to the electric resistance of graphene oxide layers and the diffusion of oxygen containing species to the reactive interface. This electrochemical reduction technique is facile, environmentally friendly, and adaptable for large-scale fabrication of the robust, and lightweight thin film for flexible electronic devices for sensing, energy storage, and wearable electronics where the interfacial charge transportation characteristics and great mechanical robustness are critical.

Chapter 8 discusses the combination of high strength with elasticity and high toughness in flexible nanocomposites is a vital requirement for the development of advanced engineering materials. However, achieving such a combination is severely restricted by mutually exclusive reinforcing and deformation mechanisms. We demonstrate exceptionally strong and record tough carbon-carbon nanocomposites composed of a cellulose nanocrystal "haystack" network encapsulated into graphene oxide monolayer sheets. The design combines two classical reinforcing components—stiff, high aspect ratio cellulose nanocrystals, and strong flexible, graphene oxide sheets-"glued" together by a polymeric binder. These nanomaterials show extremely high ultimate stress of 490 MPa and toughness of 3.9 MJ m^{-3} with the Young's modulus of 60 GPa. Moreover, an electrochemical post-treatment of the graphene oxide component further increases the elastic moduli of nanocomposites to 169 GPa. These mechanical properties with uniquely balanced strength and toughness are by far the highest known for laminated all-carbon nanomaterials.

Chapter 9 demonstrates a series of self-powered metal-GO hybrid sensing materials for detecting bio-tactile signals by outputting hundred-millivolt continuous electrical potentials upon the bare finger touching. The bio-electrolyte triggered electrochemical reaction at the metal-GO junctions and the secondary proton diffusion synergistically contribute to the high electrical potential output. By deliberately choosing the metal species (i.e., Al, Cu, Au, etc.) and the combination of the metal-GO junction pairs, various signal

output strengths and polarities are demonstrated. The tactile sensors fabricated using the hybrid metal-GO junctions are both robust and fast, with stable output by repeated actuation patterns and high response rate up to 20 Hz. Electronic skin based on the two dimensional metal-GO junction pairs show simplified device structure with only four electrodes that address nine tactile positions, excellent signal independence that screens mechanical deformation and indirect human touching, and outstanding mechanical robustness owing to the excellent physical binding mechanism of the biomolecules. The humidity sensing, especially the fast bio-tactile sensing capabilities using these mechanisms are unprecedented and ready for scaling up in the wide applications of wearable bio-signal monitors, smart tagging, electronic skin, and portable/disposable electronics.

Finally, by focusing on the scientific impact and future routes, **Chapter 10** presents the general discussions of the overall research that is included in this dissertation. Three aspects of the challenges and the corresponding suggestions of further development has been presented and discussed, including improved dispersion and distribution of the nanofillers, strengthened interface interactions between the nanocomponents, and controlled reduction of graphene oxide component for bio-electronic applications.

Chapter 3 Experimental Methods

3.1 Materials

3.1.1 Synthesis of graphite oxide

The graphene oxide aqueous suspension was prepared by Hummers method.[89] Natural 300-mesh graphite powders (Alfa Aesar) were added with 2.5 g of $NaNO_3$ in 107 ml of 98% H_2SO_4, which was cooled to 0℃ before mixing. Then 15 g of $KMnO_4$ was slowly added with vigorous stirring to avoid the temperature raising above 20℃. The mixture was heated to 35±3 °C and maintained for 30 min before adding 214 ml of H_2O, waiting for the temperature to raise to 98 ℃ and maintaining for 15 min. 850 ml of warm water and 1 - 2 ml of H_2O_2 was added to reduce $KMnO_4$ and MnO_2 to $MnSO_4$, during which the color of the solution turned from black to dark green, then brown, and finally bright yellow.

The acidic mixture with graphene oxide suspended was kept still overnight for the graphene oxide to precipitate, then the clear supernatant was removed before adding the same amount of Nanopure water (18.2 MΩ cm, Millipore Corp.). After three cycles of the acid removal, the graphene oxide suspension turns from bright yellow to dark brown, indicating the pH of the suspension has slightly raised. The graphene oxide suspension was then divided into several 45 ml centrifuge vials and centrifuged at 10000 rpm for 1 hour to separate the acidic contaminates and the graphene oxide by dumping the supernatants, which is repeated until the pH of the suspension rise above 3.3. Finally the graphene oxide was redispersed in Nanopure water and diluted to 0.3 wt% for storage, during which the suspension is occasionally stirred to prevent precipitation.

3.1.2 Silk fibroin processing

Silkworm cocoons (Air Force Office of Scientific Research) were cut in half to remove the silkworm remains and consequently peeled into thin layers. Then the collected splits (4g)

were mixed with boiling $NaCO_3$ (2 L, 0.02 M, BDH) for 30 min with occasional stir to dissolve the glue-like sericin. After that, the supernatant was removed, and the residual silk fibroin fibers were rinsed thoroughly with Nanopure water for five times and air-dried overnight. The effective removal of sericin was confirmed by ~23% weight loss compared to the original weight of the cocoon splits. Next, the dried silk fibroin filaments were dissolved in LiBr (9.3M, Alfa Aesar) at 60 °C to obtain a concentration of 10 w/v%. The silk fibroin-LiBr aqueous solution was cooled to room temperature, centrifuged to remove the foam, and dialyzed against Nanopure water (1.8L) using a Slide-A-Lyzer dialysis cassette (10,000 MWCO, Thermo Scientific) for 1 day, during which the dialysis medium was refreshed every 60 minutes during the working hours (at least 6 times). Finally, the silk fibroin aqueous solution after the dialysis was collected and purified by centrifuging twice (9000 rpm, 20 min, 5 °C). The concentration of the resulting silk fibroin solution was 3.7-4.7 wt% as determined by dry-weight method. The solution was further diluted to the desired concentration immediately and stored in the refrigerator at 2 °C. All the silk fibroin aqueous solutions are used within 2 weeks after the dialysis to ensure the random coil secondary structures.

3.1.3 Cellulose nanocrystal fabrication and modification

The aqueous suspension of CNC was prepared from microcrystalline cellulose (MCC) by acid hydrolysis followed by purification by centrifugation.[380] Chemically modified CNC material was obtained by following procedure in literature.[303] Briefly, a mixture of 1 mL of CNC suspension (1 wt%) and 2 mL of PEI solution (1 wt%, M_w=25 000) was stirred continuously for 1 h at room temperature. The pH was adjusted to 1.5 with concentrated HCl to enhance the ionic interactions between CNC and PEI. After 10 min, the mixture was centrifuged at 14000 rpm for 10 min and washed with Nanopure water to remove free PEI. Then the precipitate was re-dispersed into Nanopure water and PEI crosslinked CNC aggregation was removed by centrifuging at 8000 rpm. Finally, the uniform PEI-modified individual CNC suspension from the supernatant was diluted to 0.3 wt%. After the modification, around 10% weight fraction of PEI was introduced onto the surface of CNC, which is determined by calculating the atom mass ratio derived from XPS.

3.2 Sample fabrication

3.2.1 Spin-assisted layer-by-layer (SA-LbL)

SA-LbL is a fast and reliable technique to precisely fabricate layered nanostructures. On a 14x25 mm Piranha solution (90 ml of 30% H_2O_2 and 210 ml of 98% H_2SO_4) treated silicon wafer, we first deposit 100 nm of PS as a sacrificial layer. Then the 0.2 wt.% silk fibroin aqueous solution and 0.04% graphene oxide methanol or aqueous suspensions were deposited alternately to build the bilayer structure (**Figure 3.1**). After each deposition of graphene oxide, the sample was rinsed with Nanopure water to remove loosely binded or overlapped graphene oxide flakes. The thickness of the resulting membrane was checked by ellipsometer and AFM.

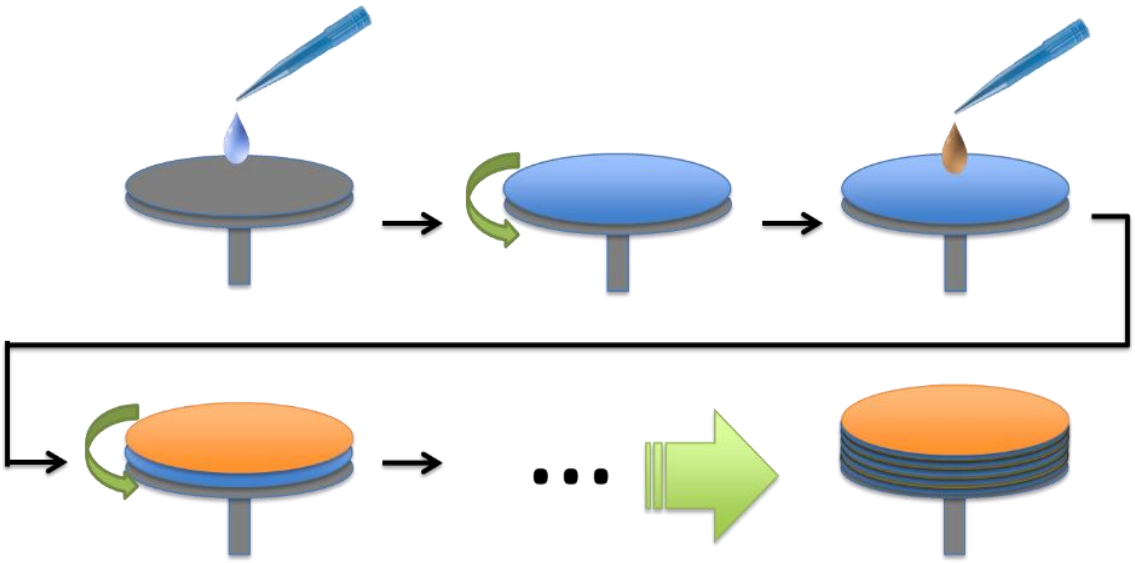

Figure 3.1 Diagram of the process for spin-assisted layer-by-layer assembly: different components in solutions are alternatively dropped on the flat surface and spun to dry. Thin films of each component are left on the top surface.

3.2.2 Dynamic spin-assisted layer-by-layer (dSA-LbL)

dSA-LbL is a modified SA-LbL by dropping the solutions while the substrate is spinning at a preset speed. The silk fibroin aqueous solution (0.02 wt%) was dropped on rotating (in contrast to the stationary substrate in conventional SA-LbL process) substrate (up to ten droplets for one step), followed by the deposition of graphene oxide suspension from 0.04 wt% solution. Between deposition steps, the surface was rinsed with Nanopure water to

remove excessive material. The routine was repeated until the desired thickness was reached.

3.2.3 Vaccum-assisted filtration (VAF)

VAF technique was employed to fabricate the bio-bond graphene paper according to the established procedures. The graphene oxide in the aqueous suspension was first deprotonated by adjusted the pH to 12 using 0.25 M sodium hydroxide solution right before mixing with silk fibroin solution. The color of the suspension turned from dark brown to black with the increased pH. By gently stirring, a total of 380 µL of the 0.2 wt% silk fibroin solution was slowly added to 10 ml of 0.3 wt% pH-adjusted graphene oxide suspension with a capillary-neck micropipette tip, making a silk concentration of 2.5 wt% with respect to the dry weight of the graphene oxide. No gelation was observed in the silk-graphene mixture. Then the solid content in the mixture was assembled into paper-like films using a vacuum filtration system (**Figure 3.2a**). The hydrophilic filter (Versapor, Pall Life Sciences) is 47 mm in diameter and with pore size of 0.45 um. The filtration took about 12 hours to finish depending on the total volume of the aqueous mixture. Right after the

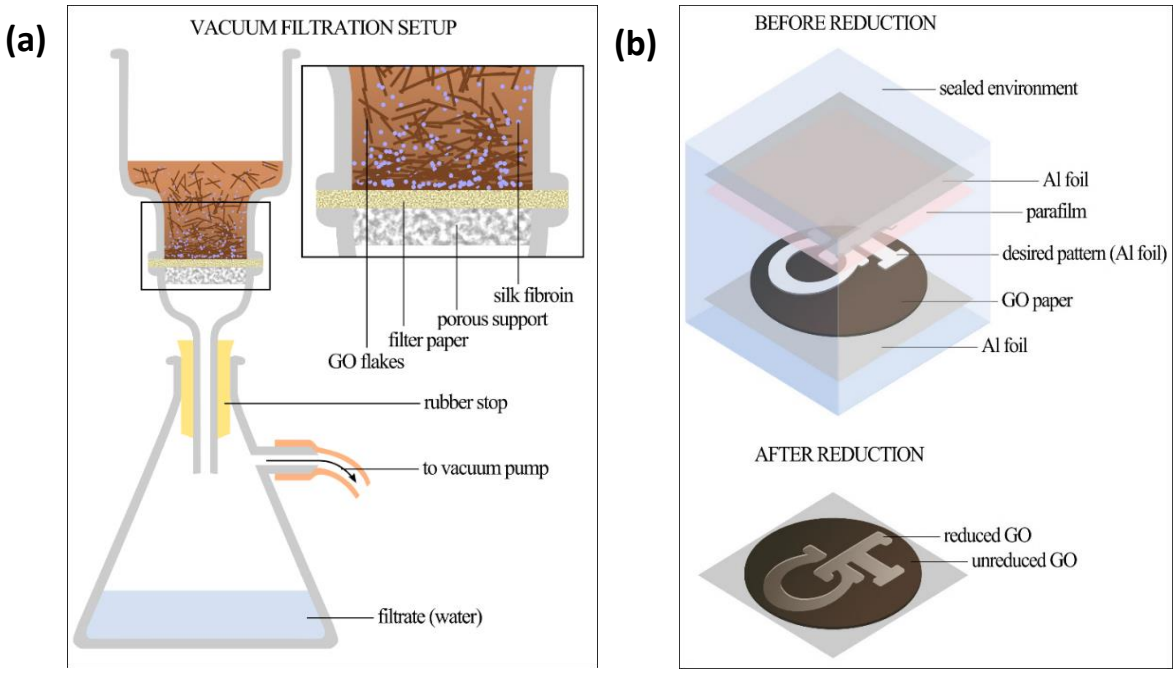

Figure 3.2 (a) the vacuum filtration setup; and (b) the scheme of the reduction procedure of the graphene oxide paper.

filtration was completed, the visually uniform film was rinsed five times and stored in deionized water for 2 hours before soaking in 1 M hydrochloric acid for 1 hour to induce further crosslinking. After that, the acid treated film was rinsed thoroughly again and soaked in an excessive amount of deionized water for 1 hour to neutralize the bio-bond graphene paper. Finally, the bio-bond graphene paper was peeled off from the filter paper and dried against a flat surface in air for reduction and further characterizations.

3.2.4 Metal deposition

The metal electrodes (Al, Cu, Au) were deposited using electron beam evaporation (Mark 40, CHA Industries) at 3 Å/s. The geometries of the electrodes are predetermined by shadow masks and the gap is fixed at 12 mm wide without further notification. For the interdigitated finger pattern, the finger width and gap are both 1 mm and the finger length is 14mm.

3.2.5 Chemical reduction of graphene oxide

The metal assisted electrochemical reduction of the bio-bond graphene paper is conducted in ambient conditions as follows. Firstly, a layer of 500 nm thick aluminum is deposited on the top surface of the bio-bond graphene paper by electron beam evaporation (Denton Explorer, Denton Vacuum, LLC.) at a deposition rate of 3 Å/s. Then the aluminum coated bio-bond graphene paper is placed on a 2”x3” glass slide and hydrochloric acids with various concentrations (10^{-5}, 10^{-3}, 10^{-1}, 10^{o}, 10^{1} M) are slowly dropped on the aluminum coating. The second glass slide is immediately covered on top of the acid activated, aluminum coated bio-bond graphene paper and pressed gently for uniform distribution of the acids and firm contact between the aluminum layer and the bio-bond graphene paper surface. The reaction is timed for 2-20 hours and quenched by rinsing the bio-bond graphene paper with Nanopure water. All the unreacted aluminum flakes are rinsed off easily by a gentle spray of nanopure water at a shallow angle. Then the surface reduced bio-bond graphene paper is soaked in Nanopure water for 1 hour and air dried to neutralize and remove the ionic contaminates from the reactions. When cyclic reduction is required, the dry surface reduced bio-bond graphene paper is coated by aluminum on the reduced surface and the aforementioned standard protocol for reduction is conducted repeatedly.

3.2.6 Photolithography

Micropatterned graphene oxide films were fabricated via a single exposure step photolithography under cleanroom conditions using a mask aligner (Karl Suss MA-6). A layer of negative photoresist (OSCoR 2313) was spun on to the film at 3000 rpm to yield a 1.2 µm thick uniform coating, followed by exposure to UV light (435 nm wavelength) with a photomask (soda lime glass coated by chrome pattern) to facilitate selective crosslinking the exposed portion of the photoresist layer. Following by a further development process, the photoresist layer formed inverted micro-patterns on the graphene oxide film, worked as a shadow mask during the following aluminum deposition.

3.3 Characterizations

3.3.1 Ellipsometry

The thickness of the resulting n-bilayer nanomembrane was estimated by M2000 spectroscopic ellipsometer (J.A. Woollam). The thickness of the PS sacrificial layer on a silicon wafer with 1.6 nm SiO_2 layer was measured beforehand, and the total thickness of the structure with an n-bilayer nanomembrane was measured immediately after the SA-LbL deposition. The light signals at three progressive angles were detected and Cauchy model was used to fit the experimental data.[304]

3.3.2 Atomic force microscopy (AFM)

AFM topographical and phase images were collected with a Dimension 3000 microscope (Digital Instrument) in the tapping mode. Silicon tips with a spring constant of 50 N m^{-1} were used for all scans at 1 Hz. ScanAsyst mode and soft tapping mode of a Digital Instruments-ICON AFM (Vecco) was used to provide the RMS roughness, topography and the graphene oxide coverage information of the nanomembrane. AFM scan data was analyzed with the Nanoscope Analysis software to obtain 1×1 um^2 RMS roughness (averaging from 10 random sites). Phase image of the AFM scan was processed by ImageJ (contrast enhancement and boundary trace) and converted to binary data for graphene oxide

coverage analysis. The average coverage was calculated from 8 random 20×20 um^2 scan areas. Sample thickness was also checked complementarily to ellipsometry by scratching the nanomembrane and analyzing the topological profile.

3.3.3 Scanning electron microscopy (SEM)

We use the Hitachi S3700 SEM to observe the microstructures of the corss sections and surfaces of the nanocomposite films at the acceleration voltage of 10 kV and work distance of 10 mm. For the contrast observation of the GO and rGO surfaces, a pre-exposure time of 1 min is applied before actual imaging. Energy dispersive x-ray spectroscopy (EDX) is done on the same SEM with the integration time of 300 seconds.

3.3.4 Transmission electron microscopy (TEM)

TEM imaging was conducted on a Hitachi HT7700 by dropcast the sample onto a carbon-Formvar TEM grid (TED PELLA, INC). To minimize radiation damage and use the smallest objective aperture for enhancing contrast, measurements were operated at 80 kV acceleration voltage.

3.3.5 X-ray diffraction (XRD)

The interlayer spacing of the GO-SF microfilms were measured by X'Pert Pro Alpha-1 diffractometer at 40mA current and 45 kV acceleration voltage. The scan range is 4-25 degrees with a step size of 0.004 degree and integration time of 4 seconds per step. Scherrer equation $D = K\lambda/(B\cos\theta)$ has been employed to estimate the stacking number of the bilayer structure and the size of the beta-sheet crystals of silk, where D is the stacking number, K=0.9 is the shape factor, λ is the wavelength of the X-ray (0.154 nm), B is the full width at half maximum (FWHM) of the diffraction peak, and θ is the Bragg angle.

3.3.6 X-ray photoelectron spectroscopy (XPS)

The elemental composition of the samples was characterized by Thermal Scientific K-alpha XPS system. XPS is an analytical technique that directs a monochromatic beam of X-rays on a sample and detects the characteristic electrons that are ejected. The energies and number of electrons are used to determine the elements present, their abundance and chemical bonding state. This technique is highly surface sensitive and the typical detection

depth is ~5nm. It can detect light elements such as Silicon at about 1% of the total surface composition and heavier elements down to ~0.1% with an accuracy of 20-50% of the given value.[305] For survey scans, two integrations and 120 seconds per scan were chosen. For high resolution elemental scans, four integrations and 20 seconds per scan were chosen.

3.3.7 Raman Spectroscopy

Raman spectra and maps were captured by a WiTek Alpha 300R confocal Raman microscope using 514 nm laser. The laser power is 0.5 mW for all measurements. The single spectra are taken by 1-second exposure and 30 integrations. And the maps are taken by 0.5-second exposure per pixel. Raman microscopy relies on vibrational spectroscopy which can provide chemical composition, structure of the material by monitoring the frequency shifts between excitation laser and scattered light. It is one of the most important tools for characterizing the microstructure of various carbon materials (graphite, amorphous carbon, carbon nanotubes, graphene), primarily due to its non-destructive approach, presence of sharp bands, and high intensity of these characteristic bands. This technique provides a wide range of critical information for bulk carbon materials, nanoscale structures, carbon-based nanocomposites, and individual carbon structures, including the composition, internal stresses and crystal orientation inside the material.[306, 307, 308, 309] Raman spectroscopy is a unique technique for probing the physical state of different carbon materials in a nondestructive manner. The Raman microscope provides a lateral resolution of ~250 nm and vertical resolution of 1μm.[310]

3.3.8 Fourier transform infrared spectroscopy (FTIR)

A vertical attenuated total reflectance Fourier transform infrared spectroscopy (ATR FTIR) was used to study silk secondary structure at the silk-GO interphase and the hydrogen bonding formation in the CNC-GO nanocomposites in ultrathin LbL films. Several GO-biopolymer bilayers were spun cast onto both immobile and mobile silicon ATR crystal. An infrared beam is directed in to the high refractive index crystal at a specific angle where is undergoes total internal reflectance. Total internal reflectance creates an evanescent wave that extends 0.5 – 5 um beyond the crystal surface. Sample IR adsorption attenuates the evanescent wave. This attenuated beam reenters the crystal then exits and is directed

by a series of mirrors to the detector that records the beam as an interferogram which analysis software OPUS 6.5 converts to an IR spectrum. Analysis was conducted in a Bruker Vertex 70 FTIR using liquid nitrogen to cool the detector to improve IR detection of the ultrathin films with resolution 4 cm^{-1}. For each sample, 200 background scans on the wafer without sample were collected then the sample was deposited and a final spectrum of 100 averaged sample scans was produced. IR spectra were analyzed in accordance with well-established wavenumber assignments for hydrogen bondings[311] and secondary structure motifs beta-sheets, beta-turns, random coils, and alpha helices and peaks noted in second derivative of the produced spectra.[312]

3.3.9 UV-Vis spectroscopy

UV-vis extinction spectra of the nanomembranes on soda lime glass slides from 350-900 nm (1 nm intervals) were collected using a Shimadzu UV-vis-2450 spectrometer with D2 and tungsten lamps offering a wavelength range of 300-1100 nm. The nanomembrane extinction spectra were corrected against air and the blank soda lime glass slide.

3.3.10 Dynamic light scattering (DLS) and ζ-potential measurements

DLS measurements were carried out after equilibrating CNC suspensions (0.1 wt%) at room temperature for 10 min Suspensions were placed in a temperature-regulated cell at a temperature of 25.0±0.1 ^{o}C. DLS measurements were conducted using a Malvern Zetasizer Nano-S instrument working at a 173^{o} scattering angle. This optimum angle was selected by the instrument maker by taking into account the inverse relation between particle sizes and scattering angle. This instrument is equipped with a 4.0 mW He–Ne laser (λ=633 nm) and an Avalanche photodiode detector. The translational self-diffusion coefficient of particles can be obtained from the decay rate of autocorrelation function from DLS measurements.[2] For spherical particles in dilute solution, the hydrodynamic diameter d_H can be related to the translational diffusion coefficient (D_t) by Stokes-Einstein relation.[313]

3.3.11 Electrical property measurements

The sheet resistance and the effective conductivity of the bio-bond graphene papers is measured by the 4-point probe system (Lucas Signatone, Corp.) with a Keithley 2400

Source Meter. At least five uniformly distributed locations on the bio-bond graphene papers are measured to calculate the average values. Fully reduced bio-bond graphene papers are sandwiched between aluminum electrodes, and the total resistance is measured. The contact resistance between the electrodes and the bio-bond graphene papers are extracted by extrapolating the linear plot of the electrical resistance versus the thickness of the bio-bond graphene papers. Then the through-thickness conductivity (σ) of the bio-bond graphene papers are calculated by the following equation and averaged $\frac{1}{\sigma} = \rho = R\frac{A}{t}$, where ρ is the resistivity, R is the measured through-thickness resistance minus the contact resistances, A is the contact area (5.5 x 15.5 mm^2), and t is the thickness of the bio-bond graphene papers.

3.3.12 Mechanical properties measurement

The resulting nanomembranes were floated on the water-air interface by dipping the sample-mounted silicon wafer at a small angle in water. We obtained the final silk fibroin-graphene oxide nanocomposite membranes by dissolving the PS sacrificial layer with toluene and catching with proper substrates (copper TEM grid or PDMS). No evidence from morphology observation by AFM shows negative impact of toluene contact to the properties of the silk fibroin. All samples were dried overnight at ambient temperature.

So far, the sensitivity of the conventional tensile or compressive test setups is not high enough to measure the small force applied on the nano-scale membranes. It is also not feasible to apply in-plane compression on the freestanding nanomembranes. Moreover, for tensile tests, proper handling of the samples without creating defects is extremely hard. Therefore, buckling and bulging tests were carried out to measure the compressive/tensile moduli, ultimate stress, ultimate strain and toughness of the sample nanomembranes.[314, 315, 316]

3.3.12.1 Buckling

For buckling test, the sample membrane was firstly caught on a 10×10 ×5 mm^3 PDMS and then the PDMS was slightly compressed (<<10% strain) by a homemade uniaxial compressor (**Figure 3.3**). Based on the mechanical relaxation theory regarding the

mismatched moduli of the PDMS substrate and membrane, sinusoidal buckling pattern will form perpendicular to the net stress direction.[317] The compressive Young's modulus of the sample membrane was calculated by the equation:[316]

$$\lambda = 2\pi d \left[\frac{E_f\left(1-\upsilon_s^2\right)}{3E_s\left(1-\upsilon_f^2\right)}\right]^{1/3} \qquad (3.1)$$

where λ is the period of the buckling pattern, d is the thickness of the sample membrane, E_f (v_f) and E_s (v_s) are the Young's moduli (Poisson's ratios) of the sample nanomembrane and the PDMS substrate, respectively.

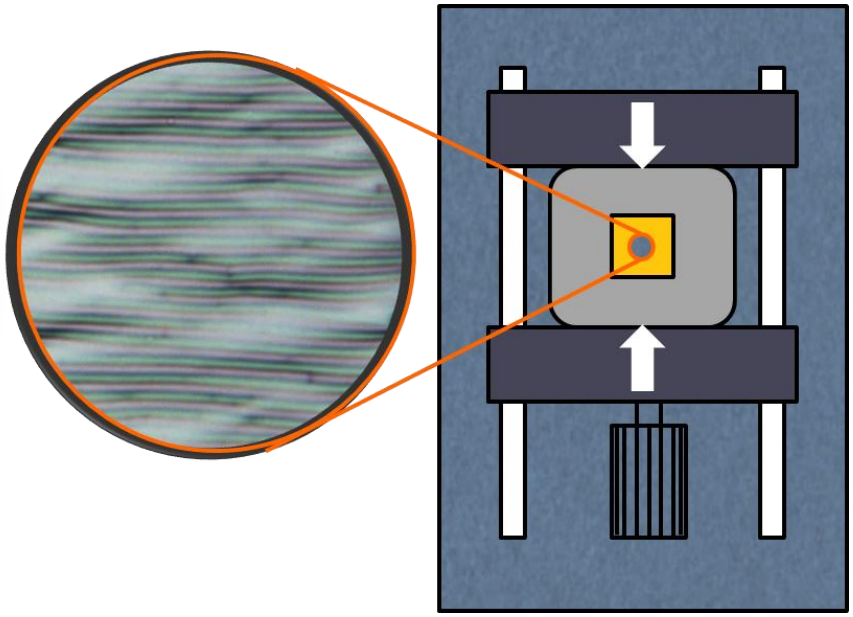

Figure 3.3 Buckling device and the buckling pattern as observed by optical microscope.

The modulus of the underlying PDMS is a critical reference value to calculate the modulus of the thin film. We measured the modulus of the PDMS by standard tensile test with dog bone shaped samples and the result was 1.80±0.16 MPa. To confirm the modulus of the PDMS, the authors conducted reversed buckling test, which used a thin film with known modulus (polystyrene, 3.5 GPa) to calculate the modulus the PDMS substrate using Equation 3.1.

The results (1.78±0.20 MPa) match those of the tensile tests (1.80±0.16 MPa). To eliminate the influence of the modulus of PDMS, we have also run a few tests using PDMS substrates with different modulus (2.2 MPa), where the measured moduli of the thin films are

consistent with those measured by PDMS with 1.8 MPa modulus after replacing the corresponding parameters in the equations.

3.3.12.2 Bulging

Bulging tests are capable of monitoring the stress vs. strain curve of the bulged sample, so the tensile Young's modulus, ultimate stress/strain and toughness can be determined.[318, 319, 320, 321] The results from bulging test match well with those made by nanoindentation and point membrane deflection tests.[322] Details in the bulging test experimental setup and data analysis can be referred from the previous publications of the laboratory.[6, 40] In short, the nanomembranes were caught on the copper TEM grids with 300-um circular apertures. The air-dried samples were mounted on a homemade interference bulging setup. A beam of 632.8 nm He-Ne laser was guided and reflected on the nanomembrane and a reference glass slide, which are aligned with a small tilting angle in order to yield a strait interference pattern (**Figure 3.4**). A syringe vacuum system with a pressure gauge provided the negative pressure to deflect the nanomembrane suspended on the copper aperture. The brightness of the reference point in the center of the suspended membrane underwent bright-dark-bright cycles due to the increase of the distance between the membrane and the reference glass slide. The incremental deflection in every cycle was half of the wavelength of the laser. The brightness evolution of the reference point due to the negative pressure were recorded by a digital camcorder and analyzed by custom-made software.

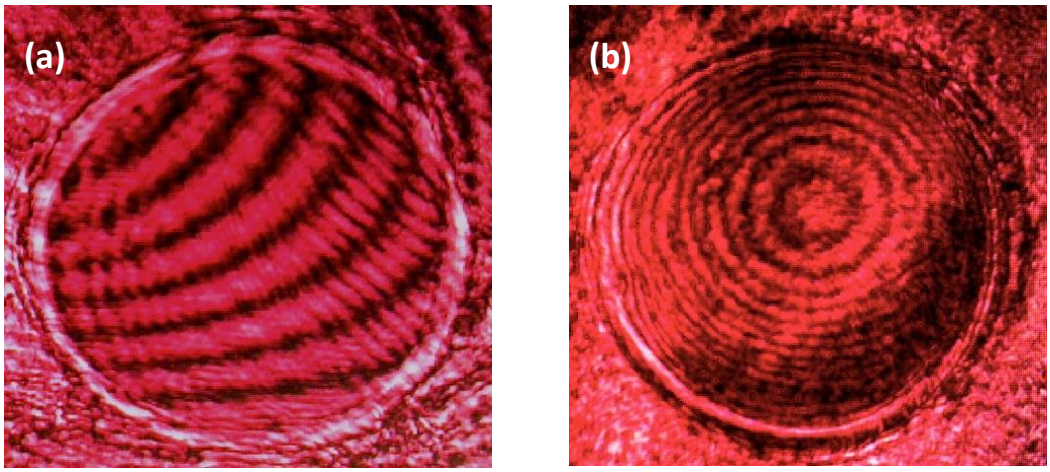

Figure 3.4 The Interference pattern of a 50 nm nanocomposite membrane subjecting negative pressure through a 300-μm copper aperture at the initial stage (a) and deformed stage (b).

Therefore, the pressure (P) and vertical deflection at the apex of the deformation dome (d) were captured simultaneously and converted to stress and strain by the relationships: $\sigma = Pr^2/4hd$ and $\varepsilon = 2\,d^2/3r^2$, where h is the thickness of the nanomembrane and r is the radius of the aperture.[6] The most sensitive parameters in the bulging measurement were the radius of the aperture (r) and the deflection of the membrane (d). The radius of the aperture was very consistent with the labeled value from the manufacture and confirmed by optical microscope. And the deflection of the membrane was precisely measured by interference pattern that has been explained above. Other than those two parameters, the pressure and membrane thickness are either linearly or reversely proportional to the stress or strain, whose errors do not affect the final results in the same dramatic way as the other parameters. Even though pressure and thickness are not as sensitive to the final results, we measured the pressure *in-situ* using a pressure gauge with ±0.01 MPa precision and the thickness using ellipsometry and AFM scratch test.

There are several models which are widely used to predict the theoretical values of the Young's modulus of the nanocomposites: Halpin-Tsai model is available for nanoparticle fillers with various geometries. [6, 127] It provides well-defined shape factor and is widely adapted by researchers. Takayanagi model is an intuitive and effective model to predict the fiber/laminate filler composite systems, which simply follows the rule of mixture.[2] Jaeger–Fratzl model describe the nacre-like biocomposites.[15] When the filler concentration is high, Jaeger-Fratzl model approaches the real modulus better. Therefore, we chose Halpin-Tsai model as a standard of the theoretical value.

3.3.12.3 Tensile tests

Stress-strain curves of the films were collected by tensile testing the 2±0.2 × 30 mm strips with a gap between grips of 10 mm at room temperature (RSA III Dynamic Mechanical Analyzer, TA Instruments). The relative humidity during the tensile tests is around 40% and the temperature is around 23 °C. The thickness of each strip was measured by a micrometer (±0.5 μm accuracy) individually. The strain rate is 1.0%/min. Overall, at least three different stress-strain curves were collected for each data point from strips broken in the middle of the gap during testing.

3.3.13 Interphase reinforcement model and data analysis approaches

Due to the strong interaction brought about by the high-density hydrogen bonding between silk fibroin and graphene oxide, the silk fibroin molecules at the direct vicinity of the graphene oxide sheets are anchored, giving rise to the thermodynamic barrier of the mobility. This immobilization effect expands into the silk fibroin region by physical entanglement and crosslinking of the silk fibroin molecules and decays within a short range.[38, 40] In addition, studies have also shown that the interface facilitates the crystallization of polymers, enhancing the interfacial strength and the local stiffness.[49] As a result, the averaged macroscopic stiffness of the region increases.[31]

In order to determine the thickness of the interphase region and the degree of enhancement of the interphase effect, we propose a sigmoid decaying model to simulate the molecular behavior at the interfacial region. It is worth to mention that the exponential decaying functions can also be used to fit the experimental data and provide the same results. However, there is an inflection point at the beginning of the exponential decaying curves. It is physically more favorable to apply sigmoid functions with continuous decaying rates for the data fitting. In addition, it is note-worthy that at such small length scale (1~2 nm, i.e. a few atoms across), continuous modulus decaying curves start to lose their theoretical rigorousness and practical meaning. But the average values from the integration over that range are still representative. According to Kovalev et al., the reduced local modulus at the interphase is:[323]

$$E'(t) = E^*(t) - E_{SF} \qquad (3.2)$$

$$E'(t) = E'(t - \Delta t) + m \cdot E'(t - \Delta t)\Delta t - n \cdot E'(t - \Delta t)\Delta t \qquad (3.3)$$

where *E'(t)* is the reduced local modulus at distance *t* from the interface, which is defined by subtracting the ground level modulus E_{SF} from the real local modulus *E*(t)*; *m* and *n* are continuous positive and negative local deviation coefficients, respectively. Equation (3.3) can be written in differential form:

$$\frac{dE'(t)}{dt} = -kE'(t) \qquad (3.4)$$

where k=m-n and k is continuous since m and n are continuous. Differential coefficient k depends on the relative value of local modulus to that of the total difference between the two components, $\Delta E = E_{GO} - E_{SF}$, where E_{GO} is the modulus of graphene oxide:

$$k = \alpha[\Delta E - E'(t)] \quad (3.5)$$

where α is the scaling coefficient. Then Equation (3.4) is rewritten as

$$\frac{dE'(t)}{dt} = -\alpha[\Delta E - E'(t)]E'(t) \qquad (3.6)$$

Rearrange to solve the differential equation

$$\frac{1}{\Delta E}\left[\frac{dE'(t)}{E'(t)} + \frac{dE'(t)}{\Delta E - E'(t)}\right] = -\alpha dt \qquad (3.7)$$

we have

$$\ln[E'(t)] - \ln[\Delta E - E'(t)] = -\alpha \Delta E t + \eta \quad (3.8)$$

where η is the integration constant depending on the boundary condition.

To solve Equation (3.8), we defined a boundary condition $E'(\tau) = \frac{\Delta E}{2}$, where τ is the distance where the reduced local modulus is equal to half of the total modulus difference between the two components. By plugging this boundary condition back to Equation (3.8), integration constant η is determined as

$$\eta = \alpha \Delta E \tau \qquad (3.9)$$

Equation (3.9) demonstrates that the integration constant η is a unitless coefficient by dimensional analysis.

We can combine Equations (3.8) and (3.9) to solve the modulus decay function:

$$\ln[E'(t)] - \ln[\Delta E - E'(t)] = -\alpha \Delta E (t - \tau) \qquad (3.10a)$$

$$E'(t) = \frac{\Delta E}{1 + \exp\left[\eta\left(\frac{t}{\tau} - 1\right)\right]} \qquad (3.10b)$$

Equation (3.10b) is an equivalent form of the Equation (4.2) by substituting *E'(t)* with $E^*(t)$-E_{SF} in the paper context. We also redefine η and τ as shape factor and relaxation distance respectively to grant them physical meanings.

With the knowledge of decay profile at interphase, the effective modulus of the silk fibroin layer, $E_{SF,eff}$, can be calculated by averaging the nominal moduli throughout the silk fibroin layer:

$$E_{SF,eff} = \frac{2}{t_{SF}} \int_0^{t_{SF}} E^*(t)dt \qquad (3.11)$$

where t_{SF} is the thickness of the silk fibroin between graphene oxide layers. Meanwhile, $E_{SF,eff}$ can also be calculated by using Takayanagi model:[15]

$$E_{comp} = \phi_{GO} \cdot E_{GO} + \phi_{SF} \cdot E_{SF}0 \qquad (3.12)$$

where E_{comp} is the modulus of the nanocomposite measured experimentally, $\phi_{SF} = 1 - \phi_{GO}$ is the volume fraction of silk fibroin in the nanomembrane. Therefore, we combined equations into a function of $E_{SF,eff}(t_{SF})$. Then we fitted the experimental modulus data to this function in order to determine the shape factor η and relaxation distance τ.

To make the fit, we calculated the effective SF layer modulus $E_{SF,eff}$ and plot $E_{SF,eff}$ versus effective SF thickness between GO layers t_{SF}. Then we use the integrated form of Equation (3.10) to fit parameters η and τ:

$$E_{SF,eff} = \frac{2\Delta E \cdot \tau}{\eta \cdot t_{SF}} \left\{ \frac{\eta \cdot t_{SF}}{\tau} - ln\left[e^{\eta\left(t_{SF}/\tau - 1\right)} + 1 \right] + ln(e^{-\eta} + 1) \right\} \qquad (3.13)$$

Chapter 4 Ultra-Robust Graphene Oxide-Silk Fibroin Nanocomposite Membranes

4.1 Introduction

High-performance structural composite materials are widely used in civil constructions, aerospace engineering and military applications. They synergistically combine the strengths of two or more macroscopic components, yielding a strength-toughness balance. However, these composite materials suffer from the unpredictable catastrophic. Most of the material failures are attributed to the debonding between different components (e.g. polymer matrix and carbon fiber fillers) and the difficulties in uniform distribution of the fillers, which greatly undermine its reliability. Nanocomposites utilize filler components in nanoscale to increase the surface-to-volume ratio and enhance the interaction at the interface, improving the performance of the composite by orders of magnitude.

Carbon nanotubes, metallic nanoparticles, graphene and intercalated clay are typical examples among the common nanofillers. Carbon nanotubes are probably the most investigated nanofiller to date. Single-walled carbon nanotubes (SWNTs) have Young's modulus up to 1 TPa, ultimate stress of 300 GPa.[31] However, the non-uniform dispersion in various matrices and lack of attracting interaction to the matrices keep being the major problems in the effective loading transfer. Chemical treatment with strong acids can modify carbon nanotubes with polar functionalities, facilitating its dispersion and interface binding. Shim et al. reported a SWNT-PVA nanocomposite membrane possessing 600 MPa ultimate strength and a record-high 121 MJ m^{-3} toughness, but the stiffness is relatively low at 16 GPa.[31] Podsiadlo et al. reported a PVA-nanoclay LbL film crosslinked by glutaraldehyde (GA) with 106 GPa Young's modulus and 400 MPa ultimate stress, but the toughness of the material was very low due to the strong covalent bonds.[32] Silver nano-platelets and MMT nano-clay were incorporated into silk fibroin matrix to enhance its mechanical properties, as well as to tune the reflectivity from completely reflective to

transparent as an optical sensor.[14] A PAH/PSS nanocomposite with gold nanoparticles embedded shows surprising compliance, pressure sensitivity and self-healing characteristics, but the low strength prohibits its structural applications.[33, 34] Graphene is emerging to become a popular nano-filler due to its ultra-low thickness, large aspect ratio, strong mechanical properties and outstanding electrical conductivity.

Graphene oxide-polyelectrolyte nanomembranes were fabricated by spin assisted LbL technique (SA-LbL) and Langmuir-Blodgett (LB) techniques and by tuning the graphene oxide concentration from 0 to 8.0 vol.%, the toughness and Young's modulus has achieved 1.9 MJ m^{-3} and 20 GPa, respectively.[24] However, the LB technique is extremely slow with a deposition rate of 45 min/layer, preventing industrial production for the time being. Polymer nanocomposite with graphene or reduced graphene fillers shows semiconducting to semimetallic properties with only a few percent concentration of fillers, giving it potential applications in next-generation electronics.[35] All these achievements applicable in nanotechnologies facilitate the further miniaturization of MEMS systems. However, with the thickness and lateral dimensions decreasing, the properties of the nano-membranes deteriorate disproportionally. Flexible polymer materials or strong ceramic materials become either too fragile or too stiff, both lacking the desired mechanical properties for nano-sensing applications. In addition, nanocomposite films also show thickness dependence of the strength. The ultimate stress of a DOPA-PEG-clay composite film with Fe^{3+} ion crosslinker decreases by 13% when the thicknesses decrease from 4.9 um to 1.2 um.[36] A significant decay of mechanical properties of the nanocomposite membranes is expected when the thickness further lowered to less than 100 nm. The need of strong nanomembrane with balanced strength, stiffness and toughness, which is capable of sustained nanosensing and nanoencapsulation is still not met.

In this chapter, we introduced a new series of ultrathin, robust nanocomposite membrane using SA-LbL technique to incorporate silk fibroin and graphene oxide. Silk fibroin and graphene oxide strongly interact by high-density hydrogen bonding between the amino groups along the silk fibroin chain and the epoxy, hydroxyl, carbonyl and carboxyl groups on both sides of graphene oxide sheet (**Figure 4.1**). In addition to uniform distribution of the LbL technique, the large aspect ratio (~5000), quasi-atomic thickness (~0.9 nm) and

outstanding mechanical properties of graphene oxide make it a perfect nanofiller to transfer load throughout the silk fibroin matrix. Moreover, due to the strong molecular interaction, a stiff interphase region of 0.5-1 nm across also exists between the graphene oxide filler and silk fibroin matrix. The interphases in composite systems were comprehensively studied by mechanical tests, thermal analysis, scanning probing microscopy and molecular dynamic simulation.[37, 38-40]

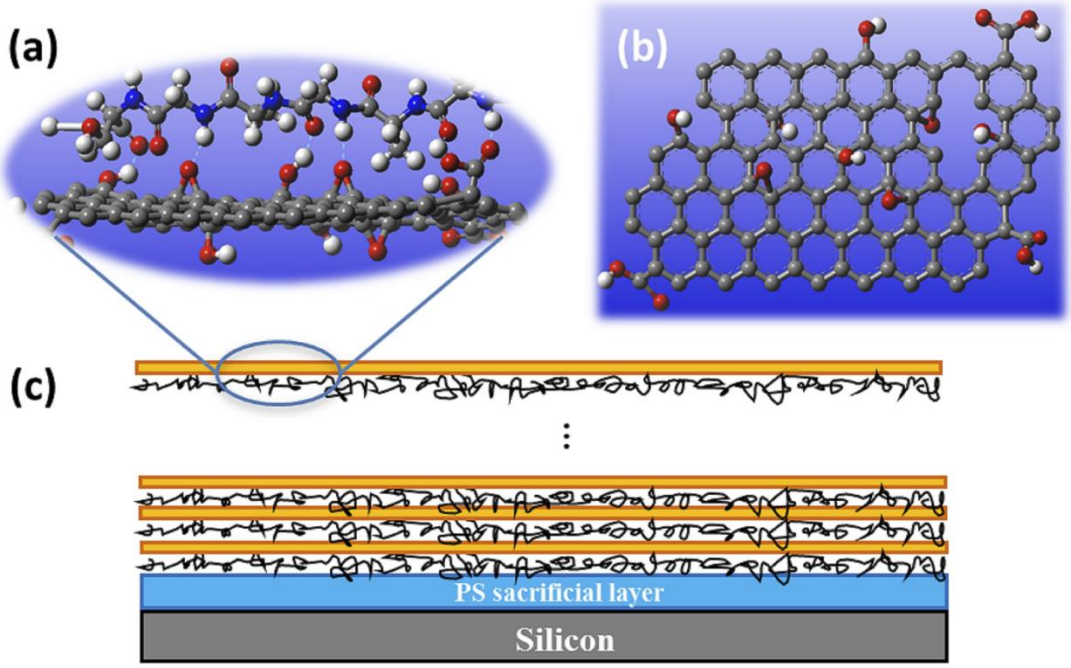

Figure 4.1 Representative molecular structure of silk fibroin (a, upper part) and GO (a, lower part – side view; b top view). Elements in the ball and stick model are color-coded: C-grey, O-red, H-white, N-blue. (c) The sequential binding structure of the LbL nanocomposite membrane. The thicknesses of the layers are not drawn in scale.

The presence of immobilized layer of polymer chains is the direct reason for the altering of thermodynamic properties, i.e. heat of fusion, glass transition temperature, chemical potential, etc. The effect of the interphase on the mechanical enhancement has been long ignored due to the relatively tiny portion of interphase region compared to the size of the fillers (micron-scale fibers). However, in the case of graphene oxide, the interphase region plays a significant role since the thickness of the filler is only 0.95 nm. Therefore, the Young's modulus of the graphene oxide-silk fibroin nanocomposite is extraordinarily high with low graphene oxide concentration. In addition, the reformable hydrogen bondings serve as excellent energy dissipater to improve extensibility and toughness of the material.

With the outstanding mechanical properties, fast fabricatin, potential electrical conductivity and inherent biocompatibility, the ultrathin graphene oxide-silk fibroin nanocomposite membranes exhibit potential applications in biosensors, nanopackaging, energy-harvesing, chemical filters and gas barriers.

4.2 Results and discussion

4.2.1 Micromorphology of the nanomembranes

AFM results of membrane roughness and graphene oxide coverage are shown in **Figure 4.2**a & b. The height profile illustrates a uniform 4.3±1.9 nm microroughness for samples with different numbers of bilayers. The microroughness of the bilayers starts around 1 nm and increases gradually with the addition of the number of bilayers, and saturate at 5 bilayers. The increase of microroughness with the layer number is because of the random distribution of graphene oxide flakes. The quality and uniformity of the nanocomposite membrane was also confirmed by optical microscopy observation (Figure 4.2a inset). The phase image confirms that graphene oxide coverage is 69±3% and 69±9% for samples prepared with graphene oxide methanol suspension and graphene oxide aqueous suspension, respectively. Molecular conformation of polymer chains adsorbed on nanofillers is proven to play an important role of the mechanical behavior of the nanocomposite.[47] Stretched chains provide higher stiffness while losing extensibility. The AFM image of the silk fibroin on graphene oxide shows globule morphology of the silk fibroin molecules uniformly adsorbed on both sides of graphene oxide sheets (Figure 4.2c), indicating the strong interactions.

Membrane thickness of the bilayer-structured nanocomposite membrane increases linearly with the number of bilayers (Figure 4.2d). The average single bilayer thickness is 5.4 nm for 0.2% silk fibroin solution with 0.04% graphene oxide methanol suspension spun at 3000 rpm. The replacement of graphene oxide aqueous suspension provided no noticeable difference in thickness accumulation. This value is reasonable when considering the ~5 nm thickness of single layer silk II and 69% coverage of 0.95 nm graphene oxide layer on top

of it. Graphene oxide volume percentage in the nanocomposite membrane is controlled by varying the number of filler layers or the thickness of silk fibroin layers. Graphene oxide concentration is calculated by

$$\phi_{GO} = \frac{n*\alpha \cdot t_{GO}}{t_f} \times 100\% \qquad (4.1)$$

where n is the total number of graphene oxide layers deposited on the sample; α is the graphene oxide coverage ratio (69%); t_{GO} and t_f are the thickness of single layer graphene oxide (0.95 nm) and the nanomembrane, respectively.

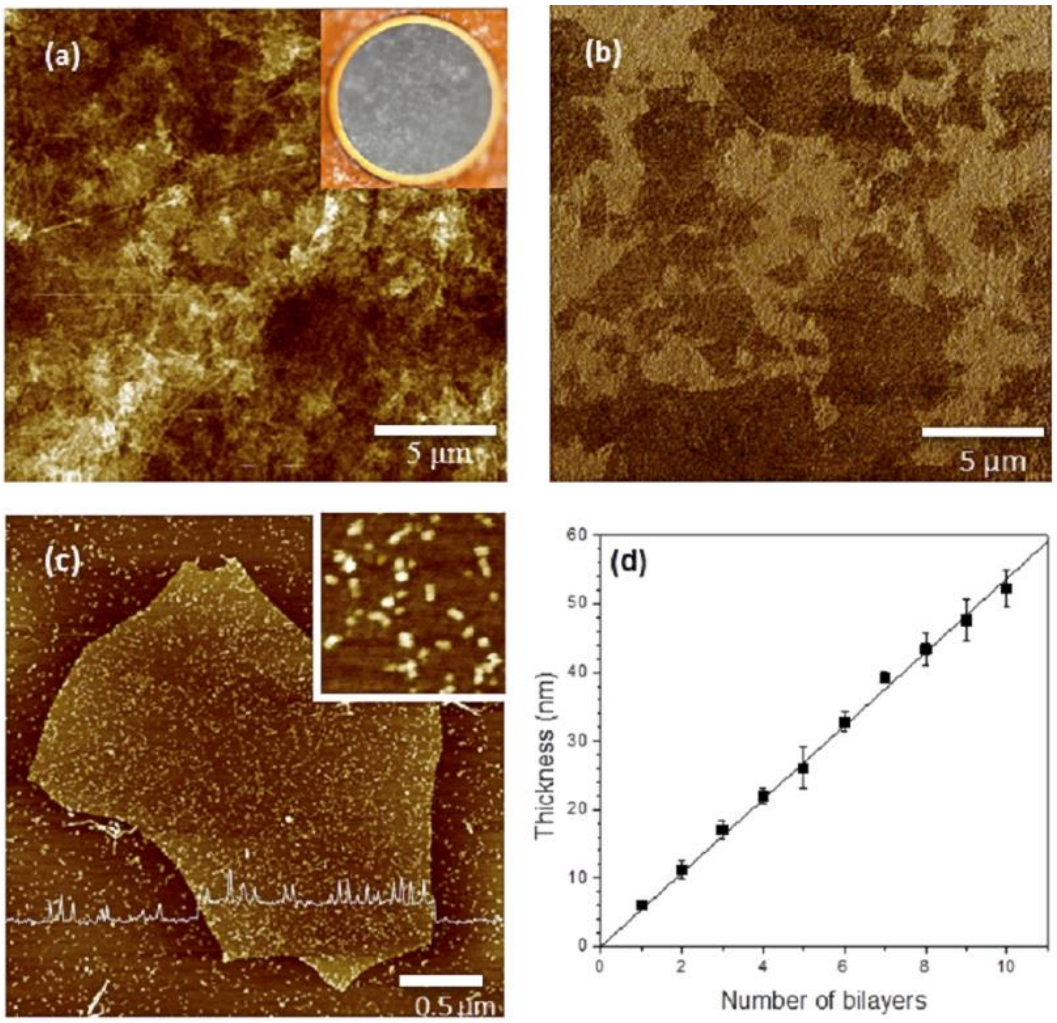

Figure 4.2 Morphology of the methanol treated GO-SF nanocomposite membrane: AFM height (z range: 60 nm) (a) (inset: optical image of the membrane suspending on a 300-um copper aperture) and phase (b) images of the nanocomposite; (c) SF molecule adsorption on GO flake (z range: 7.5 nm); (d) membrane thickness increases with the number of the bilayers.

4.2.2 Young's modulus of the nanomembranes

Figure 4.3a & b are the AFM scan and optical image of the buckling pattern of a representative graphene oxide-silk fibroin nanocomposite membrane. The period of the sinusoidal wave deformation varies from 2 to 10 microns based to the thickness and stiffness of the sample. From the pattern we know the samples are locally uniform and free of defects. Figure 4.3c shows the moduli results for samples with different graphene oxide concentration and tested by both techniques. Theoretical values predicted by Halpin-Tsai model are also plotted for reference. The pristine methanol treated silk fibroin LbL nano-membrane has a compressive Young's modulus of ~10 GPa, which is 150% higher

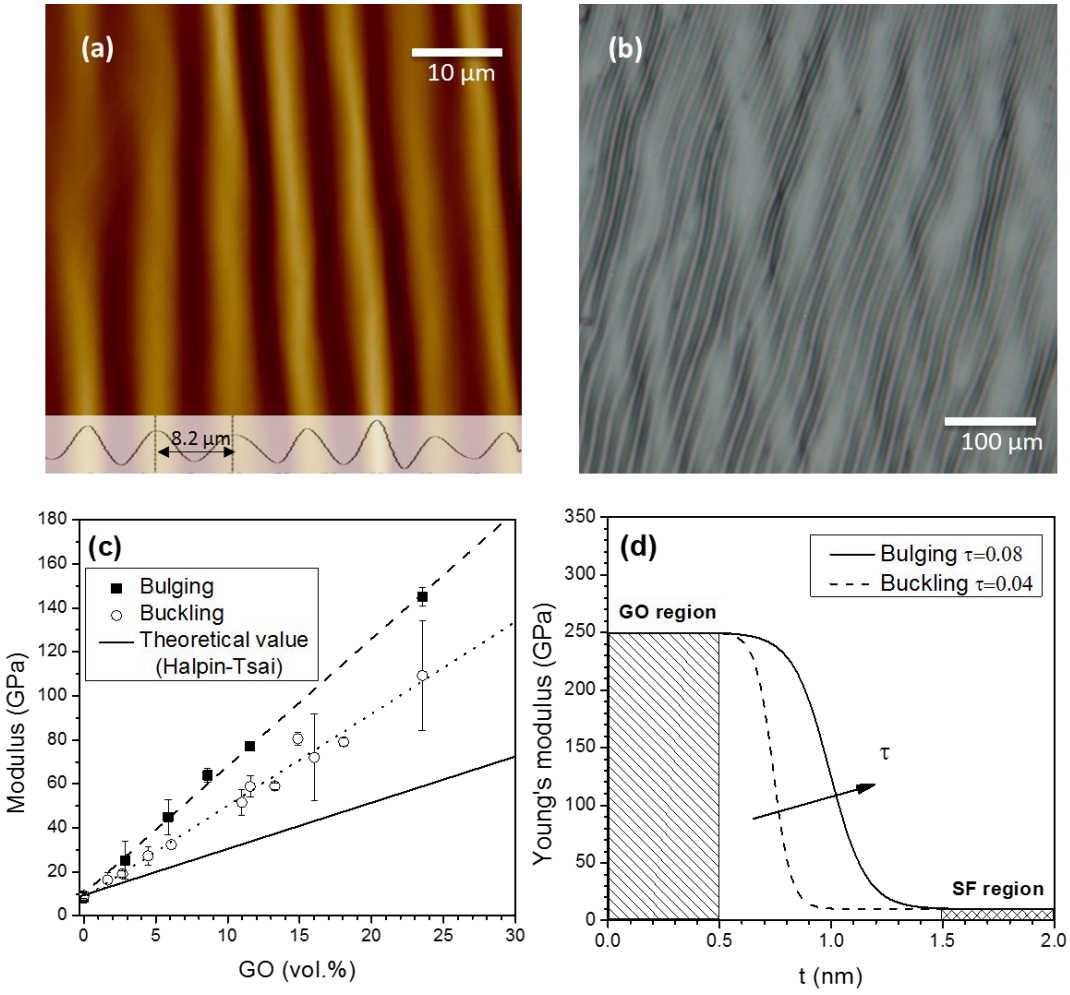

Figure 4.3 Moduli of the methanol treated GO-SF nanocomposite membrane. (a) 50 um x 50 um AFM image of the buckling pattern from a 10 bilayer GO-SF nanomembrane (Z scale: 2 um); (b) optical image of the buckling pattern; (c) the GO concentration dependence of the Young's modulus of the nanomembranes; (d) sigmoid decaying curves for buckling and bulging tests at the interphase region.

compared to the previous reported values.[8, 15] The reason for this increase is that the LbL silk fibroin membranes fabricated in this work were methanol treated on each layer, while the samples prepared by previous studies were post-treated by methanol after the whole LbL structures were finished. The β-sheet crystal inducing dehydration process driven by methanol is more effective in this work, resulting in the stronger membranes.

The tensile modulus of the pristine silk fibroin LbL membranes also have ~70% increase for the same reason. The validity of the 10±1 GPa Young's modulus reported in this work is also supported by the studies carried out by Keten et al. and Hu et al., which determined the Young's modulus of the β-sheet crystals is 22 GPa[10] by molecular dynamic simulation and combinational mechanical experiments, and the β-sheet crystal fraction in methanol treated silk fibroin samples is ~45%[13] by thermal analysis and infrared spectroscopy. With the assumption of the Young's modulus of the amorphous silk fibroin is 4 GPa[8] and applying Halpin-Tsai model for randomly oriented nanoparticles, the Young's modulus for the pristine silk fibroin nanomembrane was calculated to be 9.5 GPa, which fits well to our experimental data.

With the addition of graphene oxide filler, the Young's moduli of the samples increase linearly with the graphene oxide concentration, reaching a highest bulging value of 149 GPa. This is by far the highest modulus value recorded for nanomembranes. In contrast to similar nanocomposite with much higher thickness (a few microns), the ultrahigh stiffness is achieved without the expense of high nanofiller concentration.[31, 32, 48] And there is no sign of saturation in the plot, which together with the ultra-high stiffness values indicates that the incorporation of graphene oxide with silk fibroin is favorable. Moreover, it is shocking to find that the experimental data are systematically higher than the theoretical model values, which had been believed to be the highest performance achievable.

4.2.3 Interphase reinforcement model

We attribute this unexpected phenomenon to the unusual interphase enhancement in this nanocomposite system.[39] With the validity being discussed above, the sigmoid modulus decaying function at the interphase region is

$$E^*(t) = \frac{E_{GO} - E_{SF}}{1 + \exp\left[\frac{\eta(t-\delta)}{\tau} - \eta\right]} + E_{SF} \qquad (4.2)$$

where $E^*(t)$ is the modulus of the slice of silk fibroin material at a distance t from the graphene oxide-silk fibroin interface; E_{GO} and E_{SF} are the Young's moduli of graphene oxide and silk fibroin, respectively; η is the sigmoid transition factor (η = 6 used in this work). And δ is the retardation length and τ is the relaxation factor, which controls the start point and the rate of decaying along the thickness. We take δ = 0 in this case modeling by considering the quantum nature of the interphase and the weak hydrogen bonding interactions. The effective modulus of the silk fibroin matrix can be calculated by the weighted average of the moduli along the whole silk fibroin layer:

$$E_{sf,eff} = \frac{2}{t_{sf}} \int_0^{t_{sf}} E^*(t)\, dt \qquad (4.3)$$

where $E_{sf,eff}$ is the effective Young's modulus of the silk fibroin layer, t_{sf} is the thickness of the silk fibroin between the sandwiching graphene oxide layers. Meanwhile, $E_{sf,eff}$ can also be calculated by using Takayanagi model for conventional composites:

$$E_{comp} = \phi_{GO} \cdot E_{GO} + \phi_{SF} \cdot E_{sf,eff} \qquad (4.4)$$

where E_{comp} is the modulus of the composite material measured experimentally, Φ_{GO} and Φ_{SF} are the volume fraction of graphene oxide and silk fibroin in the composite, respectively. The modulus relaxation factor τ was determined by combining equations (4.2) to (4.4). The τ values for buckling and bulging tests are 0.24±0.05 nm and 0.49±0.05 nm respectively, indicating the single-sided interphase depth of ~0.5 nm and ~1.0 nm (Figure 4.3d). These values are lower than those determined for similar nanocomposite systems by scanning probe microscopy[38, 39], which is attributed to the ultra-low filler thickness with limited ability for solid molecular anchoring. Nevertheless, surface adsorption of silk fibroin molecule on graphene oxide forms a stiff region into the matrix, resulting in a 2.0 and 2.8 times multiplier of the effective filler concentration[50] for compressive and extensive moduli, respectively. The predicted moduli values are plotted in solid lines for both buckling and bulging results in Figure 4.3c. The difference in interphase enhancement for buckling and bulging tests is originated from their different loading condition.[8, 14]

Although the local loading condition is fairly complicated for buckling test, it is approximately a uniaxial compression in the planar direction of the layered structure. While for the bulging test, the loading condition can be reduced to a biaxial extension, which is equivalent to a uniaxial compression normal to the layer structure. The graphene oxide filler is ultra-stiff in response to tensions but loses almost all of the stiffness when compressed due to the large aspect ratio. Moreover, the bulging failure mode is stick-slip mechanism[10] and the buckling failure mode is delamination. As a result, the bulging stiffnesses are noticeably higher than those of the buckling tests. Similar LbL graphene oxide-silk fibroin samples without methanol treatment were also tested for comparison. The tensile Young's moduli are 30% lower than those of the methanol treated samples for all of the graphene oxide concentrations tested. This result is expected because of the lower β-sheet crystal content without the methanol treatment. Less crystalline domains directly cause the lower Young's modulus of the silk fibroin layers, and further diminish the correlation of the polymer chains and the thickness of the interphase region at the silk fibroin-graphene oxide interface due to the lower degree of crosslinking.

4.2.4 Other mechanical properties of the nanomembranes

Figure 4.4a & b show the relationship between ultimate stress/strain and the graphene oxide concentration. The ultimate stress of the pristine methanol treated silk fibroin LbL membranes is 100 MPa, matching the previous results well.[8] The lower ultimate stress of the silk fibroin nanomembrane as compared to the 600-800 MPa values of native silk fibers is attributed to the lack of highly-engineered and effective hierarchical loading transfer structures[51] and the degradation of silk fibroin molecules during the reconstitution.[11, 19, 52] Expectedly, the ultimate stress increases with the graphene oxide concentration. The highest ultimate stress reaches 300 MPa and saturates at 11.5 vol.% of graphene oxide. The saturation concentration and the ultimate stress are both 300% higher than those of the graphene oxide-polyelectrolyte nanomembranes[24], indicating a stronger interaction by hydrogen bonding than the electrostatic force. It is quite reasonable because the electrostatic charges only exist on the carboxyl groups surrounding the graphene oxide edges, while hydrogen-bonding sites, although the unit strength is much weaker than electrostatic interaction, are all over the planar surface (Figure 4.1b). The graphene oxide-

silk fibroin LbL nanomembranes fabricated by graphene oxide aqueous suspension were also tested for comparison. The ultimate stresses are systematically lower than those of the methanol treated samples and the gap increases with the increase of graphene oxide concentration. The lower ultimate stresses for non-methanol treated samples are caused by the lower content of β-sheet crystals in absence of methanol induction. And the lack of crosslinking provided by nanocrystals also results in the lower slope of the increasing stress trend for the non-methanol treated samples.

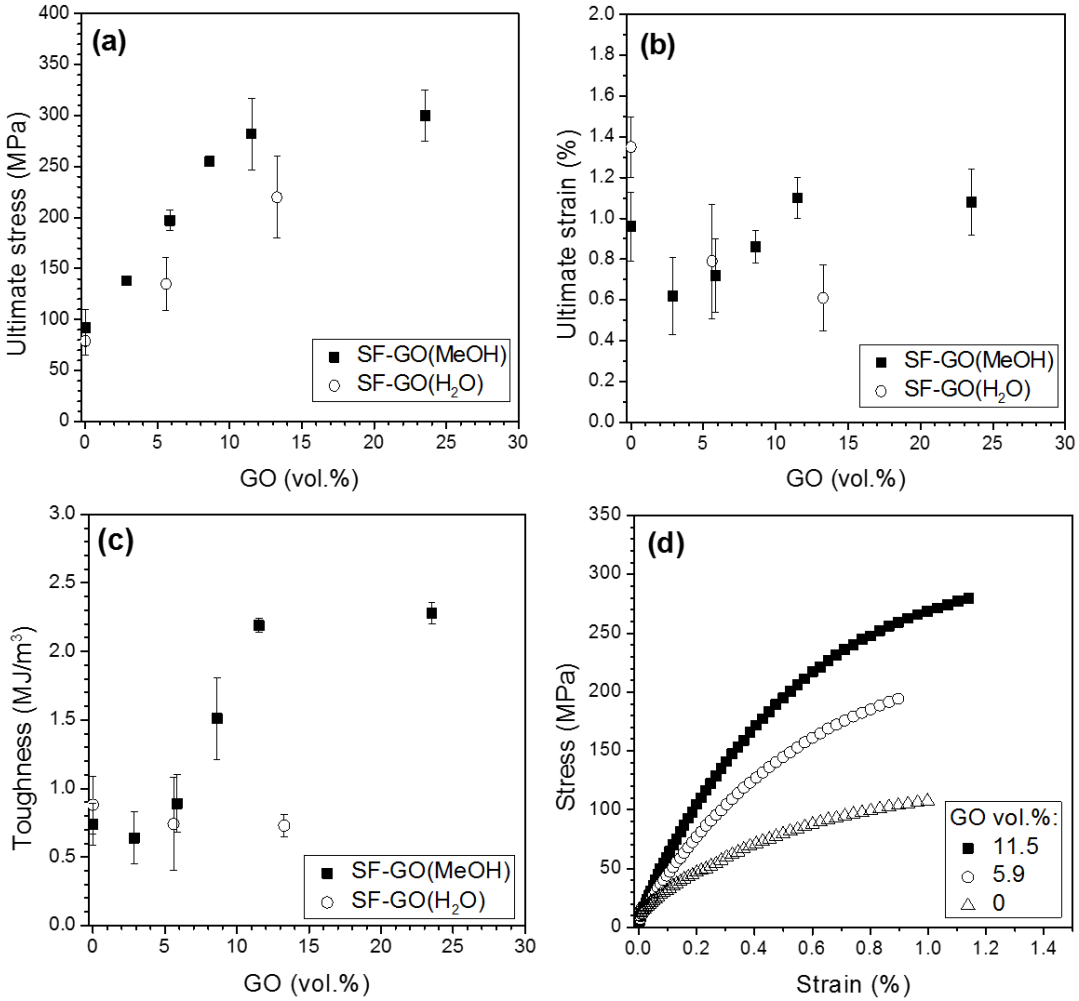

Figure 4.4 Mechanical properties of the nanocomposite membrane from bulging test. (a) Ultimate stress vs. GO concentration; (b) ultimate strain vs. GO concentration; (c) toughness vs. GO concentration; (d) representative σ-ε curves.

On the other hand, it is commonly known that the addition of filler will make the composite materials stiffer with the compromise of extensibility, as in the case for the non-methanol treated samples (Figure 4.4b). For pristine silk fibroin LbL membranes, the 1.4% ultimate

strain of non-methanol treated samples is 40% higher than that of the methanol treated ones. This is originated from the lower degree of crystallinity and the loose physical entanglement of the non-methanol treated samples. With the addition of graphene oxide, the ultimate strain of the non-methanol treated samples drops linearly by 57% from 0 to 11.5 vol.% of graphene oxide concentration. However, in the case of methanol treated samples, this trend is only valid for the very first stage of graphene oxide concentration increase. The ultimate strain for the pristine silk fibroin LbL nanomembrane decreases to 0.6% with 2.9 vol.% of graphene oxide. Then the ultimate stain climbs up gradually to 1.1% thereafter and saturates at 11.5 vol.% of graphene oxide. The increasing trend of ultimate stain with graphene oxide concentration is counterintuitive. This unusual behavior of increasing ultimate strain with increasing filler concentration again indicates the strong and recoverable interaction between silk fibroin and graphene oxide. Because the hydrogen bondings are relatively weak and permanent electronic dipole interactions in nature, they are easy to be ruptured and reform the bonding with the next neighboring polar counterparts. Molecular dynamic simulations demonstrated the ability of the hydrogen bonding recovery.[10] At a pulling out rate of 5 cm/s, which is orders of magnitudes larger than the strain rate in this work, peaks appear in the force-displacement curve of the silk β-sheet crystals, demonstrating the instant reform of hydrogen bonding during the shearing movement. Integrated by hydrogen bonding, the interface is becoming interconnecting site for more silk fibroin molecules, rather than a weak and stress-concentrating spot as in conventional composites. Both the saturation in ultimate stress and ultimate strain at 11.5 vol.% is proposed to be because that there is a threshold for the complete coverage of a single layer of silk fibroin in the LbL deposition. Graphene oxide concentration higher than 11.5 vol.% will result in discontinuous matrix distribution and stress concentration. However, the Young's moduli do not saturate at that concentration simply because the Young's modulus reflects the properties at the initial stage of the loading, while the ultimate stress/strain represents the failing stage of the loading behavior.

Toughness is another important mechanical property considered essential for sustained loading ability. The physical origin of toughness is the energy dissipated by a material before failure. During the loading cycle, the hydrogen bondings, both between silk fibroin and graphene oxide and within β-sheet crystal of silk fibroin, and covalent bondings of the

silk fibroin molecular chain are the primary loading bearers. While the covalent bondings are mainly responsible for the final failure of the material, the hydrogen bondings between silk fibroin and graphene oxide are the major energy dissipater during the loading. Because of the reformability of the hydrogen bondings described above, the higher graphene oxide concentration results in higher toughness by providing more hydrogen bondings. By combining the modulus, ultimate stress and ultimate strain, the toughness of the methanol treated nanomembranes (Figure 4.4c) takes a dip initially and monotonously increases to 2.2 MJ m^{-3} at the 11.5 vol.% saturation point. The highest recorded toughness for the materials is 3.4 MJ m^{-3}. In comparison, the toughness of the non-methanol treated samples remains essentially constant.

Representative stress-strain curves of graphene oxide-silk fibroin nanocomposite membranes are presented in Figure 4.4d. Distinct difference in mechanical performances due to various graphene oxide concentrations indicates the significant roles graphene oxide plays in this nanocomposite system. A comparison among the current films/membranes containing silk fibroin or graphene oxide provides a clear perspective to directly evaluate the performance of the materials. Pristine LbL silk fibroin membranes have relatively low mechanical properties due to the degradation of the protein caused by silk reconstitution.[8] By incorporating clay nanoparticles, the modulus of the silk membranes has doubled and the toughness is improved.[14, 15] graphene oxide-polyelectrolytes nanomembrane greatly improved the toughness of the material due to the strong electrostatic interactions between different components. [24] Graphene paper fabricated by vacuum infiltration and thermal annealing has surprisingly high ultimate stress considering the poor binding condition of the building blocks.[53] Then chemical crosslinking pushes the stiffness of the graphene oxide films to 120 GPa[27], 300% higher than that of the uncrosslinked cousin. However, the strong covalent bonds between graphene oxide flakes also resulted in a very brittle material. Finally, the graphene oxide-silk fibroin nanocomposite membranes introduced by this work occupies the lower right corner of the column chart, showing highest combination of ultimate stress and stiffness. And more interestingly, it also possesses the highest toughness of 2.2 MJ m^{-3}.

4.3 Conclusions

We have fabricated ultra-thin graphene oxide-silk fibroin nanocomposite membranes using SA-LbL technique and demonstrated the outstanding mechanical performances. SA-LbL technique has proven to be a reliable deposition method to quasi-molecular layered self-assembly. The alternating layered structure of the graphene oxide-silk fibroin nanocomposite greatly improved the filler dispersion and components interactions. The highest Young's modulus, ultimate stress and ultimate strain recorded are 145 GPa, 300 MPa and 1.1% respectively for a sample with 23.5 vol.% graphene oxide concentration. The high-density hydrogen bonding is proposed to be the origin of the balanced stiffness, strength and toughness. The low strength and reform-readily characteristic of hydrogen bondings make the membrane flexible and extensible, while the high density of the hydrogen bondings ensures the strength, stiffness and toughness.

Chapter 5 Biopolymeric Nanocomposites with Enhanced Interphases

5.1 Introduction

We demonstrate a dynamic spin-assisted LbL assembly (dSA-LbL) as an efficient method for the formation of silk-based nanocomposites with controlled molecular hierarchical structures and enhanced interphase interactions (**Figure 5.1**). In contrast to the conventional LbL assemblies reported earlier, the dSA-LbL methods suggested here provides a facile way of manipulating the secondary structures of silk fibroin proteins adsorbed on the of heterogeneous graphene oxide surface and resulting in excellent,

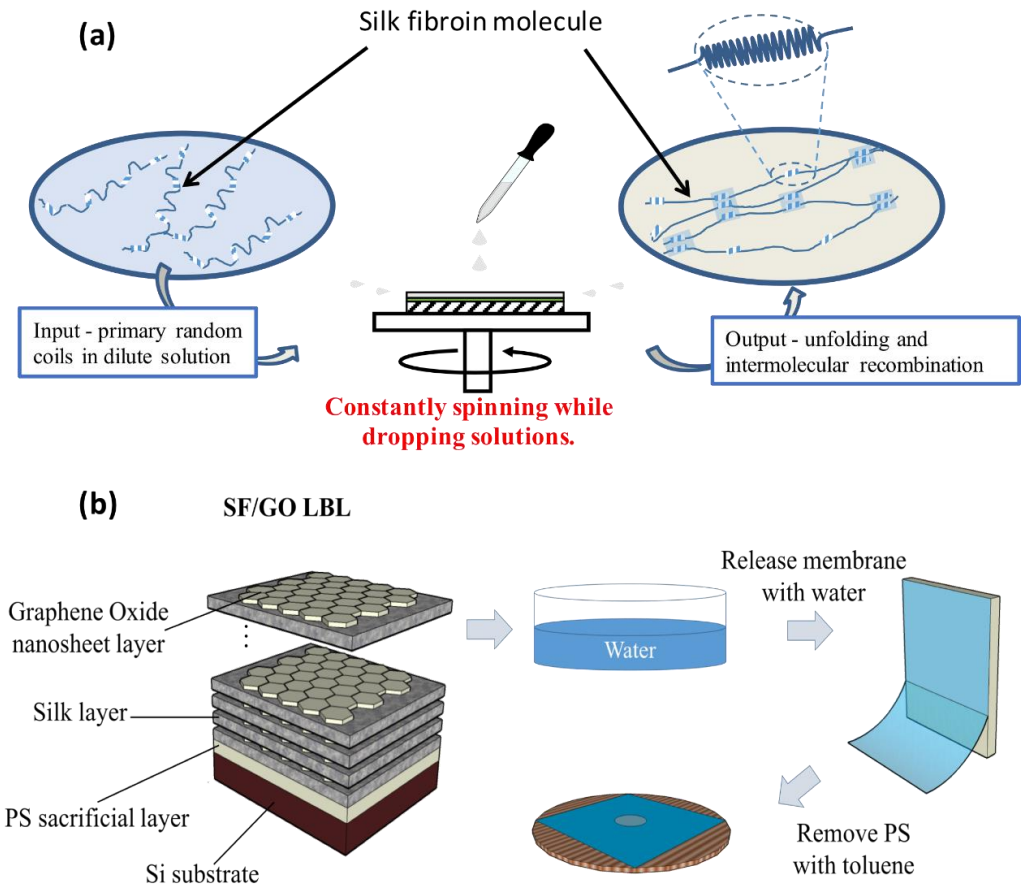

Figure 5.1 (a) The fabrication of free-standing GO-SF membranes with dSA-LbL assembly; (b) The laminated structure of the LbL membrane and the release of the free standing membrane followed by mounting on the copper aperture.

balanced ultimate strength, Young's modulus, and toughness. We suggest that the fast spreading of biomacromolecules during direct dropping of biopolymer solution on continuously spinning substrate allows for stretching of the silk fibroin molecules that favors the enhancement of their interactions with substrates. The excellent mechanical properties achieved here include the outstanding tensile modulus of around 170 GPa, the ultimate strain of around 1.5%, the ultimate tensile stress of nearly 300 MPa, and the toughness of more than 3.4 MJ m^{-3}, with all characteristics far surpassing those known for traditional ultrathin carbon-based nanocomposite.[109, 324]

5.2 Results and discussion

5.2.1 Fabrication and Morphology of Nanocomposite Membranes

The characteristic distinction of the dSA-LbL assembly over the conventional SA-LbL is the constantly rotating substrate while applying the to-be-spun solutions, which saves time, facilitates automation, and provides a novel means for the modification of the secondary structures of the molecular chains. In contrast to the conventional LbL assemblies, the highly kinetic adsorption conditions and fast solvent (water) evaporation during the dSA-LbL process eliminate the loosely attached molecules as well as "quench", fix the secondary structures and anchor the biomacromolecules on the substrate (Figure 5.1a & b). We found that, by using 0.02 wt% silk solution, 2000 rpm of the spin speed ensures a complete, uniform, and monolayer coverage of the unfolded and stretched silk molecules on the graphene oxide substrate. Lower speeds resulted in bundled and self-folded silk molecules and more than one layer of adsorption. Higher rotational speeds resulted in incomplete coverage of the substrate. Approximately 2 seconds was allowed for deposition to ensure the complete removal of the solvent and the fixation of the molecules. We kept spinning for another 20-25 seconds before dropping the next layer of constituents. Therefore, the optimal spinning condition for silk fibroin layer was determined to be 2000 rpm with 45 second between depositions. The solution concentration was limited to 0.02 wt% because higher viscosity adversely affects the film uniformity. It is critically important that with the substrate vigorously spinning, the silk solution spreads fast and the solvent

evaporates in milliseconds, resulting in the major difference and advantage over the conventional LbL techniques as discussed below.[325]

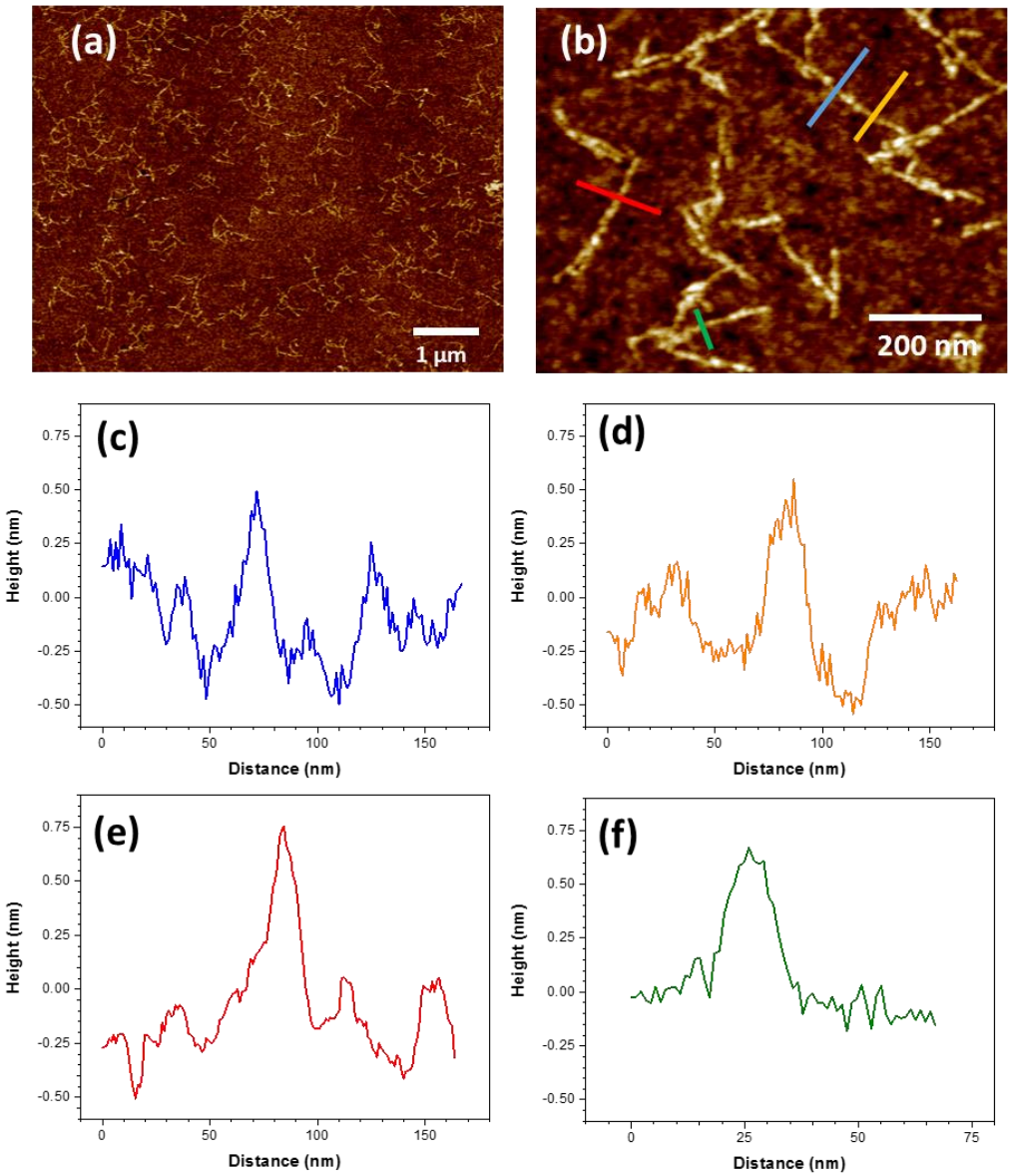

Figure 5.2 Morphologies of the stretched SF on GO surfaces: (a, b) Survey and high resolution AFM images showing the uniform distribution of SF molecules without significant aggregation or entanglement. (z-scales: 2 nm) (c)-(f) The cross sectional profile of the single molecules from the color coded lines in panel (b).

In fact, the high resolution AFM micrographs show the uniform surface distribution of the silk biomacromolecules without signs of significant aggregation **(Figure 5.2**a & b**)**. It is worth noting that the samples used to adsorb biomacromolecules for these images are diluted for clear visualization of the individual macromolecule behavior. Silk backbones

are anchored in random conformation on the surface of graphene oxide and individual biomacromolecules are stretched locally without forming larger bundles.

Distinctly different from the previously observed morphologies of silk biomacromolecules deposited by the conventional SA-LbL technique with formation of rich and large scale aggregates (nanofibrils, bundles, and globules), silk backbones during dSA-LbL deposition explored here form a dense network of individual stretched chains. Indeed, the diameter of backbones across the entire surface was measured to be 0.8 ± 0.2 nm that is close to the natural diameter of silk backbones with occasional bulky side groups of amino acids (Figure 5.2c-f). The unfolding and stretching of the silk backbones by the dynamic deposition process is essentially important for exposing the polar moieties along the backbone and forming high-density hydrogen bonding and other attractive weak interactions between individual segments of the silk backbones and the graphene oxide surfaces with random distribution of oxidized functionalities. Such maximization of interfacial interactions results in strong anchoring of the individual biomacromolecules to graphene oxide surface.

In addition, the molecular secondary structures of silk under the dSA-LbL processing have also altered significantly. High resolution deconvoluted FTIR spectra of the silk fibroin after the two different type of spin coatings has been presented in **Figure 5.3**. The vibrational bands centered at around 1625 cm^{-1} and 1680 cm^{-1} have been assigned to the antiparallel beta-sheets and beta-turns respectively, which are corresponding to the crystallinity of the silk; and the bands around 1659 cm^{-1} and 1646 cm^{-1} are from the vibrations of the alpha-helices and random coils of the silk chains, respectively.[312] From the comparison of the secondary structure composition resulted from the dSA-LbL and the conventional SA-LbL shown in Figure 5.3d, it is clear that the dSA-LbL assembly transformed around 20 % of the random coils to beta-turns, indicating a higher crystallinity induced by material shearing. And the increased fraction of beta-turns in the crystallized portion of silk also suggests a less ordered crystallinity, incurring the quenching effect of the dSA-LbL deposition as will be discussed in detail elsewhere.

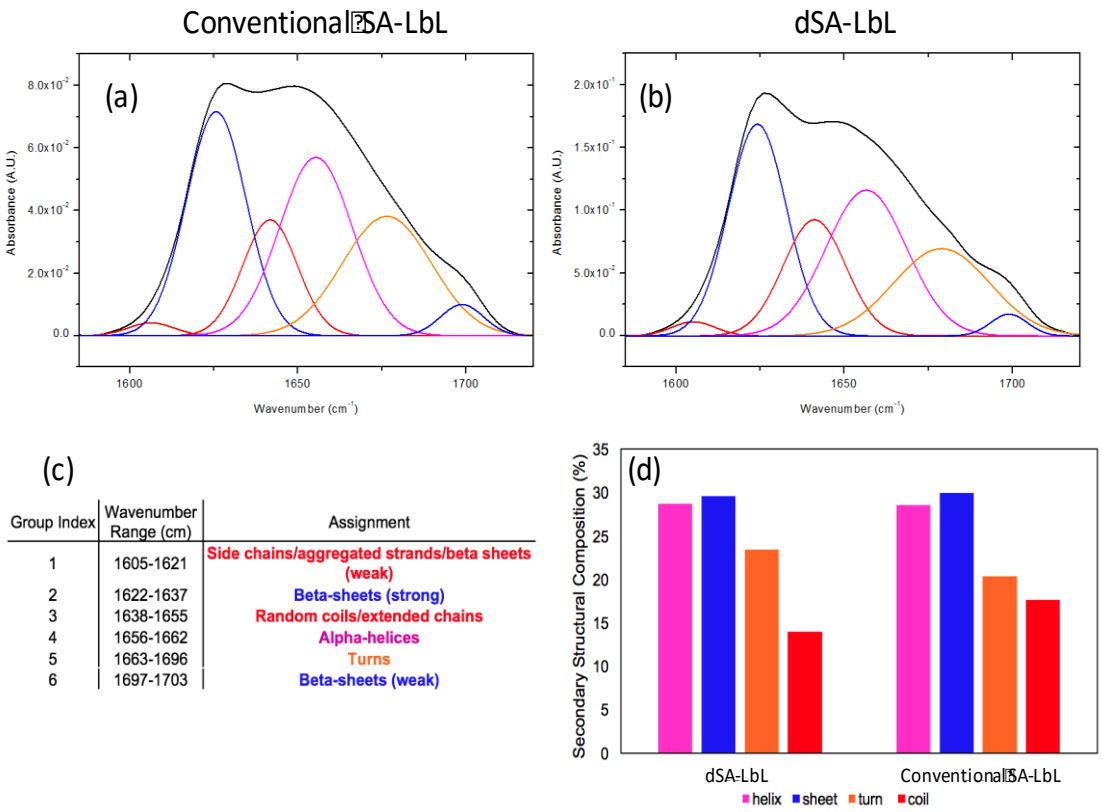

Group Index	Wavenumber Range (cm)	Assignment
1	1605-1621	Side chains/aggregated strands/beta sheets (weak)
2	1622-1637	Beta-sheets (strong)
3	1638-1655	Random coils/extended chains
4	1656-1662	Alpha-helices
5	1663-1696	Turns
6	1697-1703	Beta-sheets (weak)

Figure 5.3 The FTIR spectra of the silk spun using the (a) conventional SA-LbL and (b) dSA-LbL; (c) peak assignment of the FTIR spectra and (d) the composition of the secondary structures of the silk.

The density of the silk coverage has been controlled via applying different amount of silk solutions when spin coating to ensure the full coverage of the LbL structure. At high concentration, uniform nanometer thick silk layers are formed on the graphene oxide surface. When alternated with graphene oxide sheets, silk fibroin is uniformly covered with graphene oxide sheets without large corrugations and wrinkles thus promoting formation of uniform continuous multilayered films (**Figure 5.4**a). The representative profile of the cross section of the 15-bilayer GO-SF dSA-LbL film shows a thickness of around 45 nm. The total thickness of the silk-graphene oxide layer is around 3 nm, thus, indicating about 2 nm thick silk layer. The thickness of films was also independently confirmed by ellipsometry measurements. The root-mean-square surface microroughness, as measured within an area of 1μm×1μm, was 5.1±2.9 nm, similar to that of GO-SF multilayered films studied earlier. [69]

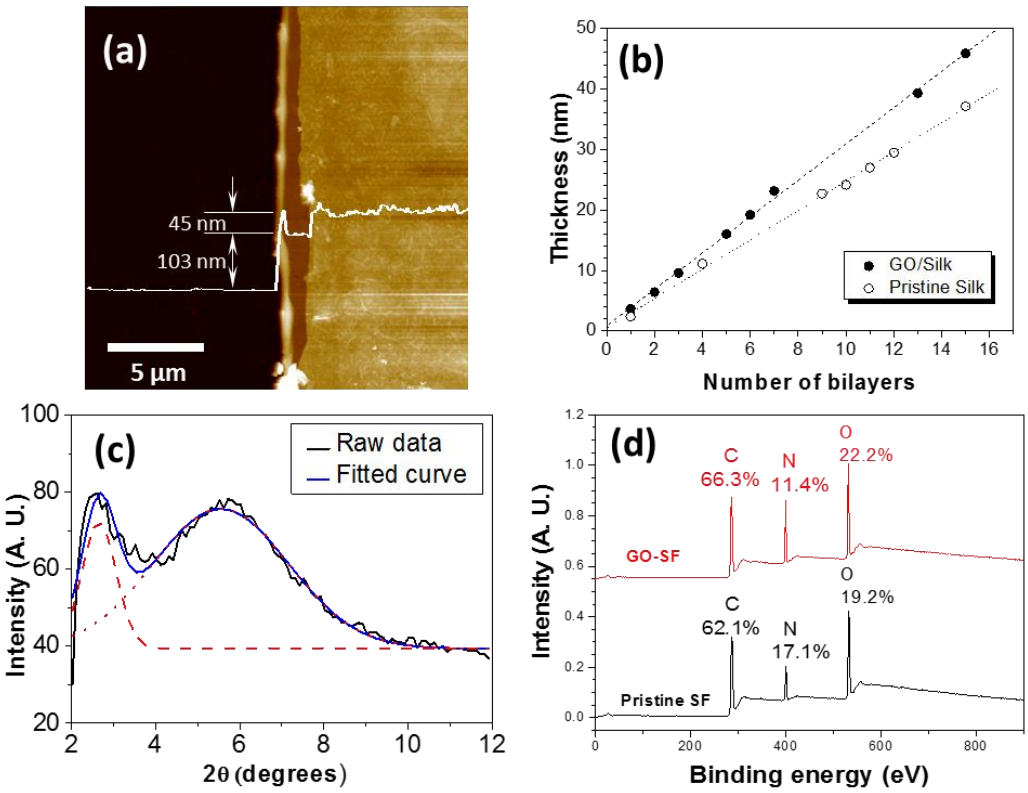

Figure 5.4 Structure and composition of the GO-SF nanocomposite membrane: (a) AFM image and height profile of film edge (z-scale: 350 nm) showing the 45 nm thick GO-SF nanocomposite membrane on top of the 103 nm thick sacrificial PS layer. (b) Ellipsometry data show that the thickness of the membranes increases linearly with the number of the GO-SF bilayers assembled. (c) XRD data and peak fitting of a 70 bilayer GO-SF dSA-LbL membrane on silicon wafer. The silicon wafer background is subtracted. (d) XPS of the GO-SF nanomembranes in comparison with that for pure silk films.

The thickness of GO-SF films increases linearly with increasing number of layers deposited, confirming the conventional stepwise growth mode, characteristic of LbL assembly (Figure 5.4b). The average bilayer thickness of 3.1±0.4 nm is lower than that observed for the conventional SA-LbL films.[69] The reduction of the effective silk layer thickness is due to the different kinetic conditions that affect the removal rate of the solvent and the adsorption rate of the individual silk chains rather than bundles and nanofibrils. [69] The reduced average bilayer thickness was also independently confirmed by multi-peaks fitting of X-ray Diffraction (XRD) data (Figure 5.4c). The broad peak at 2.6^{o} can be assigned to the first order diffraction peak with the average spacing of 3.3 nm that corresponds to the data obtained from AFM and ellipsometry. On the other hand, the diffuse halo at 5.5^{o} can be originated from the interplanar distances within β-sheet

nanocrystals of silk fibroin of 1.5 nm. [69] We have also employed the Scherrer equation to estimate the ordering of the GO-SF bilayer structure and the size of the silk beta-sheet nanocrystals and stacking number of graphene oxide sheets.[326] The stacking number of the GO-SF bilayer structure is about 8 for the 70-bilayer film, indicating a partially-ordered layering. And the size of the beta-sheet nanocrystals was estimated to be around 3.2 nm, which matches well with the previously reported dimensions for optimized stress transfer of the partially ordered silk II phase.[327]

Finally, we employed XPS to directly evaluate the chemical composition of the nanocomposite membranes (Figure 5.4d). By ignoring the weight contribution of the hydrogen atoms in the material, the weight fraction of silk fibroin (ω_{SF}) in the nanocomposite membrane can be estimated by using relationship:

$$\omega_{SF} = \frac{Z_C A_{SF}^C + Z_O A_{SF}^O + Z_N A_{SF}^N}{Z_C A^C + Z_O A^O + Z_N A^N}$$

where Z_C, Z_O, and Z_N are the atomic weight of carbon, oxygen, and nitrogen, respectively; A_{SF}^C, A_{SF}^O, and A_{SF}^N are the atomic fractions of carbon, oxygen, and nitrogen that are contributed by the silk constituent in the nanocomposite membrane, respectively; and A^C, A^O, and A^N are the total atomic fractions of carbon, oxygen, and nitrogen in the nanocomposite membrane, respectively.

Since all the nitrogen comes only from the silk constituent, $A_{SF}^N = A^N$, $A_{SF}^C = A^N \cdot \gamma_{SF}^{C/N}$, and $A_{SF}^O = A^N \cdot \gamma_{SF}^{O/N}$, where $\gamma_{SF}^{C/N}$ and $\gamma_{SF}^{O/N}$ are the atomic ratio of C/N and O/N in silk fibroin, respectively. Therefore, the atomic fractions of carbon, oxygen, and nitrogen in both the nanocomposite membrane and the pristine silk fibroin can be extracted from the XPS survey spectra at Figure 4d and used in the equation for the estimation of chemical composition. The weight fraction of silk fibroin in the nanocomposite membrane was estimated to be ω_{SF} = 65.4%. By taking the density of silk fibroin and graphene oxide as 1.3 g/cm^3 and 1.8 g/cm^3, respectively, the volume fraction of graphene oxide can be finally estimate to be around 27%, that is close to that independently obtained from the ellipsometry data.

5.2.2 Mechanical Properties from Bulging Experiments

The mechanical properties of the GO-SF nanocomposite membranes can be analyzed with the well-known bulging technique. [315, 328, 329] This technique is widely utilized for measuring the mechanical properties of freely suspended nanoscale films. [42, 69, 330, 331] In this test, the ultrathin LbL membranes were freely suspended over the copper aperture with 300 μm diameter, while the micromechanical response to the air pressure is measured as the deflection of the membrane by a laser interferometer (**Figure 5.5**). [69] An analysis of the deflection behavior of the membranes under variable pressure allows for the reconstruction of the stress-strain curves according to the known procedure. [69] From this data, the mechanical properties, including Young's modulus, ultimate strain, ultimate stress, and toughness, can be readily estimated. The ultimate strain and stress can be obtained at the maximum deflection for the nanocomposite membranes before the breaking point (Figure 5.5c, d).

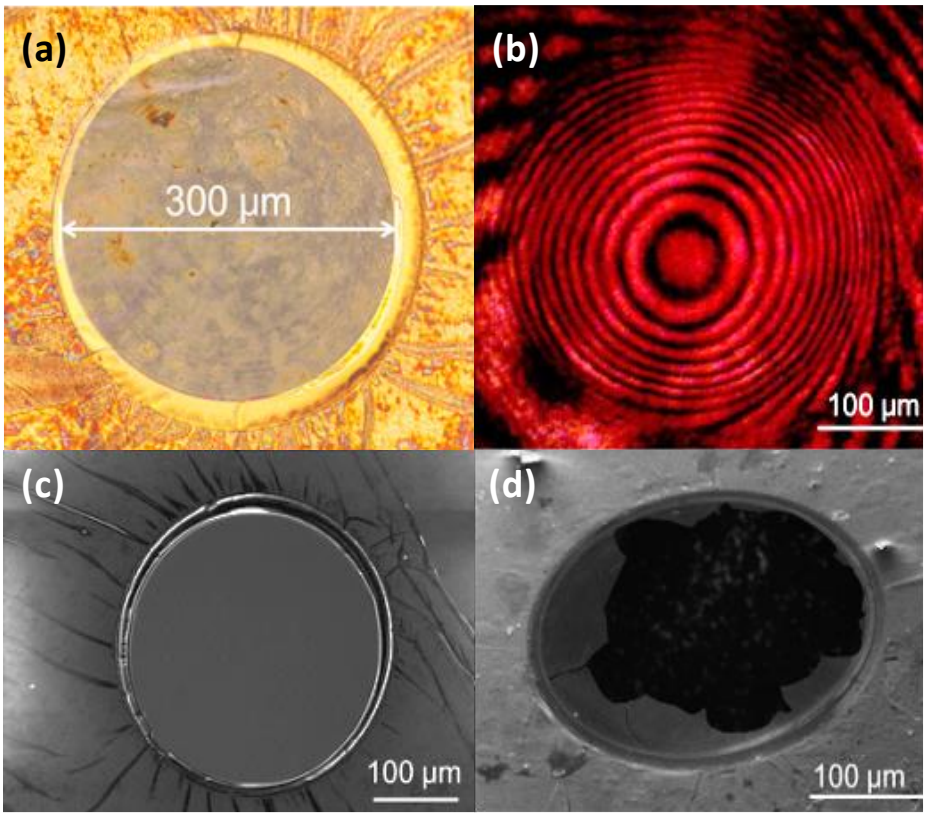

Figure 5.5 (a) Optical image of the GO-SF nanocomposite membrane suspended across a 300 μm copper aperture. (b) Interference pattern on the deflected membrane during bulging measurement. SEM image of the freely suspended nanomembrane (c) before and (d) after bulging measurements (the membrane is fractured).

For the dSA-LbL nanocomposite membranes fabricated here, the experimental values of the Young's modulus in the elastic regime are calculated from the stress-strain data in **Figure 5.6**a. We found that, an elastic modulus of 12 ± 1 GPa obtained for the pure silk membranes is around 20% higher that reported for the conventional SA-LbL silk films (about 10 GPa) that suggests the noticeable strengthening due to the alternation of the secondary structures of the silk molecules during dynamic LbL assembly. [69] The theoretical value of Young's modulus was calculated according to the Halpin–Tsai model for randomly oriented nanoparticles within confined silk fibroin matrix. [127] As reported, the Young's modulus of random silk fibroin (silk I) and β-sheet crystals is 4–5 GPa and

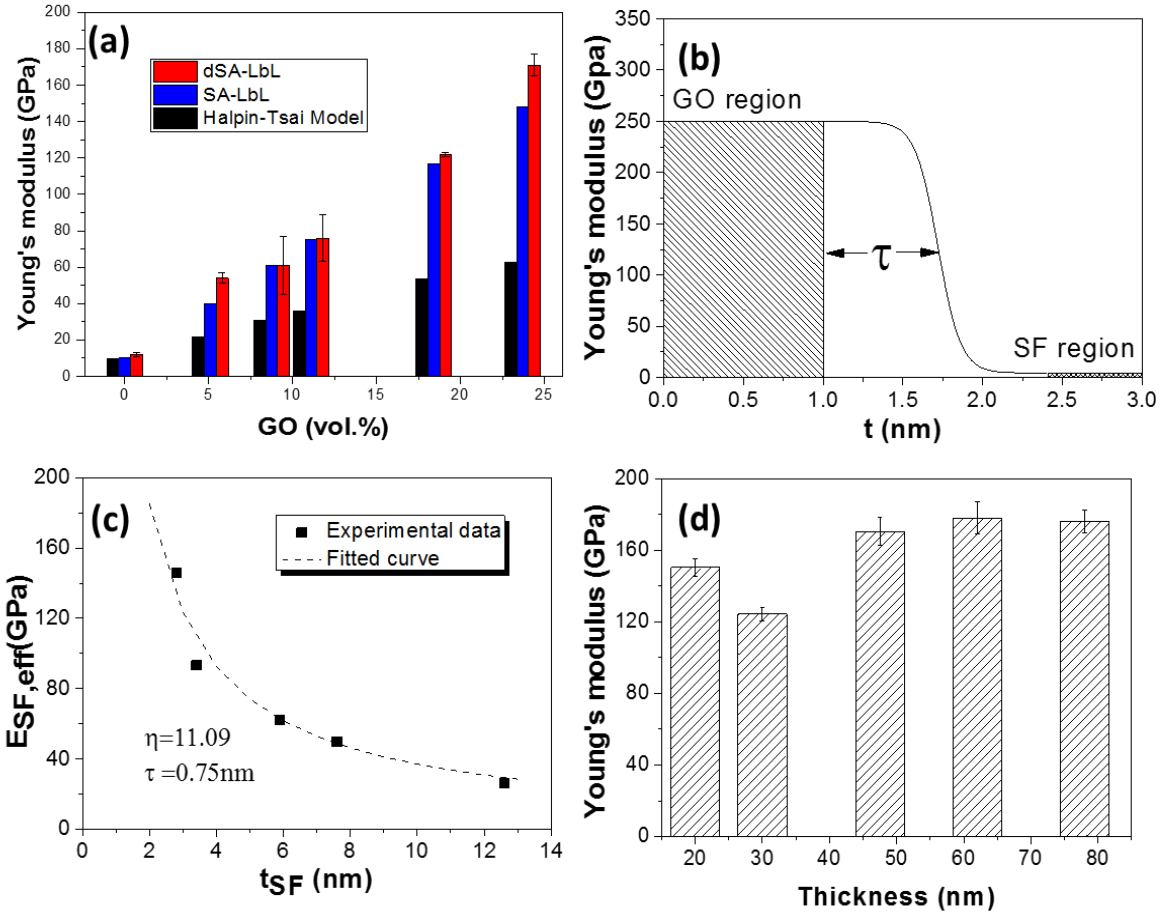

Figure 5.6 (a) Dependence of the Young's modulus of the GO-SF nanomembranes upon the volume concentration of graphene oxide. (b) Sigmoid decay curves for bulging tests at the interphase region. (c) The dependence of the effective Young's modulus of the silk layer on the thickness of the silk fibroin laminates. The dashed line is the fitted curve using the interphase reinforcement model. (d) Variation of the Young's modulus for membranes with different thicknesses.

around 22 GPa, respectively. [327] Therefore, the estimated content of the β-sheet crystal should be 63%, which is significantly higher than that calculated for the conventional SA-LbL silk films (around 45%), indicating a stronger intermolecular interactions between the silk chains due to the unfolding and the corresponding closer packing of the biomacromolecules that allow for fast formation of ordered domains. [69]

After adding graphene oxide component to the LbL films, the Young's modulus value increased dramatically, about 15 times, to 171±6 GPa at graphene oxide content of 24 vol% (Figure 5.6a). This is the highest value of the elastic modulus ever reported for flexible nanocomposites and biopolymer-based membranes. [332, 333, 334] Moreover, we found that the theoretical values of the Halpin-Tsai model calculated with the condition of ideal parallel orientation of platelets and complete stress transfer scenario are significantly lower than those obtained experimentally from the bulging measurements (Figure 5.6a).

The filler-reinforcement effect may be related to the formation of the extended interphase zone between the two components with gradually changing composition (Figure 5.6b). [69] Therefore, the shape factor η and relaxation distance τ can be determined by fitting the experimental modulus data $E_{SF,eff}$ with the Newton's iterative method. As shown in Figure 5.6c, the modulus value for different graphene oxide contents calculated according to the interphase zone fit well to the experimental results, thus, confirming the reinforcing mechanism in the nanocomposites. At limiting cases, the interphase model proposed can be transformed to standard rule-of-mixture model for composites when the effective thickness of the interphase region τ is reduced to zero.

The fitting of the compositional variation of the elastic modulus gives value of η = 11.0 and τ = 0.75 nm, respectively (Figure 5.6c). The value of η is almost twice larger than that obtained by the conventional SA-LbL technique (η=6.0). [69] This difference indicates enhanced silk-graphene oxide surface interactions caused by larger percentage of the exposed functionalities of individual backbones during the dSA-LbL deposition, which is a distinctive advantage over the conventional static and relaxed LbL deposition techniques. The effective thickness of the reinforcing region of 0.75 nm corresponds a single silk backbone diameter (Figure 5.6c), which indicates the close-to-limit reinforcement

performance. The overall fraction of the reinforcing region (graphene oxide and the effective interphase zone) reached 58% in overall volume of the nanocomposite films. Thus, even when the graphene oxide content is only 24% such a reinforcement increases the effective high-modulus filler volume by a factor of 2.5.

Additional experiments for samples with the same composition but different thicknesses (from 20 nm to 80 nm) were also conducted in order to verify if the dramatic reinforcement of the mechanical properties is significantly dependent on the thickness of the films (Figure 5.6d). The average Young's moduli of the membranes with different thicknesses are 160±23 GPa and consistent for all membranes tested here. Moreover, the modulus value reaches 175±4 GPa for membrane thickness above 50 nm (Figure 5.6d).

Figure 5.7a shows the representative stress-strain curves of the nanocomposite membranes with various GO content obtained from the bulging test. All the stress-strain curves collected here show elastic deformation at the initial stages of the loading and yield before ultimate fracture (Figure 5.7b-d). As clear from this data, the ultimate strain increases three-fold (from 0.44 to 1.51%) with increasing volume fraction of graphene oxide sheets from 5.1 to 24 vol % (Figure 7b). Similar phenomena can also be found in the comparable conventional LbL membranes (Figure 5.7b). [69] At the lower graphene oxide content, fewer layers of graphene oxide embedded in the silk matrix, thus, causing stress concentration around these sites. However, further increases in the graphene oxide content results in more uniform stress distribution throughout the whole thickness of the membrane, resulting in significant increase in the ultimate strain to very high value for silk nanocomposite films.[41]

The ultimate stress of reinforced GO-SF nanomembranes increased linearly with the increasing content of GO component from 66±9 MPa to 292±29 MPa (Figure 5.7c). This high ultimate strength is higher than those values reported earlier for the conventional SA-LbL films. Moreover, the films fabricated here are more stretchable with significantly increased ultimate strain (Figure 5.6a). This improvement can be accredited to the effective corporation of the strong and flexible sheets and the improved stress transfer induced by the enhanced interphase zone between components. Remarkably, the maximum ultimate stress value obtained at a moderate loading of 24 vol% graphene oxide sheets is higher than

that of "nacre"-like nanocomposites with extremely high content of inorganic laminates, one of the strongest known natural nanocomposites (around 110 MPa).[335] Moreover, it is twice of that for high-performance plastics (polyethylenimine (PEI), 145 MPa) and reaches 1.5-fold of that recorded for CNT-LbL membranes with 50 wt% loading of carbon nanotubes (220 MPa). [336]

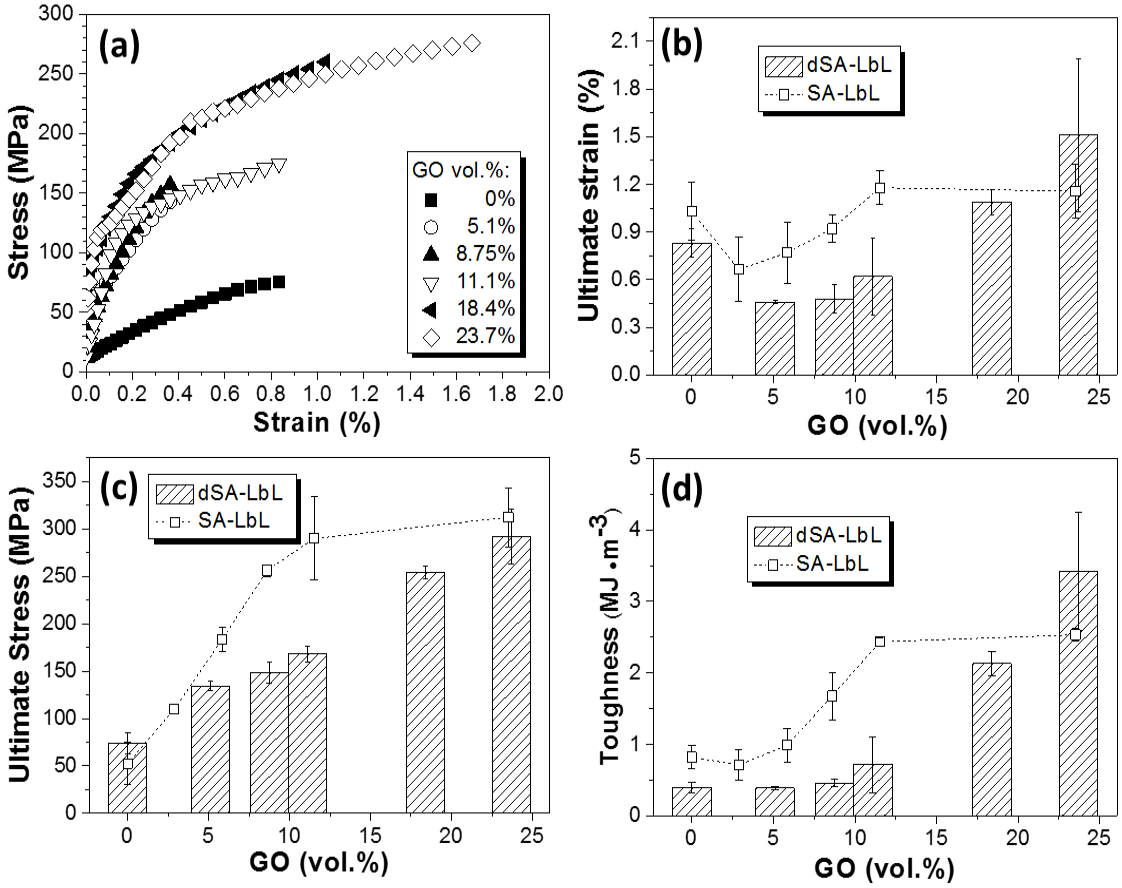

Figure 5.7 (a) Representative stress–strain curves derived from the bulging tests and (b) the ultimate strain, (c) the ultimate stress, and (d) the toughness as a function of the GO concentration for GO-SF nanocomposite membranes fabricated here as compared to the values for the conventional SA-LbL membranes (data taken from ref. 69).

An even more significant finding is that the toughness of the graphene oxide-containing nanomembranes increased exponentially up to very high value of 3.4 MJ m^{-3} at the graphene oxide content of 24%. This value is much higher than that reported for conventional SA-LbL films reported earlier (Figure 5.7d). The value recorded here is about five times higher than those reported for other reinforced LbL films containing nanoparticles and for silk-clay LbL nanocomposites. [41, 330] The increased value of the

toughness is mainly due to the combination of linearly increasing ultimate stress and the significantly improved ultimate strain at higher filler contents.

5.2.3 Fracturing behavior

Further analysis of the fractured films has been conducted with transmission electron microscopy (TEM) and scanning electron microscopy (SEM) (**Figure 5.8**). Images of fractured specimens show signs of plastic deformation of membranes before final failure. By carefully examining the morphology of the ruptured regions, we have defined two types of fracture modes. The first mode involves increased plasticity and corresponds to the yield failure mode (Figure 5.8c, e). In this mode, the edge of the fractured membrane is ragged with materials pull-outs. Significant amount of energy can be dissipated during the rupture and reconstruction of the dense and weak bonds between the graphene oxide surface and the stretched and spread silk fibroin molecules, facilitating the drastic improvement of the toughness of the dSA-LbL films fabricated here. This fracture mode is also consistent with the yielding observed in the mechanical tests, although the overall plasticity of the films is relatively low.

The second failure mode is the brittle rupture mode where the edge of the fracture is much smoother down to the nanometer scale and seldom pull-outs could be observed (Figure 5.8d). This fracture mode is formed during the crack propagation, because the smoother fracture is always observed in pairs, indicating secondary rupture event and the initiation of the ruptured front (Figure 5.8f-h). It is visible that the compliant constituent of the nanocomposite membrane, silk fibroin matrix, deforms plastically and forms bridges across the crack tip (Figure 5.8h). The circular shape of the tip of the crack demonstrates the ability of the compliant silk constituent to evenly distribute the concentrated stress at the crack tip and dissipate the tensile energy effectively due to significant plastic deformation of compliant silk matrix.

These results indicate that the combination of different deformational modes at different length scales can be associated with heterogeneous morphology with graphene oxide sheets and silk matrices behaving differently and providing complementary paths for energy dissipation during global deformation. Such a combination facilitates three-fold increase

in the ultimate strain before complete failure along with higher elastic modulus at the initial deformational stage. The increased ultimate deformation can be related to the ability undergoing a full-scale unfolding transformation of the silk backbones with a step-by-step unfolding of the soft and hard domains (tens of a nanometer) even confined in limited spacing between graphene oxide sheets.

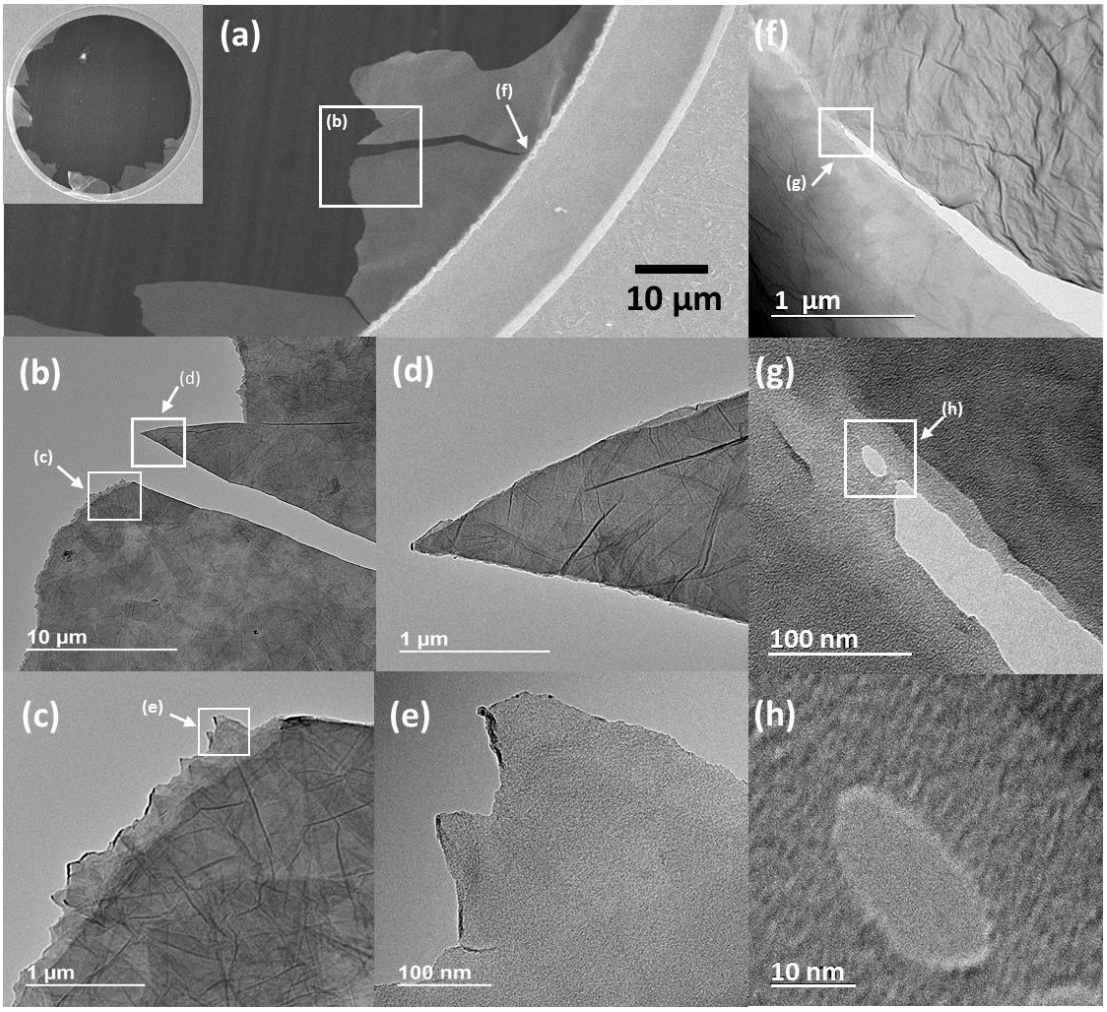

Figure 5.8 (a) The SEM image showing the broken edges of GO-SF nanomembrane. inset: the whole image of the broken membrane suspending on a 300 μm copper aperture. (b) TEM image of selected ruptured areas (framed in (a)) of the free-standing GO-SF nanomembrane. (c), (d) the TEM images of the yield failure mode and the rapid rupture mode (indicated by frames in (b)), respectively. (e) TEM image of zoomed end of the fracture edge (framed in (c)). (f) TEM images of the end of the crack (indicated by the arrow in (a)). (g) TEM images of the third failure mode (framed in (f)). (h) The higher magnification TEM images of zoomed hole (framed in (g)).

Overall, this study shows superior mechanical behavior of laminated biopolymer-GO nanocomposites fabricated here in comparison with recent literature data on similar materials. A major challenge for modern nanocomposites is the simultaneous

reinforcement of the toughness and the Young's modulus, due to the competition of strengthening mechanisms. For instance, GO-polyvinyl alcohol (PVA) drop-cast films show extremely high toughness of over 77 MJ m^{-3} owing to the very high elongation-to-break, but the ultimate stress and Young's modulus are only 62 MPa and 6 GPa, respectively.[212] Ha et al. fabricated polyimide (PI) nanocomposites films reinforced with graphene oxide and different reduced graphene oxide (rGO) sheets using a conventional solution casting method followed by thermal imidization and additional crosslinking. The incorporation of 5 wt% GO increased the tensile strength to 1.5 GPa, but their elastic modulus increased only moderately, to 36 GPa.[284] Cui et al. demonstrated high toughness rGO/poly(dopamine) (PDA) nanocomposites by dopamine cross-linking.[337] The toughness reaches 4.0±0.9 MJ m^{-3}, which is 2 times higher than that of natural nacre and about 18% higher than the value we reported in this work. However, the tensile strength is modest, around 200 MPa, and the very low elastic modulus, of 6.1 GPa, demonstrates very modest mechanical strength of these materials.[337]

Borate crosslinking of graphene oxide can significantly stiffen the resulting thin film, reaching 127 GPa of Young's modulus due to the strong and dense network of covalent bonds, but the borate crosslinked films are also extremely brittle with the toughness of only 0.12 MJ m^{-3}, limiting its practical applications.[99] Similar examples for ultrahigh Young's modulus with very low toughness can also be found in PVA/ montmorillonite (MTM) films and crosslinked GO-PEI films. [210] **Figure 5.9** summarizes the toughness and Young's modulus of the aforementioned high-performance nanocomposite materials mainly consisting of GO and other 2D nanoreinforcing materials. The extremely high Young's modulus and excellent toughness, especially the unique balancing of these two critical mechanical properties, make the GO-SF nanocomposite membranes fabricated by the dSA-LbL technique stand out.

Among silk-based nanocomposites, silk fibroin and hydrotalcite (HTlc) nanocomposites display very modest elastic modulus and ultimate stress: around 2.6 GPa and 65 MPa, respectively. [332] Moreover, the similar GO-SF laminated membranes fabricated by drop casting show the low ultimate stress below 35 MPa and elastic modulus below 1 GPa due to the plasticizing effect of the glycerol.[338]

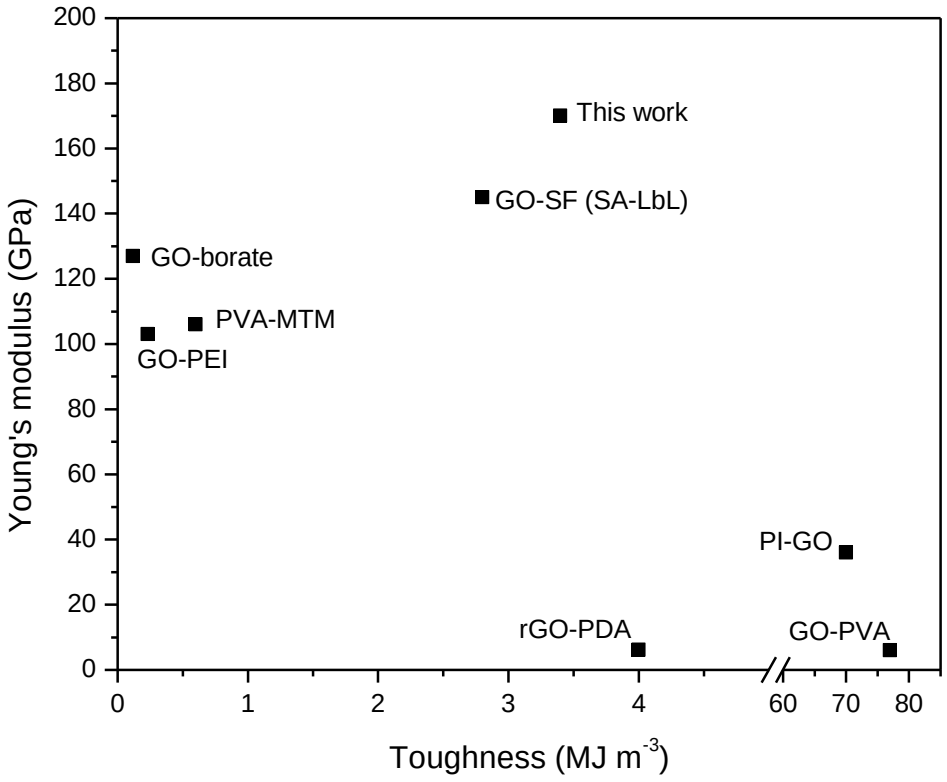

Figure 5.9 Summary of the mechanical properties of the GO based nanocomposite materials.

5.3 Conclusions

Ultrathin SF-GO nanocomposite membranes with remarkable mechanical properties were fabricated by using the novel dynamic SA-LbL assembly. Uniquely realized by the dSA-LbL, the strong interactions between stretched silk backbones and graphene oxide surface lead to effective load transfer between components with the interphase reinforcement. The silk-graphene oxide membranes with modest volume fraction of graphene oxide sheets show the elastic modulus above 170 GPa and a high toughness of 3.4 MJ m-3 due to three-fold increase in the ultimate deformation as compared to conventional LbL membranes with similar chemical composition. We suggest that the dense network of weak interactions between the individual silk fibroin chains and graphene oxide surfaces facilitates the formation of strong molecular interphase zones of confined individual silk backbones, thus, dramatically enhancing the reinforcing effect.

Chapter 6 Written-in Conductive Patterns on Robust Graphene Oxide Biopaper by Localized Electrochemical Reduction

6.1 Introduction

Although graphene-based flexible ”paper” materials[99, 134, 211, 339] made by vacuum assisted assembly have been introduced as prospective superior carbon-only replacement of inorganic-based composites with excellent mechanical properties, their further progress as protective coatings, membranes, electromagnetic shielding, and electromechanical elements is limited by several issues related to their integration in device environment.[3, 6, 41, 77, 189, 209, 217, 340, 341] Very limited options for inducing electrical conductivities and long-term stability under wet conditions are most critical issues.[69, 73, 78, 116, 208, 210, 342, 343] The epoxide, hydroxyl, carbonyl, and carboxyl groups of graphene oxide enable aqueous processibility and enhance interfacial interactions and crosslinking. The variable content of water molecules, which is a common “binder” of graphene oxide paper through hydrogen bonding, affects the reliability of mechanical performance of the graphene oxide paper.[73, 134] Moreover, graphene oxide paper is susceptible to water plasticization and easily loses its mechanical integrity in wet condition.

To tackle this challenge, many studies have focused on strengthening the graphene oxide papers by chemical crosslinking, but often resulted in compromised toughness and excessive stiffening.[210] The heterogeneous nature of surfaces of graphene oxide flakes with hydrophobic domains isolated by highly oxidized hydrophilic domains makes it difficult to apply traditional strategies for making strong layered nanocomposites with conventional organic binders and crosslinking strategies. [118, 189] Moreover, unlike “bucky paper” or other nanocomposites made from carbon nanotubes[344, 345], the integration of these graphene oxide nanocomposite films into the flexible electronic devices calls for further reduction via chemical, electrochemical, thermal, photothermal or hydrothermal routes, which usually involve harsh and toxic chemicals or intensive thermal treatments,

thus consequently damaging the structural integrity of the films and reducing their stability.[104, 106, 107, 346]

Therefore, in order to dramatically improve applicability of graphene oxide paper, we present a novel bio-inspired hierarchical approach for making much improved, robust and flexible graphene-based paper materials. [347] These papers are fabricated on a large scale (several inches across) with the use of a heterogeneous biopolymeric binder and complemented with a facile, localized, and ambient chemical reduction of graphene oxide flakes, resulting in excellent electrical conductors without compromising their mechanical stability. We suggest that the heterogeneous (hydrophilic-hydrophobic) domain-specific functionalities of silk fibroin match those random domain functionalities on the oxidized-graphitic heterogeneous surfaces of graphene oxide flakes, making silk fibroin a natural "universal" binder. [348] Moreover, in contrast to many other chemical binders, silk fibroin is mechanically strong, optically transparent, biocompatible, biodegradable, completely bio-renewable, and can serve as an additional reducing agent.[5, 50, 349, 350]

The materials design proposed here facilitates the outstanding mechanical properties, which include 300 MPa strength, 26 GPa elastic modulus, 2.8 MJ m^{-3} toughness, and around 2% ultimate strain, to well exceed most of those reported in literatures for graphene-based papers. Surprisingly, we found that the aluminum foil in direct contact with the paper can spontaneously and locally reduce graphene oxide flakes in ambient conditions. Such a readily controlled and "green" treatment combined with the ability of both surface area and depth selective electrochemical reduction creates electrically conductive paper materials with excellent 1350 S m^{-1} in-plane electrical conductivity without compromising the initial mechanical stability.

6.2 Results and discussion

6.2.1 The bio-bonded graphene oxide paper

Vacuum-assisted filtration was used to fabricate layered "paper" from the homogeneous mixture of graphene oxide and silk fibroin similar to literature but with special efforts to

prevent fast coagulation of biopolymer solution (see Methods). [88, 99, 134, 210] The resulting 2D stacking of the graphene oxide flakes within several-micron-thick freestanding paper is presented in **Figure 6.1**a. The root-mean-square surface roughness is 0.30±0.06 μm per 100 μm^2 square area for the as prepared paper, indicating their uniformity (below 4% variation in thickness) (Figure 6.1b). The incorporation of silk fibroin in the stacks of graphene oxide flakes is confirmed quantitatively by X-ray photoelectron spectroscopy (XPS), which shows the silk fibroin added in the mixture is effectively bonded to the graphene oxide flakes and retained in the final films (**Table 6.1**). The interlayer spacing of the pure film as measured from (001) peak of the X-ray diffraction (XRD) data is 0.81 nm,

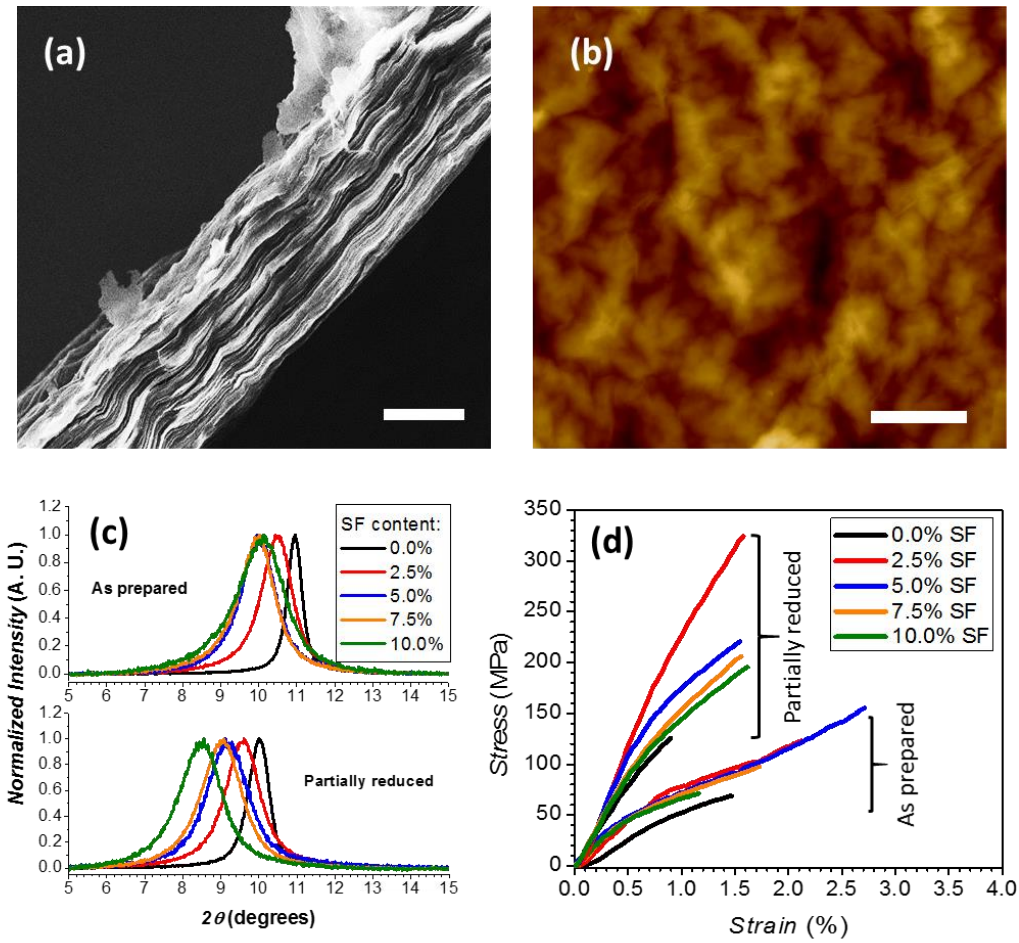

Figure 6.1 Morphologies of the graphene oxide-silk fibroin films: (a) SEM micrograph (scale bar: 5 μm) of the fractured cross section of the silk fibroin intercalated graphene oxide film, fine layered structure with mild wrinkling is observed. (b) AFM micrograph of the surfaces of the nanocomposite films before reduction (scale bar: 20 μm, z-range: 6 μm). (c) XRD data for the graphene oxide nanocomposite films with various silk fibroin contents before and after electrochemical reduction. (d) Representative stress-strain curves of the nanocomposite biopaper before and after partial reduction.

which is close to the common interlayer spacing of graphene oxide papers.[38, 351] Addition of small quantity of silk fibroin (below 10%) results in gradual increase in the interlayer spacing to 0.89 nm, which indicates the uniform intercalation of silk fibroin molecules (Figure 6.1c upper part). The width of the peaks also progressively increases, indicating fewer stacking layers of the graphene oxide flakes from 24 for pure graphene oxide paper to around 10 for higher silk content due to the intercalation of silk fibroin and flakes mis-stacking (Table 6.1). It is worth noting that the overall content of silk binder within paper calculated from XPS and XRD data is close to the initial silk content in solution (except highest 10%) which indicates effective intercalation of silk macromolecules for modest (below 7%) silk concentrations.

Table 6.1 The content analysis of the graphene oxide nanocomposite films.

			As prepared				Partially reduced				
No.	**Nominal GO content (wt%)**	**Nominal SF content (wt%)**	**Actual SF content (XPS)[a] (wt%)**	**Actual SF content (XRD)[b] (wt%)**	**C/O ratio of GO[c]**	**GO stacking (layers)[d]**	**Actual SF content (wt%)**	**Actual SF content (XRD) (wt%)**	**C/O ratio of GO**	**GO stacking (layers)**	**Al^{3+} (wt%)**
1	100.0	0.0	0.0	n/a	2.27	23.7	0.0	n/a	3.71	16.6	9.9
2	97.5	2.5	3.0	2.7	2.20	10.6	2.4	2.7	3.20	9.7	9.7
3	95.0	5.0	5.4	5.2	2.13	9.8	5.7	4.8	3.54	8.9	8.9
4	92.5	7.5	8.3	5.6	2.07	9.1	7.6	5.8	3.66	8.6	8.3
5	90.0	10.0	12.7	5.1	2.06	7.1	12.3	9.4	3.44	8.0	9.3

[a] Determined from the content of nitrogen (elemental ratio C:O:N =52:24:24 in SF).
[b] Determined from the increase of the interlayer spacings by assuming the densities of the components are the same as their bulk states.
[c] Contributions from the intercalated silk fibroin are excluded.
[d] Calculated from the Scherrer equation by taking shape factor $K = 0.9$, system broadening factor $\beta = 6\text{x}10^{-4}$ rad.

The mechanical properties of these as prepared pure graphene oxide paper with the elastic modulus value of 7 GPa and ultimate strength of 60 MPa are on par with literature data (**Figure 6.2** black columns).[73] Ruoff *et al.* fabricated stronger but stiffer graphene oxide paper, which is probably due to annealing process and different environment humidity.[134] Adding silk binder results in dramatic increase of mechanical properties: the ultimate stress,

ultimate strain, elastic modulus, and toughness reach 153 MPa, 2.8%, 13 GPa, and 2.6 MJ m^{-3} at 5% silk fibroin, respectively, which are correspondingly 125%, 90%, 105%, and 330% higher than those of the pure graphene oxide paper. The mechanical properties of the graphene oxide papers with silk binder are comparable to those reported by Huang et al., who fabricated similar films using drop casting technique after homogenizing the gelled mixture by intense sonication[343].

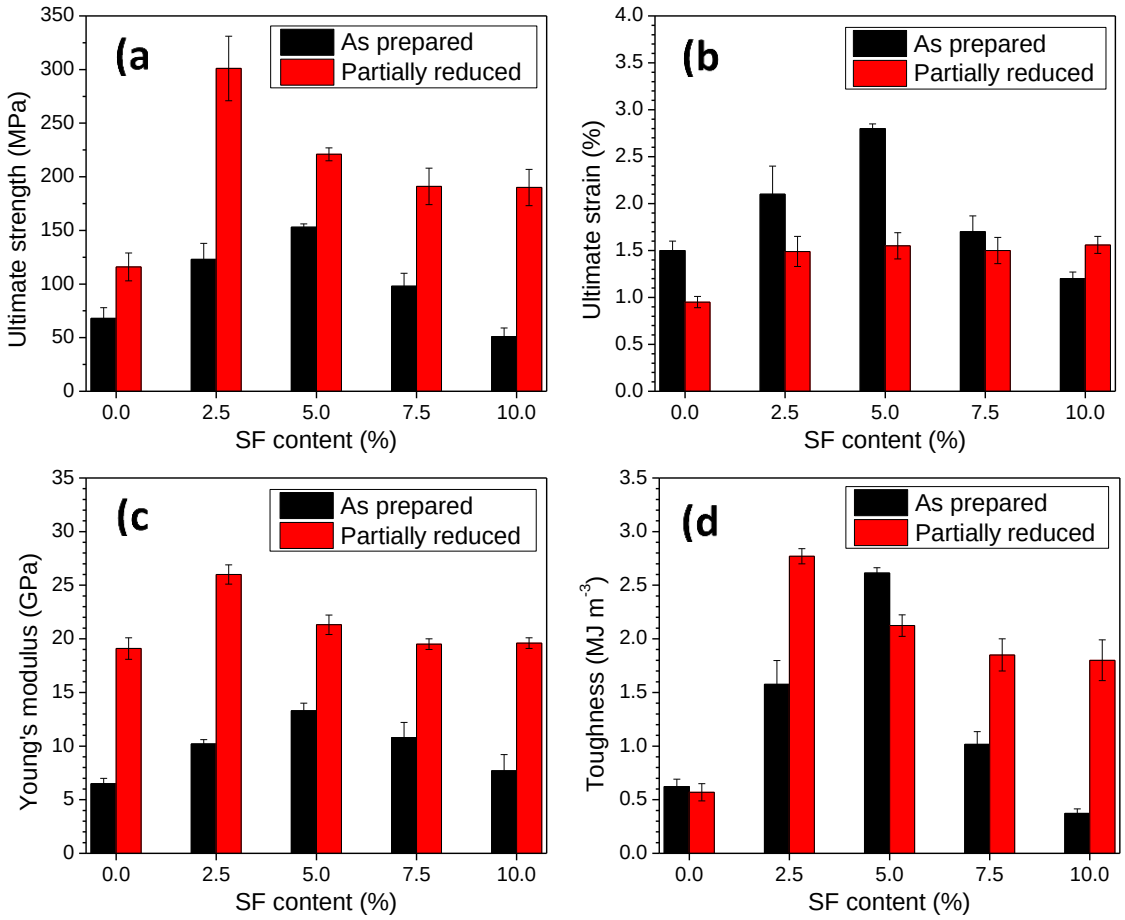

Figure 6.2 Mechanical properties of the graphene oxide nanocomposite films with various silk fibroin contents before and after electrochemical reduction. Panels (a), (b), (c), and (d) are ultimate stress, ultimate strain, elastic modulus, and toughness versus silk fibroin content, respectively.

6.2.2 The metal reduction of graphene oxide

In order to further improve mechanical performance and induce electrical conductivity we exploited aluminum initiated chemical reduction, which is known for producing reduced graphene oxide powders rather than structured films.[106] The effective chemical reduction of graphene oxide by direct physical contact with aluminum foil is first spectacularly

reflected by the alternation in color (dark brown to grey) and the appearance of metallic luster of the films (**Figure 6.3**a & b). The change in color and enhanced luster of initial

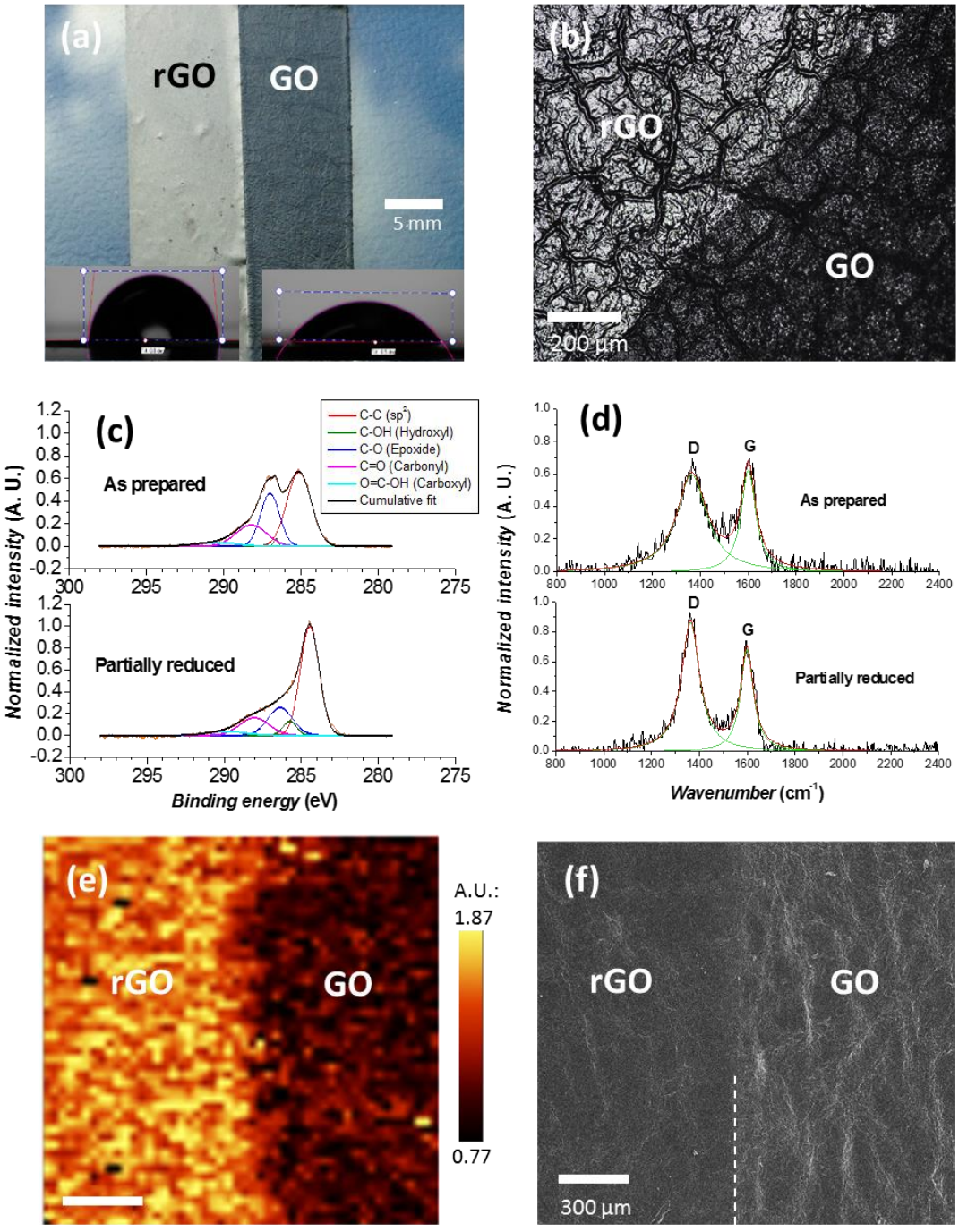

Figure 6.3 Microstamping of graphene oxide biopaper: (a) Micrographs (scale bar: 5 mm) of two strips along with contact angle measurements before (right) and after (left) reduction. (b) Reflective optical micrograph (scale bar: 200 µm) showing the border of the partially reduced region. XPS C1s high resolution spectra (c), and Raman spectra (d) before and after selective reduction; Raman mapping (e) (scale bar: 20 µm) of the ID/IG ratio and SEM image (f) (scale bar: 300 µm) of the border between the reduced and the non-reduced regions.

black paper suggests the narrowing down of the band gap of this material, which in turn indicates the reconstruction of the sp^2 hybridization chemical structures.[102] In addition, the contact angle of the film increased from 51^o to 81^o, showing a significant increase in hydrophobicity as expected for surfaces with increase graphitization. The increased hydrophobicity is also favorable for resisting water damage, which is a common problem for pristine graphene oxide papers. It is also worth noting that the surface roughness of the reduced nanocomposite films is not changed as compared to the as prepared samples (Figure 6.1b).

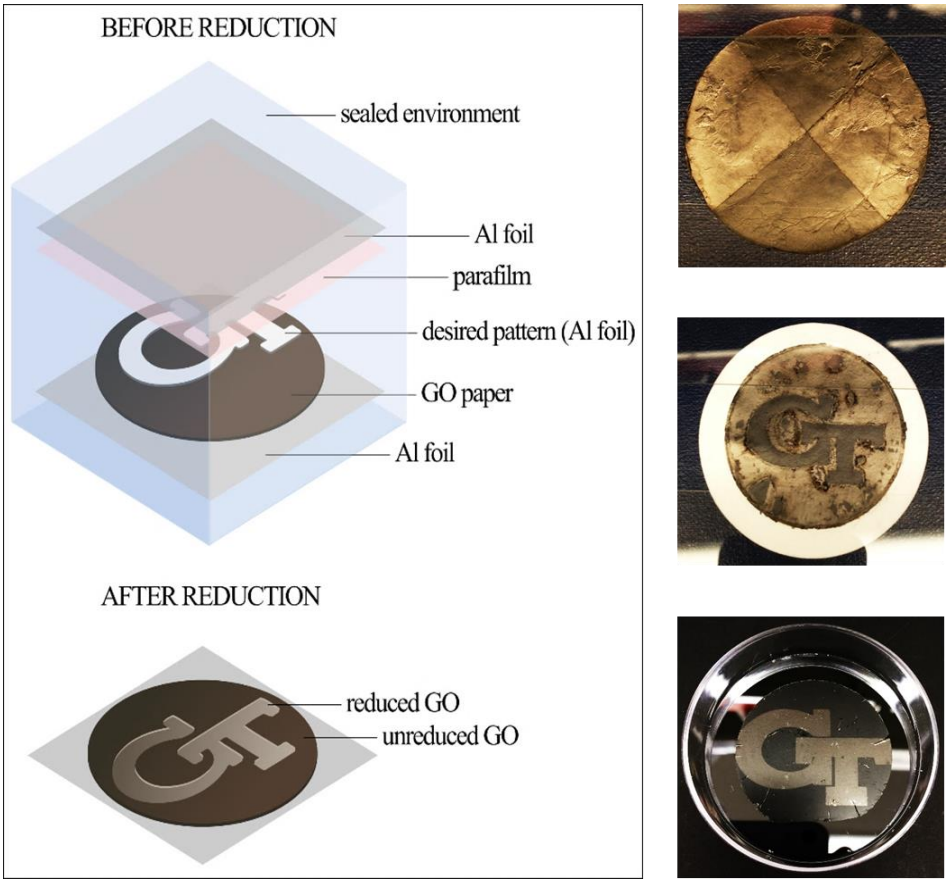

Figure 6.4 The reduction setup using electrochemical microstamping method. The resulting patterned graphene oxide biopaper specimens are shown on the right (from top to bottom): checker pattern (freestanding paper), GT logo with the background reduced (on filter paper, submerged in water), and GT logo with GT letters reduced (transferred to silicon wafer). The reduced areas have metallic luster and are light grey in color. The diameter of the specimens is around 40 mm.

Moreover, the chemically modified surface areas can be readily patterned with high selectivity by applying properly shaped aluminum foil under ambient conditions, demonstrating highly localized nature of the chemical reduction process (**Figure 6.4**). Such

contact-controlled patterning is feasible with sharp edges and micro-scale lateral resolution below 10 μm for manually cut foil patterns (Figure 6.4), which is potentially comparable to traditional labor-consuming techniques such as photolithography or laser etching[352].

Significant changes in chemical functionality of graphene oxide flakes are further confirmed by XPS, XRD, energy-dispersive X-ray (EDX) analysis, and Raman spectroscopy (Figure 6.3). Indeed, the C/O ratio increased from 2.2 to 3.5, indicating effective removal of the oxygen-containing functionalities. [102] The presence of 9 wt.% Al^{3+} is also identified independently by XPS and EDX. The aluminum ions are distributed in interior space of the films as can be concluded from the increase of the interlayer spacing by 0.11±0.04 nm, which is consistent with intercalation of partially complete monolayer ions (Figure 6.1c). [342] High resolution XPS C1s scan shows that the relative intensity of the epoxide group decreased by 29%, and that of the graphitic carbon increased by 19% after the reduction, which is a clear sign of the effective removal of oxidized chemical groups and the restoration of the conducting sp^2 hybridized carbon (Figure 6.3c).[116] Finally, Raman spectra show the width of the D band decreases and the I_D/I_G ratio increases from 0.96 to 1.27, which is another recognized sign of the homogenization of the sp^3 carbons due to the removal of oxygen-caused defects, which is also occurred in highly localized manner (Figure 6.3d).[108]

Considering these results, we can suggest that these changes of chemical functionality are due to the presence of aluminum, which is an active reducing metal with a standard reduction potential (E^0_{Al}) of -1.66 V.[106] Aluminum can reduce other materials with a standard reduction potential higher than E^0_{Al} including graphene oxide (e.g. E^0_{GO} = 0±0.6 V depending on oxidization state[106, 353, 354]) according to the following electrochemical path[355]:

$$Al \rightarrow Al^{3+} + 3e^-;\ E^0_{Al} = -1.66V \qquad (6.1)$$

$$a \cdot GO + b \cdot H^+ + b \cdot e^- \rightarrow a \cdot rGO + \frac{b}{2} \cdot H_2O;\ E^0_{GO} \approx 0 \pm 0.6\,V \qquad (6.2)$$

It is important to note that although acidic conditions facilitate the efficient reduction of graphene oxide, the chemical reaction can be conducted in neutral condition at pH = 7±0.4 and room temperature.[355]

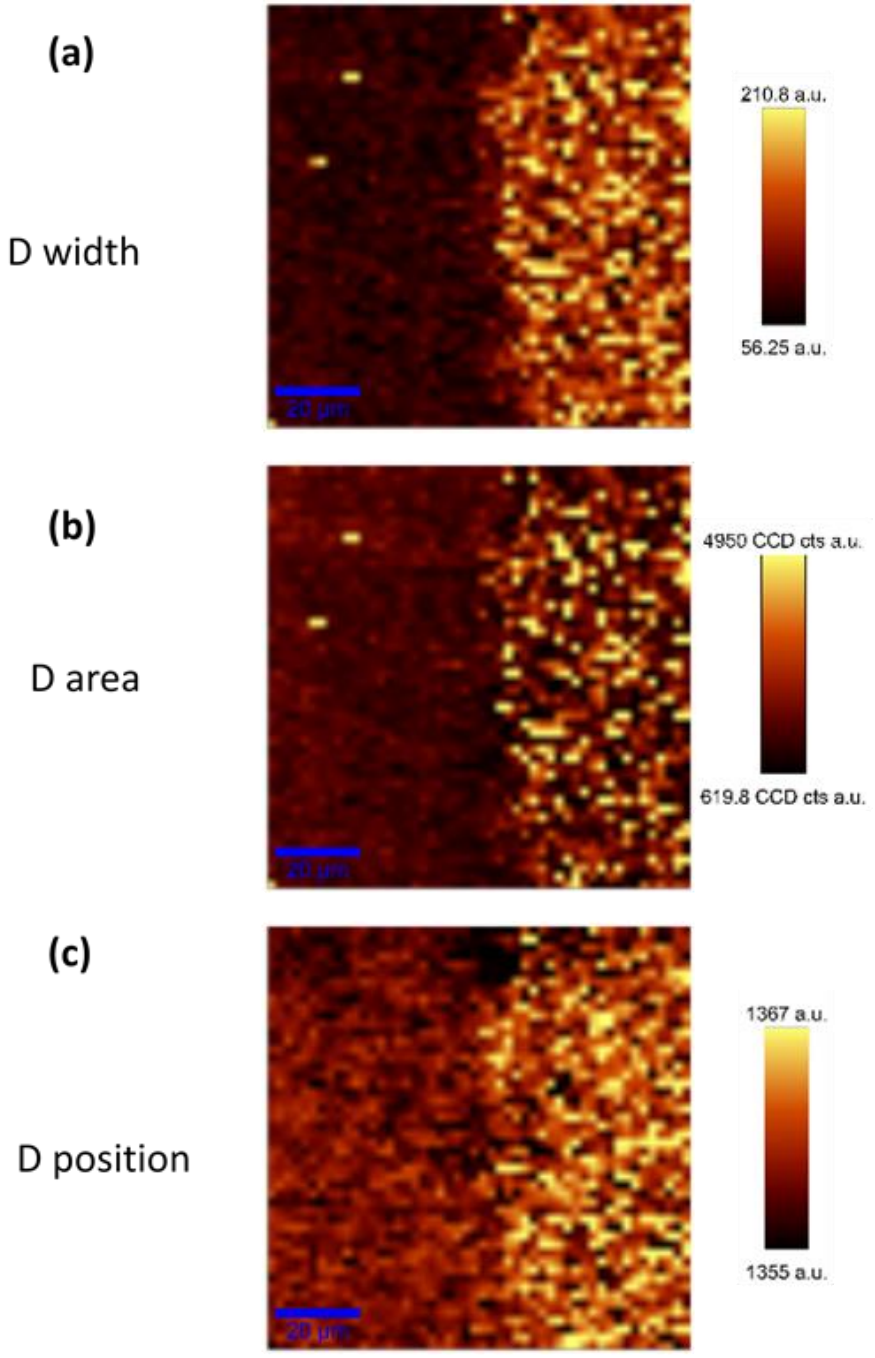

Figure 6.5 The Raman mapping of the patterned partially reduced graphene oxide nanocomposite film: (a) D band width, (b) D band area, and (c) D band position.

Indeed, Raman mapping reveals very narrow microscopic transitional zone between pristine and transformed surface regions similar to that observed in optical microscopies and SEM of surfaces (**Figure 6.5**). Moreover, depth-distribution of the transformed interior volume obtained with SEM on fractured region confirms gradual progression of the reaction from the surface to the interior (**Figure 6.6**a-c). Darker regions in proximity to the surface being in contact with aluminum foil correspond to more conductive, transformed paper sub-surface regions while brighter regions indicate high surface charges on pristine

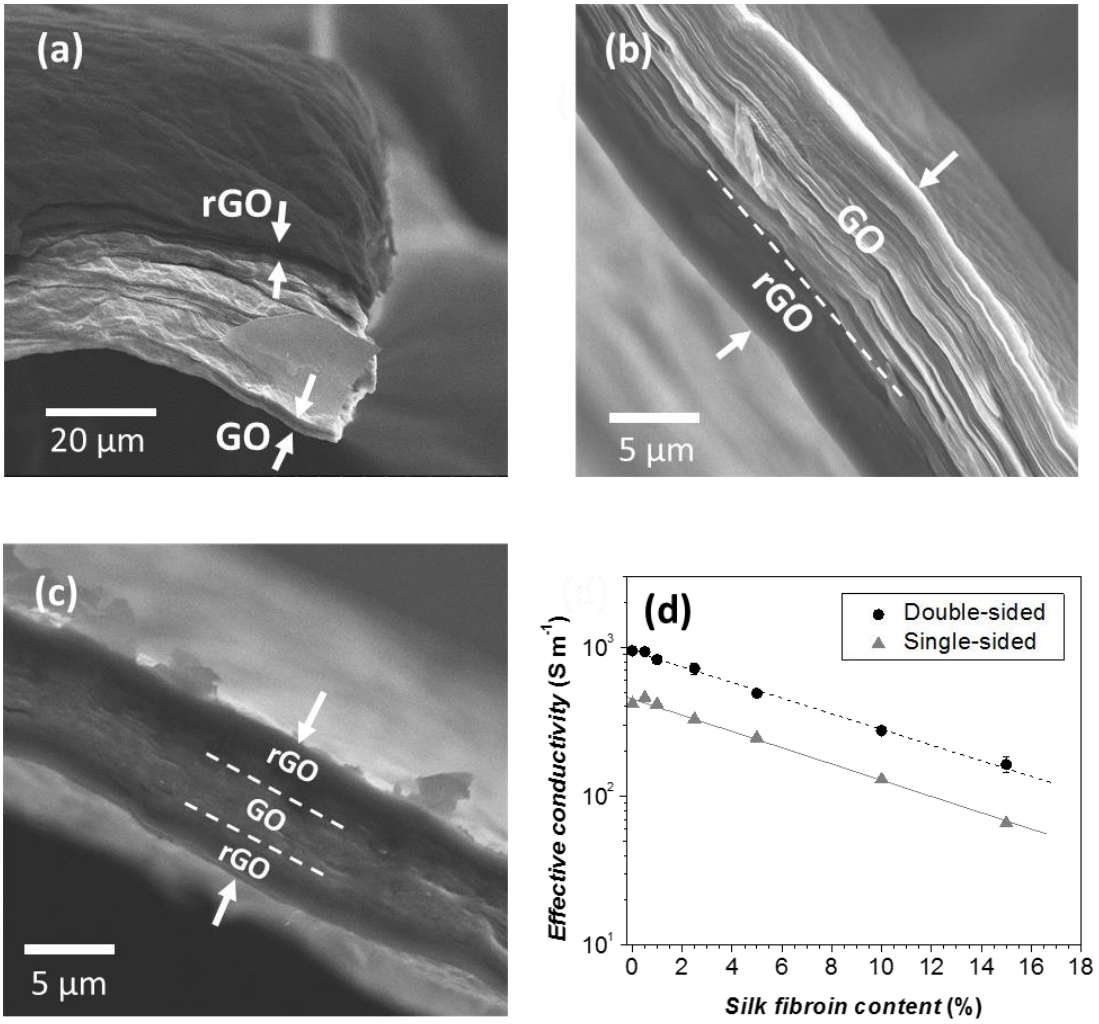

Figure 6.6 SEM micrographs of the partially reduced graphene oxide biopaper and their electrical conductivity. (a) SEM micrograph (scale bar: 20 µm) of a fractured biopaper with the reduced top layer (dark) and the pristine non-reduced bottom layers (bright). The cross sections of (b) bottom surface reduced, and (c) both surfaces reduced (scale bar: 5 µm). The white arrows indicate the thicknesses of the biopaper. (d) The electrical conductivities of the uniformly reduced graphene oxide biopaper with various contents of silk fibroin. Data points for the single-sided samples corresponding to the scenario in (b), and those for the double-sided samples corresponding to the scenario in (c).

graphene oxide dominated material, which is similar to that observed for surface charging distribution. Stopping electrochemical reaction at certain time resulted in conversion only to certain depth as controlled by electronic connectivity of the graphene oxide to the aluminum metal as in the primary batteries (Figure 6.6b & c). Placing aluminum foils on both surfaces of the film makes concurrent propagation of electrochemical transformation from both surfaces and results in virtually complete interior transformation twice faster.

6.2.3 The electrical properties of the reduced bio-bond graphene oxide paper

In fact, as a result of this electrochemical reaction at ambient conditions we observed excellent conductivity of the transformed paper, which reaches 1350 S m^{-1} for completely transformed paper with 2.5% of silk binder (**Figure 6.7**). This value is comparable to the values of 1700-2100 S m^{-1} of the graphene oxide papers reduced by traditional harsh

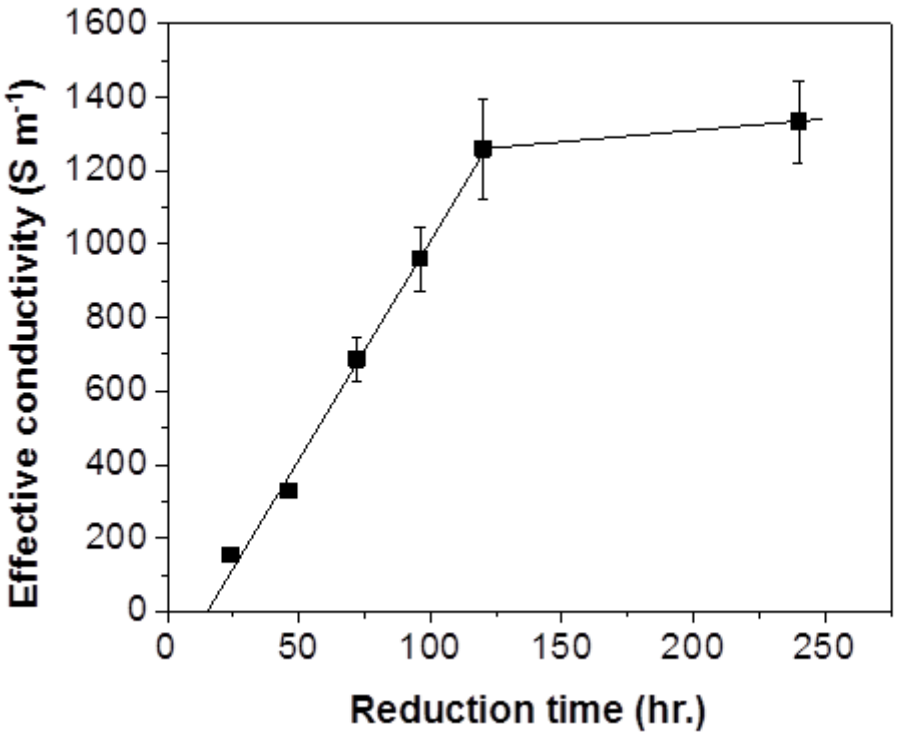

Figure 6.7 The linear increase of effective conductivity of the 5-µm thick graphene oxide nanocomposite films with 2.5 wt% silk fibroin for the first 120 hours of reduction, and then the effective conductivity saturates at around 1300 S m^{-1}. This result demonstrates the steady progress of the reduction through thickness with the intercalation of silk fibroin in the film, and 120 hours is the critical reduction time for the complete through thickness reduction of a 5-µm thick film. The reduction rate is estimated to be around 25 nm $hr.^{-1}$ per surface.

methods.[106, 356] The effective conductivity of the single-side treated film is exactly half of the double-side treated film, which suggests the critical role of the reduction depth propagation in material transformation (Figure 6.4d). We suggest that adding insulating binder (i.e. silk fibroin) results in fast reduction of the film conductivity due to the interruption of the propagation path for electrons by the presence of the aggregated silk and catastrophic defects in flake stacking (Figure 6.6d).

It is critically important that the paper after chemical transformation by our "green" technique improved its mechanical properties, in striking contrast to the current reduction techniques that involve harsh chemical or thermal treatments and inevitably damage the polymeric components (Figure 6.2 red columns). The ultimate strength of the transformed films reaches very high value of 300 MPa at low silk content, which results also in the highest toughness of 2.8 MJ m^{-3} among all the samples tested in this study. The elastic modulus of the reduced pure graphene oxide film increased almost three-fold due to defect reduction and the Al ion doping. [342] Manifold increase in the mechanical strength may be also supported by additional crosslinking and reducing ability of silk backbones. [330]

The mechanical properties of the reduced graphene oxide-silk fibroin biopapers observed here are among the best of the traditional layered graphene-based papers reported to date.[3, 116, 189, 342, 343] For example, drop casted graphene oxide-silk fibroin films have comparable ultimate strain at 1.8% but much lower tensile strength and elastic modulus[343]. A graphene oxide-polyvinyl alcohol (PVA) film that has been reduced by hydroiodic acid (HI) possesses much lower strength and modulus.[73, 217] Chemically crosslinked graphene oxide (polydopamine)-polyethyleneimine (PEI) films exhibit extremely high elastic modulus up to 103 GPa but much lower tensile strength of 210 MPa and 0.2% strain-to-failure, which is a common problem for chemically crosslinked brittle graphene paper. [210]

6.3 Conclusions

We demonstrated that the extremely mechanically strong, flexible, and tough graphene oxide-based "paper" can be readily prepared with one-step facile approach by applying

natural polymer binder, silk fibroin, which outperforms classical nacre composed of laminated aragonite (an inorganic mineral) and small amount of protein binder with toughness of 1.0 MJ m^{-3}. Furthermore, this paper can effectively and selectively reduced by localized presence of aluminum under neutral aqueous conditions and at room temperature to highly conductive graphene paper not only just without compromising their mechanical integrity, but also further improving mechanical performance and making them stable in aqueous environment.

Chapter 7 Tuning the Electronic Properties of Robust Bio-Bond Graphene Papers by Spontaneous Electrochemical Reduction: from Insulators to Flexible Semi-Metals

7.1 Introduction

As known, removal of the oxygenated groups and restoration of the electrical conductivity of graphene oxide can be realized by using a so-called "reduction" procedure. [103, 106, 107, 357] This process is generally conducted by using chemical or thermal treatments such as photon-induced thermal energy,[107] hydraulic pressure,[223] harsh reducing agents,[116, 358] or the combination of these techniques.[359] For example, reduced graphene oxide paper annealed at 220 ºC for 1 hour show electrical conductivity up to 1.0 x 10^4 S/m.[208] Treatment at high temperature (up to 2850 ºC) results in mechanical and electrical properties close to those of pristine graphene.[102, 360] However, this high-energy consuming process damages other components that are sensitive to heat, *e.g.*, crosslinkers or functional dopants. On the other hand, hydrazine and concentrated hydroiodic acid are volatile and highly toxic, posing environmental and health-related concerns for industrial productions.[102] Recently, electrochemical reduction of graphene oxide has been employed for the restoration of electrical properties of graphene oxide in various energy storage and transport applications.[361, 362] These electrochemical reduction techniques adopted from conventional electrochemical cells provide an excellent alternative route to energy-efficiently reduce graphene oxide in layer-by-layer thin films, but an external energy source is still required and the selectivity of the reduced areas is hard to achieve.

As has been demonstrated earlier, mechanically strong and moisture-resistant bio-bond graphene oxide paper can be fabricated by using silk fibroin (SF) as an efficient multifunctional binder.[186, 330, 348] And a new spontaneous electrochemical "write-in" technique allowed to selectively pattern the bio-bond graphene oxide paper with conductive paths.[109] When compared to the other pattern-enabled reduction techniques,

e.g., laser writing or "light scribing,"[107] the metal-assisted reduction technique is capable of large-area patterning, energy efficient, and preserves the outstanding mechanical properties of the graphene papers.[311] However, the electrical conductivity of the reduced graphene paper materials fabricated by the original metal-assisted reduction technique is relatively low (usually not exceeding 10^2 - 10^3 S/m), and the extent of the reduction is difficult to control due to the very low reduction rate.

We demonstrate the full control of the electrical conductivity of graphene oxide based papers, which were mechanically strengthened by a small amount of silk fibroin, over orders of magnitude by depth-controlled spontaneous electrochemical reduction at ambient conditions (aqueous environment and room temperature). The steady progression of the reduced layer and the spontaneous diffusion of the oxygen containing moieties allow for the realization of high electrical conductivity up to 1.5 x 10^4 S/m and reduced surface work function from 4.9 to 4.2 eV all across large area flexible and mechanically robust materials (>100 cm^2). To the best of our knowledge, this is the first systemic study of the environmental-aware graphene oxide reduction technique. And it demonstrates high versatility in real-world applications by controlling the electrical conductivity over orders of magnitude and significantly shifting the work function of this robust and flexible electronic material.

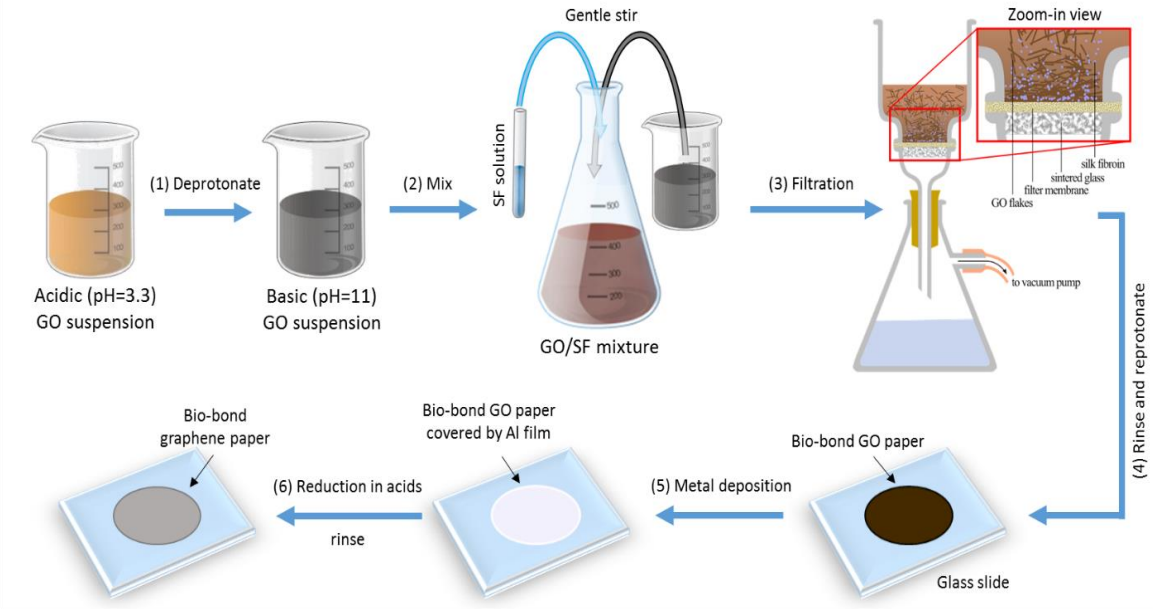

Scheme 7.1 The fabrication and reduction of the bio-bond graphene paper explored in this study.

7.2 Results and Discussion

7.2.1 Fabrication and morphologies of the bio-bond graphene oxide papers

We employed vacuum-assisted filtration (VAF) technique to assemble the graphene oxide flakes into paper-like films as demonstrated in **Scheme 7.1**.[134] Silk fibroin was mixed with the graphene oxide suspension to strengthen the resulting paper by physically binding the layers of the flakes. Graphene oxide flakes with lateral sizes between 2 µm and 20 µm and thickness around 0.9 nm were utilized for this assembly (**Figure 7.1**a & b). X-ray photoelectron spectroscopy (XPS) shows predominant carbon and oxygen peaks and no other peaks related to external contaminations (Figure 7.1c). Quantitative peak deconvolution of the XPS survey renders a 2.2 : 1 atomic ratio for carbon and oxygen elements which is consistent with the reported values.[109] The Raman spectrum shows a

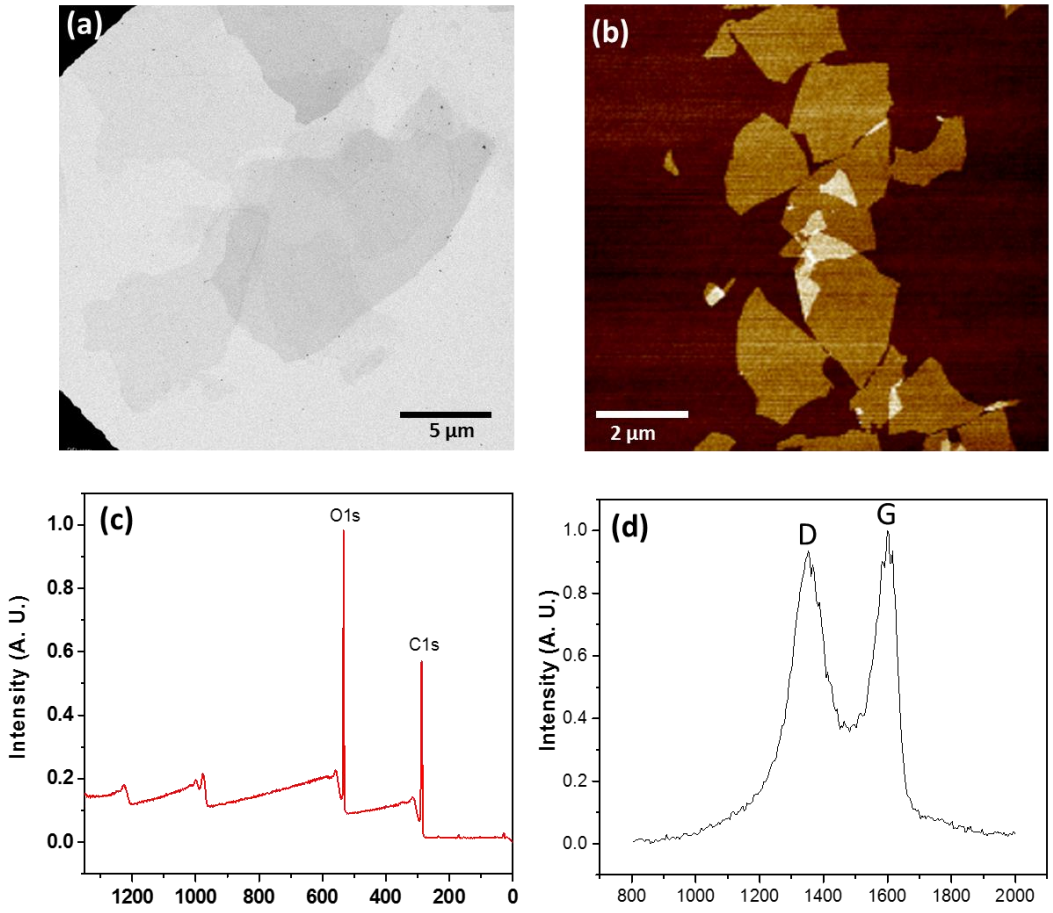

Figure 7.1 Quality characterization of the graphene oxide flakes: (a) TEM and (b) AFM (z-scale: 3.5 nm) micrographs of the graphene oxide flakes. (c) XPS survey scan of the graphene oxide. (d) Raman spectrum of the graphene oxide showing distinct D and G bands.

strong D band, which represents the oxygenated "defects" in the sp^2 hybridized basal plane (Figure 7.1d). Based on the I_D/I_G ratio, the size of the graphitic domains can be estimated to be around 7 nm, which is characteristic for amphiphilic surfaces.[363]

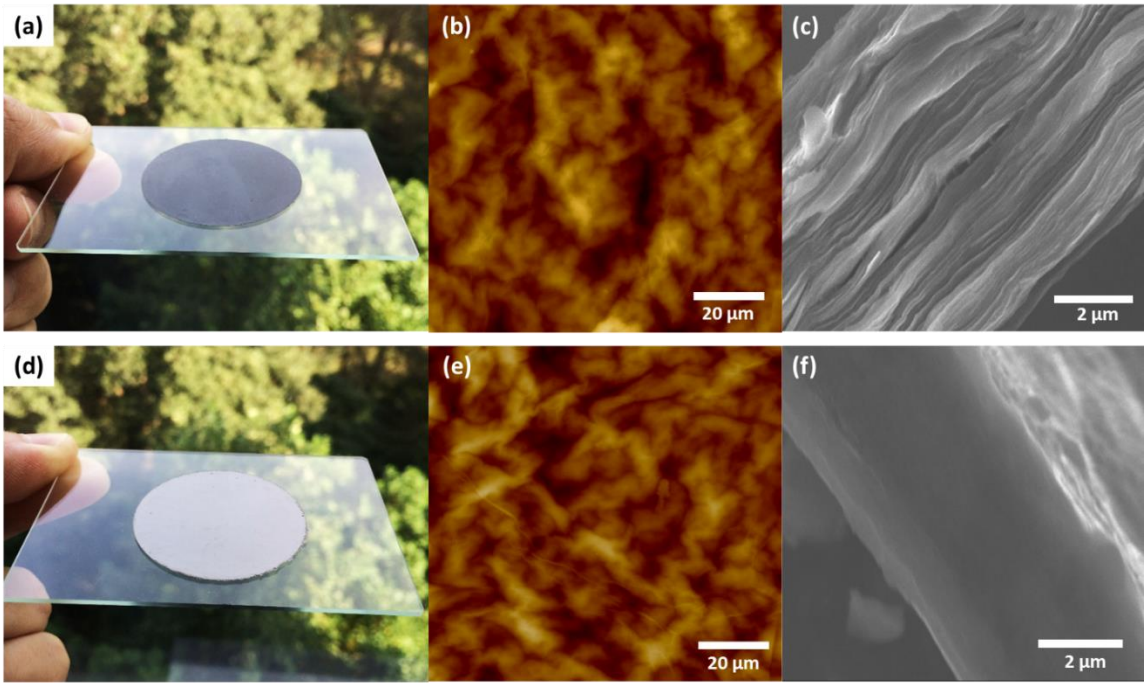

Figure 7.2 Morphologies of the bio-bond graphene paper before (top row) and after (bottom row) reduction. (a) and (d): optical photographs, (b) and (e): AFM topographies (z-scale: 6 µm), and (c) and (f): SEM cross sections of the graphene (oxide) papers that are pulled apart to reveal the embedded microstructures.

Then we applied the metal-assisted spontaneous electrochemical reduction to restore the electronic properties of the bio-bond graphene oxide paper (details in the Experimental section). Simply, a 500 nm layer of aluminum was deposited on the the paper, and then diluted hydrochloric acid was dropped on top of the metal covered paper to initiate the reaction. Finally, the unreacted metal debris were carefully washed by Nanopure water. The appearance of the bio-bond graphene paper after reduction is metallic grey in contrast to matte dark brown of the initial paper, suggesting dramatic change in electronic band structures (**Figure 7.2**a, d). The surface morphology is not affected by the reduction procedure as characterized by atomic force microscopy (AFM) (Figure 7.2b, e), where the root-mean-square roughness is about 600 nm in a selected surface area of 1x1 μm^2 for both cases. However, when observed using scanning electron microscopy (SEM), the morphology of the paper cross sections before and after reduction is distinctly different

(Figure 7.2c, f). Smoother sections of the fully reduced bio-bond graphene paper indicate reduced surface charging, characteristic of conductive materials.

7.2.2 Tuning electrical properties by polymeric binders

Here, we use the effective conductivity, which is the conductivity averaged over the whole bio-bond graphene paper as a uniform conducting material, for direct comparison across the reported results (**Figure 7.3**). As was observed, the effective conductivity decreases exponentially with the increase of the content of the bio-binder (silk fibroin) from 0.5 to 5 wt%. After the 2-hour partial reduction, the effective conductivity for the samples decreases by more than 20 folds from 350 S/m for the ones made of pure graphene oxide to 14 S/m for the sample with 5 wt% of silk fibroin. It is worth noting that the electrical conductivity of the samples of the same composition is much higher in this study because the accelerated reduction and effective removal of the oxygen containing moieties under

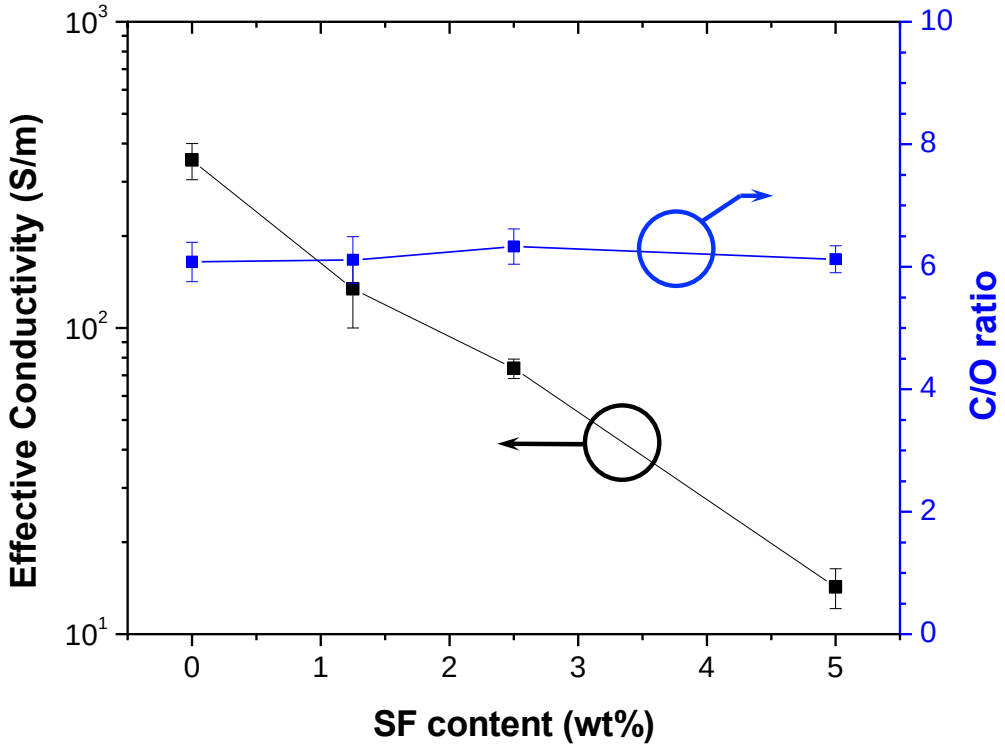

Figure 7.3 The electrical conductivity and the C/O ratio of the reduced graphene oxide measured from the 15 μm thick bio-bond graphene paper reduced at pH=0 for 2 hours for different silk contents. The C/O ratios of the reduced graphene oxide are post-corrected by subtracting the elemental contributions from the silk constituents.

acidic conditions (pH=0) (see below) in contrast to neutral conditions previously reported. Meanwhile, the level of reduction of the graphene oxide is not hindered by the addition of the silk fibroin binders as revealed by the constant C/O ratio of the bio-bond graphene papers with various silk fibroin content, indicating undisrupted network of the graphene oxide flakes (Figure 7.3). The C/O ratio of the samples is stable at around 6.2 as detected by XPS after subtracting the elemental contributions of silk in the composite paper.

7.2.3 The effect of reducing pH to the electrical and electronic properties

During electrochemical reduction, the aluminum surface is oxidized into water dissolvable high valence states and the graphene oxide close to the metal layer accepts the electrons from the metal (see more discussion below).[355] Under the standard reaction condition (pH=0), the graphene oxide gets reduced following the electrochemical redox route:[353]

$$Al \rightarrow Al^{3+} + 3e^{-};\ E^{0}_{Al} = -1.66V \qquad (7.1)$$

$$a \cdot GO + b \cdot H^{+} + b \cdot e^{-} \rightarrow a \cdot rGO + \frac{b}{2} \cdot H_2O;\ E^{0}_{GO} \approx -0.6\,V \qquad (7.2)$$

The difference between the standard reduction potentials (E^0) of aluminum and graphene oxide is around 1.0 V, which is large enough to drive an effective electrochemical reaction. Here, we have also investigated the effect of the concentration of protons (i.e., pH) on the extent of the reduction since protons are a reactant participating in the second half-reaction to reduce graphene oxide (Eq. 7.2). By keeping the reduction time and the content of the silk fibroin constant, we varied the acidity of the reduction environment (the HCl concentration varied from 10^{-5} to 10^{+1} M). It is worth noting that the actual pH of the 10^{+1} M hydrochloric acid has diverted from the negative logarithm of the concentration of the protons (i.e. $-log_{10}[H^+]$) due to the increased activity of the concentrated protons, but we still use pH=-1 to denote the environment of the 10^{+1} M HCl during the reaction for the sake of simplicity and consistency.

As shown in the high-resolution C1s electron orbital binding energy spectra of XPS, the peak around 286.2 eV that corresponds to the epoxy groups of the graphene oxide is noticeably stronger at higher pH reduction environment (**Figure 7.4**a).[364] This is caused

by the fact that with pH increased from the standard condition (pH=0), the difference of the reduction potentials (E) between aluminum and graphene oxide decreases due to the decrease of the reduction potential of graphene oxide according to the Nernst equation:[355]

$$E_{GO} = E_{GO}^{0} + \frac{RT}{F} ln[H^{+}] \qquad (7.3)$$

where R is the ideal gas constant, T is the absolute temperature, and F is the Faraday constant. For example, the gap between the reduction potentials of aluminum and graphene oxide is about 0.6 V in neutral condition (pH=7), which is 40% smaller as compared to that of the standard condition (1.0 eV at pH=0). Therefore, the increase of pH during the reduction effectively shifts the thermodynamics of the reaction to the less favorable end

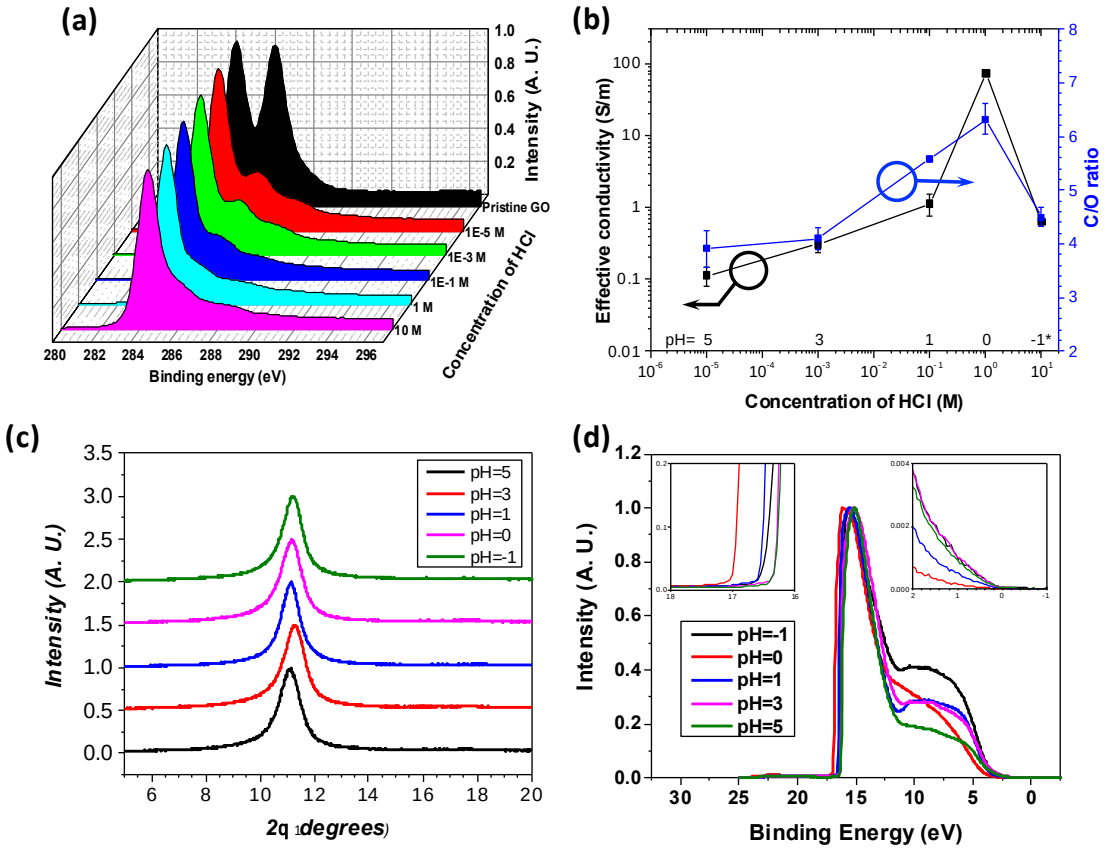

Figure 7.4 Bio-bond graphene paper with 2.5 wt% silk fibroin reduced for 2 hours under various pH environments: (a) XPS C1s spectra of the top reduced surfaces, (b) electrical conductivity and C/O ratio of the top reduced surfaces, (c) XRD data, and (d) UPS spectra of the top reduced surfaces for the measurement of work functions (insets: the zoom-in views of the starting and the ending part of the UPS spectra).

that affects the removal of the oxygen containing moieties. In addition, the reaction rate is also affected by the lower concentration of protons according to the rate law (see Eq. 7.2), slowing down the removal of the oxygen containing species.

As known, the removal of the epoxy groups greatly facilitates the restoration of the electric conductivity of the reduced graphene oxide.[365] Therefore, we can suggest that the effective conductivity of the reduced bio-bond graphene paper should increase with larger reduction potential gaps between aluminum and graphene oxide, which is promoted by lower pH. Indeed, the effective conductivity drastically increases with lower pH values, peaking at pH=0 (Figure 7.4b). However, when the pH is further decreased from 0, the effective conductivity decreased back down to a significantly lower level. Under these conditions, the competing side-reaction can consume aluminum metal and produces hydrogen gas:

$$2H^+ + 2e^- \rightarrow H_2 \uparrow \qquad (7.4)$$

In the case of the excessive consumption of aluminum by the gas forming side-reaction (Eq. 7.4), the reduction of graphene oxide sheets is limited to the very surface of the sample.

The direct correlation between C/O ratio to the effective conductivity observed here (Figure 7.4b) indicates that the higher effective conductivity for the samples reduced at pH=0 is caused by more efficient removal of the various oxygenated surface groups (i.e., epoxides) under these conditions. The highest C/O ratio achieved is about 6.3, which is high and comparable to those of the other commonly used techniques for the reduction of graphene oxides. [366] Because of that the fraction of the defected benzene rings in the graphene oxide basal plane decreases from 91% to 32%, by assuming each benzene ring can accommodate only one oxygen containing functional group and each functional group contains one oxygen atom, the restoration of the electrically conductive paths in the reduced graphene oxide flakes is effectively achieved.

More importantly, the layered microstructure of the bio-bond graphene papers is not affected by the 2-hour reduction by different pH environments (Figure 7.4c). The interlayer spacings of the samples after the reduction remains constant at 0.79±0.01 nm (2θ = 11^o),

which is consistent with the theoretical single sheet thickness of 0.76 nm. [367] We have determined the order of layering of the bio-bond graphene oxide papers by the Scherrer equation.[326] The stacking number of these samples are around 10 layers, indicating long correlation in packing of individual sheets. Moreover, after the reduction, the bio-bond graphene paper becomes a semi-metallic material as judged by the 0 eV take-off binding energy of the ultraviolet photoelectron spectroscopy (UPS) spectra, making it an excellent conductive substrate material for flexible electronics (Figure 7.4d).[368]

It is also worth noting that by merely 2 hours of mild reduction, the highest effective conductivity reaches close to 100 S/m and the final level can be easily adjusted by varying the pH values. More interestingly, we found the work function of the bio-bond graphene paper which primarily governs the charge transfer characteristics across the interface is also tunable by the variation of the pH during the reduction (Figure 7.4d).[369, 370] We progressively adjust the work function of the bio-bond graphene papers from 4.9 eV to 4.2 eV by applying the electrochemical reduction pH at 5 or 0, respectively. This is significant tuning of the work function of the graphene oxide materials by the controlled reduction process that has not been observed before. By closely matching the work function with those of the commonly used electronic materials, the hole-transporting bio-bond graphene paper could be utilized as both diode junction material and current collector. [191, 369, 371]

7.2.4 The rate of the reducing front propagation

The reduction time plays a dominant role on the extent of reduction of the bio-bond graphene paper. When reduced in 1 M HCl for 2 to 8 hours, the chemical states of carbon on the surface of the bio-bond graphene paper are consistently stable with predominant C-C peak at 284.6 eV and small trace of C-O peak at 286.2 eV, indicating completely reduced surface layers (within the detection limit of XPS, about 10 nm) after only 2 hours of reduction (**Figure 7.5**a).[372] The effective conductivity of the bio-bond graphene papers increases monotonously in the first 8 hours and remains constant after that. Meanwhile, the C/O ratio of the top (reduced) surface of the bio-bond graphene paper increases from around 2.2 for pristine graphene oxide to 6.3 after the first two hours of reduction (Figure

7.5b). However, the C/O ratio on the top of the bio-bond graphene paper gradually decreases from 6.3 to 4.0 when the reduction continues from 2 hours to 8 hours.

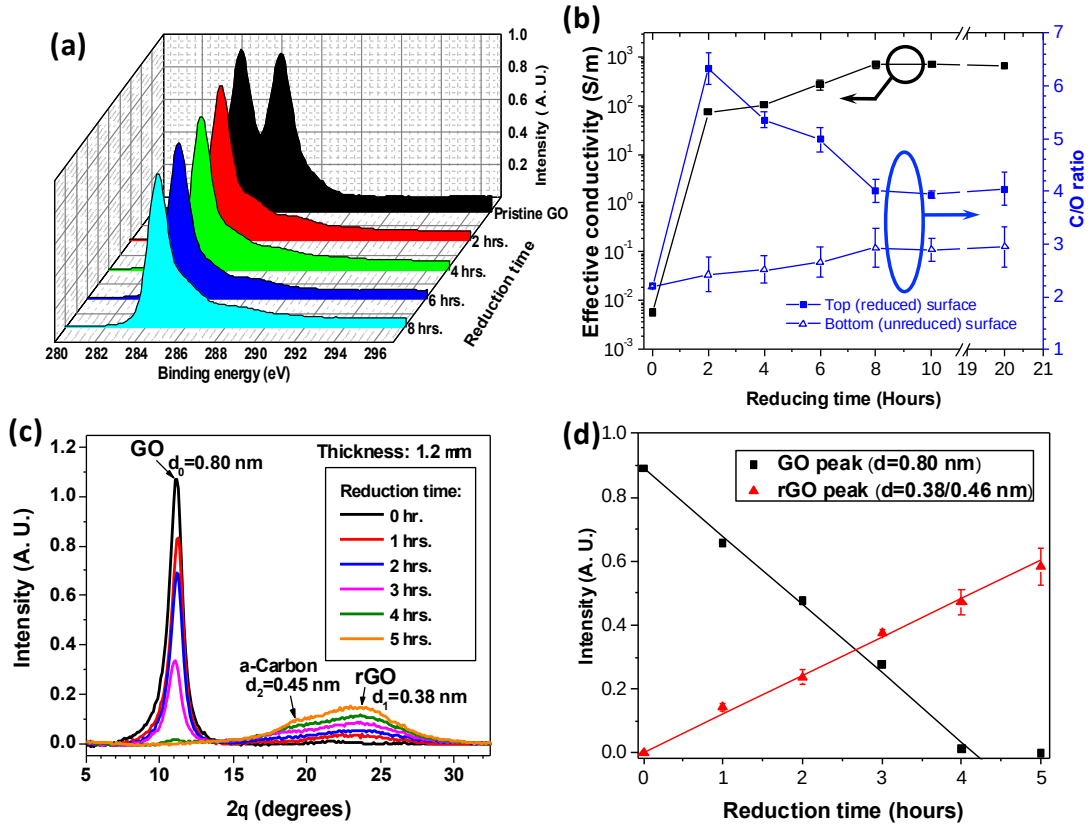

Figure 7.5 Bio-bond graphene paper with 2.5 wt% silk fibroin reduced at pH=0 for various time periods: (a) XPS C1s spectra of the top reduced surfaces, (b) overall effective electrical conductivity and the C/O ratio from both the top reduced and the bottom unreduced surfaces, (c) XRD data for the interlayer spacings of a 1.2 μm thin model sample showing three major peaks for GO, rGO and amorphous carbon (a-Carbon), and (d) the evolution of the integrated intensities of the GO and the rGO peaks with reduction time from the 1.2 μm thin model sample.

Moreover, the bottom surface of bio-bond graphene paper (not covered by aluminum layer) shows a slightly increasing C/O ratio that is inverse to that of the top surface (Figure 7.5b). This surprising observation can be due to the diffusion of the oxygen containing species from the bottom to the top, triggered by the gradient of the oxygen concentration created by the reduction occurring on the top surface. Indeed, the graphene oxide is not perfectly stable and slow decomposition or reduction of graphene oxide under wet conditions can be observed.[373, 374] This secondary mechanism of the reduction of graphene oxide that is far from the metal contacting layers facilitates the uniformity of the reduced layer and works like a "spontaneous pump" to lift the oxygen buried deep in the bio-bond graphene oxide

paper. Finally, after 8 hours of electrochemical reduction, this pumping of oxygen from the bottom layers essentially stops when the reaction and the oxygen gradient virtually dissipates (Figure 7.5b).

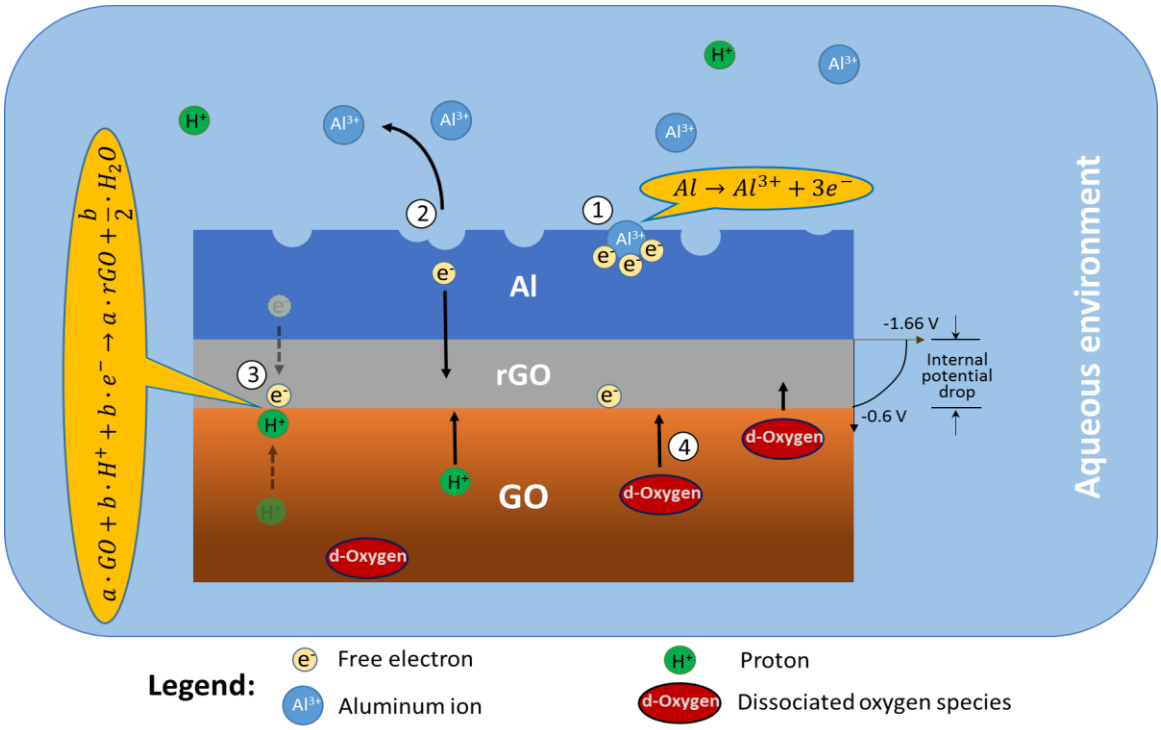

Scheme 7.2 Illustration of the electrochemical reduction process mediated by the reduced graphene oxide layer. Four major steps are numbered in the scheme: (1) the initiation of aluminum ionization; (2) the dissolving of ionized aluminum and separation of free electrons; (3) The transportation of free electrons and protons to the rGO/GO interface (reduction front) and the reduction of graphene oxide; (4) the passive diffusion of dissociated oxygen species from the deeper layers of graphene oxide to the reduced interface.

To illustrate a complex character of multiple ongoing processes we suggest a general scheme representing all three adjacent elements (partially dissolving aluminum, initial graphene oxide, and reduced graphene oxide) surrounded by the electrolyte (**Scheme 7.2**). When the partial dissolution is initiated at the aluminum-graphene oxide interface according to eq. 1, the aluminum surface supplies a cloud of electrons to the adjacent graphene oxide sheet surface. This shift in balance promotes the restoration of the oxidized surface functionalities on graphene oxide surface according to eq. 2. As soon as the first monolayer of the graphene oxide sheets is reduced and becomes conductive, the under layers of graphene oxide are affected by the surplus of electrons and the reduction progresses further into the film (Scheme 7.2). This way, the reaction continues to the deeper

graphene oxide layers for the first eight hours. However, the progression becomes limited at larger penetration depths due to the increasing internal electrical resistance. When the drop of electrical potential across the reduced layers approaches a certain threshold, which is close to the original reduction potential gap between aluminum and graphene oxide (around 1V), the reaction ceases across the film. In this case, the effective conductivity of the bio-bond graphene paper stops increasing and stays at around 700 S/m.

Furthermore, in order to get specific rate information for the first few hours of reduction, we set up a model sample with a thickness of 1.2 μm and monitored the extent of the reduction via the evolution of the microstructural characteristics of the bio-bond graphene paper by X-ray diffraction (XRD) (Figure 7.5c). At longer reduction time (up to 5 hours), the XRD peak that corresponds to the interlayer spacing of the graphene oxides packing (at 0.80 nm) diminishes and a diffuse peak at around 23.5^{o} emerges, indicating the dramatic transformation of the initial laminated structure. We assign the emerging peak at d=0.38 nm to closely packed phenyl rings of the graphene monolayer (minimum face-to-face distance of around 0.34 nm).[364] It is also noticed that with longer reduction times, another diffused peak at around 19.5^{o} (d=0.45 nm) emerges (Figure 7.5c). This secondary diffuse peak can be assigned to the presence of the amorphous component composed of amorphous carbon and silk material. From the integrated intensity of the graphene oxide peak versus the reduction time we found a linear regression of the d=0.80 nm peak intensity (Figure 7.5d). The interception of the linear fitting indicates that the total time required to fully reduce the 1.2 μm thick bio-bond graphene paper is 4.2 hours. Therefore, the linear reduction rate of the bio-bond graphene paper has been calculated to be 0.29 μm/hour under given conditions. Finally, the peak at 0.38 nm becomes dominant after full reduction thus indicating full transformation of the initial laminated structure to limited face-to-face graphitic region packing, which facilitates the high electrical conductivity through local restacking. These conducting regions coexist with a minor fraction of the amorphous carbon-rich regions.

7.2.5 Bio-bond graphene papers under cyclic reduction

As has been discussed in the previous sections, a single cycle of electrochemical reduction results only in a certain modest level of electrical conductivity to the bio-bond graphene paper. The optimal single-cycle reaction condition for the maximum effective conductivity has been determined as 1 M HCl (pH=0). Too high or too low pH values either slow down the reduction or promote the competitive gas forming reaction, respectively. Longer reduction time does not further reduce the bio-bond graphene paper due to the substantial potential drop through the reduced layers. Based upon the calculated reduction rate of 0.29 μm/hr, the total thickness of the reduced layer of the bio-bond graphene paper is around 2.3 μm for 8 hr, a small fraction of a total thickness of the flexible films investigated here (around 15 μm in most cases).

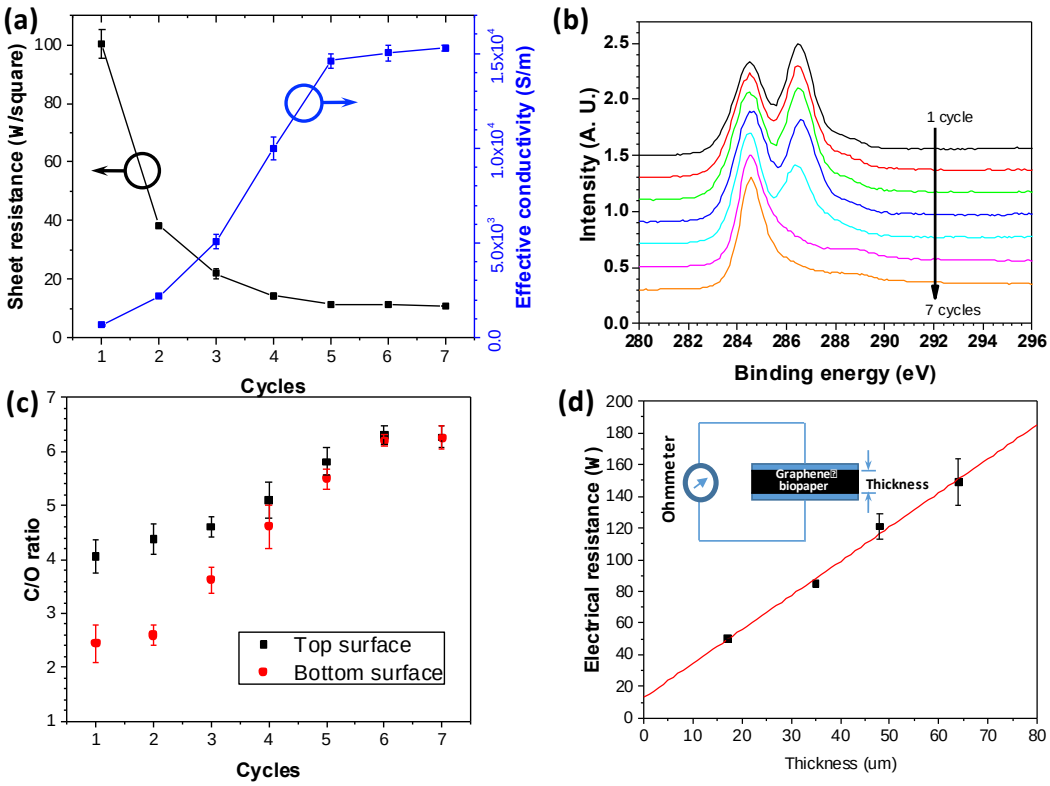

Figure 7.6 Bio-bond graphene paper with 2.5 wt% silk fibroin reduced by multiple cycles of 8 hours at pH=0: (a) Sheet resistance and effective conductivity; (b) XPS C1s spectra of the bottom surface; (c) the C/O ratios of the top and the bottom surfaces; (d) the dependence of perpendicular electrical resistance of the bio-bond graphene paper on the thicknesses measured by the two-probe method (scheme of the experimental setup is shown in the figure).

In order to further reduce the remaining volume of bio-bond graphene paper for better electrical conduction, a cyclic reduction process has been tested (Figure 7.6a). For the cycling procedure, the partially reduced bio-bond graphene paper was rinsed and dried before depositing another layer of aluminum for a new cycle of reduction. As was observed, in fact, under these conditions the conductivity of the bio-bond graphene paper increases steadily with a number of cycles (**Figure 7.6**a). The effective conductivity increases drastically by more than 20 folds from around 700 S/m to 1.45×10^4 S/m after 5 cycles and maximizes at around 1.52×10^4 S/m after 7 cycles. Further reduction beyond 7 cycles does not increase the effective conductivity, indicating a full reduction throughout the total thickness of the film of 15 μm. In fact, it is also expected from extrapolating the reduction rate of 2.3 μm/cycle (times 7 cycles).

The gradual reduction of graphene oxide surfaces and diffusion of oxygen containing moieties during the cycled reduction of the bio-bond graphene paper is confirmed by the XPS C1s spectra of the bottom unreduced surface of the bio-bond graphene paper that is not coated with aluminum (Figure 7.6b). The predominant peak at around 286.2 eV that corresponds to the epoxy groups continuously decreases from the first to the fifth cycle, confirming the slow reduction of the graphene oxide by the spontaneous diffusion of the oxygen containing moieties. By the seventh cycle, the epoxy peak for the XPS C1s spectrum disappears due to the final expansion of the reduction. Indeed, the C/O ratios of the top and the bottom surface of the bio-bond graphene paper both increase and get progressively closer in values over the first 6 cycles of the repeated reductions until they coincide after the seventh cycle at the value of 6.3 confirming the complete reduction of the bio-bond graphene paper through the entire thickness of the film (Figure 7.6c).

In addition, we used a two probe method to determine the perpendicular electrical resistance of the fully reduced bio-bond graphene papers with different thicknesses (Figure 7.6d). By extrapolating to zero thickness, the interfacial resistance between the bio-bond graphene paper and the electrodes is extracted, therefore the perpendicular conductivity of the bio-bond graphene paper is low, which is 5.8×10^{-3} S/m even at full reduction. This value is seven orders of magnitudes lower than the basal conductivity (1.52×10^4 S/m) and indicates extreme anisotropy of the conductive properties of reduced graphene oxide paper

fabricated here due to distinct laminated morphology. In addition, the insulating spacer of silk fibroin distributed throughout the graphene network may also contribute to the huge anisotropy of electrical conductivity since the blocking effect caused by the silk molecules is more pronounced in the out-of-plane direction of the 2D laminated conducting particles.

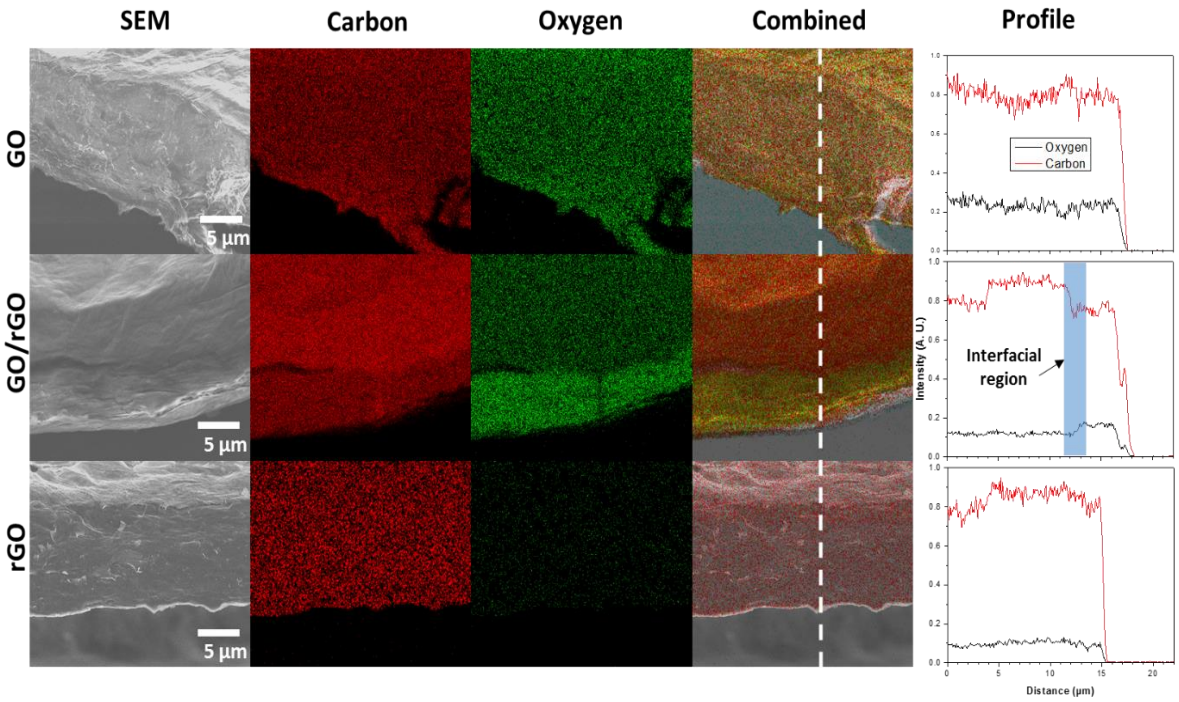

Figure 7.7 EDX mapping of the bio-bond graphene oxide paper (top), and the partially (around 40% thickness) reduced (middle) and fully reduced (bottom) bio-bond graphene paper. The white dashed line in the combined mapping indicates the position of the line profile shown on the rightmost column.

Finally, from the data of the carbon chemical states and the overall C/O ratio of the bio-bond graphene paper, it is clear that the increase in the C/O ratio is primarily caused by the removal of the oxygenated surface groups as was suggested in Scheme 7.2. In fact, the energy dispersive X-ray spectroscopy (EDX) mapping of film cross-sections clearly shows that there is compositional interface between the reduced and unreduced portions of the partially-reduced bio-bond graphene paper (**Figure 7.7**). It is also noteworthy that partial delamination might happen at the GO/rGO interface for the partially reduced sample, which is due to strong interfacial stresses. The semi-quantitative profile of the EDX scans demonstrates that the C/O ratio is much higher for the reduced graphene oxide than that of the graphene oxide cross section (Figure 7.7). And the partially reduced graphene oxide sample shows distinct steps in the line scan profile, where carbon and oxygen intensities

inversely change. Such an interface suggests that the electrochemical reduction strictly relies on the propagation of the reduction front that meets the propagation of the oxygen diffusion across the paper thickness (Scheme 7.2).

The excellent electrical conductivity of the bio-bond graphene paper of more than $1.5x10^4$ S/m achieved in this study is among the highest for graphene oxide materials which usually shows the value around 10^3 S/m. For instance, graphene paper reduced by in-situ ion-bombardment exhibits a strikingly high C/O ratio of 100, but its electrical conductivity is low at 1300 S/m due to the extremely surface specific reduction.[375] The electrical conductivity of the laser-scribed graphene paper is 1740 S/m and is limited by the incomplete penetration of the reduced layers, the thermal damage of the graphitic networks, and the highly porous morphology caused by the micro-explosion. Graphene paper fabricated by electro-spray deposition shows a moderate electrical conductivity of 2170 S/m due to the high porosity of the film, although the performance could be improved by mechanical compression and ultra-high temperature annealing at 2850 °C. The graphene paper also made by VAF technique of reduced graphene oxide possesses electrical conductivity of 7200 S/m after extensive reduction by hydrazine at elevated temperature.[88] The electrical conductivity of a PVA-GO nanocomposite film becomes 5260 S/m after being reduced in concentrated hydroiodic acid for 1 hour.[217]

A graphene film fabricated by gel-film transformation and successively reduced by 57 wt% hydroiodic acid has a high conductivity of $3.4x10^4$ S/m due to the semi-3D network of the wrinkled graphene sheets.[366] Another example of graphene paper crosslinked by conjugated polymer and reduced by hydroiodic acid has been reported with an electrical conductivity of $2.3x10^4$ S/m. It is worth noting that all the high electrical conductivities reported to date are usually achieved by employing hydrazine or concentrated hydroiodic acids, which are hazardous, corrosive, and volatile chemicals in contrast to ambient and mild conditions suggested in this study. In addition, all of these aforementioned procedures are not known to provide means for manipulation of local and global electrical and electronic properties.

It is clearly demonstrated that the metal-assisted spontaneous electrochemical reduction of the bio-bond graphene paper is highly competitive on the electrical conductivity and uniquely superior in terms of energy-efficiency and environmental awareness. Thermal annealing renders the best reduced graphene oxide in terms of the electrical conductivity and sp^2 hybridized network restoration, but the high energy consumption and the almost certain thermal degradation of other ingredients hinders its applications in graphene related nanocomposites. Chemical reduction using hydrazine or hydroiodic acid provide a fast way to effectively remove the oxygen on graphene oxide, but inevitably dope the reduced graphene oxide and the toxic reagents pose significant health concerns for industrial productions. The laser induced reduction is another versatile technique that is capable of patterning the reduced graphene oxide surfaces, but the abrupt thermal effect exfoliates the lamination of the reduced graphene layers and leaves a porous material, which is suitable for certain applications, such as organic solvent absorption and energy storage, but the mechanical integrity of the materials has been seriously damaged. Last but not least, electrochemical reduction applies only a small bias voltage and could reduce any material that contains percolated graphene oxide network, but an external energy input is still necessary.[361, 362] While in contrast, the metal-assisted spontaneous electrochemical reduction technique introduced and systematically studied in this work eliminates the requirement of external electrical energy input by applying the inherent reduction potential drop across the interface between aluminum and graphene oxide, providing excellent results on electrical conductivities and work function tunability.

To further illustrate the potential application of the electrochemically reduced bio-bond graphene papers, we have summarized the electrical conductivities and mass densities of the common electronic materials and related components in **Figure 7.8**. It is apparent that graphene materials along with other metallic materials have the highest electrical conductivities on the level of 10^7 - 10^8 S/m and graphene is also lightweight. [376] However, the very high cost of graphene, and the high densities with low flexibilities of the metals limit the applications of these materials for lightweight wearable electronics. More importantly, the bio-bond graphene paper presented in this work has a large quasi-continuous tunable range of the electrical conductivities over six orders of magnitudes by simple alternation of the reduction conditions. The highly tunable electrical conductivities

are comparable to the extreme range of silicon achieved by variable doping. PEDOT:PSS is another popular flexible, lightweight organic electrode material that has fairly large range of electrical conductivity, but the mechanical robustness is low.[377]

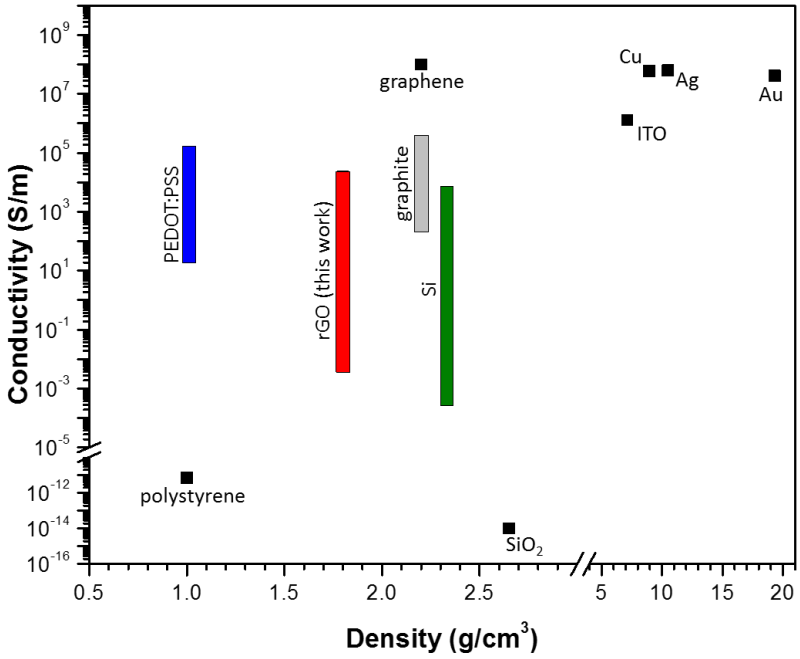

Figure 7.8 Summary of the electrical conductivity and the mass density of the common electronic and related materials. The colored bars indicate the variable range of the electrical conductivities of the materials.

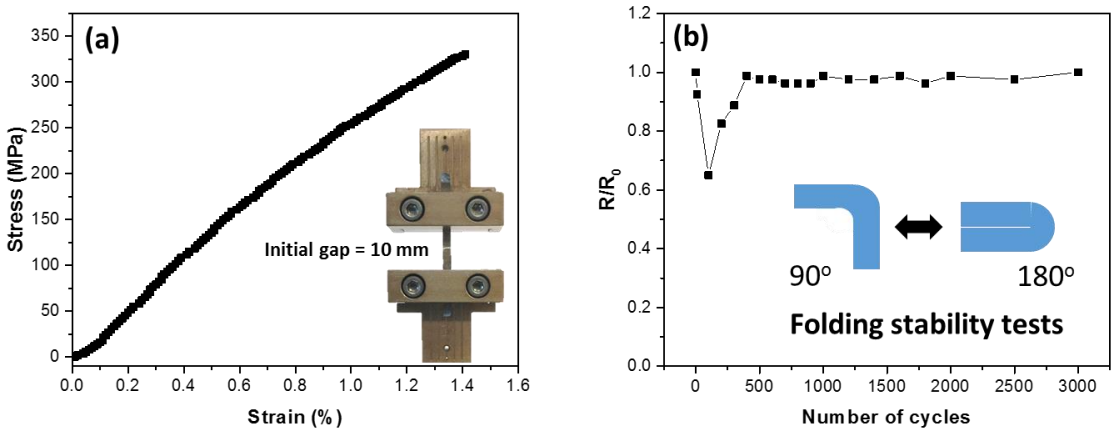

Figure 7.9 Tensile mechanical properties and durability tests of the fully reduced bio-bond graphene paper with 2.5 wt% silk binder. (a) Stress-strain curve obtained at the tensile test. Inset shows the geometry and setup of the tensile test with a fractured specimen. (b) Folding durability test with the film resistance monitored up to 3000 folding cycles. The inset shows schemes of the folding states during one testing cycle.

In contrast to the current thin coating conductive materials, large area conducting and flexible thin films fabricated here are extremely robust and preserve their conductivity after prolonged cyclic mechanical deformation. The tensile strength of the fully reduced graphene paper reaches high value of 327±6 MPa with high Young's modulus of 31.9±1.4 GPa and toughness of 2.5±0.1 MJ m^{-3}, respectively (**Figure 7.9**a). These properties are comparable to the highest values that have been reported to date for flexible electronic materials, which is originated from the slow recombination of the less-defective structure of the reduced graphene flakes during the steady reduction process.[116, 366, 378] In addition, the high mechanical and electrical stability has also been demonstrated by cyclic folding tests. Folding test is one of the harshest property durability test for current flexible electronic material films and coatings (e.g., based upon thin film silicon or conductive polymers) since the radius of curvature is minimized to the thickness of the papers (tens of microns) at the folding line, where large tensile and compressive strains are generated at the two surfaces (Figure 7.9b). As we observed, the resistance of the conductive thin film fabricated in this study subjected to multiple repeatable folding test remains unchanged after 3000 folding cycles (within ± 2%). After the first several hundred cycles, the resistance reduces (conductivity increases) initially probably due to the structural reorganization and the formation of additional conducting paths during the localized mechanical deformation and residual stress relaxation.

7.4 Conclusions

We have demonstrated that the metal-assisted electrochemical reduction is highly efficient and versatile for modifying the electronic properties of the bio-bond graphene papers and making them highly conductive. The fabrication of the highly conductive bio-bond graphene paper is facile and fast, and can be conducted under ambient wet conditions without the involvement of hazardous reagents. The electrical properties can be easily controlled by processing conditions in the ambient environment that are easily customized for different objectives and could be employed individually or combined to reveal the full spectrum of electrical and electronic properties in addition to the outstanding mechanical

robustness, folding endurance, and flexibility of conducting sheets (more than 100 cm^2 surface area and higher). We suggest the mechanism responsible for this process involves the balance of the internal potential drop due to the electric resistance of the reduced layers of graphene oxide and the diffusion of oxygen containing species to the reduced monolayers. Lower pH values promote both the kinetics (i.e., reaction rate) and dynamics (i.e., reduction potentials) of the electrochemical reduction, resulting in higher electrical conductivity and progressively lower work function. The lowering of the work function in the process of reduction is the first demonstration of such modification for the graphene papers.

Chapter 8 Ultra-robust Transparent Cellulose Nanocrystal-Graphene Membranes with High Electrical Conductivity

8.1 Introduction

In the search for advanced matrices and an effective combination of complementary components beyond those explored to date, we focus on new material components to replace those traditional rigid platelets or fibers based biopolymers and polymer nanocomposites. Here, we suggest assembling the strong and flexible 2D GO component (elastic modulus reaching 200-250 GPa[98]) with high aspect ratio 1D cellulose nanocrystals (CNC), which possess excellent mechanical properties (elastic modulus of 150 GPa), as well as being biodegradable and versatile for functional applications.[44, 45, 46, 47, 48] The high concentration of surface anionic functional groups also presents possibilities for the effective "gluing" of CNCs to primed GO sheets via non-covalent, yet strong ionic interactions, and hydrogen bonding.[379] Moreover, spin assisted layer-by-layer (SA-LbL) assembly technique was adopted to prepare these nanomembranes.[189] This fabrication approach is a facile, fast, inexpensive, and versatile process for constructing highly ordered multilayer film structures from various complementary materials. The LbL process is realized through sequential adsorption of oppositely charged components, such as grafted nanoparticles and polyelectrolytes, by ion pairing to form laminated morphology, which is analogous to the natural nacre (**Figure 8.1**a). Besides, compared with other popular approaches (*e.g.*, vacuum assisted filtration and drop-casting), SA-LbL is more appropriate to precisely tailor the thickness, size, microstructure and surface roughness of the nanomembranes by applying high-speed centrifugal force to realize effective stress transfer. In fact, these laminated nanocomposites exhibit high ultimate stress of (490±30 MPa), high Young's modulus (59±12 GPa) and outstanding toughness (3.9±0.5 MJ m^{-3}), while maintaining elongation to break up to 1.5% — a combination of mechanical characteristics that has never been observed in graphene-based nanocomposites. In addition, after

electrochemical reduction of the GO component, the ultimate stress and Young's modulus were found to reach even higher values of 655±102 MPa and 169±33 GPa respectively; both are among one of the highest reported values to the best of the authors' knowledge for graphene-based polymer nanocomposite films. We suggest that this excellent mechanical performance is caused by strong synergistic interactions between the two types of dissimilar nanocomponents, with flexible GO sheets integrated into a continuous network of densely packed nanocrystals arranged in haystack-like randomly overlaid morphology. Moreover, such outstanding mechanical performance is combined with high optical transparency and high electrical conductivity, a rare combination of physical properties.

8.2 Experimental details

For SA-LbL assembly, the nanomembranes were deposited on a sacrificial layer (≈200 nm) of cellulose acetate (CA) on silicon wafer (10 mm × 15 mm). The CNC aqueous solution (0.3 wt%) and graphene oxide suspension with desired concentration were alternatively spun on the substrate (3000 rpm, 30 s) until the desired thickness (60±10 nm) was reached. The films were released from the silicon substrates by dissolving the CA layer in acetone. Membranes prepared by using GO concentrations of 0.025, 0.05, 0.1 and 0.15 wt%, were found to have respective GO weight contents of 42.4, 56.4, 59.1 and 63.5 wt% as determined by XPS.

8.3 Results and discussions

8.3.1 Composition and morphology of the nanocomposite membrane

The GO sheets, prepared by Hummers' method[89], were predominantly 1.1 nm thick monolayers with lateral dimensions ranging from 2 to 8 μm (Figure 8.1b) and zeta-potential of -19.7 ± 0.9 mV. The rod-like CNCs were produced through a sulfuric acid hydrolysis of microcrystalline cellulose and possessed a diameter of 7±2 nm and length of 178±30 nm.[380] To enhance the interfacial interactions of anionic CNC component and anionic GO

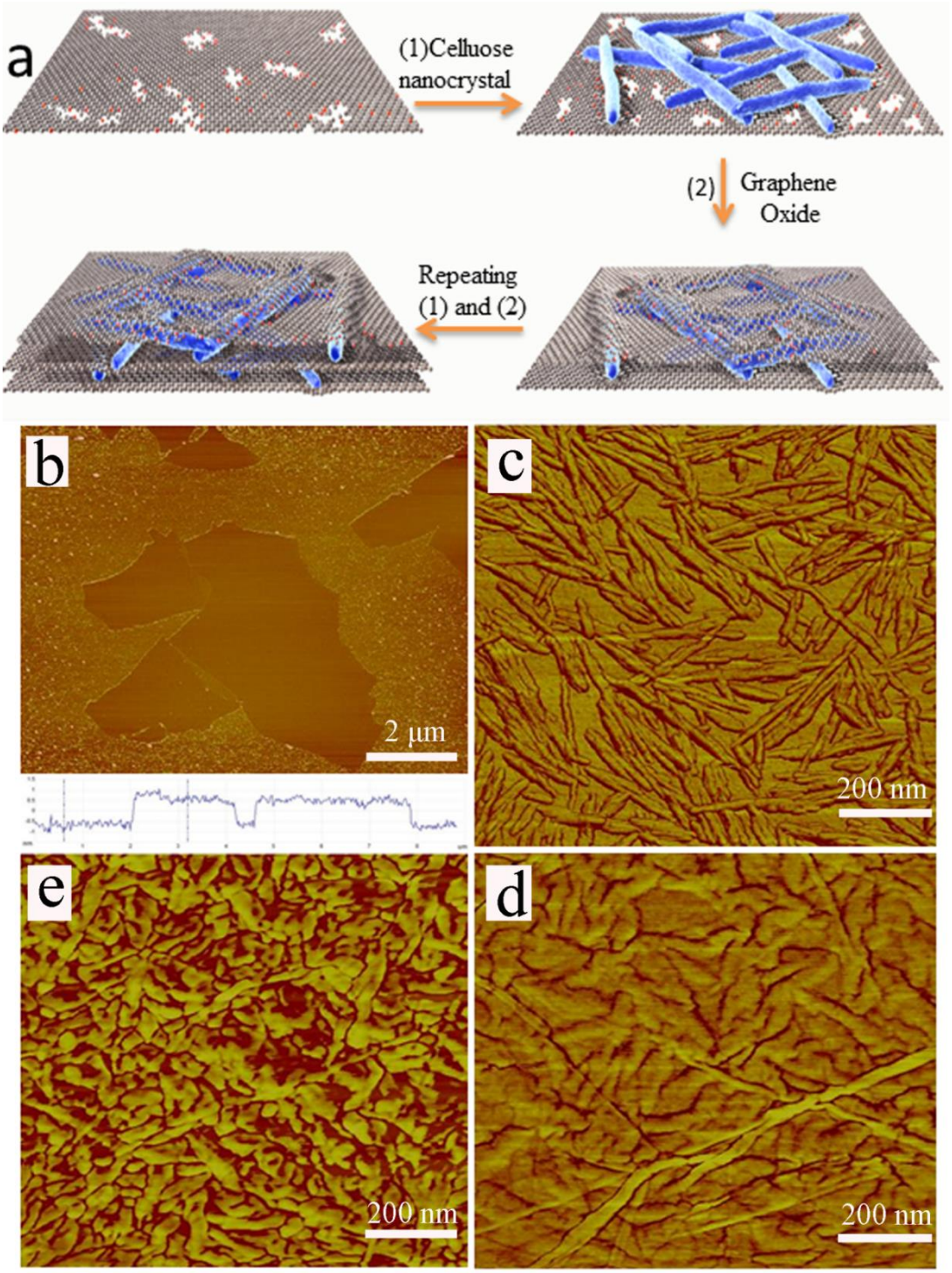

Figure 8.1 Design strategy of the Cellulose Nanocrystal-Graphene Oxide Nanomaterials. a, Fabrication of the laminated cellulose nanocrystals/graphene oxide nanomembranes. (b)The AFM phase image of graphene oxide, (c)cellulose nanocrystals on graphene oxide, (d) graphene oxide sheet on cellulose nanocrystals and (e) 6 bilayers cellulose nanocrystals/graphene oxide nanomembrane (59.1 wt% GO) with graphene oxide on top.

sheets, we modified the CNCs with a cationic polyethyleneimine (PEI) “prime” layer in order to introduce positive charged surface functionalities for strong ion pairing with GO sheets.[381] After the modification, the content of PEI in the CNC is estimated to be around 10 wt% that is sufficient for full surface recharge. In fact, the zeta-potential of CNCs jumps from strongly negative, -39.2 ± 1.0 mV, to strongly positive, 42.5 ± 0.2 mV after modification. Based on the dynamic light scattering (DLS) analysis, the effective diameter also increases from 7 nm for bare CNC to 9 nm for PEI-modified CNC. Such changes indicate the successful CNC modification with effective surface recharge (from negative to positive surface potential). The presence of strongly positively charged polymer sheath of a few nanometers thick is important to facilitate strong ionic interactions with strongly negatively charged flexible GO sheets for effective dispersion, LbL assembly and improved interfacial strength (**Figure 8.2**).

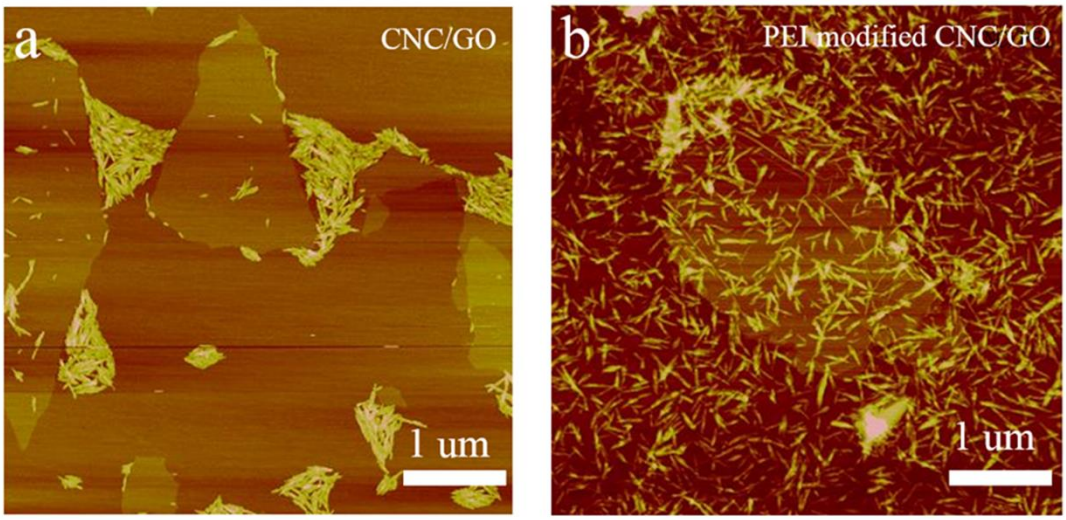

Figure 8.2 The AFM images of CNC/GO and PEI modified CNC/GO.

In addition, hydrogen bondings are the secondary interactions between the PEI modified CNC and GO required for formation of continuous films as demonstrated by the attenuated total reflection Fourier transform infrared spectra (ATR-FTIR) (**Figure 8.3**). Spectra were taken of GO-CNC nanocomposite and its components, PEI-modified CNC and GO. The FTIR spectrum for PEI-modified CNC exhibits characteristic PEI peaks at 2899 cm^{-1} (C-H, alkane) and 1598 cm^{-1} (N-H, 1^{o} amine), however similar peaks are not observed in the nanocomposite spectra due to low PEI content.[311, 382] Peaks at 2893 cm^{-1} and 2906 cm^{-1} (C-H, alkane) in spectra for PEI-modified CNC and GO-CNC nanocomposite, respectively,

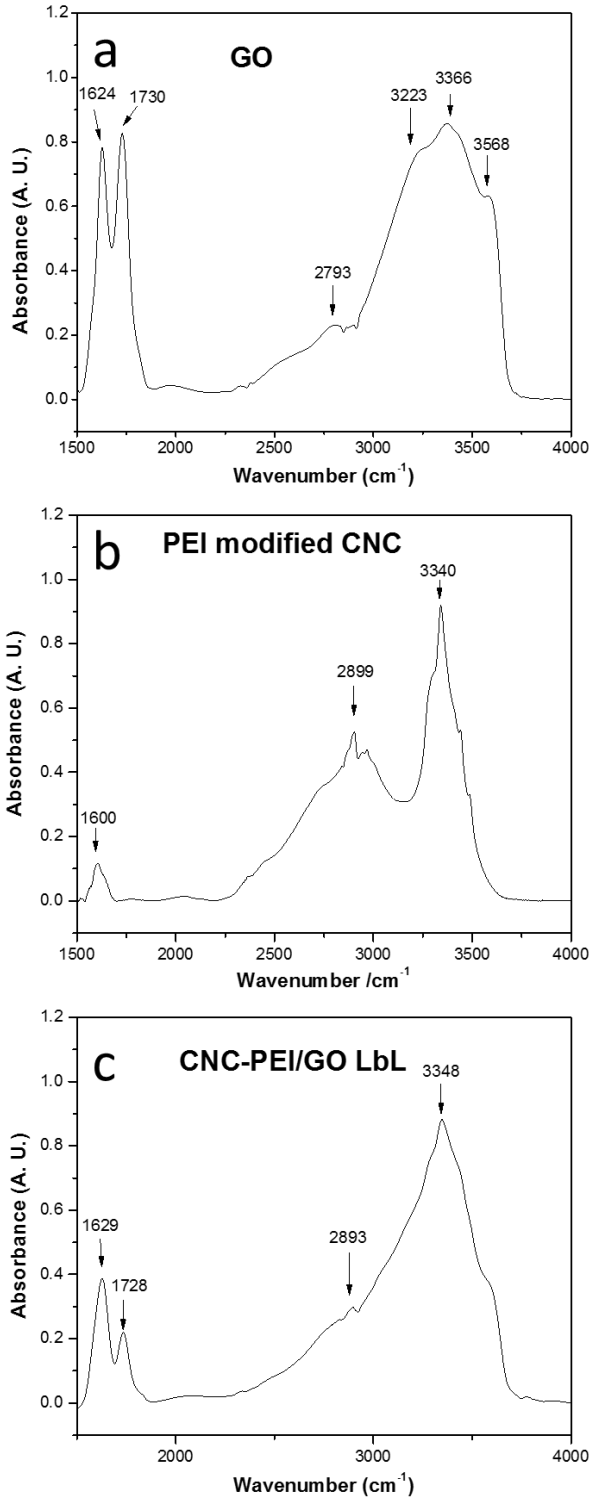

Figure 8.3 The FTIR spectra of the (a) GO, (b) PEI modified CNC, and (c) the LbL nanocomposite of CNC-GO.

are attributed to CNC.[311, 383, 384] In particular, the GO-CNC nanocomposite has a broad peak at 3348 cm^{-1} characteristic of –OH group stretching vibration that is shifted to a lower frequency with respect to the typical position at 3500 cm^{-1}. These features can be attributed to increased hydrogen bonding in the composite which alters the absorbance of –OH vibrational modes. [312, 385] Additional peaks at 2814 cm^{-1} (HC=O, aldehyde), 1728 cm^{-1} (C=O, aldehyde), and 1629 cm^{-1} (C-C, aromatic ring) in the composite spectra are characteristic of GO and notably mirror corresponding peaks at 2793 cm^{-1} (HC=O, aldehyde), 1730 cm^{-1} (C=O, aldehyde), and 1624 cm^{-1} (C-C, aromatic ring) in the FTIR spectra for GO. [311, 386]

Indeed, the thickness of the SA-LbL films increases consistently with the number of deposition cycles with a common linear growth mode with the increment from 7.0 nm to 15.1 nm per bilayer. High-resolution atomic force microscopy (AFM) images show that the dense network of long rigid nanocrystals expands across the entire surface region in a characteristic morphology resembling "randomly overlaid haystack straws" (Figure 8.1c). Individual GO sheet were found to wrap CNCs uniformly and firmly without disturbing original nanocrystal network (Figure 8.1c, d). Besides, CNCs show uniform random 2D orientation distribution, which is beneficial to form an isotropic in-plane structure without preferential orientation (**Figure 8.4**).

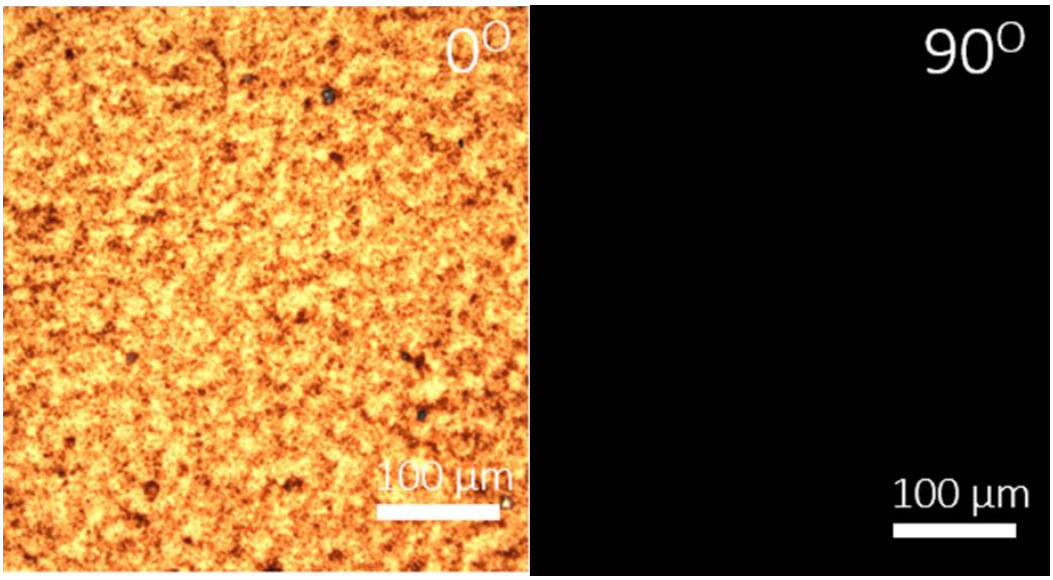

Figure 8.4 The polarizing microscope images of CNC/GO nanomembrane at different angle (0°and 90°) showing no liquid crystalline phases.

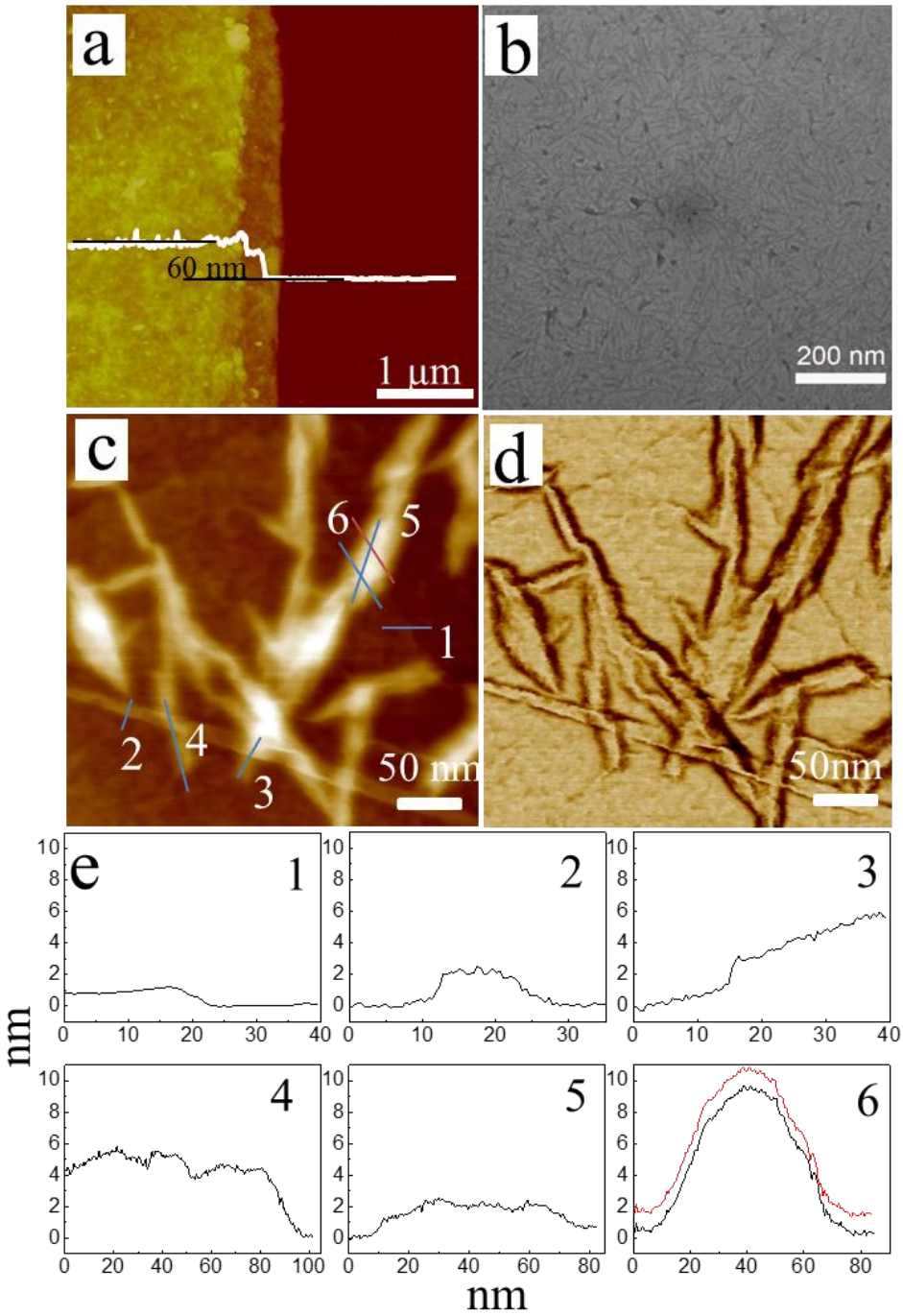

Figure 8.5 Morphology of the Cellulose Nanocrystal-Graphene Oxide Nanomaterials. (a), AFM height of image of the cross section of 6 bilayers cellulose nanocrystals/graphene oxide nanomembrane (59.1 wt% GO). (b),TEM image of the surface of the 1.5 bilayers CNC-GO nanomembrane. High resolution AFM (c) topography and (d) phase images of cellulose nanocrystals covered with graphene oxide sheet. (e) Cross section profile of different position on the image showing: (1)graphene oxide sheet edge; (2, 3, 4) graphene oxide sheet wrinkle on top of cellulose nanocrystal; (5) longitudinal and (6) transversal sections of cellulose nanocrystals partially covered by graphene oxide sheet.

The 60-nm-thick GO-CNC nanomembranes show an overall uniform surface with root-mean-square (rms) roughness of 4.7 ± 0.9 nm (within 1×1 μm^2) (**Figure 8.5**a), which is much smoother than other GO-based nanocomposites fabricated by common drop-casting or vacuum-assisted filtration methods (Figure 8.S7).[366] Such improved surface homogeneity is a sign of well-organized laminated structure with minimized random wrinkling and thus reduced localized stresses. Indeed, significant wrinkling is common for both drop-casted and vacuum filtrated GO-based films which compromise their ultimate mechanical performance. The random network of individual CNCs is also confirmed by TEM micrograph (Figure 8.5b).

Notably, wrapping deposited CNCs with the flexible GO sheets does not change the underlying morphology of the random CNC network. Cross-section profiles of individual cellulose nanocrystals partially covered with flexible GO sheets show the 1 nm-thick coating added after GO sheets deposition. Such an incremental increase corresponds to a GO monolayer and indicates that only single sheet wrapped around individual cellulose nanocrystals. Moreover, minimum contrast in the phase image suggests strong bonding between the CNCs and the flexible GO sheets, and also indicates full surface coverage by the flexible GO layers (Figure 8.5c-d). The tight wrapping is also confirmed by observing only a 2 nm high occasional wrinkles of GO sheets at the underlying nanocrystal surface (see sections in Figure 8.5e).

8.3.2 Mechanical properties of the nanocomposite membranes

The composite GO-CNC nanomembranes can be released from sacrificial substrate by solvent treatment.[189] Despite the minute thickness, the released nanomembranes are robust and freestanding even after drying, without signs of cracks, pinholes, or random wrinkles. Due to the very low thickness of these nanomembranes, conventional tensile tests are not capable of measuring their mechanical properties and instead, bulging testing had to be conducted. This testing is a common and widely accepted method designed for ultrathin films that is consistent with those measured by tensile tests [42] and verified by the authors in several comparative measurements (not shown). For this test, the films are

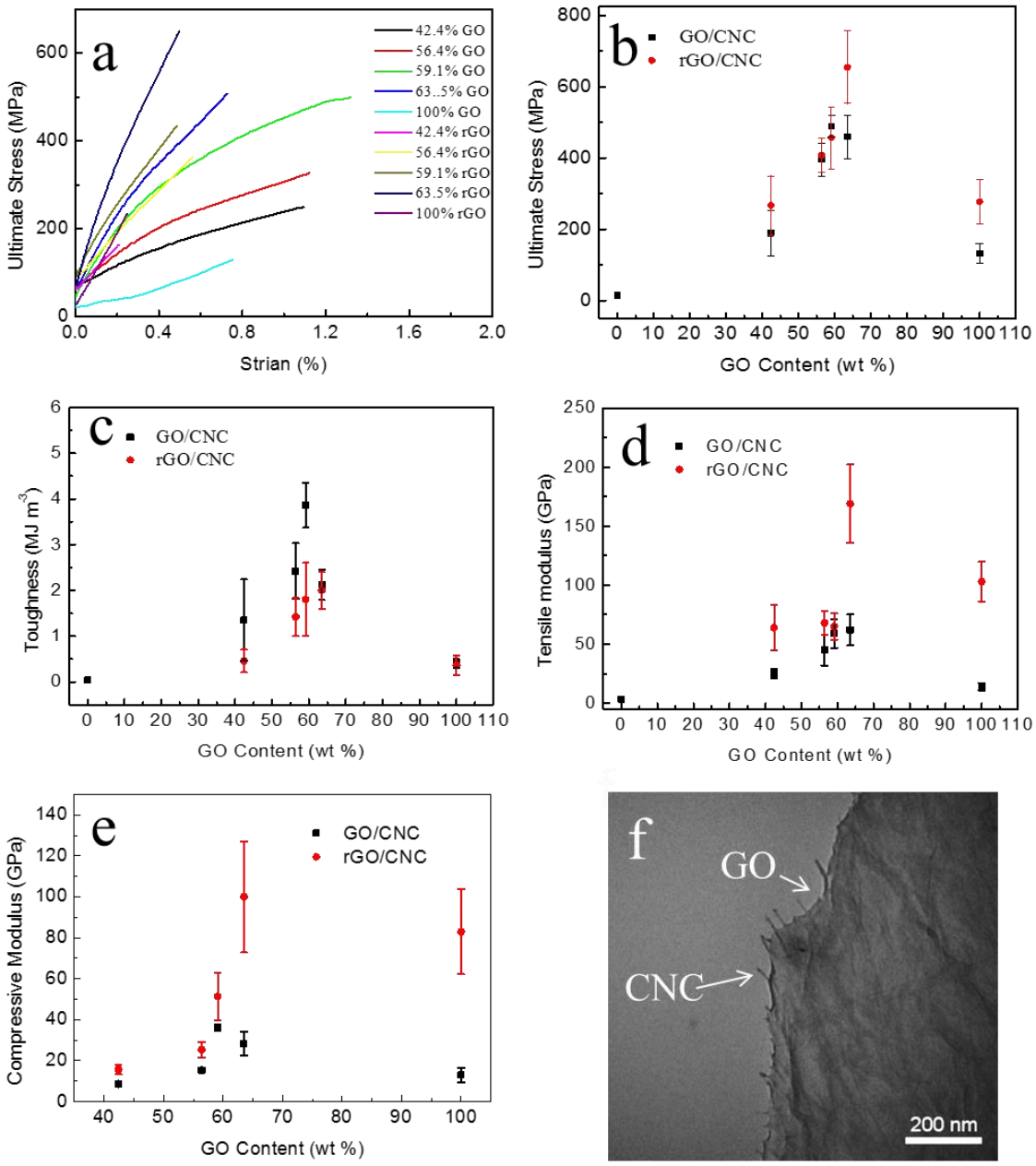

Figure 8.6 Micromechanical Properties of the Cellulose Nanocrystal-Graphene Oxide Nanomembranes and Failure Modes. a, the stress-strain curves of the CNC-GO and CNC-rGO nanomembranes with different GO contents (shown in wt %); Comparison of the ultimate stress (b), tensile modulus (c), and toughness (d) of nanomembranes with different GO contents (wt %) measured by bulging test; (the mechanical properties of pristine thick CNC films were measured by tensile test because the ultrathin pristine CNC films do not uphold their integrity when transferring to the copper apertures for bulging test. e) compressive modulus of nanomembranes with different GO contents (wt %) measured by buckling test; (f) TEM images of the fractured regions with wavy cracks, pulled sheets, and bridging nanocrystals.

released and transferred to a copper substrate with a 600 μm circular aperture for bulging mechanical testing.

Typical stress-strain curves derived from the bulging test data show a gradual rise of stress up to 200-500 MPa during elongation of 0.8-1.4% (**Figure 8.6**). A high residual stress of 20-70 MPa has been revealed in all nanomembranes due to a significant shrinkage during drying as was observed for many conventional LbL membranes.[42, 387] For the nanomembranes with GO content of 59.1%, CNC of 36.8%, and PEI of 4.1%, which are determined by X-ray photoelectron spectroscopy (XPS) measurement, high mechanical characteristics have been achieved including tensile strength of 490±30 MPa (up to 525 MPa in some cases), Young's modulus of 59±12GPa, and toughness of 3.9±0.5 MJ m^{-3} (Figure 8.6a-d). Pure GO nanomembranes without any CNC component showed poorer performance because flat GO sheets are only weekly bonded by van der Waals interactions and hydrogen-bonded water molecules that drastically decreases the toughness and strength. Adding positively charged CNC component brings stronger ionic interactions with negatively charged GO sheets to promote better interfacial bonding and resulting excellent mechanical properties. The characteristics achieved under these conditions are generally 4 to 10 times higher than common graphene-based paper materials and GO-polymer nanocomposites (see discussion below). Furthermore, the strongly bonded GO-CNC nanomembranes are stable under aqueous conditions, at which a common graphene oxide paper is prone to damage and delamination (**Figure 8.7**). [134]

We further reduced GO in the LbL nanomembranes using the metal-assisted electrochemical reduction technique, which has been demonstrated to be an effective and efficient way to remove the oxygen containing functional groups on the GO surface.[109] After the reduction of the GO component which results in tighter interlayer spacings and the addition of strong π-π interactions, the mechanical strength further increased to the even higher level – ultimate stress of 655±102 MPa and Young's modulus of 169 ± 33 GPa are achieved for multiple specimens. The elastic modulus value is comparable to that of individual CNCs and Kevlar fibers (168 ± 4 GPa) even if randomly oriented 2D morphology exists without one-dimensional uniformly-oriented fibrillary structure.[388]

Furthermore, these values exceed the known elastic modulus values reported for the strongest graphene-based nanocomposites available in the current literatures.[389]

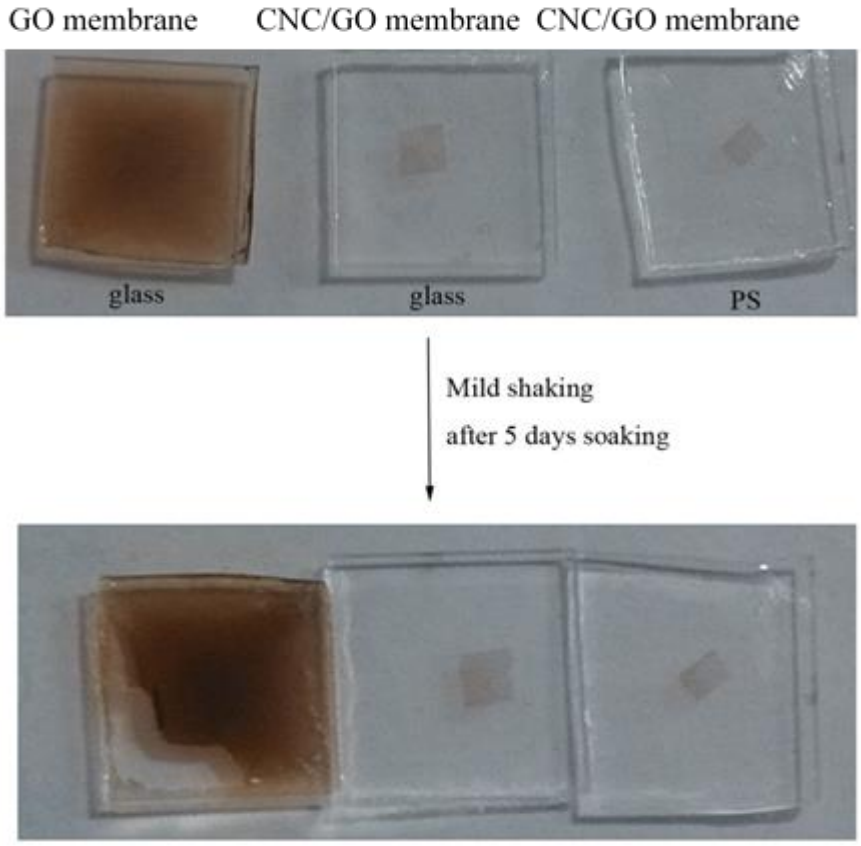

Figure 8.7 Long-term stability of CNC/GO nanomembranes under wet conditions.

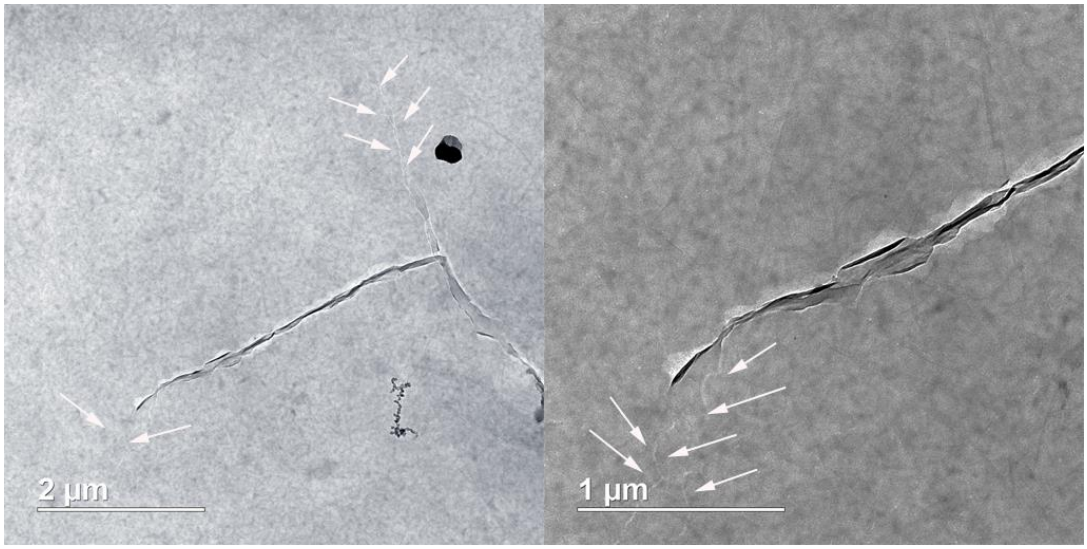

Figure 8.8 TEM images of the fractured regions with multiple cracking and crack bridging towards the end of the crack path. Arrows indicate the onset of crack branching and bridging.

Moreover, the compressive elastic modulus was evaluated by analyzing the periodic buckling patterns of the compressed nanomembranes, which is another widely used test for ultrathin films.[316] The compressive elastic modulus of all nanomembranes have a slightly lower value than the Young's modulus derived from bulging test, which is probably caused by progressive delamination of the layered nanomembranes due to local wrinkling of flexible graphene oxide sheets in buckling experiments.[69]

To explore the failure mechanisms of these nanomembranes, the morphologies of the fractured regions were examined using TEM (Figure 8.6f and **Figure 8.8**). By straining the film close to the point of failure, we see the emergence of diverging and unevenly shaped microcracks, and the pulling-outs of both GO nanosheets and CNCs. The jagged, highly-angled crack junctures indicate a high degree of contact shielding of the crack tip probably due to the enhanced local microroughness caused by the presence of the long CNC ridges that arrest sliding and shearing of the laminated structures. Meanwhile, the dense and strong bonding between CNCs hinders the separation of crack tips via the bridging GO nanosheets (Figure 8.6f). Finally, the unique hierarchy of strongly interacting structural elements in the nanocomposite membranes cover a wide range of length scales from 10^0 nm (graphene oxide sheet thickness), around 10^1 nm (diameter of cellulose nanocrystals), around 10^2 nm (length of cellulose nanocrystals), and 10^3-10^5 nm (lateral dimensions of graphene oxide flakes). Therefore, such a combination of different modes of deformation is a main cause for achieving exceptionally high mechanical characteristics.

Based on the failure analysis from the TEM micrographs, we propose the nano-structural model of the GO-CNC LbL nanocomposites (**Figure 8.9**a). Flexible GO sheets can form conformal shells on the cross-junctions of the dense CNC network via ionic interactions and hydrogen bonds. Therefore, global deformation of these nanocomposite films is mediated by local torques of the GO-jointed CNCs. Reorientation and displacement of the confined CNCs dissipates excessive mechanical energy during deformation, resulting in increased ultimate strain and overall toughness.

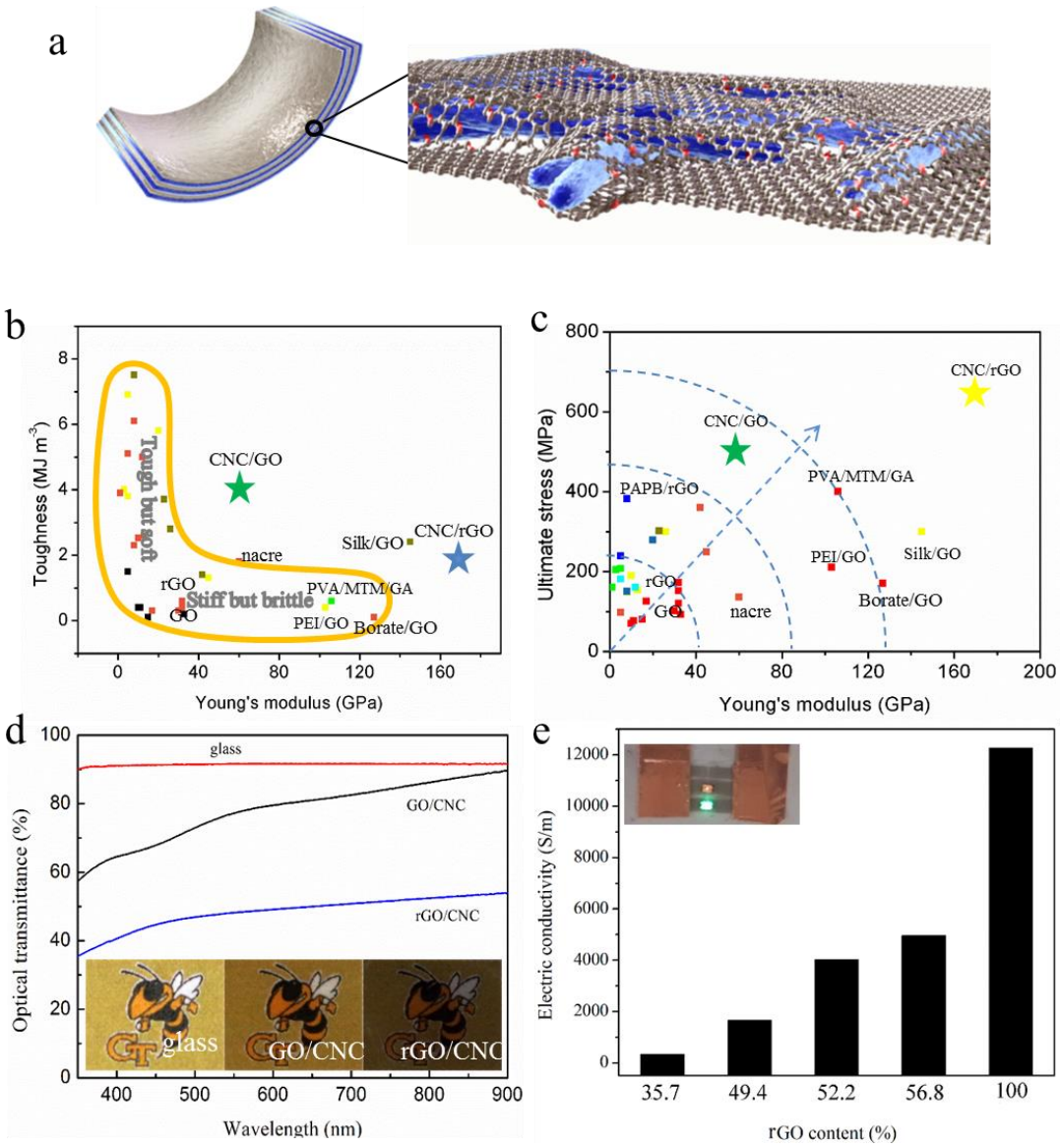

Figure 8.9 Integrated schematics, comparison of the laminated materials performance, optical transmittance, and electric conductivity of CNC-GO nanomembranes. (a) The schematic structure of the cellulose nanocrystal-graphene oxide nanomaterials. (b and c) Comparison of mechanical properties among nacre-like nanomaterials in different coordinates with stars representing results in this study. (d) Optical transmittance of soda-lime glass substrate, CNC-GO (6 biayers, 63.5 wt% GO) and CNC-rGO (6 bilayers, 56.8 wt% rGO) nanomembranes. Inserts show the pattern covered by transparent nanomembranes of different composition. (e) Electrical conductivity of CNC-rGO nanomembranes with various rGO contents. Insert demonstrates the LEDs lit up through the conductive nanomembrane.

8.4 General comparisons and conclusions.

As a common benchmark for bioinspired nanocomposites, natural nacre exhibit an excellent balance of mechanical properties, including ultimate stress of 137 MPa, toughness of 1.8 MJ m^{-3} and Young's modulus of 60 GPa, which are much better than most of the laminated nanocomposites reported to date especially those based upon flexible synthetic polymers. One of the examples from recent studies to be compared here is GO films crosslinked by borate which shows a very high modulus value of 127 GPa due to covalent borate orthoester bonds between GO sheets and borate ions.[99] However, the ultimate stress is modest at 185 MPa and thus the toughness is as low as 0.12 MJ m^{-3} (only one fifteenth of nacre). Polyvinyl alcohol/ montmorillonite nanocomposite films show excellent strength of 400 MPa and superior modulus of 106 GPa, but the toughness is only around 0.6 MJ m^{-3}. The ultimate stress and toughness of crosslinked GO-PEI film can reach 210 MPa and 103 GPa, but the toughness is only about 0.23 MJ m^{-3}.[210] Silk-GO nanomembranes possess an ultimate stress above 300 MPa combined with very high Young's modulus of 145 GPa, but the toughness is modest, around 2.4 MJ m^{-3}. [69] Another example is GO-poly(acrylic acid-*co*-(4-acrylamidophenyl) boronic acid) ($PAPB_x$) films with ultimate strength of 207 MPa and high toughness of 3.8 MJ m^{-3}, but the Young's modulus drops to very low value of 5 GPa.[366] Even after graphene reduction, both the ultimate stress and toughness has been improved dramatically to 382 MPa and 7.5 MJ m^{-3}, but the Young's modulus is still at about 8 GPa, which is only one seventh of natural nacre. Recently, it is reported that multi-layered carbon nanotube films show high strength (450 MPa) and high toughness (9.6 MJ m^{-3}), but the modulus is only 30 GPa.[390] Walther et al. reported helical plywood structure films with tailored cholesteric liquid-crystal structure through self-assembly process and interesting structural and optical properties.[391] However, the mechanical properties are modest at best, with Young's modulus of about 10 GPa and ultimate stress of 67 MPa, both are about an order of magnitude lower than those reported here.

On toughness vs. modulus and ultimate stress vs. modulus Ashby plots of laminated nanocomposites film, it can be seen that our GO-CNC composite extends beyond the property space of previously reported materials (Figure 8.9b, c). The "boomerang"-like

envelope in toughness-elastic modulus coordinates reflects the trade-off between materials with high strength (but brittle) and materials with high toughness (but soft). [392] This characteristic shape is caused by conflicting mechanisms for increasing mechanical strength on one hand, and compliance on the other hand. The ultimate strength of 490 MPa is also the highest on record among all the laminated graphene-based nanocomposites reported to date and "breaks" the traditional shape by "opening" a new position on the mechanical diagram (Figure 8.9b). The enhanced toughness is caused by improved compliance, which is two to three-fold higher in the elongation to break as compared to conventional laminated graphene with various synthetic and biopolymer binders. Moreover, further electrochemical reduction of the graphene oxide component leads to a dramatic increase in ultimate mechanical stress to 655 MPa and very high elastic modulus of 169 GPa, another set of exceptionally high characteristics (Figure 8.9c). If taking the lightweight into consideration, the specific strength and stiffness of CNC-rGO nanomembranes were determined to be 382 MPa/(g cm^{-3}) and 100 GPa/(g cm^{-3}) respectively, which are comparable to the best representatives of sophisticated nacre-like composites based upon metal and ceramic materials.

Moreover, the nanocomposite membranes fabricated here also possess excellent optical and electrical properties. The 60-nm-thick sample shows 77% optical transmittance at 550 nm wavelength for CNC-GO nanomembranes, which is higher than that of pure graphene oxide film with the same thickness thanks to the transparency of CNC components (Figure 8.9d).[393] After the metal-assisted electrochemical reduction, the transmittance reduced to around 50%, which is still transparent enough to make the covered graphics legible (see optical photographs in Figure 8.9d). The decrease in optical transmittance after reduction is due to the restoration of conjugated π electronic structure and the enhanced π-π* electron transition upon light absorption.[346] In addition, the nanomembranes with high contents of graphene oxide show high conductivities around 5000 S m^{-1} after reduction, which is hard to achieve for flexible laminated nanocomposites (Figure 8.9e). [109]

Chapter 9 Self-Powered Flexible Electronic Skin with Touching Sensitivity Triggered by Bio-Electrolytes

9.1 Introduction

Tactile sensors are a large category of human-machine interfacing devices, whose applications include wearable and portable electronics, smart automation servers, soft robotics, and active identifications.[394, 395, 396] Generally, piezoelectricity[397, 398, 399, 400], piezoresistivity[401, 402, 403], capacitance[404, 405], and triboelectrification[406, 407, 408] are the major operating mechanisms for tactile sensors, which show different characteristics in specialized applications.[409] However, most of these sensors not only rely on external power supply but also require signal amplification/analysis components due to the small response signals limited by the sensing mechanisms. Self-powered sensing and responding solutions are in urgent needs for constructing sustainable nodes for the fast growing internet-of-things, such as wearable body monitors, intelligent home appliances, smart logistic tags, and active surveillance networks.[410, 411, 412]

Moreover, although there are numerous tactile sensors detect various pressures by straining, the difficulty for the differentiation between human and artificial touches remained a major challenge due to the lack of sensitivity for unique biological interfacial cues. Despite the chemical cues that are characteristic for various interfaces, human skins naturally contain moisture and biofluids, which are abundant and distinctive for living entities.[413] Therefore, humidity sensors are potentially adaptable for biological tactile sensing applications. However, the response rate of the humidity sensors is usually low due to the relatively slow adsorption/desorption and diffusion process of biofluids.[414, 415] In addition, the sensing substances in the humidity sensors are still passive, which in other words need external power to actuate.[416] The search for functional materials suitable for designing new classes of bio-interfacial sensing that are applicable for innovative self-powered human-technology interactions has not been completed yet.

One of the recent candidates for the role of active materials at human biointerfaces is graphene and its derivatives. These abundant materials have been playing important roles in various structural and functional applications in the last decade due to their extraordinary electrical, mechanical, and chemical properties.[90, 417, 418] Sensors[419], batteries[266, 420], supercapacitors[107], and robust multifunctional nanocomposites[389] fabricated using graphenes hold promises for wide range of applications. For instance, flexible strain sensors made using graphene as the active component have been reported extensively.[419] However, purely graphene based devices usually require complicated and tedious assembly and packaging processes.[421] From other materials from this class, graphene oxide (GO) is primarily used as precursor for reduced graphene oxide (rGO, an analog to pristine graphene) or nanofillers for mechanically robust nanocomposites.[69, 422] Recently, a strong and flexible platform of bio-bond graphene oxide paper (GO bio-paper) for the wearable electronics has been suggested.[109, 423] The paperlike material becomes much stronger, stiffer, tougher, and more importantly for biological applications, water resistant.[109] The GO bio-paper is available for localized selective reduction to form electrically conductive patterns by the metal-assisted spontaneous electrochemical reaction (MASER) technique, paving a new avenue for simplified fabrication of flexible electronics.[423] By analyzing the mechanism of the process, we found that the MASER only proceed in aqueous environments due to the necessity of electrolytes for the electrochemical reaction at the metal-GO interfaces. Owing to the galvanic nature of the metal-GO reactions, the activation of the power generation by the micro-injection of the bio-electrolyte from human skin to the metal-GO junction becomes a possible approach to design self-powered human-tactile sensors.

Herein, we introduce a series of novel self-powered tactile sensing materials based on the metal-GO junction that serves as the trigger of the electrochemical reaction to exclusively respond to direct human touching, which locally delivers trace amount of bioelectrolytes. The metal-GO junctions show unprecedented, strong and continuous response signal (up to 1000 mV) for prolonged activation durations and excellent response rate up to 20 Hz, in addition to the outstanding passivation to mechanical deformation or non-human activations. These ultrathin materials also show the excellent mechanical robustness,

flexibility, and water resistivity, all make them prospective materials for self-powered human-tactile sensors of flexible electronic skins in soft robotics.

9.2 Experimental details

The ambient humidity sensing is done in a glove box and the humidity in the chamber is controlled by adjusting the speed and the path length of the dry air passing through a series of water bubblers. The ambient humidity is monitored by a commercial humidity sensor (Model 512, Electro Tech Systems, Inc.) and the device voltage output is measured by a Fluke 117 digital multimeter. The time resolved electrical signals were recorded by a potentiostat (VersaSTAT 3, Princeton Applied Research) in open circuit experimental

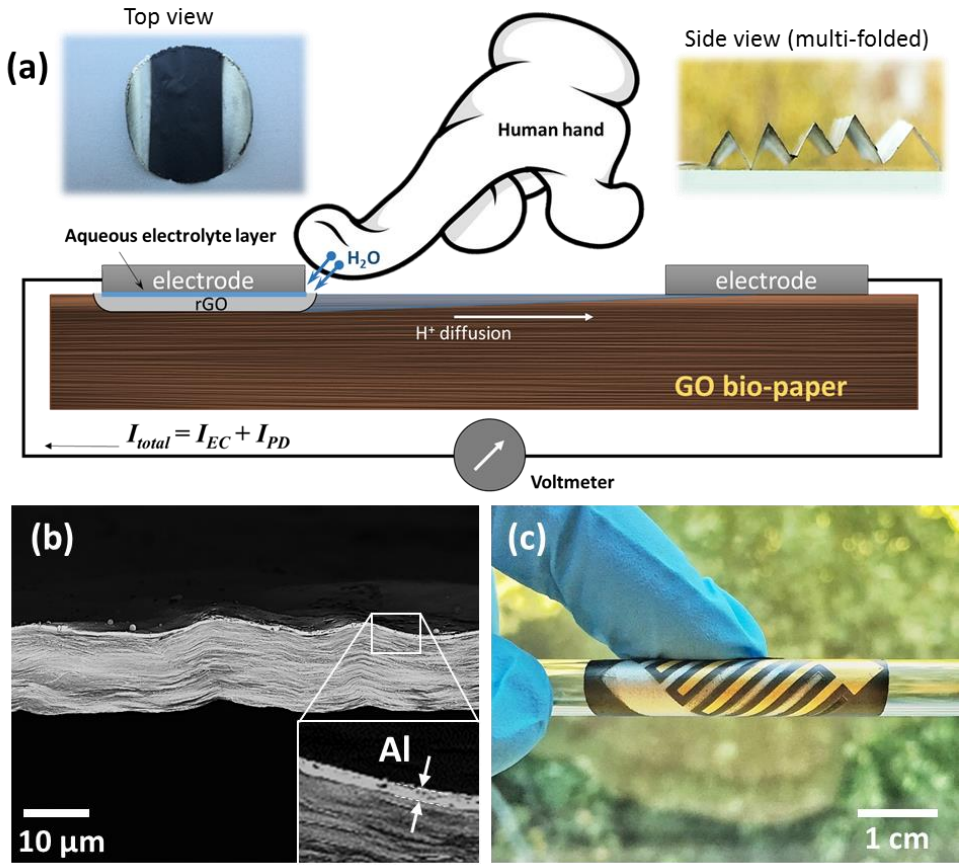

Figure 9.1 (a) Schematic drawing of the metal-GO junction structure and the mechanism of the power generation. Insets: (left) the top view of the symmetrical Al-GO junction pair, and (right) the side view of the same sample that shows its excellent folding robustness. (b) SEM micrograph showing the cross section of an Al-GO junction. The inset emphasizes the uniform Al coating layer. (c) Optical photograph demonstrating the flexibility of the Au/Al coated GO bio-paper.

setup with two electrode connection. All the electrical response tests of the bio-touch sensors were conducted in ambient conditions at 21-23 ºC and 35-45 RH%. The frequency tests were realized by a combination of an electrodynamic shaker (LW126.151-9, Labworks Inc.) and a sinusoidal wave function generator (SC-121 Sine Servo Controller system, Labworks Inc.), scanning from 2 to 20 Hz.

9.3 Results and Discussions

9.3.1 Materials design of the metal-GO junctions for tactile sensing

GO bio-paper have been fabricated by vacuum filtration of the GO aqueous suspension with 2.5 wt% of silk fibroin (SF) mixed as bio-binders for improved mechanical properties.[109] The tactile sensing hybrid materials have been assembled by depositing two separate thin metal electrodes on the surface of the laminated GO bio-paper (**Figure 9.1**a), forming opposite metal-GO junctions. The metal layers deposited by electron beam evaporation are uniform (500 nm thick) and conformed to the topography of the laminated GO bio-paper (Figure 9.1b). The surface roughness and morphology of the metal coated surfaces essentially stays the same, without noticeable pin holes or micro-cracks, indicating

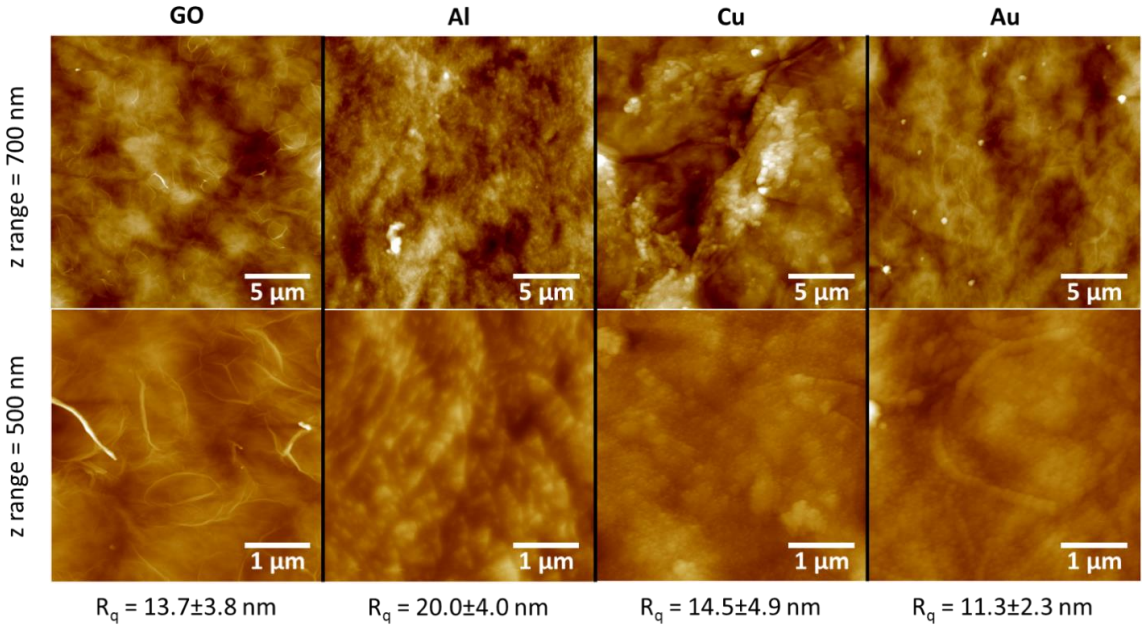

Figure 9.2 AFM height micrographs of bare GO bio-papers and GO bio-papers coated with aluminum, copper, and gold, respectively. Surface roughness is not affected (except for aluminum coating, which slightly roughens the surface) by the metal coatings, and the coated surfaces are free of microscopic defects (e.g., cracks, agglomerations, pin holes, etc.)

impermeable uniform coatings (**Figure 9.2**). The excellent flexibility of the metal-GO junction facilitates versatile attachment to curved surfaces that does not affect sensing performance (Figure 9.1c) (see below). Moreover, complete folding with sharp folds and unfolding do not damage the integrity of the films either (Figure 9.1a inset, **Figure 9.3**).

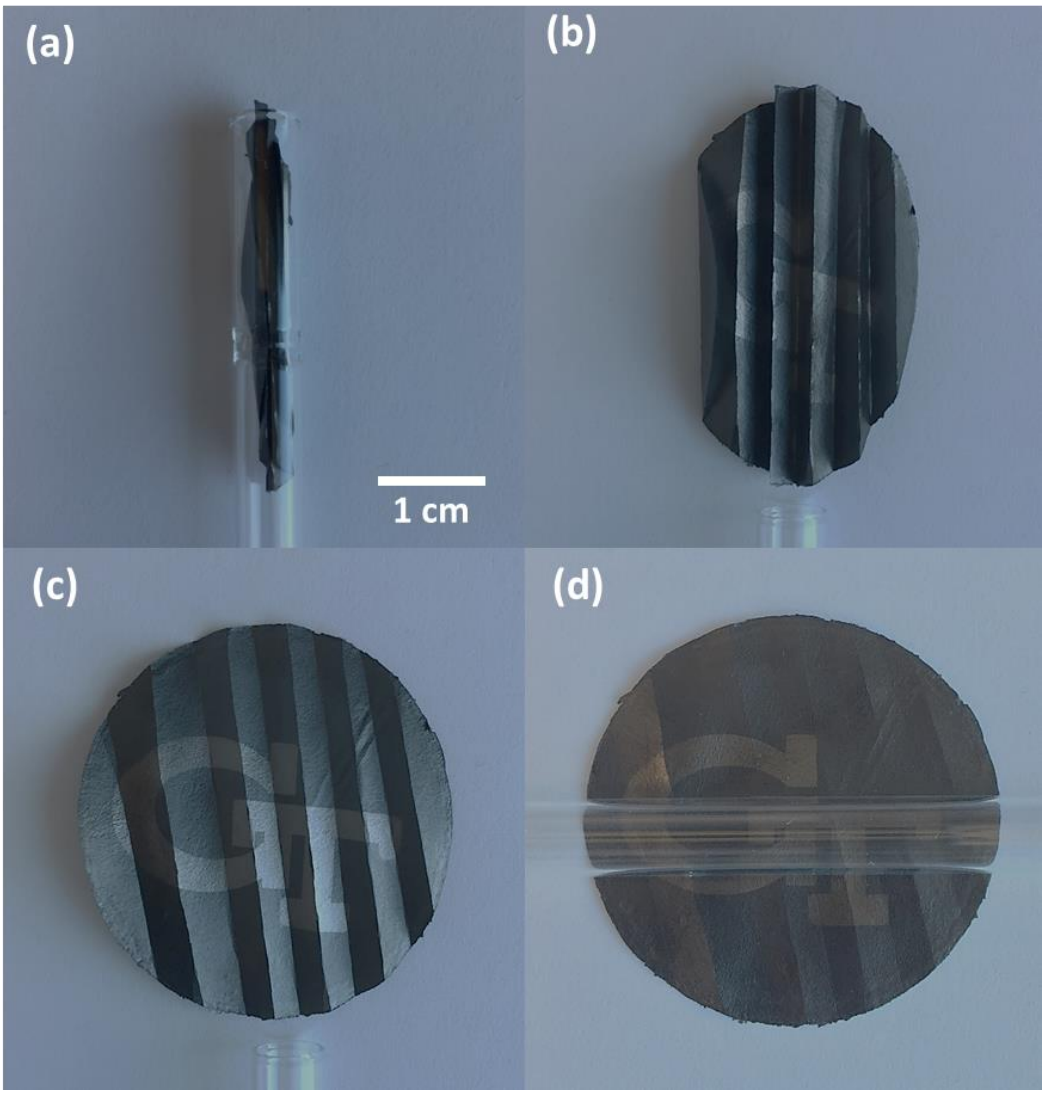

Figure 9.3 Foldability demonstration of the GO bio-paper by inserting the tightly folded sample in a glass tube (panel a, inner diameter of 5 mm) and take out before unfolding and flatten (b to d).

When one of the metal-GO junction is moisturized by either directly spraying deionized water (macroscopic moisturizing) or pressing bare finger (microscopic moisturizing) on it (Figure 9.1a), an electrical potential on the level of few hundred millivolts can be detected; if the other metal-GO junction is pressed, electrical potential with the same amplitude and opposite polarity is recorded. When both of the opposite metal-GO junctions on the same

GO bio-paper are moisturized or pressed, the electrical potential output return to zero, probably because the opposite potential outputs annihilate. Among the three metal electrode materials we have tested, gold (Au), copper (Cu), and aluminum (Al) generate sequentially larger potential outputs. When the two electrodes are the same materials, the idle (*i.e.*, not moisturized or pressed) output in ambient conditions is close to zero; if the two electrodes are made of different metals (*e.g.*, Al and Au, respectively), the idle output is not negligible and varies with the ambient humidity. It is also observed that the potential output stays at stable levels if the finger pressing holds, which is an unusual characteristic beneficial for the continuous recording of the pressure duration.

Based on the aforementioned phenomena, we suggest the working mechanism of the metal/GO tactile sensor as follows. By direct pressing using bare finger on the metal-GO junction, trace amount of bio-electrolyte transports from the human skin to the first few GO layers at the interface of the junction (Figure 9.1a). In conjunction with the bioelectrolytes from the human skin, the solubilized GO ionizes to form a thin electrolyte layer between the reactive metal anode (e.g., aluminum or copper) and the GO cathode, generating electrochemical potentials that drive current flow through the external circuit and are detected by the voltmeter. In addition, the dissociated protons from the ionized carboxyl groups of GO diffuse from the ionized area close to the pressed electrode to the opposite electrode area across the GO bio-paper driven by the concentration gradient, forming the secondary potential gap between the two electrodes.[424] Therefore, even if the inert electrodes (e.g., Au and rGO) does not participate in the electrochemical reaction, smaller potential of the same order of magnitude is still generated due to the secondary diffusion of the protons. Moreover, the polarity of the proton diffusion current (I_{PD}) matches that of the electrochemical current (I_{EC}), enhancing the signal strength of the touching activation (Figure 9.1a).

Due to the large internal resistance of the GO bio-paper (around 30 MΩ), the short circuit current (I_{SC}) of the fully activated Al-GO junction is on the order of 50 nA, being too small to be effectively detected by usual means (**Figure 9.4**). While the open circuit voltage (V_{OC}) of the same fully activated Al-GO junction reaches around 850 mV, which is a huge potential level in terms of electrical signal that is easily measured and transduced.

Therefore, we take V_{OC} as the standard output for signal analysis (for simplicity, denoted as "voltage output" in the following discussions).

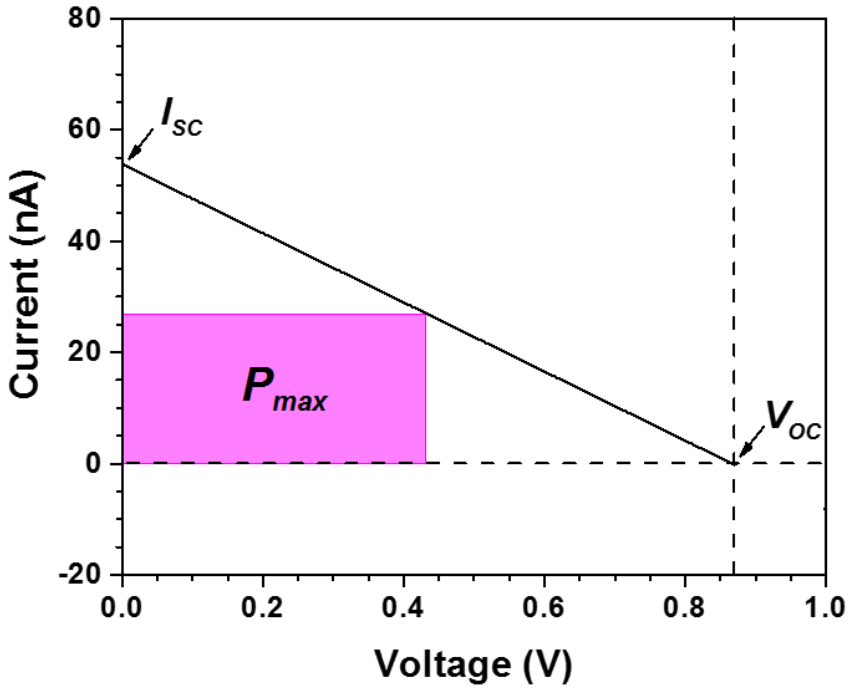

Figure 9.4 I-V output profile of a fully activated Al-GO junction, showing the maximum power output of this junction is around 12 nW.

To further illustrate the unique working mechanism of these novel hybrid sensing materials that respond to the micro-injection of bio-electrolytes, a few graphene based high-performance humidity sensors are discussed here for comparison. An impedance type polyelectrolyte/graphene bilayer humidity sensor has been reported to be able to measure ultra-low humidity level at 0.18 RH%, with the scarification of signal magnitude, output linearity, and response rate.[425] Zhao *et al.* recently reported an active humidity sensor using gradient rGO film, which records human breath humidity variation by potential pluses induced solely by the diffusion of dissociated protons.[424] However, the signal amplitude is one magnitude lower than the Al-GO junction demonstrated here, probably due to the extremely large internal impedance through the laminated graphene film, which limits its application for the necessity of signal processing components. Another ultrafast humidity sensor has been fabricated simply by depositing ultrathin GO films on printed silver electrodes. [426] Due to the fast adsorption and desorption of the water molecules on

the ultrathin GO film (tens of nanometers), the impedance of the device changes significantly and is calibrated to the environmental relative humidity. All of these examples limit themselves by ignoring the excellent chemical reactivity of GO, thus resulting in moderate signal strength or sensitivity for facile applications. Therefore, by utilizing the unique combination of the chemical activity and water affinity properties of GO, we demonstrate here a new category of humidity sensing hybrid materials that is capable of detecting trace amount of bio-moisture by bare finger touching and responding with 10^2 mV scale signals.

9.3.2 Influence of metal species to the tactile performance of metal-GO junctions

Figure 9.5a shows the voltage outputs of symmetrical metal-GO junction pairs made with various metals. All three symmetrical junction pairs show stable output signal levels throughout the prolonged activation period (60 s) for both the opposite junctions, demonstrating the human skin is an excellent bio-electrolyte source with continuous supply. The activation slope of the Al-GO junction is steep at 605 mV/s, and the deactivation slope of the same junction is 401 mV/s, showing excellent recovery rate for repeated activations. Al-GO junctions show the highest output of over 800 mV due to the largest reduction potential gap between aluminum and GO.[311] Copper can also reduce GO but has much smaller reduction potential gap, thus the output of the Cu-GO junction is moderate at around 300 mV.[354] In the case of Au-GO junctions, the output voltage is still notably high at around 250 mV probably due to the ion diffusions as proposed in the previous section. What is also important is that the output polarity of the opposite metal-GO junctions symmetrically coincides with that of the positive electrode, demonstrating the universal response of the metal-GO junctions without the need of individual calibration. It is also worth noting that by replacing human finger with finger shaped sponge wetted by deionized water, the voltage output is comparable to that actuated by human finger, indicating the water, rather than salt or oil on the skin, is the key component of the activation signal. However, extra electrolytes from the human skin also facilitates the sensing process.

It has been demonstrated that the gradient of the protons (i.e, dc_{H^+}/dL, where c_{H^+} is the initial concentration of protons upon dissolution and L is the diffusion distance) across the

two junctions is directly related to the diffusion induced voltage output, therefore the variation of the gap between the junctions may affect the overall electrical voltage output.[424] Figure 9.5b shows that by narrowing the gap between the Al-GO junctions from 24 to 6 mm, the voltage output increase linearly from 680 to 950 mV, resulting in a 14.4 mV/mm sensitivity to the gap distances. This correlation between the output amplitude and the junction distance further demonstrates the additional voltage contribution from the proton diffusion.

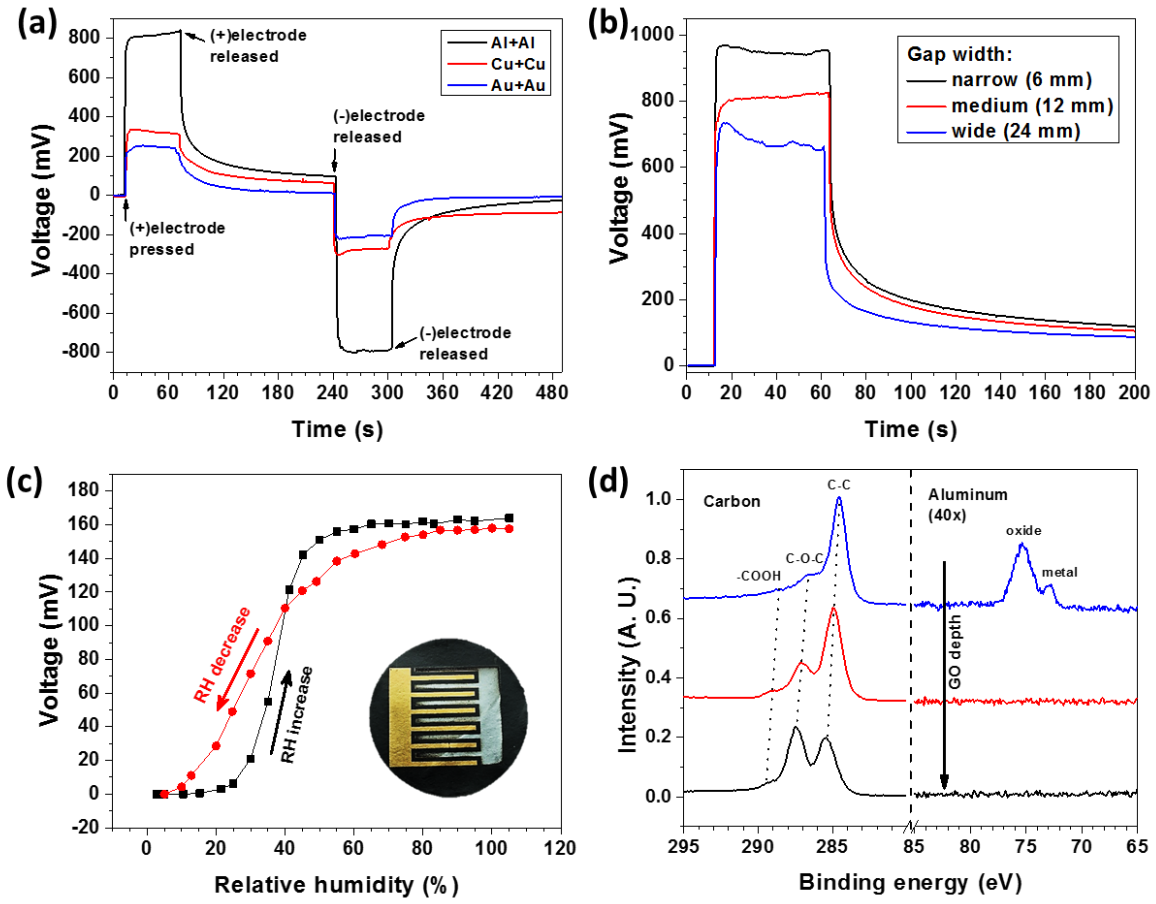

Figure 9.5 Open circuit voltage outputs of the metal-GO junction pairs with various (a) electrode metals and (b) gap widths. (c) The voltage response of an asymmetrical Au/Al-GO junction pair to humidity change (1 RH%/min), showing slight hysteresis due to the faster water adsorption than desorption (inset: optical photograph of the Ø37mm sample). (d) XPS spectra of an extensively actuated (around 5000 times) Al-GO junction at different depths from the Al/GO interface, indicating a reduced layer of GO underneath the Al coating.

Due to the large difference between the humidity output from the aluminum and gold (610 mV difference according to Figure 9.5a), asymmetrical Au/Al-GO junction pair has been tested to demonstrate a simple ambient humidity sensor (Figure 9.4c inset). The

interdigitated finger pattern for the metal layers is designed to maximize the perimeter of the junctions, where the water vapor gets transported to the metal-GO interface to initiate the electrochemical reaction. It needs to be noted that in the ambient humidity sensing setup, no proton diffusion contributes to the overall voltage output because the moisture absorption has no gradient over the lateral surface across the two junctions in the first place, generating no proton gradient to support the diffusion. When the relative humidity is slowly increased from 30 to 50 RH% by 1 RH%/min, the output voltage increases abruptly from almost 0 to 160 mV, indicating a fast while narrow adsorption window for the ambient water vapor (Figure 9.5c). When the air is slowly dried at the same rate, the humidity response of the asymmetrical Au/Al-GO junction pair show some hysteresis with wider desorption window between 80 and 10 RH%, indicating slower water desorption characteristic of GO.[426]

After prolonged humidity cycles, the GO layers underneath the aluminum coating have been characterized by the depth resolved X-ray photoelectron spectroscopy (XPS) (Figure 9.5d). It is obvious that the first few layers of GO in contact with the aluminum layer get fully reduced based on the extinction of the epoxy peak at around 286.5 eV.[102] With the progress of the depth profiling, deeper layers of GO gradually turn from completely reduced to partially reduced, and eventually to fully intact without signs of reduction. It is

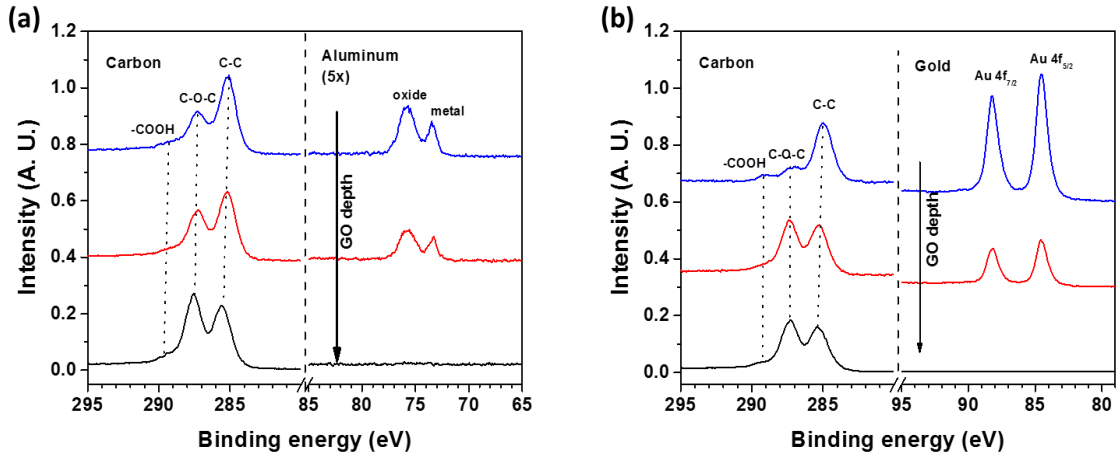

Figure 9.6 (a) XPS spectra of freshly fabricated Al-GO junction at different depths from the Al/GO interface, indicating a sub-nanometer layer of reduced graphene oxide at the Al/GO interface. The reduction of the thin graphene oxide layer at the interface is probably caused by the heat carried by the initial adsorption of the hot metal vapor during the electron beam evaporation process. The same phenomenon also happens to the extensively actuated (around 5000 times) Au-GO junction (shown in panel b).

also noteworthy that the XPS C1s spectra show slight blueshift as the probe approaching deeper, indicating progressive charging due to the removal of the electrically conductive reduced top layers. In comparison, only the very top layers of the GO show signs of reduction under freshly deposited aluminum layer, probably due to the thermal effect during the electron beam deposition process (**Figure 9.6**a). Therefore, the reduction of the GO layers is the direct evidence of the electrochemical reaction occurred during the humidity cycles and the touching activations. In addition, similar top-layer-confined reduction of GO is also observed underneath the extensively used gold electrode, confirming the chemical inertness of the gold electrode and the thermal reduction of the top GO layers when adsorbing the hot metal vapors during the electron beam evaporation (Figure 9.6b).

9.3.3 Tactile sensing stability of the metal-GO junctions

The sensing stability of the metal-GO junctions has been investigated by repeated actuations. **Figure 9.7**a and d show the scheme of the symmetrical Al-GO junction pair

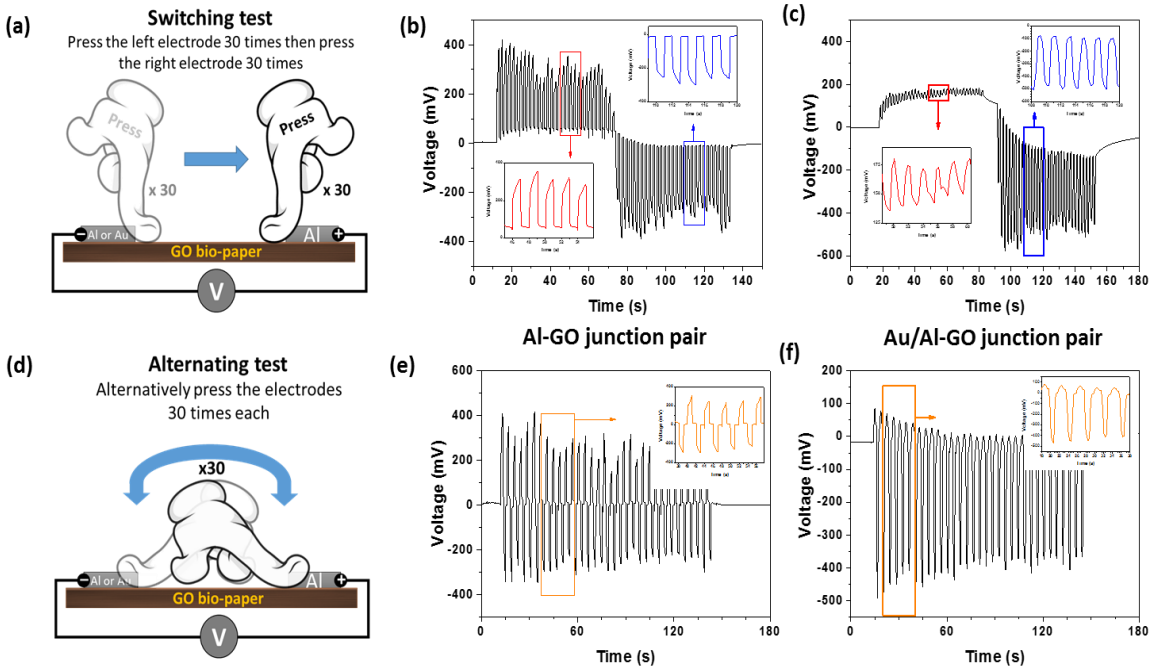

Figure 9.7 The (a) switching and (d) alternating tests for the stability of the metal-GO junctions as tactile sensing elements (the plus and minus signs on the contacts denotes the polarity of the measuring probes): open circuit voltage output of symmetrical Al-GO junction pair (b and e) and asymmetrical Au/Al-GO junction pair (c and f) under switching and alternating actuations, respectively. The insets show close views of detailed waveform as indicated by arrowed frames.

and the asymmetrical Au/Al-GO junction pair under two repeated actuation patterns of switching and alternating, respectively. For the switching tests, the positive junction is first repeatedly pressed by bare finger for 30 times and then the repeated presses were switched to the negative junction for another 30 times. The dwell and interval times are both 1 s. From Figure 9.7b we demonstrate the stable voltage output of 330±47 mV and -310±44 mV for the positive and negative Al-GO junction, respectively. The waveform of the signals (Figure 9.7b insets) shows distinct chisel shape with abrupt jump followed by a slower linear increase, and then a cliff drop to the baseline upon deactivation, being the result of the combination of different potential generating kinetics between the large potential jump due to the electrochemical reaction and the relatively smaller potential contribution from the proton diffusion. In addition, also due to the proton diffusion, the baseline of the device voltage output increased slowly and saturated at around 60 mV after repeated activations. When subjected to the alternating activations between the positive and the negative junctions, the output remains stable and the waveform keeps the chisel shape (Figure 9.7e). And due to the counterbalance between the proton diffusion in the opposite directions, the baseline is pinned at 0 mV in the alternating activation tests.

Similar stability tests have also been conducted to the symmetrical Cu-GO, Au-GO, and rGO-GO junction pairs (**Figure 9.8**). Comparable responses further demonstrate the excellent stability and the wide applicability of the operating mechanisms to electrically conductive material coatings either reactive or inert to GO. What is more interesting, by replacing the metal coatings with the rGO pattern of the same shape, the amplitude of the output peaks is identical to that of the Au-GO junction (50 mV), indicating that the universal diffusion mechanism of the protons supports the operation of the hybrid sensing materials when no reactive metal layers are available.

An asymmetrical Au/Al-GO junction pair similar to the one shown in Figure 9.5c is also fabricated to demonstrate the asymmetrical tactile output from the two junctions. It is worth noting that the humidity sensing design shown in Figure 9.5c is subject to the environmental humidity change, while the asymmetrical junction pair tested in this case receives bio-electrolyte injection from the finger touched area. Figure 9.7c and f show the switching and alternating tests in the same manner to those shown in Figure 9.7b and e,

respectively. For the asymmetrical Au/Al-GO junction pair, when activating the Au-GO junction, small peaks and large baseline shift are observed due to the sole proton diffusion effect. When the Al-GO junction is activated, much higher amplitudes of the peaks are present, which is typical for the Al-GO junction in the symmetrical junction pairs, indicating the independent operation of the two opposite junctions.

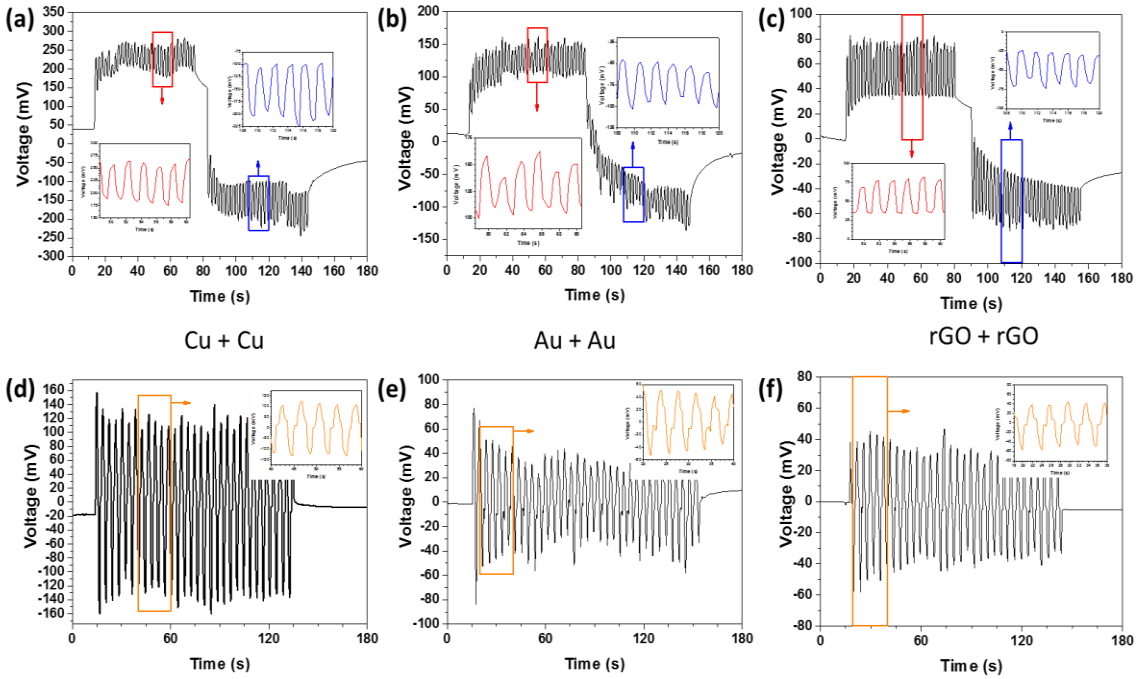

Figure 9.8 Open circuit voltage output of symmetrical Cu-GO junction pair (a and d), symmetrical Au-GO junction pair (b and e), and symmetrical rGO-GO junction pair (c and f) under repeating and alternating stimulations, respectively. The insets show close views of detailed waveform as indicated by arrowed frames.

The stability of the metal-GO junctions is also demonstrated by its irresponsiveness to mechanical deformation and false actuations that are not related to direct human touch. The junction responds normally to the bare finger touch on either of the two electrodes, but is inert to gloved finger touching. It is worth noting that the temperature elevations after the bare finger and gloved finger touching are identical based on the infrared imaging, ruling out the possible reason of thermally activated response (e.g. thermoelectricity) of the device. The inertness to the gloved finger touching is caused by the barricade of the body moisture by the nitrile rubber layer. Moreover, when bent or shaken, the device only outputs minimal background noise with the level of around 1% compared to that of the fully activated state, which is probably originated from the contact resistance undulation from the metal wire leads when deforming and easily isolated in signal identification.

9.3.4 Tactile frequency responses of the Al-GO junctions

Another critical parameter for tactile sensing materials is the responsiveness, or the maximum operation frequency. In order to test the responsiveness, we used a linear electrodynamic shaker for high actuation frequencies. Therefore, the activation frequency is precisely tunable and correlated with the response frequency (**Figure 9.9**). Figures 9a-e show the response waveform of the Al-GO junction subjected to 2, 5, 10, 15, and 20 Hz actuations, respectively. The waveforms are stable and uniform from 2 to 15 Hz with slight baseline upshift due to the relatively long relaxation time of the proton diffusion. When the activation frequency increases to 20 Hz, the waveform starts to become noisy probably due to the vigorous mechanical movement and saturated bio-electrolyte adsorption from the high-frequency repeated micro-injection. The coupling between the actuation and the response frequency has been plotted in Figure 9.9f in the form of Fourier transform of the response waveforms. The sharp peaks locate across the diagonal of the plot indicate robust correlation between the actuation and response signals. For lower frequency actuations (2, 4 and 10 Hz), higher orders of harmonic oscillation peaks are also prominent and evenly spaced, further indicating strong and strict coupling of the signals.

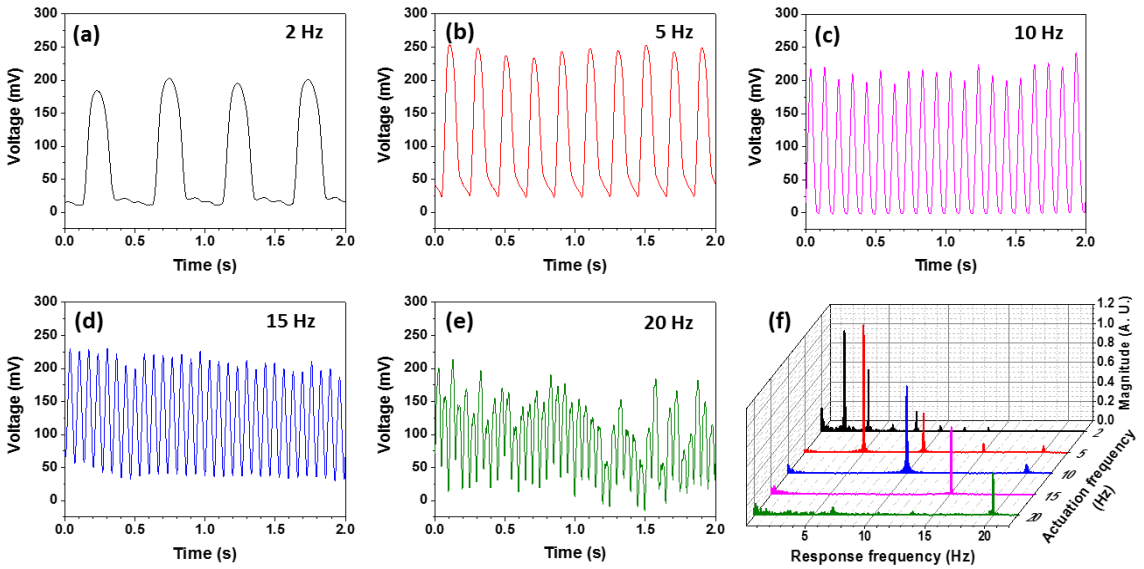

Figure 9.9 (a-e) Frequency variation test of the Al-GO junction, showing stable response to sinusoidal stimulations from 2 to 20 Hz. (f) The fast Fourier transform of the response signal based on the actuation frequency. Higher orders of harmonic response indicate a strong correlation between the input and output.

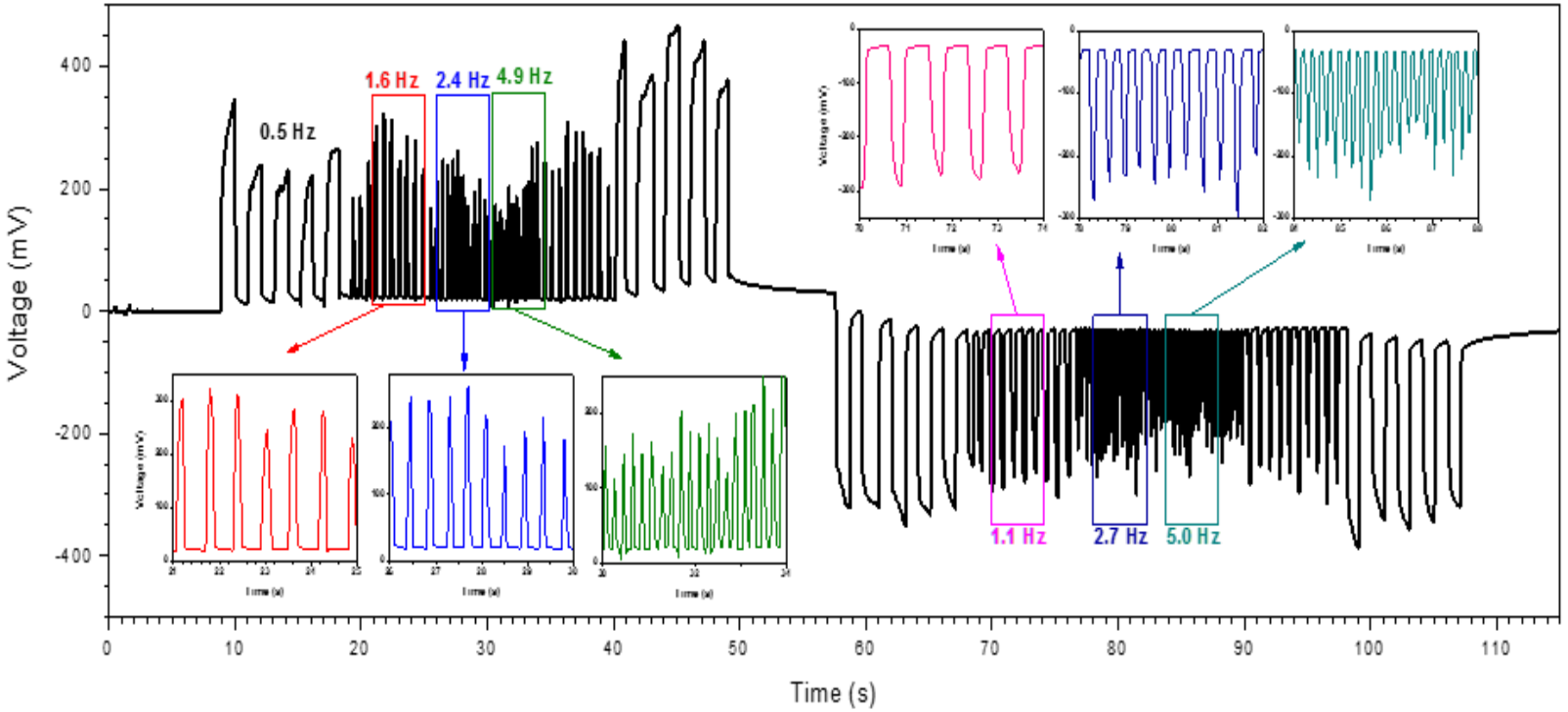

Figure 9.10 Continuous sense of finger presses with arbitrary frequency by the symmetrical Al-GO junction pair. Regardless of the polarity, the output is stable and slightly decreases in amplitudes with higher frequencies.

To further demonstrate the responsiveness of the tactile sensing metal-GO junctions, to real human finger actuations, the manual touching actuation of the tactile sensor has been tested and the result is shown in **Figure 9.10**. The device has been activated continuously in segments of various touching frequencies, the positive and negative responses are identical in terms of slight baseline shift and gradual decreasing peak amplitudes with higher actuation frequencies. The voltage output signal reliably records the human finger touching events at various frequencies from 0.5 to 5 Hz on both electrodes, demonstrating stable and directly interpretable monitoring of human-touch events. It is noteworthy that the waveform of the manual touching test is different from that of the linear motor actuations, because the movement of the linear motor is continuous following the sinusoidal pattern while the manual actuation roughly follows the square wave pattern.

9.3.5 Simplified two-dimensional tactile sensor array (electronic skin)

Conventionally, in order to fabricate electronic skins, matrices of individual sensing elements are patterned over a flexible surface and the number and size of the sensing elements determines the spatial resolution of the device. Utilizing the electrochemical touch sensing mechanism of the metal-GO junctions introduced in this research, two pairs of Al-GO junctions are capable of addressing nine tactile pixels (**Figure 9.11** and **Figure 9.12**). Specifically, each pair of orthogonally placed electrodes can output three potential levels (i.e., 1, 0, -1), therefore the two pairs of electrodes act as two ternary digits, which translates to 3x3 distinct states. To our surprise, although the two pairs of Al-GO junctions are deposited on the same piece of GO bio-paper substrate, minimal crosstalk happens for the simultaneous operation of these tactile sensors. The small leak signals to the inactive junction pair shown in Figure 9.12 are probably due to the slight shift of the touch point from the center of the designated areas, incurring concentration gradient diffusion of the protons to the neighboring junctions. Moreover, if the two pairs of metal-GO junctions are made by metals that have different output signals, the two voltage outputs could be easily added to realize single voltage level addressing of the 9 locations, further simplifying the signal analyzing components of the electronic skin. For instance, the horizontal symmetrical Al-GO junction pair integrates with the vertical symmetrical Cu-GO junction pair. Due to the inherent step difference of the voltage output from these two metal-GO

junctions (i.e., 800 mV for Al-GO and 300 mV for Cu-GO), the combined signal could be 1100, 300, -500, 800, 0, -800, 500, -300, and -1100 mV for positions 1-9, respectively.

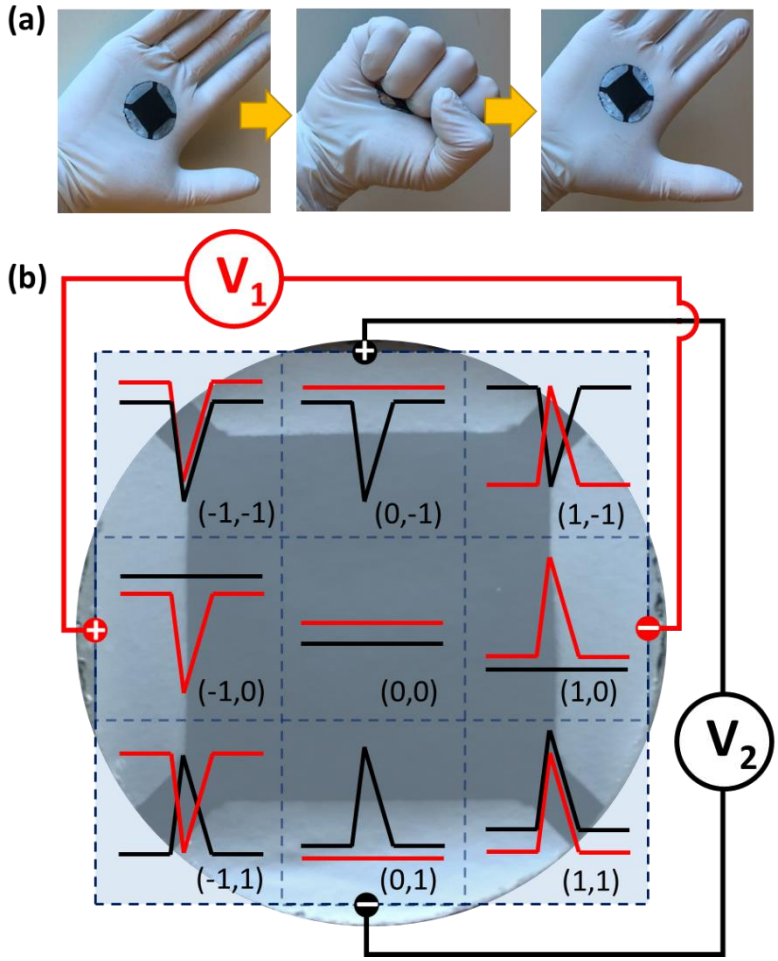

Figure 9.11 Two-dimensional touch sensing platform (electronic skin) shows highly independent open circuit voltage output for the two orthogonally orientated Al-GO junction pairs on the same piece of GO bio-paper substrate: (a) Excellent bending robustness of the electronic skin withstands repeated fisting in the palm (see Supporting Video S3); (b) diagram of the 2D sensing circuit and address allocations (the plus and minus signs on the contacts denotes the polarity of the measuring probes). The 2-digit trinary system is denoted as (V1, V2), and actual waveform of the distinctive response for the 9 locations could be found in Figure 9.12.

9.4 General comparison and conclusions

The benefit of self-powering for the sensors is of critical importance for the increasing requirements of mobile and wearable electronics. A paper based tactile sensor has been reported with the active polypropylene piezoelectric layer sandwiched between silver paste

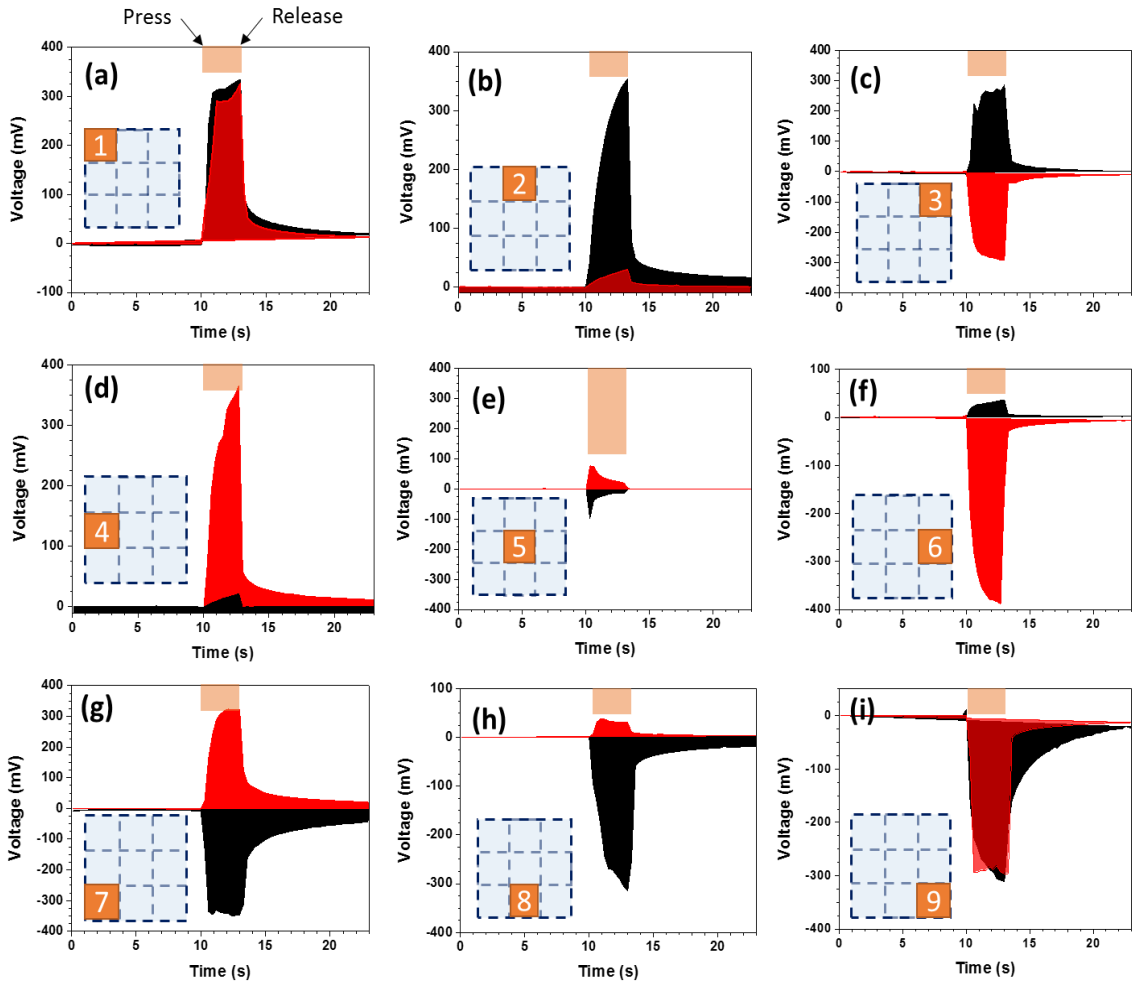

Figure 9.12 (a-i) waveform of the distinctive response for the 9 locations that are shown in Figure 5b. Each location was pressed for 3 seconds.

patterned regular paper substrates.[397] The sensor is self-powered with a maximum signal level of close to 2 V depending on actuation speed and force; and it performs robustly even after being cut in half. However, due to the inherent working principles of piezoelectricity, such tactile sensors only record the transient states of the activation and the signal decoupling between actuation speed and pressure remains a problem. Another self-powered electronic skin that senses human touch by thermoelectric effect has been reported based on rGO foam.[427] The signal level for normal human touch is around 200 nA and the signal strength is heavily dependent on the temperature gradient across the rGO foam, which is difficult to maintain in real-world field applications. Fan *et al.* have demonstrated a self-powered pressure sensor based on triboelectricity.[428] The maximum signal magnitude reached 18 V with the aid of nanostructured contact surfaces, but the transient

current output due to the contact electrification mechanism constrains its ability to monitor continuous pressure as a self-powered system.

Other than the self-powered touch sensors, it is still necessary to combine with some format of electric energy source for the proper functioning of the devices, significantly depleting the potential flexibility, portability and sustainability. Park *et al.* fabricated highly sensitive pressure sensors using polyaniline nanofibers and gold coated polydimethylsiloxane (PDMS) micropillars, which features excellent sensitivity (15 Pa) and high response rate (50 ms).[429] Another tactile sensor employing the micropillars concept uses the giant magneto-impedance mechanism, where the bending of the magnetized iron nanowire nanocomposite micropillars induces impedance change in the NiFe/Cu/NiFe laminated substrate even underwater.[430] By mimicking the interlocked epidermal-dermal layers of human skin, an electronic skin was made based on carbon nanotube filled elastomer, featuring multimodal sensing ability, which differentiates various wrist movements.[431] All these ultra-sensitive touch sensors are ideal for low-force applications, such as vital signs monitors and biomimetic robotics, but the sensing array involves tedious microfabrication and assembly process, incurring cost concerns for wide deployment.

Flexible sensors can also be made using metal nanoparticles embedded in polymeric matrix, responding to temperature, strain, volatile organic chemicals by altered electrical conductivity.[432, 433, 434] However, the poor dispersion and distribution of the nanoparticles severely limit the consistency and stability of such sensor. Moreover, due to the multi-parametric sensing characteristics (i.e., simultaneous response to multiple environmental changes), the decoupling of these stimuli could be of apex challenge. Recently, a multiplex graphitic carbon nitride (GCN) based multiplex sensor that can independently measure temperature, humidity, and stress in three modes has been reported.[435] Although the versatility and sensitivity of this flexible fiber-form sensor are impressive, the robustness of the nanoscale active GCN coating and signal strength should be continuously improved for smart textiles.

Chapter 10 General Discussions and Broader Impacts

10.1 General conclusions and discussion

We have successfully demonstrated the outstanding mechanical properties of graphene oxide-silk fibroin nanocomposites fabricated by SA-LbL and dSA-LbL assembly. Uniquely realized by the SA-LbL and further improved by the dSA-LbL, the dense network of weak interactions between the individual silk fibroin chains and graphene oxide surfaces facilitates the formation of strong molecular interphase zones of confined individual silk backbones, thus, dramatically enhancing the reinforcing effect. The outstanding mechanical properties of the ultrathin graphene oxide-silk fibroin nanocomposite membranes may inspire researchers of more combinations of functionalized components and these strong and flexible ultrathin membranes in their freely standing state can be valuable for prospective applications in sensing devices, protective molecular coatings, biological and chemical filters, cell protection and support, membranes for separation and delivery, energy harvesting and ion separation.

In addition, we demonstrated strong, tough and flexible laminated nanocomposites composed of rigid cellulose nanocrystal networks conformally wrapped by flexible graphene oxide sheets. The design proposed here combines two different classical reinforcing nanocomponents – stiff rodlike 1D cellulose nanocrystals, and strong but flexible 2D graphene oxide sheets – into one nanomaterial. This approach eliminates the overwhelming presence of the "soft and weak" polymer matrix, which is in this case repurposed to a molecular glue between two strong components. This combination of 2D flexible and 1D rigid reinforcing nanostructures promotes high mechanical strength along with excellent toughness, resulting in synergetic properties that cannot be achieved in previously reported graphene-based polymer nanocomposites. The illustrated summary of the mechanical properties of the nanocomposites developed in this study has been demonstrated in **Figure 10.1**. With outstanding mechanical properties and high flexibility

combined with high optical transparency in the visible range and high electrical conductivity, we suggest these unique material systems can serve in a broad range of technological applications, including ballistic protection, electromagnetic interference shielding, bio-fluid separation, and wearable electronic devices.

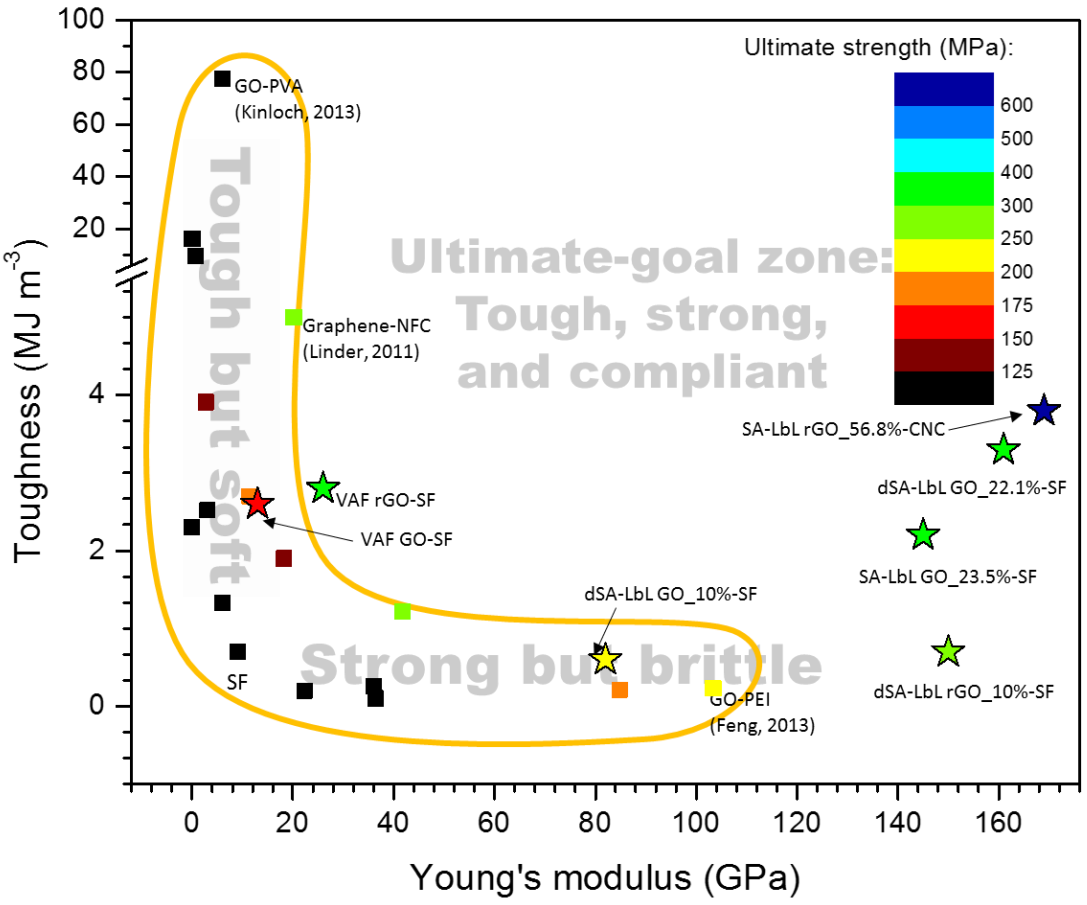

Figure 10.1 Summary of the mechanical properties from the nanocomposite materials in this research. Representative data points from recent publications are plotted and labeled in the figure for comparison. Our results are majorly located well beyond the boomerang shaped envelope of the conventional laminated nanocomposites.

Moreover, we demonstrated that the graphene oxide paper can effectively and selectively reduced by localized presence of aluminum under neutral aqueous conditions and at room temperature to highly conductive graphene paper not only just without compromising their mechanical integrity, but also further improving mechanical performance and making them stable in aqueous environment. The outstanding mechanical and electrical properties of the graphene-silk "paper" make them excellent candidates of structural and functional components, holding promising potentials in the emerging applications of protective

coatings, chemical barriers, electromagnetic interference shielding, sensory skin, and biodegradable, flexible, organic electronic components.

The fabrication of the highly conductive bio-bond graphene paper is facile and fast, and can be conducted under ambient wet conditions without the involvement of hazardous reagents. The electrical properties can be easily controlled by processing conditions in the ambient environment that are easily customized for different objectives and could be employed individually or combined to reveal the full spectrum of electrical and electronic properties in addition to the outstanding mechanical robustness, folding endurance, and flexibility of conducting sheets (more than 100 cm^2 surface area and higher). The lowering of the work function in the process of reduction is the first demonstration of such modification for the graphene papers. The metal-assisted electrochemical reduction of bio-bond graphene paper is efficient for the electrical modification of the bio-bond graphene paper. The versatility and environmental friendliness of this fabrication technique is suitable for production of flexible, conductive, and foldable thin films for large area flexible lightweight electronic components in the applications of sensing, wearable electronics, logic processing, and energy storage.

We have, for the first time, demonstrated flexible metal-GO hybrid materials for human-tactile sensing that are sensitive to the micro-injection of trace amount of bio-electrolyte and respond with high electrical potential signals. The human-tactile sensitive metal-GO junctions utilize the combination of the unique chemical activity and hydrophilicity of graphene oxide to generate close to 1000 mV electric signal through the synergistic power generation mechanisms of electrochemical reaction with active metal layers and the asymmetrical cation diffusions driven by the concentration gradient due to localized ionization. The metal-GO junctions show excellent stability of electrical potential response to repeated finger pressing, outstanding signal independency between the individual junctions, and high responsiveness to fast actuations.

The electronic skins fabricated following this materials design strategy for humidity sensing, especially the fast bio-tactile sensing applications are ready for scaling up. In addition, the electronic skins using the minimum two pairs of electrodes exhibits

outstanding versatility for human-machine interfacing with programmable signal levels. When compared to the other tactile bio-sensors, the concept introduced in this work is advantageous in facile fabrication, low cost, fast response, large continuous signal, and mechanical robustness, being promising for advanced applications in wearable bio-signal monitors, smart tagging, electronic skin, and portable/disposable electronics.

10.2 Significance and broader impact

10.2.1 Dispersion and distribution of the graphene nanofillers

A fine control of dispersion and distribution of the graphene nanofillers remains the major problem for the effective reinforcement of the mechanical properties and adding functional properties to the graphene-based nanocomposites. Distributed network morphology and suppressed flexible component aggregation enable the optimal exposure of the graphene surface to the polymer matrix. For these optimal dispersion levels, the interfacial binding can be maximized and interconnected morphology can be realized. The achievement of such optimal morphology represents a great challenge and indeed is an acute issue for the integration of graphene components that, considering their flexibility and high aspect ratio, can be easily folded, crumpled, and wrinkled by even modest shearing forces and complex force field distribution during processing.

To avoid the problems associated with of the inhomogeneous distribution and a coarse dispersion of graphene components by conventional mixing or the presence of small, broken or crumpled flakes by forcibly enhanced mixings, various assembling techniques and *in-situ* polymerization approached should be considered. One of them is LbL assembly, which is facilitated by alternative nanoscale assembly of the polymer and graphene components. The highly ordered LbL layered nanocomposite films are built through natural or force-assisted adsorption of complementary components. Although the LbL assemblies are advantageous in the maximized interfacial interactions between the nanocomponents and molecularly defined laminating structures, they are extremely slow by adding few nanometers each cycle and wasteful due to the excessive material removal during the spinning process.

Vacuum assisted formation of layered papers is another promising and practical approach. These techniques control the nanostructures of graphene-polymer nanocomposites from bottom up and result in optimized distribution and dispersion of components in a layered fashion thus enhancing interfacial interactions and mechanical performance. Vacuum filtration methods are fast and easily scaled up for mass production; it also does not waste any solid constituents in contrast to the SA-LbL approaches, but the internal structures suffers from the final drying effect to create inconsistencies such as voids or wrinkles, and the surface morphologies are largely dependent on the substance the filtrates are against, therefore the cost for the high-quality filters, such as porous alumina membranes, has to be considered for advanced applications.

10.2.2 Improving interactions between graphene materials and the biopolymer matrix

Although graphene has by far the best mechanical properties of all potential reinforcing components, the binding options are limited to weak van der Waals forces, hydrophobic interactions, and π-π interactions due to the homogeneous sp^2 carbon composition. These forces are generally too weak as the primary binding means and only π-π-interactions might be a promising candidate to assemble graphene and polymers with a strong interface. [133, 436] Therefore, enhanced functionalization of graphene components with proper surface and edge chemical groups must be considered in order to improve interfacial binding with various polymer matrices and implement reinforcing effects. To this end, graphene oxide sheets and other functionalized graphene-based components are considered as promising reinforcing agents.

Graphene oxide is a widely explored derivative of graphene with a lot of advantages over graphene itself from the prospective of nanocomposite design, including aqueous processibility, low cost, the ability to further functionalization, and large-scale production. The heterogeneous surfaces of these graphene derivatives caused by the heavy localized oxygen-containing groups might facilitate the diverse options for the strong interfacial binding. A whole class of polar interactions becomes available for designing new strong interfaces, which includes hydrogen bonding, Coulombic interactions, and polar interactions in addition to common covalent bonding and hydrophobic interactions. We

have successfully demonstrated that the biomacromolecules that show unique combination of heterogeneous domains bind strongly with graphene oxide through matching domain sizes and binding forces. By expanding and unfolding the molecule chains of proteins, the binding interactions can further be improved and the mechanical properties are pushed further over the border. We also explored the combination of the conventional nanofillers together with minimum amount of biopolymer binders that show excellent mechanical and electrical properties.

10.2.3 Controlled reduction of graphene oxide to highly conductive states in nanocomposites

It is well established that the next important property to be considered, electrical conductivity, is greatly compromised for graphene oxide by the scission of sp^2 bonds, high concentration of pinhole defects and surface oxidized functionalities. Therefore, for emerging applications, which require the ultimate conductivity of graphene-polymer nanocomposites, the graphene oxide has to be reduced through a variety of chemical and thermal methods before, during, and after nanocomposite fabrication. [66, 105, 106, 107, 346, 437, 438] Efficient reduction results in the partial restoration of pristine electrically conducting state of reduced graphene oxide sheets and graphene-polymer nanocomposites as a whole to a practically relevant high level.

The electrical conductivity may be induced to relatively high values, at least 15000 S m^{-1} which is high enough for many “soft” electronic applications such as those considered in flexible organic/polymer electronics and bioelectronics. The corresponding graphene-polymer semi-metallic materials can be considered for the integration into flexible electronic devices. It is also critically important that the mechanical properties of the reduced graphene can be improved as well due to the restoration of the sp^2 hybridized carbon network and reduction of surface defects. By controlling the reduction level of the graphene oxide in the polymer nanocomposites, both electrical and mechanical properties can be tuned up significantly to a level that is suitable for various structural and functional applications, such as sensors, flexible circuit substrates, and wearable electronics.

10.2.4 Future trends and suggestions

The combination between graphene oxide and biomaterials here and below is an ongoing research for wide spectrum of different academic interests and practical applications. We have demonstrated that by using silk as a bio-binder, graphene oxide flakes can be glued securely together and render excellent mechanical properties. Using molecular engineering approaches, various peptides and functional molecules could be synthesized to match better with the surface functionalities of the graphene oxide, resulting in further pushing over the bracket of the current limit for nanocomposites. By embedding multiscale unfolding secondary structures of the macromolecules, higher flexibility and toughness of the nanocomposite could be revisited. The current challenge for the robust nanocomposites is mainly on the extremely limited ultimate strains.

Further development in this direction may involve the multiplex interactions between the components of the nanocomposites. For example, the strong binding forces supports the stiffness of the material but are prone to permanent disruption upon large deformation; then the weak but dense secondary interactions will continue to support the mechanical integrity of the material with large strain. Therefore, the synergistic combination of the heterogeneous interactions could lead to the next-generation super-strong nanomembranes.

The surface coverage of the graphene materials in the LbL assemblies are not well controlled yet. Monolayer of graphene covering the surface in a close packed or “mosaic” pattern is highly desired but hard to achieve. LB assembly can partially resolve this problem but the process is extremely slow and the results vary from batch to batch, largely depending on the flake sizes and concentrations. Therefore, research that focuses on the surface distribution of 2D nanofillers on various surfaces (essentially various surface energies) are highly needed. In addition, VAF is great for semi-automated fabrication of laminated graphene oxide papers but the inherent micro-flux directed assembly on the filter surface causes self-constrained wrinkles that are inevitable and undermine the mechanical strength of the films. Either pre- or post-treatment of the graphene papers that could be flattened to “wrinkle-free” states is highly desired for improved mechanical and electrical properties of the products.

On the macroscale assembly of the nanocomposites, new methods that are both fast and efficient to combine various nanocomponents are to be developed. LbL assemblies are precise but slow, VAF is relatively faster but the microstructure is commonly not well defined. Industrialized techniques such as freeze drying mold casting are both promising techniques for consideration, but significant modifications are definitely needed to meet the high anticipation in the lab research. For example, hydrothermal treatment and then freeze drying of the mixture of the graphene oxide and silk fibroin is an excellent method to quench the nano- and micro-structures of the stable graphene oxide-silk fibroin complex, and the highly porous nanocomposite aerogel should be post-treated to remove the air voids to reestablish the mechanical integrity and electrical properties.

The functional properties of graphene oxide mainly base on the restoration of its electrical properties. Although the current metal-assisted reduction technique is versatile and efficient for this task, the applicability of the high-purity metal coating still needs significant improvement. Also, the localization of the reduced graphene oxide as confined by the metal coating pattern is the major obstacle to be removed before achieving high-resolution, strictly defined conducting paths on the surface of graphene oxide films. Adopted form the metal nano-rod growth techniques, electric field direction of the free electrons is a promising method to confine the reduction path strictly to the z-direction of the films. With large enough electric potential applied along the through-thickness direction of the film while in the electrolyte media, the electrons driven by the external electrical field directs, if not restricts, the reduction only in the z-direction.

Great attention should also be paid to the unique combination of electrical, chemical, and mechanical properties of graphene oxide bio-papers for possible discovery of new functional materials based on it. For example, since the metal-GO junction could sense humidity by enhanced diffusion and electrochemical reactions, the sensing of other volatile organic compounds (VOCs) is highly possible due to the great dissolvability of GO in many alcohols and organic solvents. Specific sensing and giant responses of such metal-GO junctions could be potential chemical sensors or biological cue sensors for a wider applications.

Graphene based bio-nanocomposites hold promising potentials for the flexible and bioelectronics applications, including wearable bio-signal monitors, smart tagging, electronic skin, and portable/disposable electronics. The mechanical flexibility and robustness, in combination with the high and programmable electrical conductivity, make graphene based bio-nanocomposite thin films excellent platform for a whole spectrum of electronic designs and functionalities, which are easily adopted from the classical microelectronics library. Being a new class of materials, there are countless opportunities, besides the examples demonstrated in this dissertation, for researches to explore, optimize, and innovate in all the directions of energy generation, energy storage, sensing, actuation, and finally the integration of the complete flexible bioelectronics system that is self-sustaining, self-powering, highly sensitive to multiplex stimuli, and implantable for the better life quality of human being.

Dissemination of work

This work has been distributed to the research community by the following publications and presentations.

Publications

[1] R. Xiong, **K. Hu,** R. Ma, C. Liu, X. Zhang, V. V. Tsukruk, *Ultrarobust Transparent Cellulose Nanocrystal-Graphene Membranes with High Electrical Conductivity,* Advanced Materials, **2015** *DOI: 10.1002/adma.201504438*

[2] C.Ye, S. T. Malak, **K. Hu**, W. Wu, V. V. Tsukruk, *Cellulose Nanocrystal Microcapsules as Tunable Cages for Nano- and Microparticles, ACS Nano* **2015**;9:10887-95.

[3] **K. Hu**, V. V. Tsukruk, *Tuning the Electronic Properties of Robust Graphene Biopapers by Spontaneous Electrochemical Reduction: from Insulators to Flexible Semi-Metals*, Chemistry of Materials **2015**;27:6717-29.

[4] Y. Yin*, **K. Hu***, A. M. Grant, Y. Zhang, V. V. Tsukruk, *Biopolymeric Nanocomposites with Enhanced Interphases*, Langmuir, **2015**;31:10859-70.

[5] **K. Hu**, D. D. Kulkarni, I. Choi, V. V. Tsukruk. ***Graphene-Polymer Nanocomposites for Structural and Functional Applications***. Progress in Polymer Science **2014**;39:1934-72. (Invited review)

[6] D. D. Kulkarni, S. Kim, M. Chyasnavichyus, **K. Hu**, A. G. Fedorov, V. V. Tsukruk. *Chemical Reduction of Individual Graphene Oxide Sheets as Revealed by Electrostatic Force Microscopy*. Journal of the American Chemical Society **2014**;136:6546-9.

[7] **K. Hu**, L. S. Tolentino, D. D. Kulkarni, C. Ye, S. Kumar, V. V. Tsukruk. *Written-in Conductive Patterns on Robust Graphene Oxide Biopaper by Electrochemical Microstamping.* Angewandte Chemie International Edition **2013**;52:13784-8. **(Very Important Paper)**

[8] **K. Hu**, M. K. Gupta, D. D. Kulkarni, V. V. Tsukruk. *Ultra-Robust Graphene Oxide-Silk Fibroin Nanocomposite Membranes.* Advanced Materials **2013**;25:2301-7.

[9] **K. Hu**, R. Xiong, H. Guo, R. Ma, S. Zhang, Z. L. Wang, V. V. Tsukruk, *Self-Powered Flexible Touch Sensor Triggered by Moisture Injection,* Advanced Materials *Submitted.*

[10] W. Wu*, **K. Hu***, H. Guo, A. M. Grant, Z. Wen, V. V. Tsukruk, Z. L. Wang, *Biodegradable Platform of Triboelectric Nanogenerator Featuring Tunable Output*, *in preparation*.

* These authors contribute equally to the work.

Provisional patent applications

[1] **K. Hu**, V. V. Tsukruk **–** "A Novel and Patternable Technique for Eco-Friendly Reduction of Graphene Oxide Films." EFS ID: 20189693

[2] **K. Hu**, V. V. Tsukruk – "Self-Powered Flexible Tactile Sensor Array with Exclusive Bio-Touch Sensitivity." *Submitted*.

Presentations

[1] "*Conductive Micropatterns in Graphene Oxide-Silk Fibroin Nanocomposites via Photolithography-Guided Electrochemical Reduction*", **oral presentation**, MRS Fall Meeting, Boston, MA 2015

[2] "*Break the Rule of Mixture: Ultra-Strong and Tough Biopolymeric Nanocomposites by Molecular Interphaseal Reinforcement*", **oral presentation***, MRS Fall Meeting, Boston, MA 2015

[3] "*Exceptional Mechanical Performance of Cellulose Nanocrystal - Graphene Oxide Nanomembranes: a Combination of 1D and 2D Nanofillers*", **oral presentation***, MRS Fall Meeting, Boston, MA 2015

[4] "*Giant Intrinsic Shifts of Electronic Properties in Graphene Paper by Spontaneous Electrochemical Restoration*", **poster***, MRS Fall Meeting, Boston, MA 2015

[5] "*Integrated Micro-Supercapacitors in Bio-inspired Graphene Oxide-Silk Fibroin Nanocomposites*", **poster**, MRS Fall Meeting, Boston, MA 2015

[6] *"Graphene-Polymer Nanocomposites for Structural and Functional Applications"*, **featured talk***, Chinese Academy of Sciences, Suzhou, China 2015

[7] *"Interphase Revisited – The Key to Ultra-Robust Graphene Oxide-Polymer Nanocomposites",* **invited talk***, the 38th Michigan Macro Symposium, Ann Arbor, MI 2014

[8] *"Ultra-Robust Laminated Graphene Oxide-Silk Nanocomposite Membranes Reinforced by 'Frozen' Interphases"*, **oral presentation***, LbL Assemblies: Science and Technology Conference, Hoboken, NJ 2014

[9] "*Ultrastrong Conductive Flexible Biographene Paper with Distributed Interphases*", **invited talk**, XXIII International Materials Research Congress, Cancun, Mexico 2014

[10] "*Biodegradable and Highly Conductive Reduced Graphene Oxide Nanocomposite Films Fabricated by a Facile, Green and Energy Efficient Strategy*", **oral presentation*,** MRS Fall Meeting, Boston, MA 2013

[11] "Extremely robust silk ionomer/graphene oxide microcapsules with tunable permeability", **poster**, 247th ACS National Meeting, Denver, CO 2014

[12] *"Behavior of LbL Graphene Oxide-Protein Nanomembranes as Manipulated by the Secondary Structures of Proteins"*, **poster***, LbL Assemblies: Science and Technology Conference, Hoboken, NJ 2014

[13] *"Robust Graphene Biopapers with Written-In Microelectronic Components Fabricated by Vacuum Assisted Flocculation and a Green, High-Resolution Reduction Strategy"*, **poster***, LbL Assemblies: Science and Technology Conference, Hoboken, NJ 2014

[14] *"Road to the Next Generation Flexi-electronics"*, **poster*,** MSE Graduate Poster Competition, Georgia Tech 2014

[15] "*Filtration Self-Assembly Strong and Tough Graphene Oxide – Silk Fibroin Nanocomposite Films Fabricated by pH-Assisted Vacuum Filtration*", **poster*,** MRS Fall Meeting, Boston, MA *2013*

[16] *"Using Layer-by-Layer Technique to Fabricate Graphene Oxide-Silk Fibroin Nanomembranes with Record-Breaking Mechanical Properties"*, **poster***, MSE Graduate Poster Competition, Georgia Tech, 2013

* Presented in person (12 total).

Awards and Recognitions

- Center of Organic Photonics and Electronics Fellowship, Georgia Tech 2015
- Chinese Government Award for Outstanding Self-Financed Students Abroad, 2015
- Invited Talk (two students nationwide) at the 38th Michigan Macro Symposium, University of Michigan 2014
- 2nd runner-up in Georgia Tech Polymer Network Poster Competition, Georgia Tech 2014
- 1st place in Energy & Electronic Materials, MSE Poster Competition, Georgia Tech 2014
- 1st place in Polymers, MSE Poster Competition, Georgia Tech 2013

References

[1] Baekeland, L. H. The Synthesis, Constitution, and Uses of Bakelite. *Journal of Industrial & Engineering Chemistry* **1909**, *1*, 149-161.

[2] Sperling, L. H. *Introduction to Physical Polymer Science*. 4th ed.; John Wiley & Sons, Inc.: Hoboken, **2006**.

[3] Kulkarni, D. D.; Choi, I.; Singamaneni, S. S.; Tsukruk, V. V. Graphene Oxide−Polyelectrolyte Nanomembranes. *ACS Nano* **2010**, *4*, 4667-4676.

[4] Kharlampieva, E.; Kozlovskaya, V.; Gunawidjaja, R.; Shevchenko, V. V.; Vaia, R.; Naik, R. R.; Kaplan, D. L.; Tsukruk, V. V. Flexible Silk–Inorganic Nanocomposites: From Transparent to Highly Reflective. *Adv. Funct. Mater.* **2010**, *20*, 840-846.

[5] Jiang, C.; Wang, X.; Gunawidjaja, R.; Lin, Y. H.; Gupta, M. K.; Kaplan, D. L.; Naik, R. R.; Tsukruk, V. V. Mechanical Properties of Robust Ultrathin Silk Fibroin Films. *Adv. Funct. Mater.* **2007**, *17*, 2229-2237.

[6] Podsiadlo, P.; Kaushik, A. K.; Arruda, E. M.; Waas, A. M.; Shim, B. S.; Xu, J.; Nandivada, H.; Pumplin, B. G.; Lahann, J.; Ramamoorthy, A.; Kotov, N. A. Ultrastrong and Stiff Layered Polymer Nanocomposites. *Science* **2007**, *318*, 80-83.

[7] Xue, L.; Dai, S.; Li, Z. Biodegradable Shape-Memory Block Co-Polymers for Fast Self-Expandable Stents. *Biomaterials* **2010**, *31*, 8132-8140.

[8] Li, C.; Adamcik, J.; Mezzenga, R. Biodegradable Nanocomposites of Amyloid Fibrils and Graphene with Shape-Memory and Enzyme-Sensing Properties. *Nat. Nanotechnol.* **2012**, *7*, 421-427.

[9] Bovey, F. *Macromolecules: An Introduction to Polymer Science*. Academic Press: New York, **1979**.

[10] Ram, A. *Fundamentals of Polymer Engineering*. Plenum Press: New York, **1997**.

[11] Painter, P. C.; Coleman, M. M. *Fundamentals of Polymer Science: An Introductory Text*. Technomic Publishing Company: Chicago, **1997**.

[12] Ebewele, R. O. *Polymer Science and Technology*. CRC Press: London, **2000**.

[13] Brazel, C. S.; Rosen, S. L. *Fundamental Principles of Polymeric Materials*. Wiley: Hoboken, **2012**.

[14] Dongyu, C.; Kamal, Y.; Mo, S. The Mechanical Properties and Morphology of a Graphite Oxide Nanoplatelet/Polyurethane Composite. *Nanotechnology* **2009**, *20*, 085712.

[15] Kai, W.; Hirota, Y.; Hua, L.; Inoue, Y. Thermal and Mechanical Properties of a Poly(ϵ-Caprolactone)/Graphite Oxide Composite. *J. Appl. Polym. Sci.* **2008**, *107*, 1395-1400.

[16] Fang, M.; Zhang, Z.; Li, J.; Zhang, H.; Lu, H.; Yang, Y. Constructing Hierarchically Structured Interphases for Strong and Tough Epoxy Nanocomposites by Amine-Rich Graphene Surfaces. *J. Mater. Chem.* **2010**, *20*, 9635-9643.

[17] Bao, C.; Guo, Y.; Song, L.; Kan, Y.; Qian, X.; Hu, Y. In Situ Preparation of Functionalized Graphene Oxide/Epoxy Nanocomposites with Effective Reinforcements. *J. Mater. Chem.* **2011**, *21*, 13290-13298.

[18] Bates, F. S.; Fredrickson, G. H. Block Copolymer Thermodynamics: Theory and Experiment. *Annu. Rev. Phys. Chem.* **1990**, *41*, 525-557.

[19] Lazzari, M.; López-Quintela, M. A. Block Copolymers as a Tool for Nanomaterial Fabrication. *Adv. Mater.* **2003**, *15*, 1583-1594.

[20] Gröschel, A. H.; Löbling, T. I.; Petrov, P. D.; Müllner, M.; Kuttner, C.; Wieberger, F.; Müller, A. H. E. Janus Micelles as Effective Supracolloidal Dispersants for Carbon Nanotubes. *Angew. Chem. Int. Ed.* **2013**, *52*, 3602-3606.

[21] Béguin, F.; Presser, V.; Balducci, A.; Frackowiak, E. Carbons and Electrolytes for Advanced Supercapacitors. *Adv. Mater.* **2014**, *26*, 2219-2251.

[22] Sun, H.; Xu, Z.; Gao, C. Multifunctional, Ultra-Flyweight, Synergistically Assembled Carbon Aerogels. *Adv. Mater.* **2013**, *25*, 2554-2560.

[23] Jay, S. M.; Shepherd, B. R.; Bertram, J. P.; Pober, J. S.; Saltzman, W. M. Engineering of Multifunctional Gels Integrating Highly Efficient Growth Factor Delivery with Endothelial Cell Transplantation. *FASEB J.* **2008**, *22*, 2949-2956.

[24] Kim, U.-J.; Park, J.; Li, C.; Jin, H.-J.; Valluzzi, R.; Kaplan, D. L. Structure and Properties of Silk Hydrogels. *Biomacromolecules* **2004**, *5*, 786-792.

[25] Das, P.; Schipmann, S.; Malho, J.-M.; Zhu, B.; Klemradt, U.; Walther, A. Facile Access to Large-Scale, Self-Assembled, Nacre-Inspired, High-Performance Materials with Tunable Nanoscale Periodicities. *ACS Appl. Mater. Interfaces* **2013**, *5*, 3738-3747.

[26] Mallick, P. K. *Fiber-Reinforced Composites: Materials, Manufacturing, and Design*. Marcel Dekker Inc.: New York, **1993**.

[27] Ajayan, P. M.; Schadler, L. S.; Braun, P. V. *Nanocomposite Science and Technology*. Wiley: Weinheim, **2006**.

[28] Ko, H.; Jiang, C.; Shulha, H.; Tsukruk, V. V. Carbon Nanotube Arrays Encapsulated into Freely Suspended Flexible Films. *Chem. Mater.* **2005**, *17*, 2490-2493.

[29] Cheng, Q.; Wang, B.; Zhang, C.; Liang, Z. Functionalized Carbon-Nanotube Sheet/Bismaleimide Nanocomposites: Mechanical and Electrical Performance Beyond Carbon-Fiber Composites. *Small* **2010**, *6*, 763-767.

[30] Mamedov, A. A.; Kotov, N. A. Free-Standing Layer-by-Layer Assembled Films of Magnetite Nanoparticles. *Langmuir* **2000**, *16*, 5530-5533.

[31] Aroca, R. F.; Goulet, P. J. G.; dos Santos, D. S.; Alvarez-Puebla, R. A.; Oliveira, O. N. Silver Nanowire Layer-by-Layer Films as Substrates for Surface-Enhanced Raman Scattering. *Anal. Chem.* **2004**, *77*, 378-382.

[32] Kovtyukhova, N. I.; Martin, B. R.; Mbindyo, J. K. N.; Smith, P. A.; Razavi, B.; Mayer, T. S.; Mallouk, T. E. Layer-by-Layer Assembly of Rectifying Junctions in and on Metal Nanowires†. *J. Phys. Chem. B* **2001**, *105*, 8762-8769.

[33] Podsiadlo, P.; Tang, Z.; Shim, B. S.; Kotov, N. A. Counterintuitive Effect of Molecular Strength and Role of Molecular Rigidity on Mechanical Properties of Layer-by-Layer Assembled Nanocomposites. *Nano Lett.* **2007**, *7*, 1224-1231.

[34] Sun, X.; Sun, H.; Li, H.; Peng, H. Developing Polymer Composite Materials: Carbon Nanotubes or Graphene? *Adv. Mater.* **2013**, *25*, 5153-5176.

[35] Shi, Z.; Chen, X.; Wang, X.; Zhang, T.; Jin, J. Fabrication of Superstrong Ultrathin Free-Standing Single-Walled Carbon Nanotube Films Via a Wet Process. *Adv. Funct. Mater.* **2011**, *21*, 4358-4363.

[36] Mamedov, A. A.; Kotov, N. A.; Prato, M.; Guldi, D. M.; Wicksted, J. P.; Hirsch, A. Molecular Design of Strong Single-Wall Carbon Nanotube/Polyelectrolyte Multilayer Composites. *Nat. Mater.* **2002**, *1*, 190-194.

[37] Shim, B. S.; Zhu, J.; Jan, E.; Critchley, K.; Ho, S.; Podsiadlo, P.; Sun, K.; Kotov, N. A. Multiparameter Structural Optimization of Single-Walled Carbon Nanotube Composites: Toward Record Strength, Stiffness, and Toughness. *ACS Nano* **2009**, *3*, 1711-1722.

[38] Jalili, R.; Aboutalebi, S. H.; Esrafilzadeh, D.; Konstantinov, K.; Moulton, S. E.; Razal, J. M.; Wallace, G. G. Organic Solvent-Based Graphene Oxide Liquid Crystals: A Facile Route toward the Next Generation of Self-Assembled Layer-by-Layer Multifunctional 3d Architectures. *ACS Nano* **2013**, *7*, 3981-3990.

[39] Eitan, A.; Fisher, F. T.; Andrews, R.; Brinson, L. C.; Schadler, L. S. Reinforcement Mechanisms in Mwcnt-Filled Polycarbonate. *Compos. Sci. Technol.* **2006**, *66*, 1162-1173.

[40] Gunawidjaja, R.; Jiang, C.; Peleshanko, S.; Ornatska, M.; Singamaneni, S.; Tsukruk, V. V. Flexible and Robust 2d Arrays of Silver Nanowires Encapsulated within Freestanding Layer-by-Layer Films. *Adv. Funct. Mater.* **2006**, *16*, 2024-2034.

[41] Jiang, C.; Markutsya, S.; Tsukruk, V. V. Compliant, Robust, and Truly Nanoscale Free-Standing Multilayer Films Fabricated Using Spin-Assisted Layer-by-Layer Assembly. *Adv. Mater.* **2004**, *16*, 157-161.

[42] Markutsya, S.; Jiang, C.; Pikus, Y.; Tsukruk, V. V. Freely Suspended Layer-by-Layer Nanomembranes: Testing Micromechanical Properties. *Adv. Funct. Mater.* **2005**, *15*, 771-780.

[43] Wang, J.; Cheng, Q.; Lin, L.; Chen, L.; Jiang, L. Understanding the Relationship of Performance with Nanofiller Content in the Biomimetic Layered Nanocomposites. *Nanoscale* **2013**, *5*, 6356-6362.

[44] R. J. Moon, A. Martini, J. Nairn, J. Simonsen, J. Youngblood, *Chem. Soc. Rev.* **2011**, 40, 3941.

[45] D. Klemm, F. Kramer, S. Moritz, T. Lindström, M. Ankerfors D.Gray, A. Dorris, *Angew. Chem. Int. Ed.* **2011**, 50, 5438.

[46] Y. Habibi, L. A. Lucia, O. J. Rojas, *Chem. Rev.* **2010**, 110, 3479.

[47] B. Wicklein, A. Kocjan, G. Salazar-Alvarez, F. Carosio, G. Camino, M. Antonietti, L.Bergström, *Nature Nanotech.* **2015**, 10, 277.

[48] M. M. Hamedi, A. Hajian, A. B. Fall, K. Håkansson, M. Salajkova, F. Lundell, L. Wågberg, L. A. Berglund, *ACS Nano* **2014**, 8, 2467.

[49] Luzinov, I.; Minko, S.; Tsukruk, V. V. Responsive Brush Layers: From Tailored Gradients to Reversibly Assembled Nanoparticles. *Soft Matter* **2008**, *4*, 714-725.

[50] Kharlampieva, E.; Zimnitsky, D.; Gupta, M.; Bergman, K. N.; Kaplan, D. L.; Naik, R. R.; Tsukruk, V. V. Redox-Active Ultrathin Template of Silk Fibroin: Effect of Secondary Structure on Gold Nanoparticle Reduction. *Chem. Mater.* **2009**, *21*, 2696-2704.

[51] Corbierre, M. K.; Cameron, N. S.; Sutton, M.; Mochrie, S. G. J.; Lurio, L. B.; Rühm, A.; Lennox, R. B. Polymer-Stabilized Gold Nanoparticles and Their Incorporation into Polymer Matrices. *J. Am. Chem. Soc.* **2001**, *123*, 10411-10412.

[52] Hussain, I.; Brust, M.; Papworth, A. J.; Cooper, A. I. Preparation of Acrylate-Stabilized Gold and Silver Hydrosols and Gold−Polymer Composite Films. *Langmuir* **2003**, *19*, 4831-4835.

[53] Hou, Y.; Cheng, Y.; Hobson, T.; Liu, J. Design and Synthesis of Hierarchical Mno2 Nanospheres/Carbon Nanotubes/Conducting Polymer Ternary Composite for High Performance Electrochemical Electrodes. *Nano Lett.* **2010**, *10*, 2727-2733.

[54] Beek, W. J. E.; Wienk, M. M.; Janssen, R. A. J. Efficient Hybrid Solar Cells from Zinc Oxide Nanoparticles and a Conjugated Polymer. *Adv. Mater.* **2004**, *16*, 1009-1013.

[55] Kabra, D.; Song, M. H.; Wenger, B.; Friend, R. H.; Snaith, H. J. High Efficiency Composite Metal Oxide-Polymer Electroluminescent Devices: A Morphological and Material Based Investigation. *Adv. Mater.* **2008**, *20*, 3447-3452.

[56] Sirisinha, C.; Prayoonchatphan, N. Study of Carbon Black Distribution in Br/Nbr Blends Based on Damping Properties: Influences of Carbon Black Particle Size, Filler, and Rubber Polarity. *J. Appl. Polym. Sci.* **2001**, *81*, 3198-3203.

[57] Shamir, D.; Siegmann, A.; Narkis, M. Vibration Damping and Electrical Conductivity of Styrene–Butyl Acrylate Random Copolymers Filled with Carbon Black. *J. Appl. Polym. Sci.* **2010**, *115*, 1922-1928.

[58] Hu, K.; Chung, D. D. L. Flexible Graphite Modified by Carbon Black Paste for Use as a Thermal Interface Material. *Carbon* **2011**, *49*, 1075-1086.

[59] Friddle, R. W.; Lemieux, M. C.; Cicero, G.; Artyukhin, A. B.; Tsukruk, V. V.; Grossman, J. C.; Galli, G.; Noy, A. Single Functional Group Interactions with Individual Carbon Nanotubes. *Nat. Nanotechnol.* **2007**, *2*, 692-697.

[60] Grady, B. P. *Carbon Nanotube-Polymer Composites: Manufacture, Properties, and Applications*. Wiley: Hoboken, **2011**.

[61] Koning, C.; Grossiord, N.; Hermant, M. C. *Polymer Carbon Nanotube Composites: The Polymer Latex Concept*. Pan Stanford Publishing: Singapore, **2012**.

[62] Coleman, J. N.; Khan, U.; Blau, W. J.; Gun'ko, Y. K. Small but Strong: A Review of the Mechanical Properties of Carbon Nanotube–Polymer Composites. *Carbon* **2006**, *44*, 1624-1652.

[63] Bauhofer, W.; Kovacs, J. Z. A Review and Analysis of Electrical Percolation in Carbon Nanotube Polymer Composites. *Compos. Sci. Technol.* **2009**, *69*, 1486-1498.

[64] Pandey, G.; Thostenson, E. T. Carbon Nanotube-Based Multifunctional Polymer Nanocomposites. *Polym. Rev. (Philadelphia, PA, U. S.)* **2012**, *52*, 355-416.

[65] Britnell, L.; Ribeiro, R. M.; Eckmann, A.; Jalil, R.; Belle, B. D.; Mishchenko, A.; Kim, Y.-J.; Gorbachev, R. V.; Georgiou, T.; Morozov, S. V.; Grigorenko, A. N.; Geim, A. K.; Casiraghi, C.; Neto, A. H. C.; Novoselov, K. S. Strong Light-Matter Interactions in Heterostructures of Atomically Thin Films. *Science* **2013**, *340*, 1311-1314.

[66] El-Kady, M. F.; Kaner, R. B. Scalable Fabrication of High-Power Graphene Micro-Supercapacitors for Flexible and on-Chip Energy Storage. *Nat. Commun.* **2013**, *4*, 1475.

[67] Kim, K. S.; Zhao, Y.; Jang, H.; Lee, S. Y.; Kim, J. M.; Kim, K. S.; Ahn, J.-H.; Kim, P.; Choi, J.-Y.; Hong, B. H. Large-Scale Pattern Growth of Graphene Films for Stretchable Transparent Electrodes. *Nature* **2009**, *457*, 706-710.

[68] Tetsuka, H.; Asahi, R.; Nagoya, A.; Okamoto, K.; Tajima, I.; Ohta, R.; Okamoto, A. Optically Tunable Amino-Functionalized Graphene Quantum Dots. *Adv. Mater.* **2012**, *24*, 5333-5338.

[69] Hu, K.; Gupta, M. K.; Kulkarni, D. D.; Tsukruk, V. V. Ultra-Robust Graphene Oxide-Silk Fibroin Nanocomposite Membranes. *Adv. Mater.* **2013**, *25*, 2301-2307.

[70] Mannoor, M. S.; Tao, H.; Clayton, J. D.; Sengupta, A.; Kaplan, D. L.; Naik, R. R.; Verma, N.; Omenetto, F. G.; McAlpine, M. C. Graphene-Based Wireless Bacteria Detection on Tooth Enamel. *Nat. Commun.* **2012**, *3*, 763.

[71] Shahil, K. M. F.; Balandin, A. A. Thermal Properties of Graphene and Multilayer Graphene: Applications in Thermal Interface Materials. *Solid State Commun.* **2012**, *152*, 1331-1340.

[72] Geim, A. K.; Grigorieva, I. V. Van Der Waals Heterostructures. *Nature* **2013**, *499*, 419-425.

[73] Kim, H.; Abdala, A. A.; Macosko, C. W. Graphene/Polymer Nanocomposites. *Macromolecules* **2010**, *43*, 6515-6530.

[74] Kuilla, T.; Bhadra, S.; Yao, D.; Kim, N. H.; Bose, S.; Lee, J. H. Recent Advances in Graphene Based Polymer Composites. *Prog. Polym. Sci.* **2010**, *35*, 1350-1375.

[75] Compton, O. C.; Nguyen, S. T. Graphene Oxide, Highly Reduced Graphene Oxide, and Graphene: Versatile Building Blocks for Carbon-Based Materials. *Small* **2010**, *6*, 711-723.

[76] Huang, X.; Yin, Z.; Wu, S.; Qi, X.; He, Q.; Zhang, Q.; Yan, Q.; Boey, F.; Zhang, H. Graphene-Based Materials: Synthesis, Characterization, Properties, and Applications. *Small* **2011**, *7*, 1876-1902.

[77] Yang, M.; Hou, Y.; Kotov, N. A. Graphene-Based Multilayers: Critical Evaluation of Materials Assembly Techniques. *Nano Today* **2012**, *7*, 430-447.

[78] oung, R. J.; Kinloch, I. A.; Gong, L.; Novoselov, K. S. The Mechanics of Graphene Nanocomposites: A Review. *Compos. Sci. Technol.* **2012**, *72*, 1459-1476.

[79] Wu, D.; Zhang, F.; Liang, H.; Feng, X. Nanocomposites and Macroscopic Materials: Assembly of Chemically Modified Graphene Sheets. *Chem. Soc. Rev.* **2012**, *41*, 6160-6177.

[80] Lee, C.; Wei, X.; Kysar, J. W.; Hone, J. Measurement of the Elastic Properties and Intrinsic Strength of Monolayer Graphene. *Science* **2008**, *321*, 385-388.

[81] Balandin, A. A.; Ghosh, S.; Bao, W.; Calizo, I.; Teweldebrhan, D.; Miao, F.; Lau, C. N. Superior Thermal Conductivity of Single-Layer Graphene. *Nano Lett.* **2008**, *8*, 902-907.

[82] Du, X.; Skachko, I.; Barker, A.; Andrei, E. Y. Approaching Ballistic Transport in Suspended Graphene. *Nat. Nanotechnol.* **2008**, *3*, 491-495.

[83] Allen, M. J.; Tung, V. C.; Kaner, R. B. Honeycomb Carbon: A Review of Graphene. *Chem. Rev.* **2009**, *110*, 132-145.

[84] Liu, Y.; Yu, D.; Zeng, C.; Miao, Z.; Dai, L. Biocompatible Graphene Oxide-Based Glucose Biosensors. *Langmuir* **2010**, *26*, 6158-6160.

[85] Wang, K.; Ruan, J.; Song, H.; Zhang, J.; Wo, Y.; Guo, S.; Cui, D. Biocompatibility of Graphene Oxide. *Nanoscale Res. Lett.* **2011**, *6*, 8.

[86] Zhang, X.; Yin, J.; Peng, C.; Hu, W.; Zhu, Z.; Li, W.; Fan, C.; Huang, Q. Distribution and Biocompatibility Studies of Graphene Oxide in Mice after Intravenous Administration. *Carbon* **2011**, *49*, 986-995.

[87] Compton, O. C.; An, Z.; Putz, K. W.; Hong, B. J.; Hauser, B. G.; Catherine Brinson, L.; Nguyen, S. T. Additive-Free Hydrogelation of Graphene Oxide by Ultrasonication. *Carbon* **2012**, *50*, 3399-3406.

[88] Li, D.; Muller, M. B.; Gilje, S.; Kaner, R. B.; Wallace, G. G. Processable Aqueous Dispersions of Graphene Nanosheets. *Nat. Nanotechnol.* **2008**, *3*, 101-105.

[89] Hummers, W. S.; Offeman, R. E. Preparation of Graphitic Oxide. *J. Am. Chem. Soc.* **1958**, *80*, 1339-1339.

[90] Dreyer, D. R.; Park, S.; Bielawski, C. W.; Ruoff, R. S. The Chemistry of Graphene Oxide. *Chem. Soc. Rev.* **2010**, *39*, 228-240.

[91] Bachtold, A.; Fuhrer, M. S.; Plyasunov, S.; Forero, M.; Anderson, E. H.; Zettl, A.; McEuen, P. L. Scanned Probe Microscopy of Electronic Transport in Carbon Nanotubes. *Phys. Rev. Lett.* **2000**, *84*, 6082-6085.

[92] Gómez-Navarro, C.; Moreno-Herrero, F.; de Pablo, P. J.; Colchero, J.; Gómez-Herrero, J.; Baró, A. M. Contactless Experiments on Individual DNA Molecules

Show No Evidence for Molecular Wire Behavior. *Proc. Natl. Acad. Sci.* **2002**, *99*, 8484-8487.

[93] Jespersen, T. S.; Nygård, J. Charge Trapping in Carbon Nanotube Loops Demonstrated by Electrostatic Force Microscopy. *Nano Lett.* **2005**, *5*, 1838-1841.

[94] Kulkarni, D. D.; Kim, S.; Chyasnavichyus, M.; Hu, K.; Fedorov, A. G.; Tsukruk, V. V. Chemical Reduction of Individual Graphene Oxide Sheets as Revealed by Electrostatic Force Microscopy. *J. Am. Chem. Soc.* **2014**, *136*, 6546-6549.

[95] Lv, C.; Xue, Q.; Xia, D.; Ma, M.; Xie, J.; Chen, H. Effect of Chemisorption on the Interfacial Bonding Characteristics of Graphene−Polymer Composites. *J. Phys. Chem. C* **2010**, *114*, 6588-6594.

[96] Loh, K. P.; Bao, Q.; Eda, G.; Chhowalla, M. Graphene Oxide as a Chemically Tunable Platform for Optical Applications. *Nat. Chem.* **2010**, *2*, 1015-1024.

[97] Gómez-Navarro, C.; Burghard, M.; Kern, K. Elastic Properties of Chemically Derived Single Graphene Sheets. *Nano Lett.* **2008**, *8*, 2045-2049.

[98] Suk, J. W.; Piner, R. D.; An, J.; Ruoff, R. S. Mechanical Properties of Monolayer Graphene Oxide. *ACS Nano* **2010**, *4*, 6557-6564.

[99] An, Z.; Compton, O. C.; Putz, K. W.; Brinson, L. C.; Nguyen, S. T. Bio-Inspired Borate Cross-Linking in Ultra-Stiff Graphene Oxide Thin Films. *Adv. Mater.* **2011**, *23*, 3842-3846.

[100] Chen, C.; Yang, Q.-H.; Yang, Y.; Lv, W.; Wen, Y.; Hou, P.-X.; Wang, M.; Cheng, H.-M. Self-Assembled Free-Standing Graphite Oxide Membrane. *Adv. Mater.* **2009**, *21*, 3007-3011.

[101] Park, S.; Dikin, D. A.; Nguyen, S. T.; Ruoff, R. S. Graphene Oxide Sheets Chemically Cross-Linked by Polyallylamine. *J. Phys. Chem. C* **2009**, *113*, 15801-15804.

[102] Pei, S.; Cheng, H.-M. The Reduction of Graphene Oxide. *Carbon* **2012**, *50*, 3210-3228.

[103] Mao, S.; Pu, H.; Chen, J. Graphene Oxide and Its Reduction: Modeling and Experimental Progress. *RSC Advances* **2012**, *2*, 2643-2662.

[104] Kuila, T.; Mishra, A. K.; Khanra, P.; Kim, N. H.; Lee, J. H. Recent Advances in the Efficient Reduction of Graphene Oxide and Its Application as Energy Storage Electrode Materials. *Nanoscale* **2013**, *5*, 52-71.

[105] Feng, H.; Cheng, R.; Zhao, X.; Duan, X.; Li, J. A Low-Temperature Method to Produce Highly Reduced Graphene Oxide. *Nat. Commun.* **2013**, *4*, 1539.

[106] Fan, Z.; Wang, K.; Wei, T.; Yan, J.; Song, L.; Shao, B. An Environmentally Friendly and Efficient Route for the Reduction of Graphene Oxide by Aluminum Powder. *Carbon* **2010**, *48*, 1686-1689.

[107] El-Kady, M. F.; Strong, V.; Dubin, S.; Kaner, R. B. Laser Scribing of High-Performance and Flexible Graphene-Based Electrochemical Capacitors. *Science* **2012**, *335*, 1326-1330.

[108] Moon, I. K.; Lee, J.; Ruoff, R. S.; Lee, H. Reduced Graphene Oxide by Chemical Graphitization. *Nat. Commun.* **2010**, *1*, 73.

[109] Hu, K.; Tolentino, L. S.; Kulkarni, D. D.; Ye, C.; Kumar, S.; Tsukruk, V. V. Written-in Conductive Patterns on Robust Graphene Oxide Biopaper by Electrochemical Microstamping. *Angew. Chem. Int. Ed.* **2013**, *52*, 13784-13788.

[110] Kulkarni, D. D.; Kim, S.; Fedorov, A. G.; Tsukruk, V. V. Light-Induced Plasmon-Assisted Phase Transformation of Carbon on Metal Nanoparticles. *Adv. Funct. Mater.* **2012**, *22*, 2129-2139.

[111] Israelachvili, J. N. *Intermolecular and Surface Forces: With Applications to Colloidal and Biological Systems*. Academic Press: **1985**.

[112] Adamson, A. W. *Physical Chemistry of Surfaces*. Wiley: **1990**.

[113] Jiang, L. Y.; Huang, Y.; Jiang, H.; Ravichandran, G.; Gao, H.; Hwang, K. C.; Liu, B. A Cohesive Law for Carbon Nanotube/Polymer Interfaces Based on the Van Der Waals Force. *J. Mech. Phys. Solids* **2006**, *54*, 2436-2452.

[114] Shen, B.; Zhai, W.; Chen, C.; Lu, D.; Wang, J.; Zheng, W. Melt Blending in Situ Enhances the Interaction between Polystyrene and Graphene through Π–Π Stacking. *ACS Appl. Mater. Interfaces* **2011**, *3*, 3103-3109.

[115] Zhang, H.-L.; Wei, X.-L.; Zang, Y.; Cao, J.-Y.; Liu, S.; He, X.-P.; Chen, Q.; Long, Y.-T.; Li, J.; Chen, G.-R.; Chen, K. Fluorogenic Probing of Specific Recognitions between Sugar Ligands and Glycoprotein Receptors on Cancer Cells by an Economic Graphene Nanocomposite. *Adv. Mater.* **2013**, *25*, 4097-4101.

[116] Cheng, Q.; Wu, M.; Li, M.; Jiang, L.; Tang, Z. Ultratough Artificial Nacre Based on Conjugated Cross-Linked Graphene Oxide. *Angew. Chem. Int. Ed.* **2013**, *52*, 3750-3755.

[117] Liu, J.; Fu, S.; Yuan, B.; Li, Y.; Deng, Z. Toward a Universal "Adhesive Nanosheet" for the Assembly of Multiple Nanoparticles Based on a Protein-Induced Reduction/Decoration of Graphene Oxide. *J. Am. Chem. Soc.* **2010**, *132*, 7279-7281.

[118] Kim, J.; Cote, L. J.; Kim, F.; Yuan, W.; Shull, K. R.; Huang, J. Graphene Oxide Sheets at Interfaces. *J. Am. Chem. Soc.* **2010**, *132*, 8180-8186.

[119] Berg, J. M.; Deis, F. H.; Tymoczko, J. L.; Stryer, L.; Gerber, N. C.; Gumport, R.; Koeppe, R. E. *Biochemistry Student Companion*. W. H. Freeman: New York, **2011**.

[120] Israelachvili, J.; Pashley, R. The Hydrophobic Interaction Is Long Range, Decaying Exponentially with Distance. *Nature* **1982**, *300*, 341-342.

[121] Sinnokrot, M. O.; Valeev, E. F.; Sherrill, C. D. Estimates of the Ab Initio Limit for π–π Interactions: The Benzene Dimer. *J. Am. Chem. Soc.* **2002**, *124*, 10887-10893.

[122] Bondi, A. Van Der Waals Volumes and Radii. *J. Phys. Chem.* **1964**, *68*, 441-451.

[123] Kerner, E. H. The Elastic and Thermo-Elastic Properties of Composite Media. *Proc. Phys. Soc. Sect. B* **1956**, *69*, 808-813.

[124] Smallwood, H. M. Limiting Law of the Reinforcement of Rubber. *J. Appl. Phys.* **1944**, *15*, 758-766.

[125] Agarwal, B. D.; Broutman, L. J.; Chandrashekhara, K. *Analysis and Performance of Fiber Composites*. Wiley: **2006**.

[126] Wan, C.; Chen, B. Reinforcement and Interphase of Polymer/Graphene Oxide Nanocomposites. *J. Mater. Chem.* **2012**, *22*, 3637-3646.

[127] Affdl, J. C. H.; Kardos, J. L. The Halpin-Tsai Equations: A Review. *Polym. Eng. Sci.* **1976**, *16*, 344-352.

[128] Fornes, T. D.; Paul, D. R. Modeling Properties of Nylon 6/Clay Nanocomposites Using Composite Theories. *Polymer* **2003**, *44*, 4993-5013.

[129] Tandon, G. P.; Weng, G. J. The Effect of Aspect Ratio of Inclusions on the Elastic Properties of Unidirectionally Aligned Composites. *Polym. Compos.* **1984**, *5*, 327-333.

[130] Gao, H.; Ji, B.; Jäger, I. L.; Arzt, E.; Fratzl, P. Materials Become Insensitive to Flaws at Nanoscale: Lessons from Nature. *Proc. Natl. Acad. Sci.* **2003**, *100*, 5597-5600.

[131] Lipatov, Y. S. Interfaces in Polymer-Polymer Composites. In *Controlled Interphases in Composite Materials*, Ishida, H., Ed. Springer Netherlands: **1990**; pp 599-611.

[132] Terrones, M.; Martín, O.; González, M.; Pozuelo, J.; Serrano, B.; Cabanelas, J. C.; Vega-Díaz, S. M.; Baselga, J. Interphases in Graphene Polymer-Based Nanocomposites: Achievements and Challenges. *Adv. Mater.* **2011**, *23*, 5302-5310.

[133] Stankovich, S.; Dikin, D. A.; Dommett, G. H. B.; Kohlhaas, K. M.; Zimney, E. J.; Stach, E. A.; Piner, R. D.; Nguyen, S. T.; Ruoff, R. S. Graphene-Based Composite Materials. *Nature* **2006**, *442*, 282-286.

[134] Dikin, D. A.; Stankovich, S.; Zimney, E. J.; Piner, R. D.; Dommett, G. H. B.; Evmenenko, G.; Nguyen, S. T.; Ruoff, R. S. Preparation and Characterization of Graphene Oxide Paper. *Nature* **2007**, *448*, 457-460.

[135] RamanathanT; Abdala, A. A.; StankovichS; Dikin, D. A.; Herrera Alonso, M.; Piner, R. D.; Adamson, D. H.; Schniepp, H. C.; ChenX; Ruoff, R. S.; Nguyen, S. T.; Aksay, I. A.; Prud'Homme, R. K.; Brinson, L. C. Functionalized Graphene Sheets for Polymer Nanocomposites. *Nat. Nanotechnol.* **2008**, *3*, 327-331.

[136] Xu, Y.; Wang, Y.; Liang, J.; Huang, Y.; Ma, Y.; Wan, X.; Chen, Y. A Hybrid Material of Graphene and Poly (3,4-Ethyldioxythiophene) with High Conductivity, Flexibility, and Transparency. *Nano Res.* **2009**, *2*, 343-348.

[137] Quan, H.; Zhang, B.-q.; Zhao, Q.; Yuen, R. K. K.; Li, R. K. Y. Facile Preparation and Thermal Degradation Studies of Graphite Nanoplatelets (Gnps) Filled Thermoplastic Polyurethane (Tpu) Nanocomposites. *Compos. Part A: Appl. S.* **2009**, *40*, 1506-1513.

[138] Eda, G.; Chhowalla, M. Graphene-Based Composite Thin Films for Electronics. *Nano Lett.* **2009**, *9*, 814-818.

[139] Liang, J.; Xu, Y.; Huang, Y.; Zhang, L.; Wang, Y.; Ma, Y.; Li, F.; Guo, T.; Chen, Y. Infrared-Triggered Actuators from Graphene-Based Nanocomposites. *J. Phys. Chem. C* **2009**, *113*, 9921-9927.

[140] Kim, H.; Macosko, C. W. Processing-Property Relationships of Polycarbonate/Graphene Composites. *Polymer* **2009**, *50*, 3797-3809.

[141] Ramanathan, T.; Stankovich, S.; Dikin, D. A.; Liu, H.; Shen, H.; Nguyen, S. T.; Brinson, L. C. Graphitic Nanofillers in Pmma Nanocomposites—an Investigation of Particle Size and Dispersion and Their Influence on Nanocomposite Properties. *J. Polym. Sci., Part B: Polym. Phys.* **2007**, *45*, 2097-2112.

[142] Kim, S.; Do, I.; Drzal, L. T. Multifunctional Xgnp/Lldpe Nanocomposites Prepared by Solution Compounding Using Various Screw Rotating Systems. *Macromol. Mater. Eng.* **2009**, *294*, 196-205.

[143] Liang, J.; Huang, Y.; Zhang, L.; Wang, Y.; Ma, Y.; Guo, T.; Chen, Y. Molecular-Level Dispersion of Graphene into Poly(Vinyl Alcohol) and Effective Reinforcement of Their Nanocomposites. *Adv. Funct. Mater.* **2009**, *19*, 2297-2302.

[144] Zhao, X.; Zhang, Q.; Chen, D.; Lu, P. Enhanced Mechanical Properties of Graphene-Based Poly(Vinyl Alcohol) Composites. *Macromolecules* **2010**, *43*, 2357-2363.

[145] Kalaitzidou, K.; Fukushima, H.; Drzal, L. T. A New Compounding Method for Exfoliated Graphite–Polypropylene Nanocomposites with Enhanced Flexural Properties and Lower Percolation Threshold. *Compos. Sci. Technol.* **2007**, *67*, 2045-2051.

[146] Zheng, W.; Lu, X.; Wong, S.-C. Electrical and Mechanical Properties of Expanded Graphite-Reinforced High-Density Polyethylene. *J. Appl. Polym. Sci.* **2004**, *91*, 2781-2788.

[147] Zhao, Y. F.; Xiao, M.; Wang, S. J.; Ge, X. C.; Meng, Y. Z. Preparation and Properties of Electrically Conductive Pps/Expanded Graphite Nanocomposites. *Compos. Sci. Technol.* **2007**, *67*, 2528-2534.

[148] Du, X. S.; Xiao, M.; Meng, Y. Z. Synthesis and Characterization of Polyaniline/Graphite Conducting Nanocomposites. *J. Polym. Sci., Part B: Polym. Phys.* **2004**, *42*, 1972-1978.

[149] Cho, D.; Lee, S.; Yang, G.; Fukushima, H.; Drzal, L. T. Dynamic Mechanical and Thermal Properties of Phenylethynyl-Terminated Polyimide Composites Reinforced with Expanded Graphite Nanoplatelets. *Macromol. Mater. Eng.* **2005**, *290*, 179-187.

[150] Kim, H.; Miura, Y.; Macosko, C. W. Graphene/Polyurethane Nanocomposites for Improved Gas Barrier and Electrical Conductivity. *Chem. Mater.* **2010**, *22*, 3441-3450.

[151] Li, H.; Pang, S.; Wu, S.; Feng, X.; Müllen, K.; Bubeck, C. Layer-by-Layer Assembly and Uv Photoreduction of Graphene–Polyoxometalate Composite Films for Electronics. *J. Am. Chem. Soc.* **2011**, *133*, 9423-9429.

[152] Cassagneau, T.; Fendler, J. H. High Density Rechargeable Lithium-Ion Batteries Self-Assembled from Graphite Oxide Nanoplatelets and Polyelectrolytes. *Adv. Mater.* **1998**, *10*, 877-881.

[153] Hu, H.; Wang, X.; Wang, J.; Wan, L.; Liu, F.; Zheng, H.; Chen, R.; Xu, C. Preparation and Properties of Graphene Nanosheets–Polystyrene Nanocomposites Via in Situ Emulsion Polymerization. *Chem. Phys. Lett.* **2010**, *484*, 247-253.

[154] Leroux, F.; Besse, J.-P. Polymer Interleaved Layered Double Hydroxide: A New Emerging Class of Nanocomposites. *Chem. Mater.* **2001**, *13*, 3507-3515.

[155] Stankovich, S.; Piner, R. D.; Chen, X.; Wu, N.; Nguyen, S. T.; Ruoff, R. S. Stable Aqueous Dispersions of Graphitic Nanoplatelets Via the Reduction of Exfoliated Graphite Oxide in the Presence of Poly(Sodium 4-Styrenesulfonate). *J. Mater. Chem.* **2006**, *16*, 155-158.

[156] Kim, H.; Macosko, C. W. Morphology and Properties of Polyester/Exfoliated Graphite Nanocomposites. *Macromolecules* **2008**, *41*, 3317-3327.

[157] Xu, Y.; Hong, W.; Bai, H.; Li, C.; Shi, G. Strong and Ductile Poly(Vinyl Alcohol)/Graphene Oxide Composite Films with a Layered Structure. *Carbon* **2009**, *47*, 3538-3543.

[158] Wu, Q.; Xu, Y.; Yao, Z.; Liu, A.; Shi, G. Supercapacitors Based on Flexible Graphene/Polyaniline Nanofiber Composite Films. *ACS Nano* **2010**, *4*, 1963-1970.

[159] Yang, X.; Shang, S.; Li, L. Layer-Structured Poly(Vinyl Alcohol)/Graphene Oxide Nanocomposites with Improved Thermal and Mechanical Properties. *J. Appl. Polym. Sci.* **2011**, *120*, 1355-1360.

[160] Yasmin, A.; Luo, J.-J.; Daniel, I. M. Processing of Expanded Graphite Reinforced Polymer Nanocomposites. *Compos. Sci. Technol.* **2006**, *66*, 1182-1189.

[161] Li, Y.; Umer, R.; Samad, Y. A.; Zheng, L.; Liao, K. The Effect of the Ultrasonication Pre-Treatment of Graphene Oxide (Go) on the Mechanical Properties of Go/Polyvinyl Alcohol Composites. *Carbon* **2013**, *55*, 321-327.

[162] Wajid, A. S.; Ahmed, H. S. T.; Das, S.; Irin, F.; Jankowski, A. F.; Green, M. J. High-Performance Pristine Graphene/Epoxy Composites with Enhanced Mechanical and Electrical Properties. *Macromol. Mater. Eng.* **2013**, *298*, 339-347.

[163] Sayyar, S.; Murray, E.; Thompson, B. C.; Gambhir, S.; Officer, D. L.; Wallace, G. G. Covalently Linked Biocompatible Graphene/Polycaprolactone Composites for Tissue Engineering. *Carbon* **2013**, *52*, 296-304.

[164] Wang, D.; Zhang, X.; Zha, J.-W.; Zhao, J.; Dang, Z.-M.; Hu, G.-H. Dielectric Properties of Reduced Graphene Oxide/Polypropylene Composites with Ultralow Percolation Threshold. *Polymer* **2013**, *54*, 1916-1922.

[165] Lalwani, G.; Henslee, A. M.; Farshid, B.; Lin, L.; Kasper, F. K.; Qin, Y.-X.; Mikos, A. G.; Sitharaman, B. Two-Dimensional Nanostructure-Reinforced Biodegradable Polymeric Nanocomposites for Bone Tissue Engineering. *Biomacromolecules* **2013**, *14*, 900-909.

[166] Kim, I.-H.; Jeong, Y. G. Polylactide/Exfoliated Graphite Nanocomposites with Enhanced Thermal Stability, Mechanical Modulus, and Electrical Conductivity. *Journal of Polymer Science Part B: Polymer Physics* **2010**, *48*, 850-858.

[167] Zhang, H.-B.; Zheng, W.-G.; Yan, Q.; Yang, Y.; Wang, J.-W.; Lu, Z.-H.; Ji, G.-Y.; Yu, Z.-Z. Electrically Conductive Polyethylene Terephthalate/Graphene Nanocomposites Prepared by Melt Compounding. *Polymer* **2010**, *51*, 1191-1196.

[168] Dasari, A.; Yu, Z.-Z.; Mai, Y.-W. Electrically Conductive and Super-Tough Polyamide-Based Nanocomposites. *Polymer* **2009**, *50*, 4112-4121.

[169] Sherif, A.; Izzuddin, Z.; Qingshi, M.; Nobuyuki, K.; Andrew, M.; Hsu-Chiang, K.; Peter, M.; Jun, M.; Liqun, Z. Melt Compounding with Graphene to Develop Functional, High-Performance Elastomers. *Nanotechnology* **2013**, *24*, 165601.

[170] Steurer, P.; Wissert, R.; Thomann, R.; Mülhaupt, R. Functionalized Graphenes and Thermoplastic Nanocomposites Based Upon Expanded Graphite Oxide. *Macromol. Rapid Commun.* **2009**, *30*, 316-327.

[171] Han, Y.; Wu, Y.; Shen, M.; Huang, X.; Zhu, J.; Zhang, X. Preparation and Properties of Polystyrene Nanocomposites with Graphite Oxide and Graphene as Flame Retardants. *J. Mater. Sci.* **2013**, *48*, 4214-4222.

[172] Ping'an, S.; Lina, L.; Shenyuan, F.; Youming, Y.; Chunde, J.; Qiang, W.; Yan, Z.; Qian, L. Striking Multiple Synergies Created by Combining Reduced Graphene Oxides and Carbon Nanotubes for Polymer Nanocomposites. *Nanotechnology* **2013**, *24*, 125704.

[173] Gao, T.; Ye, Q.; Pei, X.; Xia, Y.; Zhou, F. Grafting Polymer Brushes on Graphene Oxide for Controlling Surface Charge States and Templated Synthesis of Metal Nanoparticles. *J. Appl. Polym. Sci.* **2013**, *127*, 3074-3083.

[174] Luzinov, I.; Minko, S.; Tsukruk, V. V. Adaptive and Responsive Surfaces through Controlled Reorganization of Interfacial Polymer Layers. *Prog. Polym. Sci.* **2004**, *29*, 635-698.

[175] Shen, B.; Zhai, W.; Tao, M.; Lu, D.; Zheng, W. Chemical Functionalization of Graphene Oxide toward the Tailoring of the Interface in Polymer Composites. *Compos. Sci. Technol.* **2013**, *77*, 87-94.

[176] Li, D.; Huang, J.; Kaner, R. B. Polyaniline Nanofibers: A Unique Polymer Nanostructure for Versatile Applications. *Acc. Chem. Res.* **2009**, *42*, 135-145.

[177] Wei, H.; Zhu, J.; Wu, S.; Wei, S.; Guo, Z. Electrochromic Polyaniline/Graphite Oxide Nanocomposites with Endured Electrochemical Energy Storage. *Polymer* **2013**, *54*, 1820-1831.

[178] Zhu, J.; Chen, M.; Qu, H.; Zhang, X.; Wei, H.; Luo, Z.; Colorado, H. A.; Wei, S.; Guo, Z. Interfacial Polymerized Polyaniline/Graphite Oxide Nanocomposites toward Electrochemical Energy Storage. *Polymer* **2012**, *53*, 5953-5964.

[179] Ning, G.; Li, T.; Yan, J.; Xu, C.; Wei, T.; Fan, Z. Three-Dimensional Hybrid Materials of Fish Scale-Like Polyaniline Nanosheet Arrays on Graphene Oxide and Carbon Nanotube for High-Performance Ultracapacitors. *Carbon* **2013**, *54*, 241-248.

[180] Ye, L.; Meng, X.-Y.; Ji, X.; Li, Z.-M.; Tang, J.-H. Synthesis and Characterization of Expandable Graphite–Poly(Methyl Methacrylate) Composite Particles and Their Application to Flame Retardation of Rigid Polyurethane Foams. *Polym. Degrad. Stab.* **2009**, *94*, 971-979.

[181] Chen, G.; Wu, D.; Weng, W.; Wu, C. Exfoliation of Graphite Flake and Its Nanocomposites. *Carbon* **2003**, *41*, 619-621.

[182] Mostafa Moujahid, E.; Besse, J.-P.; Leroux, F. Poly(Styrene Sulfonate) Layered Double Hydroxide Nanocomposites. Stability and Subsequent Structural Transformation with Changes in Temperature. *J. Mater. Chem.* **2003**, *13*, 258-264.

[183] Shi, H.; Li, Y.; Guo, T. In Situ Preparation of Transparent Polyimide Nanocomposite with a Small Load of Graphene Oxide. *J. Appl. Polym. Sci.* **2013**, *128*, 3163-3169.

[184] Decher, G. Fuzzy Nanoassemblies: Toward Layered Polymeric Multicomposites. *Science* **1997**, *277*, 1232-1237.

[185] Decher, G.; Schlenoff, J. B. *Multilayer Thin Films: Sequential Assembly of Nanocomposite Materials*. Wiley: **2012**.

[186] *Protein Architecture: Interfacing Molecular Assemblies and Immobilization Biotechnology*. Taylor & Francis: **1999**.

[187] Ariga, K. *Organized Organic Ultrathin Films: Fundamentals and Applications*. Wiley: **2012**.

[188] Jiang, C.; Tsukruk, V. V. Freestanding Nanostructures Via Layer-by-Layer Assembly. *Adv. Mater.* **2006**, *18*, 829-840.

[189] Jiang, C.; Markutsya, S.; Pikus, Y.; Tsukruk, V. V. Freely Suspended Nanocomposite Membranes as Highly Sensitive Sensors. *Nat. Mater.* **2004**, *3*, 721-728.

[190] Kotov, N. A.; Dékány, I.; Fendler, J. H. Ultrathin Graphite Oxide–Polyelectrolyte Composites Prepared by Self-Assembly: Transition between Conductive and Non-Conductive States. *Adv. Mater.* **1996**, *8*, 637-641.

[191] Kovtyukhova, N. I.; Ollivier, P. J.; Martin, B. R.; Mallouk, T. E.; Chizhik, S. A.; Buzaneva, E. V.; Gorchinskiy, A. D. Layer-by-Layer Assembly of Ultrathin Composite Films from Micron-Sized Graphite Oxide Sheets and Polycations. *Chem. Mater.* **1999**, *11*, 771-778.

[192] Zhu, J.; Zhang, H.; Kotov, N. A. Thermodynamic and Structural Insights into Nanocomposites Engineering by Comparing Two Materials Assembly Techniques for Graphene. *ACS Nano* **2013**, *7*, 4818-4829.

[193] Fan, W.; Zhang, C.; Tjiu, W. W.; Liu, T. Fabrication of Electrically Conductive Graphene/Polystyrene Composites Via a Combination of Latex and Layer-by-Layer Assembly Approaches. *J. Mater. Res.* **2013**, *28*, 611-619.

[194] Choi, I.; Kulkarni, D. D.; Xu, W.; Tsitsilianis, C.; Tsukruk, V. V. Star Polymer Unimicelles on Graphene Oxide Flakes. *Langmuir* **2013**, *29*, 9761-9769.

[195] Layek, R. K.; Samanta, S.; Nandi, A. K. The Physical Properties of Sulfonated Graphene/Poly(Vinyl Alcohol) Composites. *Carbon* **2012**, *50*, 815-827.

[196] Wagner, H. D.; Vaia, R. A. Nanocomposites: Issues at the Interface. *Mater. Today* **2004**, *7*, 38-42.

[197] Velasco-Santos, C.; Martinez-Hernandez, A. L.; Castano, V. M. Carbon Nanotube-Polymer Nanocomposites: The Role of Interfaces. *Compos. Interface.* **2005**, *11*, 567-586.

[198] Giannelis, E. P. Polymer Layered Silicate Nanocomposites. *Adv. Mater.* **1996**, *8*, 29-35.

[199] Vaia, R. A.; Vasudevan, S.; Krawiec, W.; Scanlon, L. G.; Giannelis, E. P. New Polymer Electrolyte Nanocomposites: Melt Intercalation of Poly(Ethylene Oxide) in Mica-Type Silicates. *Adv. Mater.* **1995**, *7*, 154-156.

[200] Moniruzzaman, M.; Winey, K. I. Polymer Nanocomposites Containing Carbon Nanotubes. *Macromolecules* **2006**, *39*, 5194-5205.

[201] Wang, M. C.; Yan, C.; Ma, L. Graphene nanocomposites. In: Hu, N. Ed., *Composites and Their Properties*. In Tech: Shanghai, **2012**.

[202] Coleman, J. N.; Khan, U.; Blau, W. J.; Gun'ko, Y. K. Small but Strong: A Review of the Mechanical Properties of Carbon Nanotube–Polymer Composites. *Carbon* **2006**, *44*, 1624-1652.

[203] Gong, X.; Liu, J.; Baskaran, S.; Voise, R. D.; Young, J. S. Surfactant-Assisted Processing of Carbon Nanotube/Polymer Composites. *Chem. Mater.* **2000**, *12*, 1049-1052.

[204] Spitalsky, Z.; Tasis, D.; Papagelis, K.; Galiotis, C. Carbon Nanotube–Polymer Composites: Chemistry, Processing, Mechanical and Electrical Properties. *Prog. Polym. Sci.* **2010**, *35*, 357-401.

[205] Sahoo, N. G.; Rana, S.; Cho, J. W.; Li, L.; Chan, S. H. Polymer Nanocomposites Based on Functionalized Carbon Nanotubes. *Prog. Polym. Sci.* **2010**, *35*, 837-867.

[206] Haque, A.; Ramasetty, A. Theoretical Study of Stress Transfer in Carbon Nanotube Reinforced Polymer Matrix Composites. *Compos. Struct.* **2005**, *71*, 68-77.

[207] Fischer, H. Polymer Nanocomposites: From Fundamental Research to Specific Applications. *Mater. Sci. Eng. C* **2003**, *23*, 763-772.

[208] Chen, H.; Müller, M. B.; Gilmore, K. J.; Wallace, G. G.; Li, D. Mechanically Strong, Electrically Conductive, and Biocompatible Graphene Paper. *Adv. Mater.* **2008**, *20*, 3557-3561.

[209] Gao, Y.; Liu, L.-Q.; Zu, S.-Z.; Peng, K.; Zhou, D.; Han, B.-H.; Zhang, Z. The Effect of Interlayer Adhesion on the Mechanical Behaviors of Macroscopic Graphene Oxide Papers. *ACS Nano* **2011**, *5*, 2134-2141.

[210] Tian, Y.; Cao, Y.; Wang, Y.; Yang, W.; Feng, J. Realizing Ultrahigh Modulus and High Strength of Macroscopic Graphene Oxide Papers through Crosslinking of Mussel-Inspired Polymers. *Adv. Mater.* **2013**, *25*, 2980-2983.

[211] Putz, K. W.; Compton, O. C.; Palmeri, M. J.; Nguyen, S. T.; Brinson, L. C. High-Nanofiller-Content Graphene Oxide–Polymer Nanocomposites Via Vacuum-Assisted Self-Assembly. *Adv. Funct. Mater.* **2010**, *20*, 3322-3329.

[212] Li, Z.; Young, R. J.; Kinloch, I. A. Interfacial Stress Transfer in Graphene Oxide Nanocomposites. *ACS Appl. Mater. Interfaces* **2013**, *5*, 456-463.

[213] Xu, P.; Loomis, J.; Bradshaw, R. D.; Panchapakesan, B. Load Transfer and Mechanical Properties of Chemically Reduced Graphene Reinforcements in Polymer Composites. *Nanotechnology* **2012**, *23*, 505713.

[214] Srivastava, I.; Mehta, R. J.; Yu, Z.-Z.; Schadler, L.; Koratkar, N. Raman Study of Interfacial Load Transfer in Graphene Nanocomposites. *Appl. Phys. Lett.* **2011**, *98*, 063102-063103.

[215] Chen, Y.; Qi, Y.; Tai, Z.; Yan, X.; Zhu, F.; Xue, Q. Preparation, Mechanical Properties and Biocompatibility of Graphene Oxide/Ultrahigh Molecular Weight Polyethylene Composites. *Eur. Polym. J.* **2012**, *48*, 1026-1033.

[216] Laaksonen, P.; Walther, A.; Malho, J.-M.; Kainlauri, M.; Ikkala, O.; Linder, M. B. Genetic Engineering of Biomimetic Nanocomposites: Diblock Proteins, Graphene, and Nanofibrillated Cellulose. *Angew. Chem. Int. Ed.* **2011**, *50*, 8688-8691.

[217] Li, Y.-Q.; Yu, T.; Yang, T.-Y.; Zheng, L.-X.; Liao, K. Bio-Inspired Nacre-Like Composite Films Based on Graphene with Superior Mechanical, Electrical, and Biocompatible Properties. *Adv. Mater.* **2012**, *24*, 3426-3431.

[218] Hoare, T. R.; Kohane, D. S. Hydrogels in Drug Delivery: Progress and Challenges. *Polymer* **2008**, *49*, 1993-2007.

[219] Van Vlierberghe, S.; Dubruel, P.; Schacht, E. Biopolymer-Based Hydrogels as Scaffolds for Tissue Engineering Applications: A Review. *Biomacromolecules* **2011**, *12*, 1387-1408.

[220] Zhang, L.; Shi, G. Preparation of Highly Conductive Graphene Hydrogels for Fabricating Supercapacitors with High Rate Capability. *J. Phys. Chem. C* **2011**, *115*, 17206-17212.

[221] Gao, H.; Xiao, F.; Ching, C. B.; Duan, H. High-Performance Asymmetric Supercapacitor Based on Graphene Hydrogel and Nanostructured Mno2. *ACS Appl. Mater. Interfaces* **2012**, *4*, 2801-2810.

[222] Stuart, M. A. C.; Huck, W. T. S.; Genzer, J.; Muller, M.; Ober, C.; Stamm, M.; Sukhorukov, G. B.; Szleifer, I.; Tsukruk, V. V.; Urban, M.; Winnik, F.; Zauscher, S.; Luzinov, I.; Minko, S. Emerging Applications of Stimuli-Responsive Polymer Materials. *Nat. Mater.* **2010**, *9*, 101-113.

[223] Xu, Y.; Sheng, K.; Li, C.; Shi, G. Self-Assembled Graphene Hydrogel Via a One-Step Hydrothermal Process. *ACS Nano* **2010**, *4*, 4324-4330.

[224] Kozlovskaya, V.; Kharlampieva, E.; Khanal, B. P.; Manna, P.; Zubarev, E. R.; Tsukruk, V. V. Ultrathin Layer-by-Layer Hydrogels with Incorporated Gold Nanorods as Ph-Sensitive Optical Materials. *Chem. Mater.* **2008**, *20*, 7474-7485.

[225] Shen, J.; Yan, B.; Li, T.; Long, Y.; Li, N.; Ye, M. Mechanical, Thermal and Swelling Properties of Poly(Acrylic Acid)-Graphene Oxide Composite Hydrogels. *Soft Matter* **2012**, *8*, 1831-1836.

[226] Lutz, J.-F.; Akdemir, Ö.; Hoth, A. Point by Point Comparison of Two Thermosensitive Polymers Exhibiting a Similar Lcst: Is the Age of Poly(Nipam) Over? *J. Am. Chem. Soc.* **2006**, *128*, 13046-13047.

[227] Zhang, Y.; Furyk, S.; Bergbreiter, D. E.; Cremer, P. S. Specific Ion Effects on the Water Solubility of Macromolecules: Pnipam and the Hofmeister Series. *J. Am. Chem. Soc.* **2005**, *127*, 14505-14510.

[228] Ruel-Gariépy, E.; Leroux, J.-C. In Situ-Forming Hydrogels—Review of Temperature-Sensitive Systems. *Eur. J. Pharm. Biopharm.* **2004**, *58*, 409-426.

[229] Zhang, X.-Z.; Wu, D.-Q.; Chu, C.-C. Synthesis, Characterization and Controlled Drug Release of Thermosensitive Ipn–Pnipaam Hydrogels. *Biomaterials* **2004**, *25*, 3793-3805.

[230] Alzari, V.; Nuvoli, D.; Scognamillo, S.; Piccinini, M.; Gioffredi, E.; Malucelli, G.; Marceddu, S.; Sechi, M.; Sanna, V.; Mariani, A. Graphene-Containing Thermoresponsive Nanocomposite Hydrogels of Poly(N-Isopropylacrylamide) Prepared by Frontal Polymerization. *J. Mater. Chem.* **2011**, *21*, 8727-8733.

[231] Sun, S.; Wu, P. A One-Step Strategy for Thermal- and Ph-Responsive Graphene Oxide Interpenetrating Polymer Hydrogel Networks. *J. Mater. Chem.* **2011**, *21*, 4095-4097.

[232] Bai, H.; Sheng, K.; Zhang, P.; Li, C.; Shi, G. Graphene Oxide/Conducting Polymer Composite Hydrogels. *J. Mater. Chem.* **2011**, *21*, 18653-18658.

[233] Rafiee, M. A.; Rafiee, J.; Wang, Z.; Song, H.; Yu, Z.-Z.; Koratkar, N. Enhanced Mechanical Properties of Nanocomposites at Low Graphene Content. *ACS Nano* **2009**, *3*, 3884-3890.

[234] Zhang, K.; Zhang, L. L.; Zhao, X. S.; Wu, J. Graphene/Polyaniline Nanofiber Composites as Supercapacitor Electrodes. *Chem. Mater.* **2010**, *22*, 1392-1401.

[235] Jung, J.-H.; Jeon, J.-H.; Sridhar, V.; Oh, I.-K. Electro-Active Graphene–Nafion Actuators. *Carbon* **2011**, *49*, 1279-1289.

[236] Brownson, D. A. C.; Kampouris, D. K.; Banks, C. E. An Overview of Graphene in Energy Production and Storage Applications. *J. Power Sources* **2011**, *196*, 4873-4885.

[237] Huang, X.; Qi, X.; Boey, F.; Zhang, H. Graphene-Based Composites. *Chem. Soc. Rev.* **2012**, *41*, 666-686.

[238] Li, J.; Guo, S.; Zhai, Y.; Wang, E. Nafion–Graphene Nanocomposite Film as Enhanced Sensing Platform for Ultrasensitive Determination of Cadmium. *Electrochem. Commun.* **2009**, *11*, 1085-1088.

[239] Fang, M.; Wang, K.; Lu, H.; Yang, Y.; Nutt, S. Covalent Polymer Functionalization of Graphene Nanosheets and Mechanical Properties of Composites. *J. Mater. Chem.* **2009**, *19*, 7098-7105.

[240] Li, J.; Guo, S.; Zhai, Y.; Wang, E. High-Sensitivity Determination of Lead and Cadmium Based on the Nafion-Graphene Composite Film. *Anal. Chim. Acta* **2009**, *649*, 196-201.

[241] Al-Mashat, L.; Shin, K.; Kalantar-zadeh, K.; Plessis, J. D.; Han, S. H.; Kojima, R. W.; Kaner, R. B.; Li, D.; Gou, X.; Ippolito, S. J.; Wlodarski, W. Graphene/Polyaniline Nanocomposite for Hydrogen Sensing. *J. Phys. Chem. C* **2010**, *114*, 16168-16173.

[242] Zeng, Y.; Zhou, Y.; Kong, L.; Zhou, T.; Shi, G. A Novel Composite of Sio2-Coated Graphene Oxide and Molecularly Imprinted Polymers for Electrochemical Sensing Dopamine. *Biosensors and Bioelectronics* **2013**, *45*, 25-33.

[243] Kim, S.; Oh, W.-K.; Jeong, Y. S.; Jang, J. Dual-Functional Poly(3,4-Ethylenedioxythiophene)/Mno2 Nanoellipsoids for Enhancement of Neurite Outgrowth and Exocytosed Biomolecule Sensing in Pc12 Cells. *Adv. Funct. Mater.* **2013**, *23*, 1947-1956.

[244] Wang, L.; Pu, K.-Y.; Li, J.; Qi, X.; Li, H.; Zhang, H.; Fan, C.; Liu, B. A Graphene–Conjugated Oligomer Hybrid Probe for Light-up Sensing of Lectin and Escherichia Coli. *Adv. Mater.* **2011**, *23*, 4386-4391.

[245] He, Q.; Wu, S.; Gao, S.; Cao, X.; Yin, Z.; Li, H.; Chen, P.; Zhang, H. Transparent, Flexible, All-Reduced Graphene Oxide Thin Film Transistors. *ACS Nano* **2011**, *5*, 5038-5044.

[246] Llobet, E. Gas Sensors Using Carbon Nanomaterials: A Review. *Sens. Actuators B Chem.* **2013**, *179*, 32-45.

[247] Kumar, S. K.; Castro, M.; Saiter, A.; Delbreilh, L.; Feller, J. F.; Thomas, S.; Grohens, Y. Development of Poly(Isobutylene-Co-Isoprene)/Reduced Graphene Oxide Nanocomposites for Barrier, Dielectric and Sensingapplications. *Mater. Lett.* **2013**, *96*, 109-112.

[248] Zheng, Z.; Du, Y.; Feng, Q.; Wang, Z.; Wang, C. Facile Method to Prepare Pd/Graphene–Polyaniline Nanocomposite and Used as New Electrode Material for Electrochemical Sensing. *J. Mol. Catal. A: Chem.* **2012**, *353–354*, 80-86.

[249] Konwer, S.; Guha, A.; Dolui, S. Graphene Oxide-Filled Conducting Polyaniline Composites as Methanol-Sensing Materials. *J. Mater. Sci.* **2013**, *48*, 1729-1739.

[250] Xing, X.-J.; Liu, X.-G.; He, Y.; Lin, Y.; Zhang, C.-L.; Tang, H.-W.; Pang, D.-W. Amplified Fluorescent Sensing of DNA Using Graphene Oxide and a Conjugated Cationic Polymer. *Biomacromolecules* **2012**, *14*, 117-123.

[251] Wang, Y.; Wu, Z.; Liu, Z. Upconversion Fluorescence Resonance Energy Transfer Biosensor with Aromatic Polymer Nanospheres as the Lable-Free Energy Acceptor. *Anal. Chem.* **2012**, *85*, 258-264.

[252] Tung, T. T.; Castro, M.; Kim, T. Y.; Suh, K. S.; Feller, J.-F. Graphene Quantum Resistive Sensing Skin for the Detection of Alteration Biomarkers. *J. Mater. Chem.* **2012**, *22*, 21754-21766.

[253] Qiu, J.-D.; Shi, L.; Liang, R.-P.; Wang, G.-C.; Xia, X.-H. Controllable Deposition of a Platinum Nanoparticle Ensemble on a Polyaniline/Graphene Hybrid as a Novel Electrode Material for Electrochemical Sensing. *Chem. Eur. J.* **2012**, *18*, 7950-7959.

[254] Worsley, M. A.; Pauzauskie, P. J.; Olson, T. Y.; Biener, J.; Satcher, J. H.; Baumann, T. F. Synthesis of Graphene Aerogel with High Electrical Conductivity. *J. Am. Chem. Soc.* **2010**, *132*, 14067-14069.

[255] Yang, Y.-H.; Bolling, L.; Priolo, M. A.; Grunlan, J. C. Super Gas Barrier and Selectivity of Graphene Oxide-Polymer Multilayer Thin Films. *Adv. Mater.* **2012**, *25*, 503-508.

[256] Choudalakis, G.; Gotsis, A. D. Permeability of Polymer/Clay Nanocomposites: A Review. *Eur. Polym. J.* **2009**, *45*, 967-984.

[257] Lee, D.; Choi, M.-C.; Ha, C.-S. Polynorbornene Dicarboximide/Amine Functionalized Graphene Hybrids for Potential Oxygen Barrier Films. *J. Polym. Sci., Part A: Polym. Chem.* **2012**, *50*, 1611-1621.

[258] Liu, H.; Kuila, T.; Kim, N. H.; Ku, B.-C.; Lee, J. H. In Situ Synthesis of the Reduced Graphene Oxide-Polyethyleneimine Composite and Its Gas Barrier Properties. *Journal of Materials Chemistry A* **2013**, *1*, 3739-3746.

[259] Tseng, I. H.; Liao, Y.-F.; Chiang, J.-C.; Tsai, M.-H. Transparent Polyimide/Graphene Oxide Nanocomposite with Improved Moisture Barrier Property. *Mater. Chem. Phys.* **2012**, *136*, 247-253.

[260] Song, P. a.; Yu, Y.; Zhang, T.; Fu, S.; Fang, Z.; Wu, Q. Permeability, Viscoelasticity, and Flammability Performances and Their Relationship to Polymer Nanocomposites. *Ind. Eng. Chem. Res.* **2012**, *51*, 7255-7263.

[261] Yun, J.-M.; Yeo, J.-S.; Kim, J.; Jeong, H.-G.; Kim, D.-Y.; Noh, Y.-J.; Kim, S.-S.; Ku, B.-C.; Na, S.-I. Solution-Processable Reduced Graphene Oxide as a Novel Alternative to PEDOT:PSS Hole Transport Layers for Highly Efficient and Stable Polymer Solar Cells. *Adv. Mater.* **2011**, *23*, 4923-4928.

[262] Li, S.-S.; Tu, K.-H.; Lin, C.-C.; Chen, C.-W.; Chhowalla, M. Solution-Processable Graphene Oxide as an Efficient Hole Transport Layer in Polymer Solar Cells. *ACS Nano* **2010**, *4*, 3169-3174.

[263] Tung, V. C.; Kim, J.; Huang, J. Graphene Oxide:Single-Walled Carbon Nanotube-Based Interfacial Layer for All-Solution-Processed Multijunction Solar Cells in Both Regular and Inverted Geometries. *Adv. Energy Mater.* **2012**, *2*, 299-303.

[264] Angmo, D.; Krebs, F. C. Flexible Ito-Free Polymer Solar Cells. *J. Appl. Polym. Sci.* **2013**, *129*, 1-14.

[265] Zhang, W.; Zhao, B.; He, Z.; Zhao, X.; Wang, H.; Yang, S.; Wu, H.; Cao, Y. High-Efficiency Ito-Free Polymer Solar Cells Using Highly Conductive Pedot:Pss/Surfactant Bilayer Transparent Anodes. *Energy. Environ. Sci.* **2013**, *6*, 1956-1964.

[266] Sun, Y.; Shi, G. Graphene/Polymer Composites for Energy Applications. *J. Polym. Sci., Part B: Polym. Phys.* **2013**, *51*, 231-253.

[267] Dai, L. Functionalization of Graphene for Efficient Energy Conversion and Storage. *Acc. Chem. Res.* **2013**, *46*, 31-42.

[268] Iwan, A.; Chuchmała, A. Perspectives of Applied Graphene: Polymer Solar Cells. *Prog. Polym. Sci.* **2012**, *37*, 1805-1828.

[269] Akhtar, M. S.; Kwon, S.; Stadler, F. J.; Yang, O. B. High Efficiency Solid State Dye Sensitized Solar Cells with Graphene-Polyethylene Oxide Composite Electrolytes. *Nanoscale* **2013**, *5*, 5403-5411.

[270] Qiao, Z.; Guojia, F.; Fei, C.; Hongwei, L.; Pingli, Q.; Caimao, Z. Low-Temperature Solution-Processed Graphene Oxide Derivative Hole Transport Layer for Organic Solar Cells. *J. Phys. D: Appl. Phys.* **2013**, *46*, 135101.

[271] Ran, C.; Wang, M.; Gao, W.; Ding, J.; Shi, Y.; Song, X.; Chen, H.; Ren, Z. Study on Photoluminescence Quenching and Photostability Enhancement of Meh-Ppv by Reduced Graphene Oxide. *J. Phys. Chem. C* **2012**, *116*, 23053-23060.

[272] Qu, S.; Li, M.; Xie, L.; Huang, X.; Yang, J.; Wang, N.; Yang, S. Noncovalent Functionalization of Graphene Attaching [6,6]-Phenyl-C61-Butyric Acid Methyl Ester (PCBM) and Application as Electron Extraction Layer of Polymer Solar Cells. *ACS Nano* **2013**, *7*, 4070-4081.

[273] Chuchmała, A.; Palewicz, M.; Sikora, A.; Iwan, A. Influence of Graphene Oxide Interlayer on PCE Value of Polymer Solar Cells. *Synth. Met.* **2013**, *169*, 33-40.

[274] Liu, X.; Kim, H.; Guo, L. J. Optimization of Thermally Reduced Graphene Oxide for an Efficient Hole Transport Layer in Polymer Solar Cells. *Organic Electronics* **2013**, *14*, 591-598.

[275] Lee, R.-H.; Huang, J.-L.; Chi, C.-H. Conjugated Polymer-Functionalized Graphite Oxide Sheets Thin Films for Enhanced Photovoltaic Properties of Polymer Solar Cells. *J. Polym. Sci., Part B: Polym. Phys.* **2013**, *51*, 137-148.

[276] Wang, D. H.; Kim, J. K.; Seo, J. H.; Park, I.; Hong, B. H.; Park, J. H.; Heeger, A. J. Transferable Graphene Oxide by Stamping Nanotechnology: Electron-Transport

Layer for Efficient Bulk-Heterojunction Solar Cells. *Angew. Chem. Int. Ed.* **2013**, *52*, 2874-2880.

[277] Huxtable, S. T.; Cahill, D. G.; Shenogin, S.; Xue, L.; Ozisik, R.; Barone, P.; Usrey, M.; Strano, M. S.; Siddons, G.; Shim, M.; Keblinski, P. Interfacial Heat Flow in Carbon Nanotube Suspensions. *Nat. Mater.* **2003**, *2*, 731-734.

[278] Yu, A.; Ramesh, P.; Sun, X.; Bekyarova, E.; Itkis, M. E.; Haddon, R. C. Enhanced Thermal Conductivity in a Hybrid Graphite Nanoplatelet – Carbon Nanotube Filler for Epoxy Composites. *Adv. Mater.* **2008**, *20*, 4740-4744.

[279] Veca, L. M.; Meziani, M. J.; Wang, W.; Wang, X.; Lu, F.; Zhang, P.; Lin, Y.; Fee, R.; Connell, J. W.; Sun, Y.-P. Carbon Nanosheets for Polymeric Nanocomposites with High Thermal Conductivity. *Adv. Mater.* **2009**, *21*, 2088-2092.

[280] Ma, W.-S.; Li, J.; Zhao, X.-S. Improving the Thermal and Mechanical Properties of Silicone Polymer by Incorporating Functionalized Graphene Oxide. *J. Mater. Sci.* **2013**, *48*, 5287-5294.

[281] Cheng, H. K. F.; Basu, T.; Sahoo, N. G.; Li, L.; Chan, S. H. Current Advances in the Carbon Nanotube/Thermotropic Main-Chain Liquid Crystalline Polymer Nanocomposites and Their Blends. *Polymers* **2012**, *4*, 889-921.

[282] Hsiao, M.-C.; Ma, C.-C. M.; Chiang, J.-C.; Ho, K.-K.; Chou, T.-Y.; Xie, X.; Tsai, C.-H.; Chang, L.-H.; Hsieh, C.-K. Thermally Conductive and Electrically Insulating Epoxy Nanocomposites with Thermally Reduced Graphene Oxide-Silica Hybrid Nanosheets. *Nanoscale* **2013**, *5*, 5863-5871.

[283] Wu, C.; Huang, X.; Wu, X.; Xie, L.; Yang, K.; Jiang, P. Graphene Oxide-Encapsulated Carbon Nanotube Hybrids for High Dielectric Performance Nanocomposites with Enhanced Energy Storage Density. *Nanoscale* **2013**, *5*, 3847-3855.

[284] Ha, H. W.; Choudhury, A.; Kamal, T.; Kim, D.-H.; Park, S.-Y. Effect of Chemical Modification of Graphene on Mechanical, Electrical, and Thermal Properties of Polyimide/Graphene Nanocomposites. *ACS Appl. Mater. Interfaces* **2012**, *4*, 4623-4630.

[285] Huang, X.; Iizuka, T.; Jiang, P.; Ohki, Y.; Tanaka, T. Role of Interface on the Thermal Conductivity of Highly Filled Dielectric Epoxy/Aln Composites. *J. Phys. Chem. C* **2012**, *116*, 13629-13639.

[286] Wang, Z.; Nelson, J. K.; Hillborg, H.; Zhao, S.; Schadler, L. S. Graphene Oxide Filled Nanocomposite with Novel Electrical and Dielectric Properties. *Adv. Mater.* **2012**, *24*, 3134-3137.

[287] Qi, X.-Y.; Yan, D.; Jiang, Z.; Cao, Y.-K.; Yu, Z.-Z.; Yavari, F.; Koratkar, N. Enhanced Electrical Conductivity in Polystyrene Nanocomposites at Ultra-Low Graphene Content. *ACS Appl. Mater. Interfaces* **2011**, *3*, 3130-3133.

[288] Huang, Y.; Qin, Y.; Zhou, Y.; Niu, H.; Yu, Z.-Z.; Dong, J.-Y. Polypropylene/Graphene Oxide Nanocomposites Prepared by in Situ Ziegler−Natta Polymerization. *Chem. Mater.* **2010**, *22*, 4096-4102.

[289] Liu, A.; Li, C.; Bai, H.; Shi, G. Electrochemical Deposition of Polypyrrole/Sulfonated Graphene Composite Films. *J. Phys. Chem. C* **2010**, *114*, 22783-22789.

[290] Wang, H.; Hao, Q.; Yang, X.; Lu, L.; Wang, X. Graphene Oxide Doped Polyaniline for Supercapacitors. *Electrochem. Commun.* **2009**, *11*, 1158-1161.

[291] Zhou, X.; Wu, T.; Hu, B.; Yang, G.; Han, B. Synthesis of Graphene/Polyaniline Composite Nanosheets Mediated by Polymerized Ionic Liquid. *Chem. Commun.* **2010**, *46*, 3663-3665.

[292] Yu, D.; Dai, L. Self-Assembled Graphene/Carbon Nanotube Hybrid Films for Supercapacitors. *The Journal of Physical Chemistry Letters* **2010**, *1*, 467-470.

[293] Ouyang, W.; Sun, J.; Memon, J.; Wang, C.; Geng, J.; Huang, Y. Scalable Preparation of Three-Dimensional Porous Structures of Reduced Graphene Oxide/Cellulose Composites and Their Application in Supercapacitors. *Carbon* **2013**, *62*, 501-509.

[294] Secor, E. B.; Prabhumirashi, P. L.; Puntambekar, K.; Geier, M. L.; Hersam, M. C. Inkjet Printing of High Conductivity, Flexible Graphene Patterns. *The Journal of Physical Chemistry Letters* **2013**, *4*, 1347-1351.

[295] Huang, P.; Chen, W.; Yan, L. An Inorganic-Organic Double Network Hydrogel of Graphene and Polymer. *Nanoscale* **2013**, *5*, 6034-6039.

[296] Liu, H.-H.; Peng, W.-W.; Hou, L.-C.; Wang, X.-C.; Zhang, X.-X. The Production of a Melt-Spun Functionalized Graphene/Poly(E-Caprolactam) Nanocomposite Fiber. *Compos. Sci. Technol.* **2013**, *81*, 61-68.

[297] Cong, H.-P.; Ren, X.-C.; Wang, P.; Yu, S.-H. Flexible Graphene-Polyaniline Composite Paper for High-Performance Supercapacitor. *Energy. Environ. Sci.* **2013**, *6*, 1185-1191.

[298] Okhay, O.; Krishna, R.; Salimian, M.; Titus, E.; Gracio, J.; Guerra, L. M.; Ventura, J. Conductivity Enhancement and Resistance Changes in Polymer Films Filled with Reduced Graphene Oxide. *J. Appl. Phys.* **2013**, *113*, 064307.

[299] Shi, Z.; Phillips, G. O.; Yang, G. Nanocellulose Electroconductive Composites. *Nanoscale* **2013**, *5*, 3194-3201.

[300] Tang, L.; Li, X.; Du, D.; He, C. Fabrication of Multilayer Films from Regenerated Cellulose and Graphene Oxide through Layer-by-Layer Assembly. *Prog. Nat. Sci.: Mat. Int.* **2012**, *22*, 341-346.

[301] Zhuang, H.; Xu, X.; Liu, Y.; Zhou, Q.; Xu, X.; Li, H.; Xu, Q.; Li, N.; Lu, J.; Wang, L. Dual-Mechanism-Controlled Ternary Memory Devices Fabricated by Random Copolymers with Pendent Carbazole and Nitro-Azobenzene. *J. Phys. Chem. C* **2012**, *116*, 25546-25551.

[302] Yan, D.; Zhang, H.-B.; Jia, Y.; Hu, J.; Qi, X.-Y.; Zhang, Z.; Yu, Z.-Z. Improved Electrical Conductivity of Polyamide 12/Graphene Nanocomposites with Maleated Polyethylene-Octene Rubber Prepared by Melt Compounding. *ACS Appl. Mater. Interfaces* **2012**, *4*, 4740-4745.

[303] Incani, V.; Danumah, C.; Boluk, Y. Nanocomposites of Nanocrystalline Cellulose for Enzyme Immobilization. *Cellulose* **2013**, *20*, 191-200.

[304] Tompkins H. G.; McGahan, W. A. *Spectroscopic Ellipsometry and Reflectometry*, John Wiley & Sons Inc, **1999**.

[305] Anderson, K. D.; Slocik, J. M.; McConney, M. E.; Enlow, J. O.; Jakubiak, R.; Bunning, T. J.; Naik, R. R.; Tsukruk, V. V. S*mall* **2009**, *5*, 741-749.

[306] Wang, Y.; Alsmeyer, D. C.; McCreery, R. L. *Chem. Mater.* **1990**, *2*, 557-563.

[307] Ko, H.; Pikus, Y.; Jiang, C.; Jauss, A.; Hollricher, O.; Tsukruk, V. V. *Appl. Phys. Lett.* **2004**, *85*, 2598-2600.

[308] Jiang, C.; Ko, H.; Tsukruk, V. V. *Adv. Mater.* **2005**, *17*, 2127-2131.

[309] Raravikar, N. R.; Keblinski, P.; Rao, A. M.; Dresselhaus, M. S.; Schadler, L. S.; Ajayan, P. M. *Phys. Rev. B.* **2002**, *66*, 235424.

[310] Singamaneni, S.; Gupta, M. K.; Yang, R.; Tomczak, M.; Naik, R. R.; Wang, Z. L.; Tsukruk, V. V. *ACS Nano* **2009**, *3*, 2593.

[311] G. Socrates, *Infrared and Raman Characteristic Group Frequencies: Tables and Charts*; John Wiley & Sons: New York, **2001**.

[312] Hu, X.; Kaplan, D.; Cebe, P. Determining Beta-Sheet Crystallinity in Fibrous Proteins by Thermal Analysis and Infrared Spectroscopy. Macromolecules **2006**, *39*, 6161-6170.

[313] Boluk, Y.; Danumah, C. Analysis of Cellulose Nanocrystal Rod Lengths by Dynamic Light Scattering and Electron Microscopy. *J. Nanopart. Res.* **2013**, *16*, 2174.

[314] Freund, L. B.; Suresh, S. *Thin film materials: stress, defect formation, and surface evolution*, Cambridge University Press: Cambridge, UK, **2003**.

[315] Timoshenko, S. *Theory of Plates and Shells*, 2nd ed., McGraw-Hill Book Company: New York, **1959**.

[316] Stafford, C. M.; Harrison, C.; Beers, K. L.; Karim, A.; Amis, E. J.; VanLandingham, M. R.; Kim, H.-C.; Volksen, W.; Miller, R. D.; Simonyi, E. E. A Buckling-Based Metrology for Measuring the Elastic Moduli of Polymeric Thin Films. *Nat. Mater.* **2004**, *3*, 545-550.

[317] Vandeparre, H.; Damman, P. Wrinkling of Stimuloresponsive Surfaces: Mechanical Instability Coupled to Diffusion. *Phys. Rev. Lett.* **2008**, *101*, 124301.

[318] Griffin Jr, A. J.; Brotzen, F. R.; Dunn, C. F. Mechanical Properties and Microstructures of Al-1%Si Thin Film Metallizations. *Thin Solid Films* **1987**, *150*, 237-244.

[319] El Khakani, M. A.; Chaker, M.; Jean, A.; Boily, S.; Kieffer, J. C.; O'Hern, M. E.; Ravet, M. F.; Rousseaux, F. Hardness and Young's Modulus of Amorphous a-Sic Thin Films Determined by Nanoindentation and Bulge Tests. *J. Mater. Res.* **1994**, *9*, 96-103.

[320] Edwards, R. L.; Coles, G.; Sharpe, W. N., Jr. Comparison of Tensile and Bulge Tests for Thin-Film Silicon Nitride. *Experimental Mechanics* **2004**, *44*, 49-54.

[321] Zheng, D. W.; Xu, Y. H.; Tsai, Y. P.; Tu, K. N.; Patterson, P.; Zhao, B.; Liu, Q.-Z.; Brongo, M. Mechanical Property Measurement of Thin Polymeric-Low Dielectric-

Constant Films Using Bulge Testing Method. *Appl. Phys. Lett.* **2000**, *76*, 2008-2010.

[322] Poilane, C.; Delobelle, P.; Lexcellent, C.; Hayashi, S.; Tobushi, H. Analysis of the Mechanical Behavior of Shape Memory Polymer Membranes by Nanoindentation, Bulging and Point Membrane Deflection Tests. *Thin Solid Films* **2000**, *379*, 156-165.

[323] Kovalev, A.; Shulha, H.; Lemieux, M.; Myshkin, N.; Tsukruk, V. V. Nanomechanical Probing of Layered Nanoscale Polymer Films with Atomic Force Microscopy. *J. Mater. Res.* **2004**, *19*, 716-728.

[324] Gojny, F. H.; Wichmann, M. H. G.; Köpke, U.; Fiedler, B.; Schulte, K. Carbon Nanotube-Reinforced Epoxy-Composites: Enhanced Stiffness and Fracture Toughness at Low Nanotube Content. *Compos. Sci. Technol.* **2004**, *64*, 2363-2371.

[325] Prest, W. M.; Luca, D. J. The Origin of the Optical Anisotropy of Solvent Cast Polymer Films. *J. Appl. Phys*. **1979**, *50*, 6067-6071.

[326] Holzwarth, U.; Gibson, N. The Scherrer Equation versus the 'Debye-Scherrer Equation'. *Nat. Nano.* **2011**, *6*, 534-534.

[327] Keten, S.; Xu, Z.; Ihle, B.; Buehler, M. J. Nanoconfinement Controls Stiffness, Strength and Mechanical Toughness of β-Sheet Crystals in Silk. *Nat. Mater.* **2010**, *9*, 359-367.

[328] Vlasak, J. J.; Nix, W. D. A New Bulge Test Technique for The Determination of Young's Modulus and Poisson's Ratio of Thin Films. *J. Mater. Res*. **1992**, *7*, 3242-3249.

[329] J. W. Beams, Structure and Properties of Thin Solid Films, John Wiley: New York, **1959**.

[330] Kharlampieva, E.; Kozlovskaya, V.; Wallet, B.; Shevchenko, V. V.; Naik, R. R.; Vaia, R.; Kaplan, D. L.; Tsukruk, V. V. Co-Cross-Linking Silk Matrices with Silica Nanostructures for Robust Ultrathin Nanocomposites. *ACS Nano* **2010**, *4*, 7053-7063.

[331] Law, C. W.; Wong, K. S.; Yang, Z.; Horsburgh, K. S.; Monkman, A. P. Observation of In-Plane Optical Anisotropy of Spin-Cast Rigid-Rod Electroluminescent Polymer Films. *Appl. Phys. Lett*. **2000**, *76*, 1416-1418.

[332] Posati, T.; Benfenati, V.; Sagnella, A.; Pistone, A.; Nocchetti, M.; Donnadio, A.; Ruani, G.; Zamboni, R.; Muccini, M. Innovative Multifunctional Silk Fibroin and Hydrotalcite Nanocomposites: A Synergic Effect Of The Components. *Biomacromolecules* **2014**, *15*, 158-168.

[333] Moraes, M. A.; Crouzier, T.; Rubner, M.; Beppu, M. M. Factors Controlling The Deposition of Silk Fibroin Nano-Fibrils During Layer-by-Layer Assembly. *Biomacromolecules* **2015**, *16*, 97-104.

[334] Yun, H. S.; Kim, M. K.; Kwak, H. W.; Lee, J. Y.; Kim, M. H.; Kim, E. H.; Lee, K. H. Preparation and Characterization of Silk Sericin/Glycerol/Graphene Oxide Nanocomposite Film. *Fiber. Polym.* **2013**, *14*, 2111-2116.

[335] Tang, Z.; Kotov, N. A.; Magonov, S.; Ozturk, B. Nanostructured Artificial Nacre. *Nat. Mater*. **2003**, *2*, 413-418.

[336] Pandey, J. K.; Handbook of Polymer Nanocomposites: Processing, Performance and Application, Springer: Heidelberg New York Dordrecht London, **2014**.

[337] Cui, W.; Li, M. Z.; Liu, J. Y.; Wang, B.; Zhang, C.; Jiang, L.; Cheng. Q. F. A Strong Integrated Strength and Toughness Artificial Nacre Based on Dopamine Cross-Linked Graphene Oxide. *ACS Nano* **2014**, *8*, 9511-9517.

[338] Wang, L.; Lu, C. X.; Zhang, B. P.; Zhao, B.; Wu, F.; Guan, S. Y. Fabrication and Characterization of Flexible Silk Fibroin Films Reinforced with Graphene Oxide for Biomedical Applications. *RSC. Adv.* **2014**, *4*, 40312-40320.

[339] Compton, O. C.; Cranford, S. W.; Putz, K. W.; An, Z.; Brinson, L. C.; Buehler, M. J.; Nguyen, S. T. Tuning the Mechanical Properties of Graphene Oxide Paper and Its Associated Polymer Nanocomposites by Controlling Cooperative Intersheet Hydrogen Bonding. *ACS Nano* **2011**, *6*, 2008-2019.

[340] Munch, E.; Launey, M. E.; Alsem, D. H.; Saiz, E.; Tomsia, A. P.; Ritchie, R. O. Tough, Bio-Inspired Hybrid Materials. *Science* **2008**, *322*, 1516-1520.

[341] Xu, Z.; Sun, H.; Zhao, X.; Gao, C. Ultrastrong Fibers Assembled from Giant Graphene Oxide Sheets. *Adv. Mater.* **2012**, *25*, 188-193.

[342] Park, S.; Lee, K.-S.; Bozoklu, G.; Cai, W.; Nguyen, S. T.; Ruoff, R. S. Graphene Oxide Papers Modified by Divalent Ions—Enhancing Mechanical Properties Via Chemical Cross-Linking. *ACS Nano* **2008**, *2*, 572-578.

[343] Huang, L.; Li, C.; Yuan, W.; Shi, G. Strong Composite Films with Layered Structures Prepared by Casting Silk Fibroin-Graphene Oxide Hydrogels. *Nanoscale* **2013**, *5*, 3780-3786.

[344] Zhang, X.; Sreekumar, T. V.; Liu, T.; Kumar, S. Properties and Structure of Nitric Acid Oxidized Single Wall Carbon Nanotube Films. *J. Phys. Chem. B* **2004**, *108*, 16435-16440.

[345] Guo, H.; Sreekumar, T. V.; Liu, T.; Minus, M.; Kumar, S. Structure and Properties of Polyacrylonitrile/Single Wall Carbon Nanotube Composite Films. *Polymer* **2005**, *46*, 3001-3005.

[346] Yuan, J.; Ma, L.-P.; Pei, S.; Du, J.; Su, Y.; Ren, W.; Cheng, H.-M. Tuning the Electrical and Optical Properties of Graphene by Ozone Treatment for Patterning Monolithic Transparent Electrodes. *ACS Nano* **2013**, *7*, 4233-4241.

[347] Aizenberg, J.; Weaver, J. C.; Thanawala, M. S.; Sundar, V. C.; Morse, D. E.; Fratzl, P. Skeleton of Euplectella Sp.: Structural Hierarchy from the Nanoscale to the Macroscale. *Science* **2005**, *309*, 275-278.

[348] Shulha, H.; Po Foo, C. W.; Kaplan, D. L.; Tsukruk, V. V. Unfolding the Multi-Length Scale Domain Structure of Silk Fibroin Protein. *Polymer* **2006**, *47*, 5821-5830.

[349] Altman, G. H.; Diaz, F.; Jakuba, C.; Calabro, T.; Horan, R. L.; Chen, J.; Lu, H.; Richmond, J.; Kaplan, D. L. Silk-Based Biomaterials. *Biomaterials* **2003**, *24*, 401-416.

[350] Porter, D.; Vollrath, F. Silk as a Biomimetic Ideal for Structural Polymers. *Adv. Mater.* **2009**, *21*, 487-492.

[351] Park, S.; Ruoff, R. S. Chemical Methods for the Production of Graphenes. *Nat. Nanotechnol.* **2009**, *4*, 217-224.

[352] Menard, E.; Meitl, M. A.; Sun, Y.; Park, J.-U.; Shir, D. J.-L.; Nam, Y.-S.; Jeon, S.; Rogers, J. A. Micro- and Nanopatterning Techniques for Organic Electronic and Optoelectronic Systems. *Chem. Rev.* **2007**, *107*, 1117-1160.

[353] Mei, X.; Zheng, H.; Ouyang, J. Ultrafast Reduction of Graphene Oxide with Zn Powder in Neutral and Alkaline Solutions at Room Temperature Promoted by the Formation of Metal Complexes. *J. Mater. Chem.* **2012**, *22*, 9109-9116.

[354] Cao, X.; Qi, D.; Yin, S.; Bu, J.; Li, F.; Goh, C. F.; Zhang, S.; Chen, X. Ambient Fabrication of Large-Area Graphene Films Via a Synchronous Reduction and Assembly Strategy. *Adv. Mater.* **2013**, *25*, 2957-2962.

[355] Bockris, J. O. M.; Reddy, A. K. N. *Modern Electrochemistry*. Plenum Press: New York, **1998**.

[356] Park, S.; An, J.; Jung, I.; Piner, R. D.; An, S. J.; Li, X.; Velamakanni, A.; Ruoff, R. S. Colloidal Suspensions of Highly Reduced Graphene Oxide in a Wide Variety of Organic Solvents. *Nano Lett.* **2009**, *9*, 1593-1597.

[357] Abdelkader, A. M.; Vallés, C.; Cooper, A. J.; Kinloch, I. A.; Dryfe, R. A. W. Alkali Reduction of Graphene Oxide in Molten Halide Salts: Production of Corrugated Graphene Derivatives for High-Performance Supercapacitors. *ACS Nano* **2014**, *8*, 11225-11233.

[358] Li, M.; Tang, Z.; Leng, M.; Xue, J. Flexible Solid-State Supercapacitor Based on Graphene-Based Hybrid Films. *Adv. Funct. Mater.* **2014**, *24*, 7495-7502.

[359] Eda, G.; Fanchini, G.; Chhowalla, M. Large-Area Ultrathin Films of Reduced Graphene Oxide as a Transparent and Flexible Electronic Material. *Nat Nano* **2008**, *3*, 270-274.

[360] Xin, G.; Sun, H.; Hu, T.; Fard, H. R.; Sun, X.; Koratkar, N.; Borca-Tasciuc, T.; Lian, J. Large-Area Freestanding Graphene Paper for Superior Thermal Management. *Adv. Mater.* **2014**, *26*, 4521-4526.

[361] Kwon, S. R.; Jeon, J.-W.; Lutkenhaus, J. L. Sprayable, Paintable Layer-by-Layer Polyaniline Nanofiber/Graphene Electrodes. *RSC Advances* **2015**, *5*, 14994-15001.

[362] Jeon, J.-W.; Kwon, S. R.; Lutkenhaus, J. L. Polyaniline Nanofiber/Electrochemically Reduced Graphene Oxide Layer-by-Layer Electrodes for Electrochemical Energy Storage. *J. Mater. Chem. A* **2015**, *3*, 3757-3767.

[363] Cancado, L. G.; Takai, K.; Enoki, T.; Endo, M.; Kim, Y. A.; Mizusaki, H.; Jorio, A.; Coelho, L. N.; Magalhaes-Paniago, R.; Pimenta, M. A. General Equation for the

Determination of the Crystallite Size L[Sub a] of Nanographite by Raman Spectroscopy. *Appl. Phys. Lett.* **2006**, *88*, 163106-163103.

[364] Shi, L.; Chu, Z.; Liu, Y.; Jin, W.; Xu, N. In Situ Fabrication of Three-Dimensional Graphene Films on Gold Substrates with Controllable Pore Structures for High-Performance Electrochemical Sensing. *Adv. Funct. Mater.* **2014**, *24*, 7032-7041.

[365] Gao, X.; Jang, J.; Nagase, S. Hydrazine and Thermal Reduction of Graphene Oxide: Reaction Mechanisms, Product Structures, and Reaction Design. *J. Phys. Chem. C* **2009**, *114*, 832-842.

[366] Zhang, M.; Huang, L.; Chen, J.; Li, C.; Shi, G. Ultratough, Ultrastrong, and Highly Conductive Graphene Films with Arbitrary Sizes. *Adv. Mater.* **2014**, *26*, 7588-7592.

[367] Meng, Y.; Wang, K.; Zhang, Y.; Wei, Z. Hierarchical Porous Graphene/Polyaniline Composite Film with Superior Rate Performance for Flexible Supercapacitors. *Adv. Mater.* **2013**, *25*, 6985-6990.

[368] Eda, G.; Mattevi, C.; Yamaguchi, H.; Kim, H.; Chhowalla, M. Insulator to Semimetal Transition in Graphene Oxide. *J. Phys. Chem. C* **2009**, *113*, 15768-15771.

[369] Streetman, B. G.; Banerjee, S. *Solid State Electronic Devices*. Pearson Education, Limited: 2014.

[370] Mao, H.; Hu, F.; Ye, Q.-L.; Xu, Y.; Yang, X.; Lu, B. Manipulating the Charge Transfer at Cupc/Graphene Interface by O2 Plasma Treatments. *Nanoscale* **2014**, *6*, 8149-8154.

[371] Muhammad, R. I.; Daeha, J.; Saiful, I. K. Schottky Diode Via Dielectrophoretic Assembly of Reduced Graphene Oxide Sheets between Dissimilar Metal Contacts. *New Journal of Physics* **2011**, *13*, 035021.

[372] Fan, Z.-J.; Kai, W.; Yan, J.; Wei, T.; Zhi, L.-J.; Feng, J.; Ren, Y.-m.; Song, L.-P.; Wei, F. Facile Synthesis of Graphene Nanosheets Via Fe Reduction of Exfoliated Graphite Oxide. *ACS Nano* **2010**, *5*, 191-198.

[373] Kim, S.; Zhou, S.; Hu, Y.; Acik, M.; Chabal, Y. J.; Berger, C.; de Heer, W.; Bongiorno, A.; Riedo, E. Room-Temperature Metastability of Multilayer Graphene Oxide Films. *Nat. Mater.* **2012**, *11*, 544-549.

[374] Dimiev, A. M.; Alemany, L. B.; Tour, J. M. Graphene Oxide. Origin of Acidity, Its Instability in Water, and a New Dynamic Structural Model. *ACS Nano* **2012**, *7*, 576-588.

[375] Šimek, P.; Sofer, Z.; Jankovský, O.; Sedmidubský, D.; Pumera, M. Oxygen-Free Highly Conductive Graphene Papers. *Adv. Funct. Mater.* **2014**, *24*, 4878-4885.

[376] Lide, D. R. *Handbook of Chemistry and Physics, 76th Edition.* CRC Press: 1996.

[377] Kim, Y. H.; Sachse, C.; Machala, M. L.; May, C.; Müller-Meskamp, L.; Leo, K. Highly Conductive PEDOT:PSS Electrode with Optimized Solvent and Thermal Post-Treatment for Ito-Free Organic Solar Cells. *Adv. Funct. Mater.* **2011**, *21*, 1076-1081.

[378] Cheng, T.; Zhang, Y.; Lai, W.-Y.; Huang, W. Stretchable Thin-Film Electrodes for Flexible Electronics with High Deformability and Stretchability. *Adv. Mater.* **2015**, *27*, 3349-3376.

[379] Hamedi, M.; Karabulut, E.; Marais, A.; Herland, A.; Nyström, G.; Wågberg, L. Nanocellulose Aerogels Functionalized by Rapid Layer-by-Layer Assembly for High Charge Storage and Beyond. *Angew. Chem. Int. Ed.* **2013**, *52*, 12038-12042.

[380] Bondeson, D.; Mathew, A.; Oksman, K. Optimization of the Isolation of Nanocrystals from Microcrystalline Cellulose by Acid Hydrolysis. *Cellulose* **2006**, *13*, 171-180.

[381] Zhang, T.; Wang, W.; Zhang, D.; Zhang, X.; Ma, Y.; Zhou, Y.; Qi, L. Biotemplated Synthesis of Gold Nanoparticle–Bacteria Cellulose Nanofiber Nanocomposites and Their Application in Biosensing. *Adv. Funct. Mater.* **2010**, *20*, 1152-1160.

[382] Huang, Y.; Hu, D.; Wen, S.; Shen, M.; Zhu, M.; Shi, X. Selective Removal of Mercury Ions Using Thymine-Grafted Electrospun Polymer Nanofibers. *New J. Chem.* **2014**, *38*, 1533-1539.

[383] Huang, J.-L.; Li, C.-J.; Gray, D. G. Functionalization of Cellulose Nanocrystal Films Via "Thiol-Ene" Click Reaction. *RSC Advances* **2014**, *4*, 6965-6969.

[384] Ye, C.; Malak, S. T.; Hu, K.; Wu, W.; Tsukruk, V. V. Cellulose Nanocrystal Microcapsules as Tunable Cages for Nano- and Microparticles. *ACS Nano* **2015,** *9*, 10887-10895.

[385] Sukhishvili, S. A.; Granick, S. Layered, Erasable Polymer Multilayers Formed by Hydrogen-Bonded Sequential Self-Assembly. *Macromolecules* **2002**, *35*, 301-310.

[386] T. Yang, L. Liu, J. Liu, M. Chen, J. Wang, Sukhishvili, S. A.; Granick, S. Layered, Erasable Polymer Multilayers Formed by Hydrogen-Bonded Sequential Self-Assembly. *Macromolecules* **2002**, *35*, 301-310.

[387] Reiter, G.; Hamieh, M.; Damman, P.; Sclavons, S.; Gabriele, S.; Vilmin, T.; Raphael, E. Residual Stresses in Thin Polymer Films Cause Rupture and Dominate Early Stages of Dewetting. *Nat. Mater.* **2005**, *4*, 754-758.

[388] Raja, S. N.; Basu, S.; Limaye, A. M.; Anderson, T. J.; Hyland, C. M.; Lin, L.; Alivisatos, A. P.; Ritchie, R. O. Strain-dependent dynamic mechanical properties of Kevlar to failure: Structural correlations and comparisons to other polymers. *Mater. Today Commun.* **2015**, *2*, e33.

[389] Hu, K.; Kulkarni, D. D.; Choi, I.; Tsukruk, V. V. Graphene-Polymer Nanocomposites for Structural and Functional Applications. *Prog. Polym. Sci.* **2014**, *39*, 1934-1972.

[390] Cheng, Q.; Li, M.; Jiang, L.; Tang, Z. Bioinspired Layered Composites Based on Flattened Double-Walled Carbon Nanotubes. *Adv. Mater.* **2012**, *24*, 1838-1843.

[391] Wang, B.; Walther, A. Self-Assembled, Iridescent, Crustacean-Mimetic Nanocomposites with Tailored Periodicity and Layered Cuticular Structure. *ACS Nano* **2015**, *9*, 10637-10646.

[392] Espinosa, H. D.; Rim, J. E.; Barthelat, F.; Buehler, M. J. Merger of Structure and Material in Nacre and Bone – Perspectives on De Novo Biomimetic Materials. *Progress in Materials Science* **2009**, *54*, 1059-1100.

[393] Becerril, H. A.; Mao, J.; Liu, Z.; Stoltenberg, R. M.; Bao, Z.; Chen, Y. Evaluation of Solution-Processed Reduced Graphene Oxide Films as Transparent Conductors. *ACS Nano* **2008**, *2*, 463-470.

[394] Tiwana, M. I.; Redmond, S. J.; Lovell, N. H. A Review of Tactile Sensing Technologies with Applications in Biomedical Engineering. *Sensors and Actuators A: Physical* **2012**, *179*, 17-31.

[395] Dario, P.; Piaggio, C. E. *Sensors and Sensory Systems for Advanced Robots*. Springer Berlin Heidelberg: **2012**.

[396] Dahiya, R. S.; Valle, M. *Robotic Tactile Sensing: Technologies and System*. Springer Netherlands: **2012**.

[397] Zhong, Q.; Zhong, J.; Cheng, X.; Yao, X.; Wang, B.; Li, W.; Wu, N.; Liu, K.; Hu, B.; Zhou, J. Paper-Based Active Tactile Sensor Array. *Adv. Mater.* **2015,** *27*, 7130-7136.

[398] Wu, W.; Wen, X.; Wang, Z. L. Taxel-Addressable Matrix of Vertical-Nanowire Piezotronic Transistors for Active and Adaptive Tactile Imaging. *Science* **2013**, *340*, 952-957.

[399] Wang, Z. L. Nanopiezotronics. *Adv. Mater.* **2007**, *19*, 889-892.

[400] Pan, C.; Dong, L.; Zhu, G.; Niu, S.; Yu, R.; Yang, Q.; Liu, Y.; Wang, Z. L. High-Resolution Electroluminescent Imaging of Pressure Distribution Using a Piezoelectric Nanowire Led Array. *Nat. Photon.* **2013**, *7*, 752-758.

[401] Pang, C.; Lee, G.-Y.; Kim, T.-i.; Kim, S. M.; Kim, H. N.; Ahn, S.-H.; Suh, K.-Y. A Flexible and Highly Sensitive Strain-Gauge Sensor Using Reversible Interlocking of Nanofibres. *Nat. Mater.* **2012**, *11*, 795-801.

[402] Yao, H.-B.; Ge, J.; Wang, C.-F.; Wang, X.; Hu, W.; Zheng, Z.-J.; Ni, Y.; Yu, S.-H. A Flexible and Highly Pressure-Sensitive Graphene–Polyurethane Sponge Based on Fractured Microstructure Design. *Adv. Mater.* **2013**, *25*, 6692-6698.

[403] Tee, B. C. K.; Wang, C.; Allen, R.; Bao, Z. An Electrically and Mechanically Self-Healing Composite with Pressure- and Flexion-Sensitive Properties for Electronic Skin Applications. *Nat. Nanotechnol.* **2012**, *7*, 825-832.

[404] Mannsfeld, S. C. B.; Tee, B. C. K.; Stoltenberg, R. M.; Chen, C. V. H. H.; Barman, S.; Muir, B. V. O.; Sokolov, A. N.; Reese, C.; Bao, Z. Highly Sensitive Flexible Pressure Sensors with Microstructured Rubber Dielectric Layers. *Nat. Mater.* **2010**, *9*, 859-864.

[405] Vandeparre, H.; Watson, D.; Lacour, S. P. Extremely Robust and Conformable Capacitive Pressure Sensors Based on Flexible Polyurethane Foams and Stretchable Metallization. *Appl. Phys. Lett.* **2013**, *103*, 204103.

[406] Yang, Y.; Zhang, H.; Lin, Z.-H.; Zhou, Y. S.; Jing, Q.; Su, Y.; Yang, J.; Chen, J.; Hu, C.; Wang, Z. L. Human Skin Based Triboelectric Nanogenerators for

Harvesting Biomechanical Energy and as Self-Powered Active Tactile Sensor System. *ACS Nano* **2013**, *7*, 9213-9222.

[407] Zhu, G.; Yang, W. Q.; Zhang, T.; Jing, Q.; Chen, J.; Zhou, Y. S.; Bai, P.; Wang, Z. L. Self-Powered, Ultrasensitive, Flexible Tactile Sensors Based on Contact Electrification. *Nano Lett.* **2014**, *14*, 3208-3213.

[408] Yi, F.; Lin, L.; Niu, S.; Yang, J.; Wu, W.; Wang, S.; Liao, Q.; Zhang, Y.; Wang, Z. L. Self-Powered Trajectory, Velocity, and Acceleration Tracking of a Moving Object/Body Using a Triboelectric Sensor. *Adv. Funct. Mater.* **2014**, *24*, 7488-7494.

[409] Zang, Y.; Zhang, F.; Di, C.-a.; Zhu, D. Advances of Flexible Pressure Sensors toward Artificial Intelligence and Health Care Applications. *Mater. Horiz.* **2015**, *2*, 140-156.

[410] Wang, Z. L.; Song, J. Piezoelectric Nanogenerators Based on Zinc Oxide Nanowire Arrays. *Science* **2006**, *312*, 242-246.

[411] Xu, S.; Qin, Y.; Xu, C.; Wei, Y.; Yang, R.; Wang, Z. L. Self-Powered Nanowire Devices. *Nat. Nanotechnol.* **2010**, *5*, 366-373.

[412] Fan, F.-R.; Tian, Z.-Q.; Lin Wang, Z. Flexible Triboelectric Generator. *Nano Energy* **2012**, *1*, 328-334.

[413] Mole, R. H. The Relative Humidity of the Skin. *J. Physio.* **1948**, *107*, 399-411.

[414] Chen, Z.; Lu, C. Humidity Sensors: A Review of Materials and Mechanisms. *Sensor Lett.* **2005**, *3*, 274-295.

[415] Farahani, H.; Wagiran, R.; Hamidon, M. Humidity Sensors Principle, Mechanism, and Fabrication Technologies: A Comprehensive Review. *Sensors* **2014**, *14*, 7881-7839.

[416] Lee, C.-Y.; Lee, G.-B. Humidity Sensors: A Review. *Sensor Lett.* **2005**, *3*, 1-15.

[417] Mukhopadhyay, P.; Gupta, R. K. *Graphite, Graphene, and Their Polymer Nanocomposites*. CRC Press: **2012**.

[418] Singh, V.; Joung, D.; Zhai, L.; Das, S.; Khondaker, S. I.; Seal, S. Graphene Based Materials: Past, Present and Future. *Prog. Mater. Sci.* **2011**, *56*, 1178-1271.

[419] Zhao, J.; Zhang, G.-Y.; Shi, D.-X. Review of Graphene-Based Strain Sensors. *Chin. Phys. B* **2013**, *22*, 057701.

[420] Dai, L. Functionalization of Graphene for Efficient Energy Conversion and Storage. *Acc. Chem. Res.* **2012**, *46*, 31-42.

[421] Wolf, E. L. *Applications of Graphene: An Overview*. Springer International Publishing: **2014**.

[422] Yin, Y.; Hu, K.; Grant, A. M.; Zhang, Y.; Tsukruk, V. V. Biopolymeric Nanocomposites with Enhanced Interphases. *Langmuir* **2015**, *31*, 10859-10870.

[423] Hu, K.; Tsukruk, V. V. Tuning the Electronic Properties of Robust Bio-Bond Graphene Papers by Spontaneous Electrochemical Reduction: From Insulators to Flexible Semi-Metals. *Chem. Mater.* **2015**, *27*, 6717-6729.

[424] Zhao, F.; Cheng, H.; Zhang, Z.; Jiang, L.; Qu, L. Direct Power Generation from a Graphene Oxide Film under Moisture. *Adv. Mater.* **2015,** *27*, 4351-4357.

[425] Li, Y.; Fan, K.; Ban, H.; Yang, M. Detection of Very Low Humidity Using Polyelectrolyte/Graphene Bilayer Humidity Sensors. *Sensor Actuat. B-Chem.* **2016**, *222*, 151-158.

[426] Borini, S.; White, R.; Wei, D.; Astley, M.; Haque, S.; Spigone, E.; Harris, N.; Kivioja, J.; Ryhänen, T. Ultrafast Graphene Oxide Humidity Sensors. *ACS Nano* **2013**, *7*, 11166-11173.

[427] Hou, C.; Wang, H.; Zhang, Q.; Li, Y.; Zhu, M. Highly Conductive, Flexible, and Compressible All-Graphene Passive Electronic Skin for Sensing Human Touch. *Adv. Mater.* **2014**, *26*, 5018-5024.

[428] Fan, F.-R.; Lin, L.; Zhu, G.; Wu, W.; Zhang, R.; Wang, Z. L. Transparent Triboelectric Nanogenerators and Self-Powered Pressure Sensors Based on Micropatterned Plastic Films. *Nano Lett.* **2012**, *12*, 3109-3114.

[429] Park, H.; Jeong, Y. R.; Yun, J.; Hong, S. Y.; Jin, S.; Lee, S.-J.; Zi, G.; Ha, J. S. Stretchable Array of Highly Sensitive Pressure Sensors Consisting of Polyaniline Nanofibers and Au-Coated Polydimethylsiloxane Micropillars. *ACS Nano* **2015**, *9*, 9974-9985.

[430] Alfadhel, A.; Kosel, J. Magnetic Nanocomposite Cilia Tactile Sensor. *Adv. Mater.* **2015**, DOI:10.1002/adma.201504015

[431] Park, J.; Lee, Y.; Hong, J.; Lee, Y.; Ha, M.; Jung, Y.; Lim, H.; Kim, S. Y.; Ko, H. Tactile-Direction-Sensitive and Stretchable Electronic Skins Based on Human-Skin-Inspired Interlocked Microstructures. *ACS Nano* **2014**, *8*, 12020-12029.

[432] Segev-Bar, M.; Haick, H. Flexible Sensors Based on Nanoparticles. *ACS Nano* **2013**, *7*, 8366-8378.

[433] Olichwer, N.; Leib, E. W.; Halfar, A. H.; Petrov, A.; Vossmeyer, T. Cross-Linked Gold Nanoparticles on Polyethylene: Resistive Responses to Tensile Strain and Vapors. *ACS Appl. Mater. Interfaces* **2012**, *4*, 6151-6161.

[434] Lee, D.; Choi, M.-C.; Ha, C.-S. Polynorbornene Dicarboximide/Amine Functionalized Graphene Hybrids for Potential Oxygen Barrier Films. *Journal of Polymer Science Part A: Polymer Chemistry* **2012**, *50*, 1611-1621.

[435] Zhao, F.; Zhao, Y.; Cheng, H.; Qu, L. A Graphene Fibriform Responsor for Sensing Heat, Humidity, and Mechanical Changes. *Angew. Chem. Int. Ed.* **2015**, *54*, 14951-14955.

[436] Su, Q.; Pang, S.; Alijani, V.; Li, C.; Feng, X.; Müllen, K. Composites of Graphene with Large Aromatic Molecules. *Adv. Mater.* **2009**, *21*, 3191-3195.

[437] Ambrosi, A.; Chua, C. K.; Bonanni, A.; Pumera, M. Lithium Aluminum Hydride as Reducing Agent for Chemically Reduced Graphene Oxides. *Chem. Mater.* **2012**, *24*, 2292-2298.

[438] Edwards, R. S.; Coleman, K. S. Graphene Synthesis: Relationship to Applications. *Nanoscale* **2013**, *5*, 38-51.